UNIVERSIDAD DE CÓRDOBA

Programa de doctorado: Química Fina

Título de la tesis:

Diseño de nanomateriales mediante procesos de molienda mecanoquímica para aplicaciones catalíticas y electroquímicas

Design of nanomaterials through mechanochemical grinding processes for catalytic and electrochemical applications

Directores: Alina Mariana Balu Balu

Rafael Luque Álvarez de Sotomayor

Autor de la tesis: Daily Rodríguez Padrón

Fecha de depósito tesis en el Idep: 31/10/2019

TITULO: *DISEÑO DE NANOMATERIALES MEDIANTE PROCESOS DE MOLIENDA MECANOQUÍMICA PARA APLICACIONES CATALÍTICAS Y ELECTROQUIMICAS*

AUTOR: *Daily Rodríguez Padrón*

Campus de Rabanales
Ctra. Nacional IV, Km. 396 A
14071 Córdoba

https://www.uco.es/ucopress/index.php/es/
ucopress@uco.es

UNIVERSIDAD DE CÓRDOBA

Diseño de nanomateriales mediante procesos de molienda mecanoquímica para aplicaciones catalíticas y electroquímicas

Daily Rodríguez-Padrón

Grupo FQM-383. NANOQUÍMICA Y VALORIZACIÓN DE BIOMASA Y RESIDUOS
Departamento de Química Orgánica, Universidad de Córdoba

Índice general

Índice general

Abstract

The present doctoral thesis project deals with the design of nanomaterials with potential applications in two important fields: 1) the design of energy storage devices and 2) heterogeneous catalysis, in both cases for the development of more sustainable processes that contribute to ameliorate climate change. Today, most of the challenges humanity faces are related to energy and environment, including the scarcity of water and resources, energy requirements and the depletion of fossil fuel sources. In particular, energy demands, whether in the transport sector or for stationary applications, are priorities in all the scientific programs and agendas of the world. Hence, many investigations are currently aimed to find new materials with better electrochemical results for the development of a new generation of sustainable energy storage devices. In addition, the development of a more sustainable chemical industry requires high efficient processes and therefore the preparation of active and selective catalytic systems.

Mechanochemical methods have been employed in this doctoral thesis for the design of nanomaterials, including various nanobioconjugates based on proteins and magnetic nanoparticles, as well as metal oxide nanoparticles supported on mesoporous supports and biomass-templated metal oxide nanomaterials. Mechanochemistry offers several advantages regarding its high reproducibility, versatility, simplicity and, specially, to its green character related to the possibility to avoid the use of solvents and additional reagents. Studies on mechanochemistry have greatly increased in the past two decades, nonetheless as an open research line, a lot of efforts still need to be devoted in order to take full advantages of its great potentialities.

Biomass valorization has been one of the main issues covered in this thesis, towards both chemicals and materials. Biomass constitutes, together with CO_2, one of the most abundant renewable carbon sources. Therefore, the use of biomass-derived platform molecules for the preparation of added-value chemicals, replacing the petro-based chemical industry, is a highly attractive option. In particular, along this thesis, biomass derived platform molecules such as levulinic acid and isoeugenol have been employed for the synthesis of *N*-heterocycles and vanillin, respectively. It is important to highlight that, through the valorisation of biomass, added value materials can be also obtained, representing an environmentally friendly methodology. In this regard,, several biomass residues, including spent coffee grounds, egg-white form expired eggs and orange peel have been treated by mechanochemical protocols for the preparation of nanostructured materials with controlled morphology and textural properties.

In particular, through this work a mechanochemical synthetic strategy have been designed for the preparation of bioconjugates, minimizing reaction times and

costs associated with the use of solvents and other reactants. As an alternative to inorganic materials, organic electroactive products, such as proteins have opened new opportunities for the design of innovative energy storage devices with a greater theoretical capacity, safety, sustainability and low cost. Rechargeable batteries and electrochemical supercapacitors (ECs) are among the most representative examples of energy storage devices. The construction of ECs with high energy density and high power has become a priority issue for the development of future devices. Research in this field has focused on the synthesis of active porous nanomaterials such as metal oxides, hydroxides, or carbon-based materials. These materials provide a high capacity, but have several disadvantages including high costs, manufacturing stages, difficult scalability, besides not being respectful with the environment. In order to overcome the inherent drawbacks of conventional inorganic materials, metalloproteins containing heme groups have recently been employed.

However, the development of hybrid systems of hemoproteins and nanoparticles (NPs) for the design of sustainable supercapacitors has not yet been deeply investigated, being a highly innovative and relevant idea for the design of materials that could become a potentially applicable product. Therefore, this doctoral thesis also aimed to synthesize hybrid nanostructures of metalloproteins and nanoparticles through a mechanochemical methodology, as a cheap, sustainable, and versatile strategy, for the design of a new generation of electrochemical supercapacitors.

Another potential application of these hybrid protein-nanoparticle systems is their use in biomimetic catalysis processes. Inspired by the *in vivo* synthesis of natural polymers, where enzymes play an important role as catalysts, *in vitro* enzymatic polymerization has been widely developed to design a wide range of advanced materials. In particular in this project, bioconjugates based on hemoproteins have been used for the preparation of fluorescent carbon-based nanoparticles following a bottom-up strategy. Similarly, carbon quantum dots with fluorescent behavior have been prepared by a top-down methelody from biomass residues and using an iron oxide containing material as catalyst.

In summary, mechanochemistry, as a powerful tool, has been successfully employed to produce a wide range of nanomaterials, from bioconjugates to metal oxides, with applications in catalysis and energy storage. Taking into account the above mentioned premises, the objectives of the proposed work are very relevant for the development of a Sustainable Chemistry and to integrate the strategies of Green Chemistry and Engineering.

Keywords: Mechanochemistry, Nanomaterials, Biomass, Catalysis, Energy storage, Bioconjugates, Metal oxide nanoparticles, Sustainability, Green Chemistry.

1. Introducción

1. Introducción

1.1. Mecanoquímica: hacia el diseño sostenible de nanomateriales

Motivados por los procesos metabólicos, que normalmente ocurren en agua, a lo largo de la historia los científicos han asumido erróneamente que los medios líquidos son un factor indispensable para el desarrollo de las reacciones químicas. Ciertamente, la presencia de disolventes podría favorecer la transferencia de calor y la interacción entre los reactivos. Si bien es cierto que algunas reacciones son incompatibles con condiciones sin disolventes, la posibilidad de evitar su uso podría resultar en procesos más sostenibles. En este sentido, los protocolos mecanoquímicos han surgido como una alternativa prometedora debido a su simplicidad, versatilidad, reproducibilidad y especialmente debido a su inherente sostenibilidad.

Las reacciones asistidas mecánicamente se han empleado desde hace mucho tiempo. Sin embargo, la terminología "mecanoquímica" ha sido recientemente acuñada por la IUPAC como: "una reacción química inducida por la absorción directa de energía mecánica". Wilhelm Ostwald definió por primera vez este término como una rama de la química física (al igual que la termoquímica, la electroquímica o la fotoquímica).[1]

Las fuerzas mecánicas pueden modificar la escena energética de las reacciones químicas y crear nuevas vías de reacción, proporcionando un enfoque sintético que complementa la química convencional.[2] Durante la molienda, tienen lugar varios procesos como la transferencia de masa y la generación y relajación del estrés mecánico asociado con la ruptura del entramado cristalino.[3] Los procesos mecanoquímicos implican varias energías relacionadas con el agrietamiento de los cristales, la alta densidad de defectos y el aumento de la temperatura macroscópica. Dichas energías pueden romper los enlaces y dar lugar a intermedios de reacción de una manera diferente a los procesos en disolución.

1.1.1. Historia de la mecanoquímica

La historia de la mecanoquímica se remonta al siglo IV a. C., cuando Teofrasto de Eresos observó la formación de mercurio elemental al moler el cinabrio (HgS) con vinagre en un recipiente de cobre (Figura 1).[4] Este proceso, considerado como una "molienda asistida mediante disolvente", es una alternativa para minimizar la cantidad de disolventes en las reacciones químicas.[5,6]

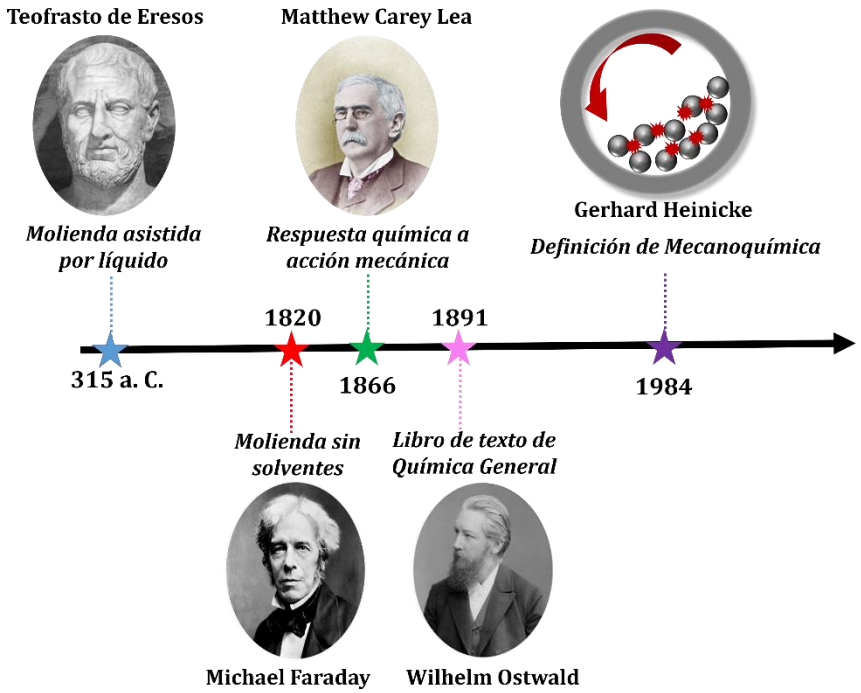

Figure 1. Orden cronológico de los avances en Mecanoquímica.

Michael Faraday realizó una de las primeras investigaciones sistemáticas sobre procesos mecanoquímicos en 1820.[7] Dicho estudio se basó en la reducción de AgCl con varios metales (Zn, Fe, Cu, Sn) mediante molienda sin disolventes. Sin embargo, estos resultados se interpretaron suponiendo que el único efecto directo de la molienda era la generación de calor y, por lo tanto, los cambios químicos observados estaban relacionados con procesos termoquímicos posteriores.

No fue hasta 1866 que se llevó a cabo el primer estudio que asociaba el efecto químico y la acción mecánica. Matthew Carey Lea investigó el

comportamiento de varios sistemas químicos en condiciones termoquímicas o de molienda.[8] En particular, los haluros de plata dieron como resultado la formación de plata elemental por molienda, mientras que por calentamiento solo se observó que los materiales se fundían sin descomposición adicional. El trabajo de Carey representó un cambio radical para la comunidad científica, ayudando al reconocimiento de la mecanoquímica como una subdisciplina de la química.

El término mecanoquímica fue establecido por primera vez en 1891 por Wilhelm Ostwald en un libro de texto de Química General.[1] Además, Gerhard Heinicke en 1984 presentó una definición ampliamente aceptada de mecanoquímica: "esa rama de la química relacionada con los cambios químicos y físicos de sólidos, inducidos por la acción de la influencia mecánica ".[9] A pesar de la larga historia de la mecanoquímica, la mayoría de los desarrollos en este campo se han descrito casi exclusivamente desde hace dos décadas (Figura 2).

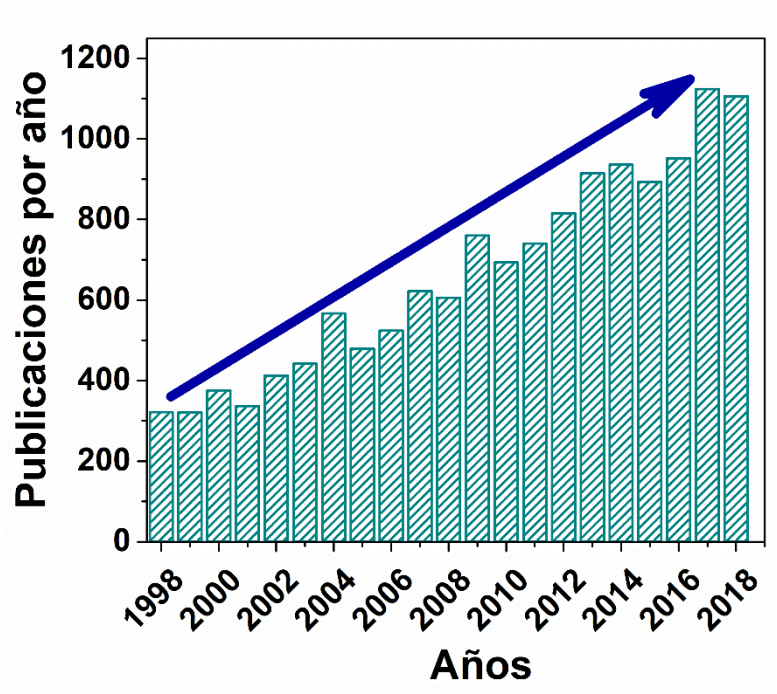

Figura 2. Publicaciones anuales sobre mecanoquímica en el período de 1998-2018.[10]

1.1.2. Aspectos teóricos

A lo largo de la historia de la mecanoquímica, se han propuesto varias teorías. Entre ellas, Bowden y colaboradores establecieron en 1952 la teoría del punto caliente, según la cuál, debido a los procesos de fricción, se generan altas temperaturas en superficie, lo que provoca el inicio de la reacción mecanoquímica.[11,12] Sin embargo, esta idea fue muy criticada. Más tarde, Heinicke propuso el modelo de plasma de magma.[13] De acuerdo con este modelo, se produce una gran cantidad de energía en el punto de contacto de las partículas en colisión, que es el responsable de la formación de un "*estado plasmático"* especial. Los autores afirmaron que las reacciones pueden ocurrir en el plasma o en la superficie de las partículas y, por lo tanto, no obedecen a un mecanismo único. Además, muchos otros científicos han estudiado las reacciones asistidas mecánicamente, desarrollando varias teorías y modelos.[14-16]

Vale la pena señalar que, a diferencia de las reacciones asistidas térmicamente, los procesos activados mecánicamente tienen lugar en condiciones de no-equilibrio, donde la reactividad química está influenciada por fuerzas mecánicas. Además, la deformación mecánica, y por lo tanto la transformación mecanoquímica, tienen lugar localmente, mientras que la temperatura es una variable termodinámica de estado intensiva.[17,18] Por consiguiente, debe esperarse que las condiciones mecánicas y térmicas den como resultado diferentes procesos de transporte de masas y diferentes comportamientos físicos y químicos de los reactivos.

Desde un punto de vista cinético, las reacciones mecanoquímicas pueden interpretarse empleando la teoría de la colisión, teniendo en cuenta que el proceso de dispersión y la activación mecánica son procesos estadísticamente probables.[19] La energía cinética, producida durante la reacción mecanoquímica puede promover la abrasión, la fractura y refinamiento de la microestructura del sistema.[20,21] En particular, la fractura determina un aumento del área superficial, mejora la probabilidad de contacto entre los reactivos y, por lo tanto, influye directamente en la velocidad de la reacción mecanoquímica.[22,23] En este sentido, se ha estudiado que moléculas de etanol interaccionaban con los sitios activos en la superficie de partículas de cuarzo fracturadas, dando lugar a radicales hidrógeno. Además, el papel crucial de estos sitios en la

reacción química se demostró mediante reacciones conocidas como *scavenger*.[24]

El mecanismo de las reacciones mecanoquímicas sigue siendo motivo de estudio y discusión. En este sentido, la molienda se puede detener después de diferentes intervalos de tiempo para estudiar *ex-situ* la mezcla de reacción. Sin embargo, este análisis no es exacto, especialmente cuando compuestos volátiles están involucrados en los procesos de reacción. En algunos casos, la molienda solo es necesaria para proporcionar la energía de activación para dar comienzo a la reacción, la cual puede continuar sin molienda. La espectroscopía Raman *in-situ* se ha empleado recientemente para controlar una reacción mecanoquímica, utilizando una cámara translúcida.[25] Esta técnica, al igual que la difracción de rayos X *in-situ*, han resultado ser herramientas muy útiles para el estudio de los mecanismos involucrados en reacciones mecanoquímicas.[25] Friščić y colaboradores[26] realizaron un estudio en tiempo real del progreso de una reacción mediante difracción de rayos X en un sincrotrón de alta energía. En este caso, fue estudiada la preparación de un *Metal Organic Framework* (MOF): Zn-MOF-74,[27] sintetizado directamente a partir de un óxido metálico mediante molienda mecanoquímica, empleando la técnica antes mencionada.[28] Sin embargo, las investigaciones *in-situ* de reacciones realizadas por procesos de molienda todavía están en un estado incipiente y muchos más esfuerzos debe ser dirigidos en esta dirección.
Hoy en día, la mayoría de los mecanismos de reacción se infieren a partir de mediciones *ex-situ* mediante difracción de Rayos-X (XRD), Resonancia Magnética Nuclear (RMN) de estado sólido y Espectroscopía Infrarroja (FT-IR). Un ejemplo de este tipo de estudios ha sido llevado a cabo para investigar los cambios estructurales inducidos mediante procesos de molienda en materiales tipo Al-SBA-15, con un precursor de hierro, utilizando análisis de Espectroscopia Infrarroja de Reflectancia Difusa (DRIFT). Esta técnica, a la par con mediciones XRD, reveló la formación de hidróxidos, sugieriendo que la reacción tenía lugar a través de la deshidroxilación de los materiales.

1.1.3. Equipos

Las reacciones mecanoquímicas se pueden llevar a cabo utilizando una amplia gama de condiciones con varios tipos de equipos.[29] El mortero convencional se ha estudiado ampliamente, siendo una de las

herramientas menos costosas para llevar a cabo procesos mecanoquímicos. No obstante, el empleo de este tipo de instrumentos no es reproducible, ya que no es posible controlar fuertemente las condiciones de reacción como la frecuencia y la resistencia.[30] Los morteros manuales han servido de inspiración para el diseño de morteros de molienda de alto rendimiento con control electrónico (Figura 3). Además, se han desarrollado molinos de bolas especializados, entre los que se incluyen molinos mezcladores y molinos planetarios. Estos instrumentos son reconocidos por ser capaces de realizar moliendas de alta energía con un gran control de las condiciones de reacción. Los molinos mezcladores emplean matraces cilíndricos que oscilan horizontalmente, lo que produce altas fuerzas de impacto entre el rodamiento de bolas y los extremos curvos del matraz. Además, los molinos planetarios realizan movimientos giratorios sobre el eje del recipiente y de traslación al mismo tiempo, proporcionando altas fuerzas centrífugas y de fricción entre los materiales. Los molinos de bolas generalmente permiten una mayor distribución de la energía mecánica y el uso de mayores volúmenes de reacción, mientras que los molinos mezcladores normalmente producen mayores energías de impacto.[31]

Además también destacan otros instrumentos, entre los que se incluyen molinos de tambor y molinos criogénicos (para molienda criogénica). Recientemente se han desarrollado nuevos diseños de molinos de bolas de alta energía, con velocidades máximas de 2000 rpm. Estos instrumentos poseen sistemas de enfriamiento de agua, que permiten liberar la energía durante el proceso de molienda sin sobrecalentamiento de la muestra.

Entre las variables que afectan el rendimiento mecanoquímico, la velocidad de molienda, el tiempo de molienda, la atmósfera de reacción, la relación bola-material y el tipo de instrumento de molienda son algunos de los más relevantes. Se ha empleado una gran variedad de materiales para el diseño tanto de las bolas como de los recipientes para reacciones mecanoquímicas, entre los que cabe mencionar el teflón, la alúmina, la circonia, el acero inoxidable y el carburo de tungsteno.[32]

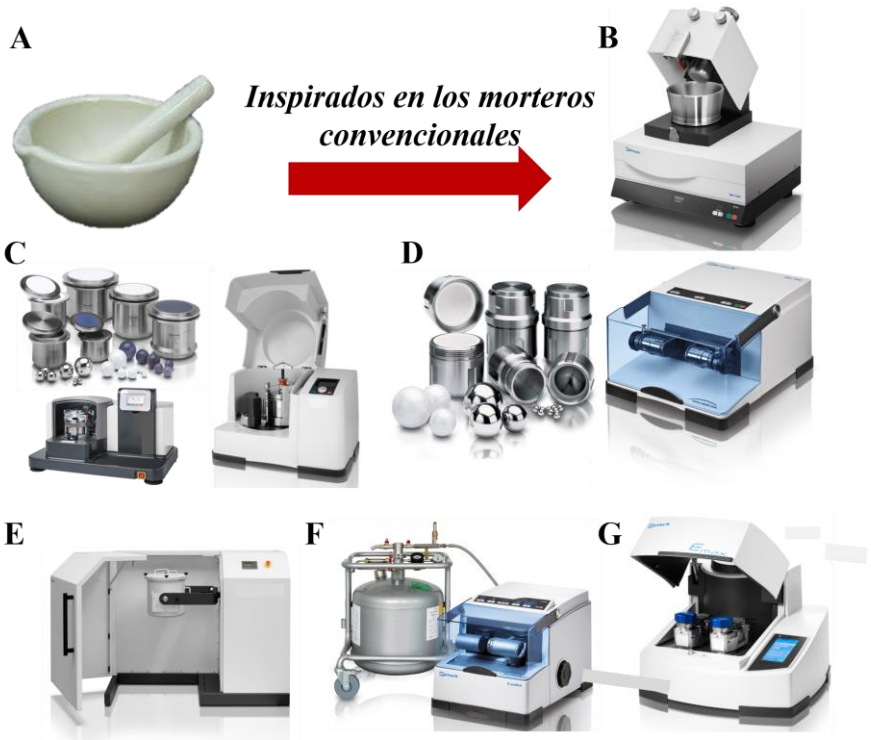

Figura 3. Descripción general del equipo para la síntesis mecanoquímica (Fritsch y Retsch). (A). Mortero convencional (B) Molino de mortero (C) Molinos planetarios (recipientes, bolas y equipos). (D) Molino mezclador (recipientes y equipos). (E) Molino de tambor. (F) Crio-molino. (G) Molino de alta energía (Emax).

1.1.4. Nanomateriales avanzados para almacenamiento de energía y aplicaciones catalíticas

Los catalizadores heterogéneos han ganado gran atención por parte de la comunidad científica, ya que juegan un papel crucial en el desarrollo de la industria química.[33-36] De hecho, la alta actividad y selectividad de los sistemas catalíticos ha dado lugar a procesos más eficientes tanto desde el punto de vista económico como ambiental. Los métodos convencionales para la preparación de materiales catalíticos incluyen (co-)precipitación, impregnación, técnicas sol-gel, microemulsión, síntesis asistidas por microondas y síntesis hidrotermales, entre otros.[37-40] Tales procedimientos han mostrado varias ventajas y han dado lugar a una gran cantidad de materiales aplicables. Sin embargo, dichos protocolos también poseen desventajas relacionadas con los largos

tiempos de reacción, las altas temperaturas y el uso de disolventes y reactivos adicionales, que podrían tener un impacto negativo en el medio ambiente. En este sentido, la síntesis mecanoquímica ha surgido como una alternativa sobresaliente. Este protocolo se ha utilizado para la preparación de una amplia gama de nanomateriales con aplicaciones catalíticas, como nanopartículas de óxidos metálicos y de metales soportados, perovskitas, nanocomposites, estructuras organometálicas de tipo MOF y bioconjugados (por ejemplo, basados en proteínas y nanopartículas de óxido metálico), como se representa esquemáticamente en la Figura 4.[41-47]

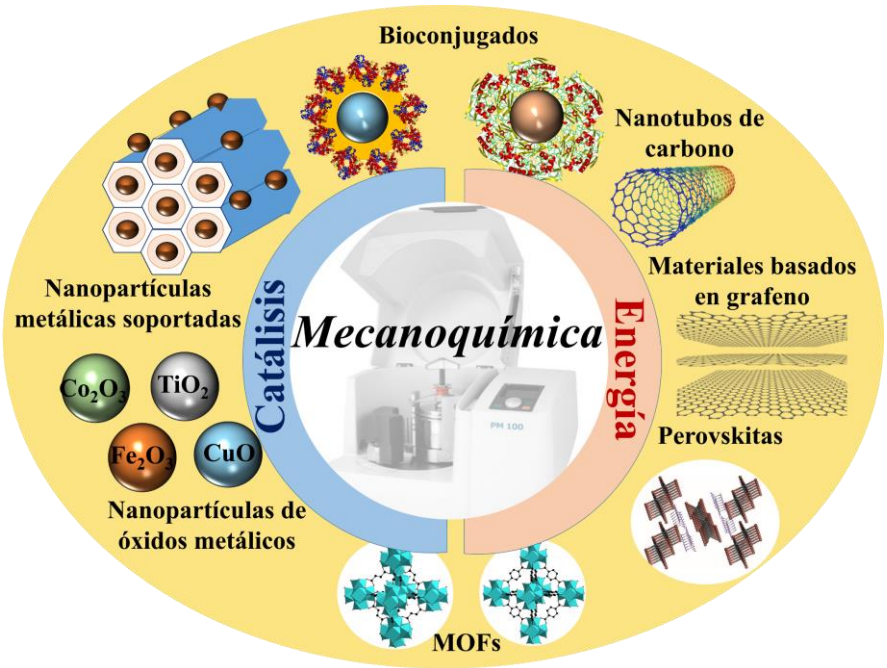

Figura 4. Representación de nanomateriales avanzados sintetizados por protocolos mecanoquímicos para aplicaciones catalíticas y de almacenamiento de energía.

En los últimos años, la mecanoquímica se ha convertido en una alternativa poderosa y prometedora para la fabricación de nanomateriales basados en carbono y bioconjugados con potenciales aplicaciones en el diseño de dispositivos de almacenamiento de energía, abriendo nuevos horizontes en el campo de la nanoenergía. En esta tesis doctoral, centraremos nuestra atención en dispositivos de almacenamiento de energía de tipo electroquímico, tales como, baterías

y supercapacitores, que se basan en la carga/descarga de electrones e iones.[48]

Varios nanomateriales basados en carbono, tales como los nanotubos de carbono (CNT), las nanofibras de carbono (CNF), los materiales carbonosos derivados de carburo (CDC) y el grafeno son algunos de los ejemplos más utilizados para la fabricación de supercapacitores ultrarrápidos y baterías altamente eficientes.[48-53] En este sentido, se ha demostrado que la activación de la superficie mediante diferentes tratamientos químicos y/o funcionalización con O, N y B pueden mejorar los rendimientos electroquímicos.[54,55] En general, la funcionalización o activación química requiere una gran cantidad de disolventes y reactivos tóxicos y corrosivos, incluidos el acetonitrilo, hexano, HF y H_2SO_4, lo que contribuye a la contaminación ambiental. Además, la mayoría de estos procesos requieren varios pasos, como la impregnación, la carbonización y el lavado, lo que suele dar como resultado bajos rendimientos hacia los productos deseados. En cambio, la mecanoquímica se ha empleado con éxito para preparar materiales anódicos para baterías de iones litio (LIBs),[56] entre los que se encuentran muestras basadas en grafeno y nanopartículas de óxido de hierro. De igual forma, los procedimientos mecanoquímicos se han empleado en la preparación de nanocomposites de grafeno con SnO_2, así como con Sn_3P_4. Destacan también los materiales carbonosos dopados con nitrógeno, sintetizados por ejemplo a partir de lignina y urea,[57] o a partir de grafeno y nitrógeno gaseoso.[58]

Además de las ventajas antes mencionadas (protocolos sintéticos ecológicos, baratos, fáciles, etc.), el enfoque mecanoquímico surge como un método eficiente para producir nanocatalizadores altamente activos y estables. En este sentido, se ha sintetizado una amplia gama de catalizadores mediante transformaciones químicas inducidas por compresión mecánica, cizallamiento o fricción.[33]

En cuanto a la preparación de nanopartículas (NP), la mecanoquímica permite abordar diferentes estrategias de síntesis. Varios ejemplos han demostrado que los materiales preparados mediante estos protocolos muestran mejores resultados de actividad que aquellos obtenidos por métodos sintéticos típicos como deposición química o impregnación. Por ejemplo, un procedimiento simple de molienda permitió la preparación de catalizadores activos de Ag/Al_2O_3 para la reducción catalítica selectiva de gases NO_x con octano, a baja temperatura (inferior a 200 °C). En

cambio, el catalizador preparado por el método de impregnación típico no mostró buenos resultados en dichas condiciones de reacción a relativamente baja temperatura.[59]

Asimismo, se ha descrito la preparación una aleación de Au-Pd y sus contrapartes de Au y Pd soportadas en dióxido de titanio comercial (P25) y SiO_2, mostrando una actividad notable durante la oxidación del alcohol bencílico y la síntesis directa de peróxido de hidrógeno. Este estudio también demostró que los catalizadores sintetizados mediante protocolos mecanoquímicos pueden resultar más activos que los catalizadores equivalentes preparados mediante la ruta de impregnación, lo que sugiere que puede haber una mejor interacción, o incluso un efecto sinérgico, entre ambos metales. Otro tipo de soportes como nanotubos de carbono también pueden modificarse mediante procedimientos mecanoquímicos para la preparación de materiales activos y eficientes en catálisis. En este sentido, se puede resaltar la preparación mecanoquímica a temperatura ambiente de nanotubos de carbono simples modificados con Pd. Las muestras mostraron una distribución homogénea de partículas y una notable actividad catalítica en reacciones de acoplamiento C-C de tipo Suzuki.[60]

Tanto para NP de metales nobles, como para otras estructuras avanzadas, la presencia de aditivos en el proceso de molienda puede definir las propiedades finales y la eficiencia de la ruta sintética. Recientemente, se ha descrito el papel de carbohidratos como aditivos en la síntesis mecanoquímica de nanopartículas de oro y el uso de los materiales resultantes como catalizadores en la reducción de varios derivados de nitrobenceno sustituidos, para obtener productos de tipo anilina sustituidos. Este es un caso muy interesante en el que el aditivo permitió, al mismo tiempo, la estabilización de las nanopartículas y la formación selectiva de productos derivados de la anilina. Los autores demostraron que el rendimiento catalítico depende en gran medida de la naturaleza del aditivo, la naturaleza y posición del sustituyente, así como de las condiciones de molienda.[61]

Los óxidos metálicos obtenidos por mecanoquímica constituyen también una nueva alternativa la la obtención de nuevos materiales catalíticos. La modificación de la forma y el tamaño de las partículas, el desorden estructural y los defectos en la estructura cristalina pueden conducir a propiedades catalíticas interesantes y novedosas. Puede destacarse un

trabajo reciente, en el cuál se desarrolló una familia de catalizadores mesoporosos de metales de transición dopados con cerio, con alta área superficial, mediante procesos mecanoquímicos.[62]

Teniendo en cuenta todo lo abordado en los apartados anteriores, la presente tesis doctoral se centrará en explorar las amplias potencialidades de los procedimientos mecanoquímicos para la síntesis de materiales con aplicaciones tanto en catálisis como para el diseño de dispositivos de almacenamiento de energía.

1.2. Catálisis ambiental: presente y futuro

Actualmente, las limitadas reservas de petróleo (que pueden provocar una crisis futura en la producción de compuestos químicos, materiales, polímeros, energía y combustibles), así como la tendencia creciente del calentamiento global y los posibles efectos sobre la seguridad humana y ambiental, han alertado a la comunidad científica para avanzar hacia el diseño de procesos más ecológicos. En este sentido, la Química Verde propone el uso, preferentemente, de recursos renovables, disminuyendo las cantidades de residuos y evitando el uso de reactivos y disolventes adicionales, que puedan tener un impacto desfavorable en el medio ambiente.[63] Teniendo en cuenta los principios de la Química Verde,[64] la catálisis ha emergido como un factor clave para el desarrollo sostenible de la economía mundial,[65,66] donde puede definirse desarrollo sostenible como el desarrollo que satisface las necesidades de la generación actual sin comprometer las necesidades de las futuras generaciones.[67]

La catálisis ofrece varias ventajas desde un punto de vista sostenible, evitando el uso de cantidades estequiométricas, favoreciendo el aumento de la selectividad y la disminución de los requerimientos energéticos.[68-70] Específicamente, la valorización de biomasa, la producción de hidrógeno a partir de agua y la reducción de CO_2, son procesos claves, que requieren el desarrollo urgente de materiales catalíticos más eficientes y sostenibles.[71] Definidos por la IUPAC, los catalizadores son sustancias que aumentan la velocidad sin modificar la variación de energía interna de Gibbs en una reacción.[72] La catálisis puede considerarse como una ciencia multidisciplinaria, que involucra ingeniería química, química sintética y física, química teórica y química del estado sólido. Entre las diferentes alternativas en catálisis, la biocatálisis, la fotocatálisis y la electrocatálisis

han surgido como las posibilidades más prometedoras (Figura 5). Además, otros enfoques como la foto-electrocatálisis o la foto-termocatálisis, aparecen como opciones relevantes para mejorar la eficiencia de los procesos catalíticos.[73,74]

Hoy en día, la mayoría de los procesos químicos (85-90%) empleados en las industrias alimentaria, farmacéutica y energética, implican al menos un paso catalítico. En este sentido, la eficiencia es un factor esencial, relacionado con la maximización de los beneficios con un costo mínimo desde diferentes puntos de vista, considerando el consumo de energía y materiales y el impacto ambiental, entre otros factores.[75] El parámetro mencionado anteriormente se puede clasificar como: a) eficiencia atómica, relacionada con la reducción de desechos y subproductos, b) rentabilidad, asociada a la reducción de las inversiones de capital y el tiempo de producción y c) eficiencia energética, vinculada a la reducción de la energía consumida durante el proceso. Además, el término factor E (ambiental), definido como la cantidad de desechos producidos por kg de producto, se ha empleado como un parámetro conveniente, particularmente, para determinar el impacto ambiental de un proceso determinado. El factor E tiene en cuenta, no solo la cantidad prevista de residuos, teniendo en cuenta la ecuación estequiométrica, sino también los residuos reales formados en el proceso, incluyendo los disolventes y otros materiales auxiliares.[76,77]

Teniendo en cuenta todo lo anteriormente mencionado, en esta tesis doctoral se abordará la aplicación de la catálisis heterogénea para el diseño de procesos más eficientes, que propicien el desarrollo de un mundo sostenible con una utilización plena de las energías renovables.

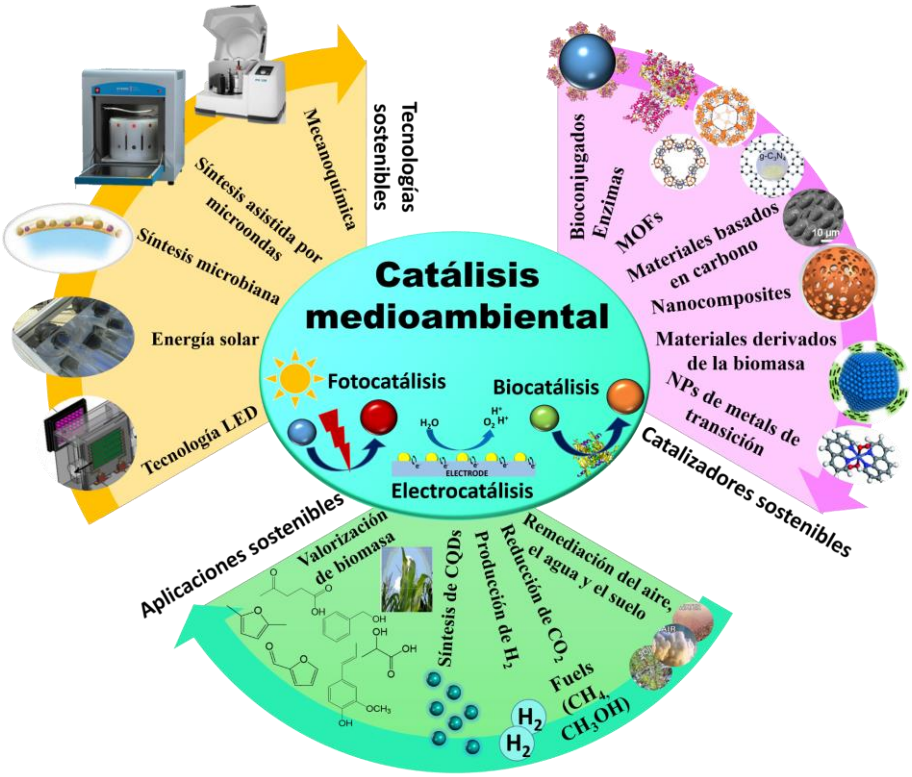

Figura 5. Representación esquemática de materiales catalíticos sostenibles, procedimientos de preparación de catalizadores y nuevas tecnologías, así como aplicaciones relevantes en el campo de la catálisis ambiental y la química verde.

1.2.1. Materiales catalíticos sostenibles. Nanocatalizadores preparados a partir de biomasa

Numerosos estudios se han centrado en el desarrollo de nuevos materiales con posibles aplicaciones catalíticas.[78-82] Desde un punto de vista medioambiental, se ha prestado especial atención al diseño de catalizadores derivados de biomasa.[83-85] La biomasa es un concepto amplio, que incluye materiales lignocelulósicos, almidón/semillas oleaginosas/azúcar, cultivos acuáticos y desechos bioderivados (residuos agrícolas/animales/antropológicos).

Es bien sabido que el rendimiento catalítico está profundamente relacionado con las propiedades texturales, especialmente con el área

superficial. Por lo tanto, una de las estrategias más empleadas para el diseño de catalizadores se basa en la inmovilización/incorporación de especies activas en la superficie de materiales que sirvan de soporte y ofrezcan buenas propiedades texturales. Varios soportes basados en carbono se han obtenido principalmente mediante procesos hidrotermales, que permiten aumentar o cambiar la solubilidad, acelerar las interacciones químicas y físicas y finalmente conducir a la formación de estructuras carbonosas.

Por otro lado, se ha prestado especial atención a la síntesis directa de materiales mesoporosos basados en carbono y derivados de diferentes polisacáridos, como el almidón, los alginatos obtenido a partir de especies de macroalgas y las pectinas derivadas de las cáscaras de los cítricos, entre otros. Dicha familia de materiales carbonosos, también llamados *Starbons*, ha mostrado propiedades texturales notables, lo cual los convierte en buenos candidatos como catalizadores y soportes catalíticos.[86,87] Los materiales anteriormente mencionados han sido diseñados mediante una metodología simple basada en la formación de un gel acuoso, seguido de intercambio de disolvente y carbonización térmica. Además, se han preparado otros soportes carbonosos con áreas superficiales sobresalientes (hasta 3000 m^2 g^{-1}) a partir de varios residuos de biomasa, como cáscara de arroz, cáscaras de piña y tallos de maíz.[88] También, se han empleado con éxito residuos de biomasa vegetal, incluidos el bambú, el algodón y la madera, para fabricar soportes catalíticos porosos a través de un enfoque sin reactivos químicos.[89] En general, los residuos de biomasa pueden conferir un gran número de grupos funcionales, tales como grupos carboxilo, carbonilo e hidróxilo, a los materiales resultantes, los cuáles pueden actuar como sitios de anclaje facilitando la posterior deposición de metales.

Por otra parte, el método de la utilización de agentes directores de la estructura o método *plantilla* (*Template method*) es una estrategia efectiva y simple para obtener nanoestructuras con diferentes morfologías y elevadas áreas superficiales. La mayoría de los enfoques presentados en la bibliografía, en este sentido, incluyen dos pasos: en primer lugar, los materiales o precursores deseados se ensamblan alrededor de la superficie de un agente director de la estructura mediante adherencia química o física para formar compuestos de transición. Posteriormente, los agentes directores de la estructura se eliminan selectivamente en un segundo paso. Cuando dicho agente director de la

estructura se elimina completamente para dar lugar a los materiales deseados, el método es conocido como método de plantilla de sacrificio (*Sacrificial template method*). Dicha metodología se ha empleado para la síntesis de una amplia gama de materiales, a través de la valorización de la biomasa (empleando por ejemplo cáscaras de plátano).[88]

Se puede mencionar, asimismo, a modo de ejemplo, la síntesis de catalizadores basados en óxido de hierro empleando huminas como plantilla de sacrificio,[90] para dar lugar a nanomateriales.[91] Curiosamente, las especies de óxido de hierro y los restos de carbono del residuo empleado presentaron un efecto sinérgico en la oxidación de isoeugenol. Tales resultados sugieren que los desechos de biomasa pueden representar una alternativa a los materiales carbonosos típicos, resultando, no solo en sistemas catalíticos más baratos, sino más efectivos. Basándose en los mismos principios, se han preparado nanocatalizadores de óxido de hierro empleando polisacáridos derivados de hongos como plantilla de sacrificio.[92]

Otros materiales emergentes, como los bioconjugados basados en nanopartículas de óxidos metálicos y proteínas han mostrado resultados catalíticos prometedores en reacciones de polimerización oxidativa. Al combinar las ventajas, desde un punto de vista medioambiental, de las reacciones catalizadas por proteínas tales como las condiciones de operación moderadas y la alta selectividad, con la fácil recuperación y reutilización de las nanopartículas de óxidos metálicos, se pueden abrir nuevos horizontes para el diseño de catalizadores.[93-95]

1.2.2. Aplicaciones ambientales. Valorización de biomasa

Como se mencionó anteriormente, la catálisis tiene una importancia notable para el medio ambiente. Actualmente, los catalizadores están presentes en la mayoría de las ciencias ambientales con aplicaciones mayormente para la remediación del aire, el agua y el suelo, así como para el uso de energías renovables.[96]

En relación con los contaminantes del aire, tales como CO, NO_X, hidrocarburos (HC), compuestos orgánicos volátiles (COVs) y partículas, se han desarrollado varias investigaciones para mejorar la eficiencia catalítica, así como para reducir el coste asociado con los catalizadores basados en metales nobles.[97] La eliminación catalítica de hollín y gases de tipo NO_X ha sido uno de los principales objetivos de la industria

automotriz.[98,99] Las emisiones de los últimos compuestos pueden regularse mediante trampas de NO_x, descomposición catalítica asistida por plasma, reducción catalítica y reducción de NO_x combinada con combustión de hollín.[100] La oxidación de NO_x también se ha propuesto como una opción prometedora para regular las emisiones de NO, a través de la formación de HNO_3 en presencia de agua.[101]

La eliminación de COVs como metanol, acetona, benceno, tolueno, naftaleno, acetato de etilo y formaldehído, siendo el último uno de los COVs más comunes, también se ha realizado por procesos de oxidación empleando catalizadores heterogéneos.[102] De igual forma, los tratamientos de agua, para aguas residuales, agua potable y lodos, tienen una gran importancia para el medioambiente debido al incremento actual de la demanda de agua, el rápido proceso de industrialización y el amplio uso de pesticidas, herbicidas y fármacos.[103] Los métodos catalíticos pueden representar una alternativa ecoeficiente para reducir este tipo de contaminantes. Además, la desulfuración de las fracciones de combustible diesel ha representado un reto ampliamente abordado y estudiado en todo el mundo para minimizar las emisiones nocivas y obtener combustibles respetuosos con el medio ambiente.[104] La utilización de materiales catalíticos eficaces ha representado un factor clave para lograr este objetivo.[105]

Además del CO_2, los residuos de biomasa representan la única fuente de energía abundante y renovable terrestre basada en carbono.[106-108] Particularmente, la biomasa lignocelulósica se compone principalmente de lignina (15-30%), celulosa (35-50%) y hemicelulosa (20- 35%).[109] Esta materia prima de base biológica se ha convertido en una de las fuentes más ventajosas, debido a su gran abundancia, para obtener compuestos químicos como carbohidratos, terpenos, compuestos aromáticos y ésteres grasos.[110,111] Por lo tanto, la conversión de residuos de biomasa para la obtención productos químicos puede representar una alternativa interesante para la industria química.[112] Sin embargo, la valorización eficiente de biomasa lignocelulósica sigue siendo un desafío desde un punto de vista económico. En este sentido, la catálisis puede allanar el camino para una utilización más amplia de las energías renovables.

Se han estudiado varios compuestos-plataforma derivados de la biomasa, incluyendo etanol, furanos, glicerol, ácido succínico, ácido levulínico, biohidrocarburos, sorbitol y ácido láctico, entre otros.

En particular, el ácido levulínico y sus derivados de tipo éster, los levulinatos de alquilo, se encuentran entre las moléculas plataforma más importantes, que pueden dar lugar a una amplia variedad de productos químicos, incluidos aditivos para combustibles, monómeros y heterociclos *N*-substituidos. La γ-valerolactona (empleada en la producción de biocombustibles y biopolímeros), el 1,4-pentanodiol (compuesto intermedio en la preparación de biopolímeros), el 2-metiltetrahidrofurano (con aplicaciones como biocombustible y para la industria farmacéutica como un disolvente verde alternativo) y las pirrolidonas *N*-sustituidas, son solo algunos ejemplos de los posibles compuestos de alto valor añadido derivados del ácido levulínico.[113-118]

En particular, los heterociclos *N*-substituidos representan una familia atractiva de compuestos orgánicos que están presentes en muchos de los productos químicos más demandados en la sociedad moderna.[119] Entre esta amplia gama de productos caben destacar colorantes, compuestos agroquímicos, polímeros y compuestos farmacéuticos.[120-123] Se han desarrollado varios enfoques para la preparación de *N*-heterociclos. Por ejemplo, el Prof. Yan y colaboradores han desarrollado un protocolo sintético sencillo para generar moléculas de pirrol a partir de compuestos derivados de residuos alimentarios con rendimientos significativos.[124] Además, el grupo de investigación del Prof. Xu ha presentado un método innovador para transformar directamente biomasa lignocelulósica en varios heterociclos, tales como el pirrol, la piridina e indoles, utilizando zeolitas comerciales como catalizadores a través de una conversión termocatalítica. Por otra parte, el ácido levulínico se ha empleado para producir *N*-pirrolidonas sustituidas mediante un proceso de aminación reductiva seguida de una posterior ciclación.[115-117]

Otros compuestos tales como el 2,5-dimetilfurano (DMF) y el 5-hidroximetilfurfural (HMF), ambos derivados de la biomasa, también han atraído la atención de la comunidad científica en los últimos años debido a su potencial para la preparación de productos químicos valiosos.[125,126] Entre la amplia gama de ejemplos que se pueden dar, vale la pena mencionar la síntesis de *p*-xileno (PX), el cual es un compuesto importante en la industria petroquímica y se emplea como co-monómero,

junto con el monoetilenglicol (MEG) para la preparación del tereftalato de polietileno (PET). El polímero antes mencionado se usa ampliamente para la fabricación de plásticos y fibras sintéticas.[127]

Otras moléculas preeminentes derivadas de la lignina como el eugenol, isoeugenol y ácido ferúlico se han empleado para la síntesis de vainillina mediante reacciones de oxidación. La vainillina sintética, actualmente producida a partir de productos derivados del petróleo (ácido glioxílico y guayacol), posee un alto valor como agente aromatizante en las industrias cosmética, farmacéutica y alimentaria.[128] Para minimizar los residuos químicos y evitar metodologías sintéticas no sostenibles, la comunidad científica ha avanzado hacia el uso de la biomasa como materia prima para la producción de vainillina sintética, a través de estrategias de oxidación catalítica, empleando como oxidantes verdes el H_2O_2 y el oxígeno molecular.[129-132]

El ácido láctico, otro producto químico obtenido a partir de biomasa,[133] ofrece nuevas posibilidades para la síntesis de productos químicos debido a sus grupos funcionales (hidroxilo y carboxilo).[134,135] Dicha molécula puede dar lugar a varios compuestos de alto valor añadido como el acetaldehído mediante procesos de descarbonilación/descarboxilación, la 2,3-pentanodiona mediante reacciones de condensación, el ácido acrílico mediante procesos de deshidratación, el ácido pirúvico mediante reacciones de deshidrogenación y el ácido poliláctico mediante reacciones de polimerización.[136] La elección adecuada del sistema catalítico es un factor crucial para la formación selectiva del producto deseado.

Además, la conversión de residuos lignocelulósicos en materiales fotoluminiscentes ha despertado recientemente el interés de la comunidad científica debido a la amplia gama de aplicaciones en pantallas, sensores biológicos, dispositivos LED (diodos emisores de luz) y dispositivos optoelectrónicos. En particular, los puntos cuánticos de carbono (CQD) han atraído considerablemente la atención de la comunidad científica, debido a sus propiedades biocompatibles. Sin embargo, la preparación de este tipo de nanopartículas generalmente requiere altos tiempos de reacción y altas temperaturas. Por lo tanto, la catálisis representa una opción innovadora para la síntesis de este tipo de materiales.

1.2.3. Electrocatálisis ambiental

Como se mencionó anteriormente, las fuentes de energía convencionales, derivadas de los combustibles fósiles, dan lugar a contaminantes tóxicos con un impacto negativo en el aire y la naturaleza. En consecuencia, el desarrollo de tecnologías limpias para generar combustibles a través de rutas eficientes y de bajo costo se ha convertido en un objetivo crucial para la sociedad moderna. Para lograr este propósito, la electrocatálisis, que se define comúnmente como un tipo de catálisis que da como resultado la modificación de las velocidades de la reacción electroquímica en las interfaces electrodo/electrolito, constituye una herramienta útil hacia un futuro más sostenible. Esta rama de la electroquímica ha ganado un interés especial recientemente, debido a las grandes posibilidades de los electrocatalizadores para facilitar la generación de combustibles de forma eficiente y sostenible.[137-140]

En este sentido, las reacciones electroquímicas pueden permitir eficientemente la generación de hidrógeno a partir de agua y la electroreducción de CO_2 para producir combustibles sostenibles a partir de recursos renovables. Entre las diversas ventajas de los métodos electrocatalíticos se debe mencionar que: (1) el proceso está controlado por el potencial en las interfaces electrodo/electrolito, (2) es posible acoplar otras técnicas para obtener una visión más profunda del sistema (3) la energía para desencadenar el proceso electrocatalítico se puede obtener a partir de recursos naturales utilizando energía solar, eólica, hidráulica, geotérmica, de mareas y termoeléctrica, y (4) la configuración electroquímica es fácil, compacta y se puede escalar fácilmente.

Un gran número de estrategias respetuosas con el medio ambiente dirigidas a la síntesis de electrocatalizadores han sido ampliamente estudiadas en los últimos años debido a la creciente demanda en conversión y almacenamiento de energía renovable para garantizar la sostenibilidad energética mundial. La mayoría de las estrategias actuales para fabricar electrocatalizadores generalmente requiere precursores tóxicos y costosos y productos químicos adicionales, que a su vez, aumentan los costes y limitan sus aplicaciones. Para superar estos inconvenientes, la conversión de recursos naturales en materiales basados en carbono, así como la síntesis microbiana y el diseño de sistemas electrocatalíticos sostenibles basados por ejemplo en proteínas, han abierto nuevos horizontes en este sentido.

En particular, la conversión de biomasa en materiales carbonosos ha sido una estrategia utilizada para obtener electrocatalizadores a partir de materias primas más económicas, abundantes y renovables.[141,142] Los materiales basados en carbono resultantes se han aplicado con éxito a varias reacciones electrocatalíticas como la reacción de evolución del hidrógeno (HER), las reacciones de evolución (OER) y de reducción del oxígeno (ORR) y la reducción electrocatalítica del CO_2.

La electrólisis del agua, generando hidrógeno (H_2) y oxígeno (O_2) mediante las reacciones HER y OER, presenta una serie de ventajas que la convierten en una alternativa prometedora, entre las que destacan la alta eficiencia de conversión de energía, la insignificante contaminación ambiental y por tanto el carácter altamente sostenible. En condiciones ácidas, la oxidación del agua a oxígeno (OER) tiene lugar en el ánodo según la ecuación: $2H_2O \rightarrow O_2+4e^- + 4H^+$, mientras en el cátodo, se obtiene hidrógeno (HER) mediante la recombinación de protones y electrones, según la ecuación: $4e^- + 4H^+ \rightarrow 2H_2$. Entre las metodologías tradicionales de electrólisis del agua, las celdas electrolíticas de membrana de intercambio de protones constituyen un enfoque versátil para generar combustibles que, a su vez, pueden combinarse con varias fuentes de energía sostenibles. Además, poseen muchas ventajas que incluyen un tiempo de respuesta dinámico rápido, una relación favorable entre la eficiencia y densidad de energía, la alta pureza del hidrógeno obtenido y el diseño robusto.[143,144]

Por otra parte, la reacción de reducción del oxígeno también ha sido foco de la atención de la comunidad científica en los últimos años, ya que es la reacción catódica de las celdas de combustible. Por lo tanto, uno de los mayores desafíos actuales es la preparación de catalizadores eficientes tanto para las reacciones de evolución como para las reacciones de reducción de oxígeno, particularmente, para celdas de combustible regenerativas o reversibles, un sistema de almacenamiento de energía que funciona como una celda de combustible y a su vez, reversiblemente producen H_2 y O_2, por electrolisis del agua, para la alimentación de la celda de combustible.[145]

A pesar de los enormes esfuerzos, desarrollar electrocatalizadores con alta actividad y a bajos costes, sigue siendo un gran reto. El actual cuello de botella de las celdas de combustible reside en las reacciones ORR, el cual es el paso limitante para la generación de electricidad. Principalmente, los materiales de platino (o sus aleaciones) constituyen,

hasta el momento, los sistemas más utilizados para reacciones de tipo ORR. Debido al alto costo del Pt, se han buscado activamente catalizadores alternativos basados en otros metales menos costosos, como metales de transición, así como otros materiales que no contengan metales.[145,146]

Por otra parte, la reducción electroquímica del CO_2 para la preparación de compuestos químicos valiosos se ha convertido también en una estrategia útil para generar combustibles, reduciendo, a su vez, las emisiones de carbono. Especialmente, también se ha propuesto integrar de los sistemas electroquímicos de conversión del CO_2 con fuentes de energía renovables.

1.3. Bioconjugados: nuevos materiales bioinspirados para aplicaciones electrocatalíticas

Actualmente, muchos investigadores, motivados por la alta eficiencia observada en la naturaleza, han dirigido sus estudios hacia el diseño de materiales jerárquicos bioinspirados. En este sentido, las enzimas son catalizadores biológicos altamente eficientes y selectivos. Además la presencia de grupos redox en este tipo de biomoléculas, ha llevado a su utilización en diferentes aplicaciones electroquímicas. Las enzimas pueden catalizar una serie de reacciones redox de gran importancia tecnológica, que generalmente requieren un alto sobrepotencial.[147] Es importante destacar, que el uso de enzimas proporciona muchas ventajas, como las altas corrientes electrocatalíticas y la posibilidad de llevar a cabo los procesos electrocatalíticos en una manera reversible.
Las metaloenzimas conocidas como hidrogenasas catalizan la conversión reversible de hidrógeno.[148] Teniendo en cuenta el contenido de metal de los sitios activos, hay tres clases principales de hidrogenasas: [FeFe], que contienen dos átomos de hierro en su sitio activo y son los catalizadores biológicos más rápidos para la oxidación/reducción de hidrógeno; [NiFe], que poseen un sitio heterobimetálico activo; y [Fe] que contiene solo un átomo de hierro en su estructura. Dadas sus capacidades para electrocatalizar eficientemente la producción de hidrógeno, una serie de celdas de combustible de hidrógeno han sido diseñadas empleado dichas enzimas, constituyendo una valiosa alternativa para el diseño de dispositivos de energía biodegradables.[149-152]

La hemoglobina, es otra proteína que también contiene átomos de hierro en su estructura, y que está ampliamente caracterizada debido a su importancia en la vida de los seres vivos. Esta enzima es una proteína redox, globular y tetramérica. Cada subunidad está formada por cadenas de polipéptidos, mayoritariamente en conformación alfa-hélice y que engloban en su estructura de forma accesible al exterior un grupo hemo que contiene un átomo de Fe. Este ión Fe^{2+} se encuentra en el centro de un heterociclo orgánico llamado porfirina, el cual es el responsable de reaccionar con el oxígeno y efectuar el transporte sanguíneo[153]. Estas características hacen que pudiera actuar como una plataforma catalítica inteligente en la reacción de evolución de oxígeno, así como en otro tipo de reacciones de oxidación. Otras enzimas que se han utilizado como electrocatalizadores sostenibles, son las peroxidasas. Estas proteínas catalizan la oxidación de moléculas orgánicas empleando H_2O_2, gracias a la presencia del grupo Fe-porfirina.[154]

En particular, las enzimas conocidas como oxidasas multicobre muestran excelentes propiedades hacia la electroreducción de O_2 a altos potenciales.[155] Las oxidasas multicobre son una familia de metaloenzimas que se distinguen por tener tres sitios distintos de cobre, Cu tipos 1, 2 y 3; la oxidación del sustrato reductor ocurre en el sitio de Cu tipo 1 (T1) mientras que la reducción de O_2 se produce en el grupo trinuclear T2/T3.[156] Una amplia gama de estrategias han sido llevadas acabas para la inmovilización de dichas enzimas, desde la unión covalente a nanotubos de carbono y nanomateriales conductores de grafeno,[157] hasta la encapsulación en estructuras de sílice.[155]

Además, se conoce que enzimas específicas que exhiben una excelente capacidad para reducir CO_2 a CO y ácido fórmico, se pueden comportar como electrocatalizadores reversibles. Por ejemplo, las enzimas monóxido de carbono-deshidrogenasas, presentes en los organismos anaerobios contienen un grupo [NiFe-4 S] que cataliza la interconversión de CO_2 y CO.[154] La enzima formiato-deshidrogenasa, con sitios activos de piranopterina molibdeno/tungsteno, puede catalizar la interconversión de CO_2 y formiato.[158] En particular, el formiato ha atraído mucho interés como fuente de energía, ya que es más fácil de almacenar y transportar que el hidrógeno. Usando un enfoque bio-sintético, muchos científicos han desarrollado modelos para imitar una serie de metaloenzimas como hidrogenasas, óxido nítrico reductasa y citocromo, entre otros.[159-161] A pesar de que las eficiencias catalíticas obtenidas para estos sistemas artificiales son aún bajas en comparación con los sistemas naturales,

estas estrategias son muy prometedoras y poseen un gran potencial para el futuro.

1.4. References

1. A. Reis, *Zeitschrift für Elektrochemie und Angew. Phys. Chemie* **1919**, *25*, 371–372.
2. H. Yan, F. Yang, D. Pan, Y. Lin, J. N. Hohman, D. Solis-Ibarra, F. H. Li, J. E. P. Dahl, R. M. K. Carlson, B. A. Tkachenko, A. A. Fokin, P. R. Schreiner, G. Galli, W. L. Mao, Z. X. Shen and N. A. Melosh, *Nature* **2018**, *554*, 505–510.
3. E. Boldyreva, *Chem. Soc. Rev.* **2013**, *42*, 7719–7738.
4. E. R. Caley, J. F. C. Richards, Theophrastus on Stones, 2nd ed.; Cambridge University Press: Cambridge, 1956.
5. T. Friščić, A. V. Trask, W. Jones, W. D. S. Motherwell, *Angew. Chemie* **2006**, *118*, 7708–7712.
6. N. Shan, F. Toda, W. Jones, *Chem. Commun.* **2002**, *0*, 2372–2373.
7. M, Faraday, *Q J Sci, Lit, Arts.* **1820**, *8*, 374–376.
8. M. C. Lea, *Am. J. Sci.* **1892**, *s3-43*, 527–531.
9. G. Heinicke, H.-P. Hennig, E. Linke, U. Steinike, K.-P. Thiessen, K. Meyer, *Cryst. Res. Technol.* **1984**, *19*, 1424–1424.
10. C. M. Cova, R. Luque, *BMC Chemical Engineering*, **2019**, *1*, 16.
11. F. P. Bowden, A. Yoffe, Initiation and Growth of Explosion in Liquids and Solids; Cambridge University Press: Cambridge, **1952**.
12. F. P. Bowden, A. Yoffe, Fast Reactions in Solids; Butterworths: London, **1958**.
13. P. A. Thiessen, K. Meyer, G. Heinicke, Grundlagen Der Tribochemie; Akademie-Verlag: Berlin, **1967**.
14. E. M. Gutman, Mechanochemistry of Metals and Protection against Corrosion; Metallurgiya: Moscow, **1974**.
15. V. K. Smolyakov, O. V. Lapshin, V. V. Boldyrev, *Int. J. Self-Propagating High-Temperature Synth.* **2008**, *17*, 20–29.
16. V. K. Smolyakov, O. V. Lapshin, V. V. Boldyrev, *Int. J. Self-Propagating High-Temperature Synth.* **2007**, *16*, 1–11.
17. V. I. Levitas, High Pressure Surface Science and Engineering; Institute of Physics: Bristol, **2004**; pp 159–292.
18. S. R. Berry, S. A. Rice, J. Ross, Matter in Equilibrium: Statistical Mechanics and Thermodynamics; **2004**.
19. E. Avvakumov, M. Senna, N. Kostova, Soft Mechanochemical

Synthesis: A Basis for New Chemical Technologies; Kluwer Academic Publischers: Dordrecht, **2001**.
20. E. Gdoutos, Fracture of Nano and Engineering Materials and Structures; Springer: Dordrecht, **2006**.
21. R. W. Hertzberg, Deformation and Fracture Mechanics of Engineering Materials; John Wiley & Sons: New York, **1995**.
22. J. M. Thomas, W. J. Thomas, Principles and Practice of Heterogeneous Catalysis; VCH Publishers: New York, **2005**.
23. P. Meloni, G. Carcangiu, F. Delogu, *Mater. Res. Bull.* **2012**, *47*, 146–151.
24. F. Delogu, *J. Phys. Chem. C* **2011**, *115*, 21230–21235.
25. L. Batzdorf, F. Fischer, M. Wilke, K.-J. Wenzel, F. Emmerling, *Angew. Chemie Int. Ed.* **2015**, *54*, 1799–1802.
26. A. D. Katsenis, A. Puškarić, V. Štrukil, C. Mottillo, P. A. Julien, K. Užarević, M.-H. Pham, T.-O. Do, S. A. J. Kimber, P. Lazić, O. Magdysyuk, R. E. Dinnebier, I. Halasz, T. Friščić. *Nat. Commun.* **2015**, *6*, 6662.
27. T. Friščić, Metal-Organic Frameworks: Mechanochemical Synthesis Strategies. In *Encyclopedia of Inorganic and Bioinorganic Chemistry*; John Wiley & Sons, Ltd: Chichester, UK, **2014**; pp 1–19.
28. P. A. Julien, K. Užarević, A. D. Katsenis, S. A. J. Kimber, T. Wang,; O. K. Farha, Y. Zhang, J. Casaban, L. S. Germann, M. Etter, R. E. Dinnebier, S. L. James, I. Halasz, T. Friščić, *J. Am. Chem. Soc.* **2016**, *138*, 2929–2932.
29. N. R. Rightmire, T. P. Hanusa, *Dalt. Trans.* **2016**, *45*, 2352–2362.
30. J. G. Hernández, T. Friščić, *Tetrahedron Lett.* **2015**, *56*, 4253–4265.
31. A. L. Garay, A. Pichon, S. L. James, *Chem. Soc. Rev.* **2007**, *36*, 846–855.
32. P. Baláž, M. Achimovičová, M. Baláž, P. Billik, Z. Cherkezova-Zheleva, J. M. Criado, F. Delogu, E. Dutková, E. Gaffet, F. J. Gotor, R. Kumar, I. Mitov, T. Rojac, M. Senna, A. Streletskiikl, K. Wieczorek-Ciurowam, *Chem. Soc. Rev.* **2013**, *42*, 7571–7637.
33. C. Xu, S. De, A. M. Balu, M. Ojeda, R. Luque, *Chem. Commun.* **2015**, *51*, 6698–6713.
34. R. J. White, R. Luque, V. L. Budarin, J. H. Clark, D. J. Macquarrie, *Chem. Soc. Rev.* **2009**, *38*, 481–494.
35. D. Astruc, F. Lu, J. R. Aranzaes, *Angew. Chemie Int. Ed.* **2005**, *44,* 7852–7872.
36. V. Polshettiwar, R. Luque, A. Fihri, H. Zhu, M. Bouhrara, J.-M. Basset, *Chem. Rev.* **2011**, *111*, 3036–3075.
37. K. Haas-Santo, M. Fichtner, K. Schubert, *Appl. Catal. A Gen.* **2001**, *220*, 79–92.
38. A. Zuliani, A. M. Balu, R. Luque, *ACS Sustain. Chem. Eng.* **2017**, *5*,

11584–11587.
39. M. J. Muñoz-Batista, D. Motta Meira, G. Colón, A. Kubacka, M. Fernández-García, *Angew. Chemie - Int. Ed.* **2018**, *57*, 1199–1203.
40. J. C. Colmenares, M. A. Aramendía, A. Marinas, J. M. Marinas, F. J.Urbano, *Appl. Catal. A Gen.* **2006**, *306*, 120–127.
41. T. Friščić, New Opportunities for Materials Synthesis Using Mechanochemistry. *J. Mater. Chem.* **2010**, *20* (36), 7599–7605.
42. M. Klimakow, P. Klobes, A. F. Thünemann, K. Rademann, F. Emmerling, *Chem. Mater.* **2010**, *22*, 5216–5221.
43. K. Ralphs, C. Hardacre, S. L. James, *Chem. Soc. Rev.* **2013**, *42*, 7701–7718.
44. A. Franco, S. De, A. M. Balu, A. Garcia, R. Luque, *Beilstein J. Org. Chem.* **2017**, *13*, 1439–1445.
45. A. D. Jodlowski, A. Yépez, R. Luque, L. Camacho, G. de Miguel, *Angew. Chemie Int. Ed.* **2016**, *55*, 14972–14977.
46. W. Ouyang, E. Kuna, A. Yepez, A. Balu, A. Romero, J. Colmenares, R. Luque, *Nanomaterials* **2016**, *6*, 93.
47. M. Ojeda, A. M. Balu, V. Barrón, A. Pineda, Á. G. Coleto, A. A. Romero, R. Luque, *J. Mater. Chem. A* **2014**, *2*, 387–393.
48. C. Liu, F. Li, L.-P. Ma, H.-M. Cheng, *Adv. Mater.* **2010**, *22*, E28–E62.
49. L. Qie, W. Chen, H. Xu, X. Xiong, Y. Jiang, F. Zou, X. Hu, Y. Xin, Z. Zhang, Y. Huang, *Energy Environ. Sci.* **2013**, *6*, 2497–2504.
50. J. B. Goodenough, Y. Kim, *Chem. Mater.* **2010**, *22*, 587–603.
51. H. Zhang, G. Cao, Y. Yang, *Energy Environ. Sci.* **2009**, *2*, 932–943.
52. R. R. Gaddam, D. Yang, R. Narayan, K. Raju, N. A. Kumar, X. S. Zhao, *Nano Energy* **2016**, *26*, 346–352.
53. Q. Wu, L. Yang, X. Wang, Z. Hu, *Acc. Chem. Res.* **2017**, *50*, 435–444.
54. W. Long, B. Fang, A. Ignaszak, Z. Wu, Y.-J. Wang, D. Wilkinson, *Chem. Soc. Rev.* **2017**, *46*, 7176–7190.
55. E. Raymundo-Piñero, M. Cadek, F. Béguin, *Adv. Funct. Mater.* **2009**, *19*, 1032–1039.
56. T. Yang, T. Qian, M. Wang, X. Shen, N. Xu, Z. Sun, C. Yan, *Adv. Mater.* **2016**, *28*, 539–545.
57. C. Schneidermann, N. Jäckel, S. Oswald, L. Giebeler, V. Presser, L. Borchardt, *ChemSusChem* **2017**, *10*, 2416–2424.
58. G. Wang, J. Zhang, S. Hou, W. Zhang, J. Zhou, Z. Zhao, *Electrochim. Acta* **2016**, *208*, 47–54.
59. U. Kamolphop, S. F. R. Taylor, J. P. Breen, R. Burch, J. J. Delgado, S. Chansai, C. Hardacre, S. Hengrasmee, S. L. James, *ACS Catal.* **2011**, *1*,

1257–1262.
60. A. R. Siamaki, Y. Lin, K. Woodberry, J. W. Connell, B. F. Gupton, *J. Mater. Chem. A* **2013**, *1*, 12909–12918.
61. S. Menuel, B. Léger, A. Addad, E. Monflier, F. Hapiot, *Green Chem.* **2016**, *18*, 5500–5509.
62. W. Zhan, S. Yang, P. Zhang, Y. Guo, G. Lu, M. F. Chisholm, S. Dai, *Chem. Mater.* **2017**, *29*, 7323–7329.
63. J. H. Clark, R. Luque and A. S. Matharu, *Annu. Rev. Chem. Biomol. Eng.*, **2012**, *3*, 183–207.
64. P. T. Anastas, J. C. Warner and W. J. Anastas PT, *Green Chemistry: Theory and Practice.*, Oxford University Press, New York, **1998**.
65. A. Rani, S. Jain, S. K. Sharma, in *Green Chemistry for Environmental Remediation*, John Wiley & Sons, Inc., Hoboken, NJ, USA, **2012**, pp. 357–378.
66. D. Rodríguez-Padrón, A. R. Puente-Santiago, A. M. Balu, M. J. Muñoz-Batista, R. Luque, *ChemCatChem*, **2019**, *11*(1), 18-38.
67. R. A. Sheldon, *J. R. Soc. Interface*, **2016**, *13*, 20160087.
68. V. Polshettiwar, R. S. Varma, *Green Chem.*, **2010**, *12*, 743.
69. G. Centi, S. Perathoner, *Catal. Today*, **2003**, *77*, 287–297.
70. P. T. Anastas, M. M. Kirchhoff, T. C. Williamson, *Appl. Catal. A Gen.*, **2001**, *221*, 3–13.
71. I. Dincer, C. Acar, *Int. J. Hydrogen Energy*, **2015**, *40*, 11094–11111.
72. R. Dybkær, *Pure Appl. Chem.*, **2001**, *73*, 927–931.
73. M. J. Muñoz-Batista, A. M. Eslava-Castillo, A. Kubacka, M. Fernández-García, *Appl. Catal. B Environ.*, **2018**, 225, 298–306.
74. C.-Y. Lee, H. S. Park, J. C. Fontecilla-Camps, E. Reisner, *Angew. Chemie Int. Ed.*, **2016**, *55*, 5971–5974.
75. J. Vedrine, *Metal Oxides in Heterogeneous Catalysis*, Elsevier, Amsterdam, **2018**, 551–569.
76. R. A. Sheldon, *Green Chem.*, **2007**, *9*, 1273.
77. J. H. Clark, *Pure Appl. Chem.*, **2001**, *73*, 103–111.
78. B. Sarkar, R. Goyal, L. N. Sivakumar Konathala, C. Pendem, T. Sasaki, R. Bal, *Appl. Catal. B Environ.*, **2017**, *217*, 637–649.
79. E. Chiurchiù, S. Gabrielli, R. Ballini, A. Palmieri, *Green Chem.*, **2017**, *19*, 4956–4960.
80. X. Jin, Y. Koizumi, K. Yamaguchi, K. Nozaki, N. Mizuno, *J. Am. Chem. Soc.*, **2017**, *139*, 13821–13829.
81. Z. Zhang, B. Xu, X. Wang, *Chem. Soc. Rev.*, **2014**, *43*, 7870–7886.
82. Y. Liu, G. Zhao, D. Wang, Y. Li, *Natl. Sci. Rev.*, **2015**, *2*, 150–166.

83. S. De, A. M. Balu, J. C. van der Waal, R. Luque, *ChemCatChem*, **2015**, *7*, 1608–1629.
84. E. S. Gomes, G. Lutzweiler, P. Losch, A. V. Silva, C. Bernardon, K. Parkhomenko, M. M. Pereira, B. Louis, *Microporous Mesoporous Mater.*, **2017**, *254*, 28–36.
85. M. J. Muñoz Batista, D. Rodríguez-Padrón, A. R. Puente Santiago, R. Luque, *ACS Sustain. Chem. Eng.*, **2018**, 9530-9544.
86. V. Budarin, J. H. Clark, J. J. E. Hardy, R. Luque, K. Milkowski, S. J. Tavener, A. J. Wilson, *Angew. Chem. Int. Ed.*, **2006**, *118*, 3866–3870.
87. E. Lam, J. H. T. Luong, *ACS Catal.*, **2014**, *4*, 3393–3410.
88. R.-L. Liu, W.-J. Ji, T. He, Z.-Q. Zhang, J. Zhang, F.-Q. Dang, *Carbon N. Y.*, **2014**, *76*, 84–95.
89. T. Ji, L. Chen, L. Mu, R. Yuan, M. Knoblauch, F. S. Bao, Y. Shi, H. Wang, J. Zhu, *Chem. Eng. J.*, **2016**, *295*, 301–308.
90. L. Filiciotto, G. de Miguel, A. M. Balu, A. A. Romero, J. C. van der Waal, R. Luque, *Chem. Commun.*, **2017**, *53*, 7015–7017.
91. L. Filiciotto, A. M. Balu, A. A. Romero, E. Rodríguez-Castellón, J. C. van der Waal, R. Luque, *Green Chem.*, **2017**, *19*, 4423–4434.
92. D. Rodríguez-Padrón, A. M. Balu, A. A. Romero, R. Luque, *Beilstein J. Org. Chem.*, **2017**, *13*, 1982–1993.
93. J. L. Burt, C. Gutiérrez-Wing, M. Miki-Yoshida, M. José-Yacamán, *Langmuir*, **2004**, *20*, 11778-11783.
94. S. A. Walper, K. B. Turner, I. L. Medintz, *Current opinion in biotechnology*, **2015**, *34*, 232-241.
95. A. Gole, C. Dash, C. Soman, S. R. Sainkar, M. Rao, M. Sastry, *Bioconjugate chemistry*, **2001**, *12*, 684-690.
96. M. Bahri, F. Haghighat, *CLEAN-Soil, Air, Water*, **2014**, *42*, 1667–1680.
97. R. Caporali, S. Chansai, R. Burch, J. J. Delgado, A. Goguet, C. Hardacre, L. Mantarosie, D. Thompsett, *Appl. Catal. B Environ.*, **2014**, *147*, 764–769.
98. H. S. Gandhi, G. W. Graham, R. W. McCabe, *J. Catal.*, **2003**, *216*, 433–442.
99. M. Zabłocka-Malicka, W. Szczepaniak, A. Zielińska, P. Rutkowski, *Ecol Chem Eng S.*, **2016**, *23*, 33–48.
100. Y. Shen, X. Ge, M. Chen, *RSC Adv.*, **2016**, *6*, 8469–8482.
101. A. Shiotari, S. Hatta, H. Okuyama, T. Aruga, *Chem. Sci.*, **2014**, *5*, 922–926.
102. H. Huang, Y. Xu, Q. Feng, D. Y. C. Leung, *Catal. Sci. Technol.*, **2015**, *5*, 2649–2669.

103. M. T. Amin, A. A. Alazba, U. Manzoor, *Adv. Mater. Sci. Eng.*, **2014**, *2014*, 1–24.
104. J. He, P. Wu, Y. Wu, H. Li, W. Jiang, S. Xun, M. Zhang, W. Zhu, H. Li, *ACS Sustain. Chem. Eng.*, **2017**, *5*, 8930–8938.
105. M. Benzaazoua, H. Bouzahzah, Y. Taha, L. Kormos, D. Kabombo, F. Lessard, B. Bussière, I. Demers, M. Kongolo, *J. Clean. Prod.*, **2017**, *162*, 86–95.
106. S. Sankaranarayanapillai, S. Sreekumar, J. Gomes, A. Grippo, G. E. Arab, M. Head-Gordon, F. D. Toste and A. T. Bell, *Angew. Chem. Int. Ed.*, **2015**, *54*, 4673–4677.
107. C. O. Tuck, E. Pérez, I. T. Horváth, R. A. Sheldon, M. Poliakoff, *Science,* **2012**, *337*, 695–9.
108. L. Filiciotto, A. M. Balu, J. C. Van der Waal, R. Luque, *Catal. Today*, **2018**, *302*, 2–15.
109. L. Filiciotto and R. Luque, *Curr. Green Chem.*, **2018**, *5*, 47–59.
110. S. De, B. Saha, R. Luque, *Bioresour. Technol.*, **2015**, *178*, 108–118.
111. A. M. Robinson, J. E. Hensley, J. W. Medlin, *ACS Catal.*, **2016**, *6*, 5026–5043.
112. C. M. Friend, B. Xu, *Acc. Chem. Res.*, **2017**, *50*, 517–521.
113. Q. Xu, X. Li, T. Pan, C. Yu, J. Deng, Q. Guo, Y. Fu, *Green Chem.*, **2016**, *18*, 1287–1294.
114. S. S. Chen, T. Maneerung, D. C. W. Tsang, Y. S. Ok, C.-H. Wang, *Chem. Eng. J.*, **2017**, *328*, 246–273.
115. Y.-B. Huang, J.-J. Dai, X.-J. Deng, Y.-C. Qu, Q.-X. Guo, Y. Fu, *ChemSusChem*, **2011**, *4*, 1578–1581.
116. X.-L. Du, L. He, S. Zhao, Y.-M. Liu, Y. Cao, H.-Y. He, K.-N. Fan, *Angew. Chem. Int. Ed.*, **2011**, *123*, 7961–7965.
117. A. S. Touchy, S. M. A. Hakim Siddiki, K. Kon, K. Shimizu, *ACS Catal.*, **2014**, *4*, 3045–3050.
118. A. M. Ruppert, M. Jędrzejczyk, O. Sneka-Płatek, N. Keller, A. S. Dumon, C. Michel, P. Sautet, J. Grams, *Green Chem.*, **2016**, *18*, 2014–2028.
119. E. Vitaku, D. T. Smith, J. T. Njardarson, *J. Med. Chem.*, **2014**, *57*, 10257–10274.
120. B. Kurpil, A. Savateev, V. Papaefthimiou, S. Zafeiratos, T. Heil, S. Özenler, D. Dontsova, M. Antonietti, *Appl. Catal. B Environ.*, **2017**, *217*, 622–628.
121. S. G. Agalave, S. R. Maujan, V. S. Pore, *Chem.-An Asian J.*, **2011**, *6*, 2696–2718.

122. M. Hong, X. Tang, L. Falivene, L. Caporaso, L. Cavallo, E. Y. X. Chen, *J. Am. Chem. Soc.*, **2016**, *138*, 2021–2035.
123. L. Q. Lu, , J. R. Chen, W. J. Xiao, *Acc. Chem. Res.*, **2012**, *45*, 1278–1293.
124. X. Gao, X. Chen, J. Zhang, W. Guo, F. Jin, N. Yan, *ACS Sustain. Chem. Eng.*, **2016**, *4*, 3912–3920.
125. P. Bhanja, A. Bhaumik, *Fuel*, **2016**, *185*, 432–441.
126. L. Hu, L. Lin, Z. Wu, S. Zhou, S. Liu, *Renew. Sustain. Energy Rev.*, **2017**, *74*, 230–257.
127. T.-W. Kim, S.-Y. Kim, J.-C. Kim, Y. Kim, R. Ryoo, C.-U. Kim, *Appl. Catal. B Environ.*, **2016**, *185*, 100–109.
128. T. Furuya, M. Kuroiwa, K. Kino, *J. Biotechnol.*, **2017**, *243*, 25–28.
129. F. Saberi, D. Rodriguez-Padrón, A. Garcia, H. Shaterian, R. Luque, *Catalysts*, **2018**, *8*, 167.
130. S. Ostovar, A. Franco, A. R. Puente-Santiago, M. Pinilla-de Dios, D. Rodríguez-Padrón, H. R. Shaterian, R. Luque, *Front. Chem.*, **2018**, *6*, 77.
131. G. Chen, S. Wu, H. Liu, H. Jiang, Y. Li, *Green Chem.*, **2013**, *15*, 230–235.
132. L. Geng, B. Zheng, X. Wang, W. Zhang, S. Wu, M. Jia, W. Yan, G. Liu, *ChemCatChem*, **2016**, *8*, 805–811.
133. L. S. Sharninghausen, J. Campos, M. G. Manas and R. H. Crabtree, *Nat. Commun.*, **2014**, *5*, 5084.
134. S. Lomate, B. Katryniok, F. Dumeignil, S. Paul, *Sustain. Chem. Process.*, **2015**, *3*, 5.
135. Y. Matsuura, A. Onda, K. Yanagisawa, *Catal. Commun.*, **2014**, *48*, 5–10.
136. Y. Fan, C. Zhou, X. Zhu, *Catal. Rev.*, **2009**, *51*, 293–324.
137. T. Asefa, *Acc. Chem. Res.*, **2016**, *49*, 1873–1883.
138. M. Borghei, J. Lehtonen, L. Liu and O. J. Rojas, *Adv. Mater.*, **2018**, *30*, 1703691.
139. B. You, Y. Sun, *Acc. Chem. Res.*, **2018**, *51*, 1571-1580.
140. J. Qiao, Y. Liu, F. Hong, J. Zhang, *Chem. Soc. Rev.*, **2013**, *43*, 631–675.
141. J. Deng, M. Li, Y. Wang, *Green Chem.*, **2016**, *18*, 4824–4854.
142. M. Graglia, J. Pampel, T. Hantke, T.-P. Fellinger, D. Esposito, *ACS Nano*, **2016**, *10*, 4364–4371.
143. B. Han, S. M. Steen, J. Mo, F.-Y. Zhang, *Int. J. Hydrogen Energy*, **2015**, *40*, 7006–7016.

144. O. Khaselev, A. Bansal, J. A. Turner, *Int. J. Hydrogen Energy*, **2001**, *26*, 127–132.
145. Y. Gorlin, T. F. Jaramillo, *J. Am. Chem. Soc.*, **2010**, *132*, 13612-13614.
146. K. Lee, L. Zhang, H. Lui, R. Hui, Z. Shi, J. Zhang, *Electrochim. Acta*, **2009**, *54*, 4704-4711.
147. H. S. Shafaat, O. Rüdiger, H. Ogata, W. Lubitz, *Biochim. Biophys. Acta-Bioenerg.*, **2013**, *1827*, 986–1002.
148. I. Mazurenko, X. Wang, A. de Poulpiquet, E. Lojou, *Sustain. Energy Fuels*, **2017**, *1*, 1475–1501.
149. S. Gentil, S. M. Che Mansor, H. Jamet, S. Cosnier, C. Cavazza, A. Le Goff, *ACS Catal.*, **2018**, *8*, 3957–3964.
150. T. J. McDonald, D. Svedruzic, Y.-H. Kim, J. L. Blackburn, S. B. Zhang, P.W. King, M. J. Heben, *Nano Lett*. **2007**, *11*, 3528-3534.
151. A. Franco, S. Cebrián-García, D. Rodríguez-Padrón, A. R. Puente-Santiago, M. J. Muñoz-Batista, A. Caballero, A. M. Balu, A. A. Romero, R. Luque, *ACS Sustain. Chem. Eng.*, **2018**, *6*, 11058-11062.
152. F. J. Enguita, L. O. Martins, A. O. Henriques, M. A. Carrondo, *J. Biol. Chem.*, **2003**, *278*, 19416–25.
153. D. Gell, *Blood Cells, Mol. Dis.,* **2018**, *70*, 13-42.
154. N. Yeung, Y.-W. Lin, Y.-G. Gao, X. Zhao, B. S. Russell, L. Lei, K. D. Miner, H. Robinson, Y. Lu, *Nature*, **2009**, *462*, 1079–1082.
155. L. B. Maia, L. Fonseca, I. Moura, J. J. G. Moura, *J. Am. Chem. Soc.*, **2016**, *138*, 8834–8846.
156. J. Esselborn, C. Lambertz, A. Adamska-Venkatesh, T. Simmons, G. Berggren, J. Noth, J. Siebel, A. Hemschemeier, V. Artero, E. Reijerse, M. Fontecave, W. Lubitz, T. Happe, *Nat. Chem. Biol.*, **2013**, *9*, 607–609.
157. B. Jin, G.-X. Wang, D. Millo, P. Hildebrandt, X.-H. Xia, *J. Phys. Chem. C*, **2012**, *116*, 13038–13044.
158. S. Mukherjee, A. Mukherjee, A. Bhagi-Damodaran, M. Mukherjee, Y. Lu, A. Dey, *Nat. Commun.*, **2015**, *6*, 8467.
159. J. Liu, Y. Zheng, Z. Hong, K. Cai, F. Zhao, H. Han, *Sci. Adv.*, **2016**, *2*, e1600858–e1600858.
160. Y.-N. Hou, H. Liu, J.-L. Han, W.-W. Cai, J. Zhou, A.-J. Wang, H.-Y. Cheng, *ACS Sustain. Chem. Eng.*, **2016**, *4*, 5392–5397.
161. G. Reguera, K. D. McCarthy, T. Mehta, J. S. Nicoll, M. T. Tuominen, D. R. Lovley, *Nature*, **2005**, *435*, 1098–1101.

Capítulo 2

2. Novel solventless mechanochemical preparation of magnetic bioconjugates. Energy storage and catalytic applications

2.1. Hypothesis

The high efficiency observed in nature has motivated the scientific community to extrapolate natural systems for the development of new materials with enhanced features for different kind of applications. In this regard, the use of enzymes could offer a broad range of possibilities. Nowadays, such biomolecules have been employed as biocatalyst due to their high selectivity and good performance. Nonetheless, the real time industrial application of enzymes still faces complications related to their recovery and re-use, along with the absence of long-term operational stability. In this regard, enzyme immobilization emerged as a feasible alternative for the use of these biomolecules in many areas such as pharmaceutical chemistry, food modification and energy (e.g., biodiesel and bioethanol production). Among all reported solid carriers, magnetic nanoparticles have evident advantages related to the easy separation and manipulation from the bulk solution by a magnetic field gradient. Additionally, enzyme immobilization generally give rise to an increment of stability, under both storage and operational conditions. Moreover, conventional methods for enzyme immobilization, normally required the use of solvents and long reactions times. In order to simplify the synthesis of bioconjugates, mechanochemical methods could represent alternative and sustainable option.

2.2. Objetives

A solventless mechanochemical protocol will be developed for the synthesis of nanobioconjugates based on proteins and magnetic nanoparticles. Different proteins will be investigated, such as hemoglobin (Hb), laccase (LAC) and bovine serum albumin (BSA), in order to get more insights into the effect of mechanochemical protocols on the native-like structure of the enzimes. The prepared materials will be fully characterized aiming to corroborate the suitability of mechanochemical approaches for the synthesis of such kind of materials. A muti-technique

strategy will be employed for characterization, including X-ray diffraction analysis, X-ray Photoelectronic Spectroscopy (XPS), Electronic Paramagnetic Spectroscopy (EPR), UV-vis and Fluorescence Spectroscopies, Transmission Electronic Microscopy (TEM), Dynamic Light Scattering (DLS) and Zeta-Potential measurements, Thermogravimetric analysis (TGA-DTA), Fourier Transform-Infrared Spectroscopy (FT-IR) and Raman spectroscopy. The synthesized nanobioconjugates will be employed for different applications, including catalysis and energy storage. Specifically, a bioconjugate based on Hb will be used for the design of a bioinspired supercapacitor. Moreover, the catalytic applications of bioconjugates based on LAC will be explored in the electrocatalytic reduction of oxygen. Additional research related to bioconjugates based on LAC and graphitic carbonitrile has been included in Appendice 8.3. As well, studies focused on the design of supercapacitors have been added in Appendice 8.4.

2.3. Solventless mechanochemical preparation of novel magnetic bioconjugates

As first approximation, a solventless mechanochemical approach was desveloped and used for the preparation of a bioconjugate based on bovine serum albumin (BSA) and iron oxide magnetic nanoparticles. Dopamine (DA) was used as robust anchor. A full characterization analysis was performed in order to demonstrate the suitability of the mechanochemical protocol for the preparation of the bioconjugate, as well as to investigated the influence of the milling process on the native like structure of the protein.

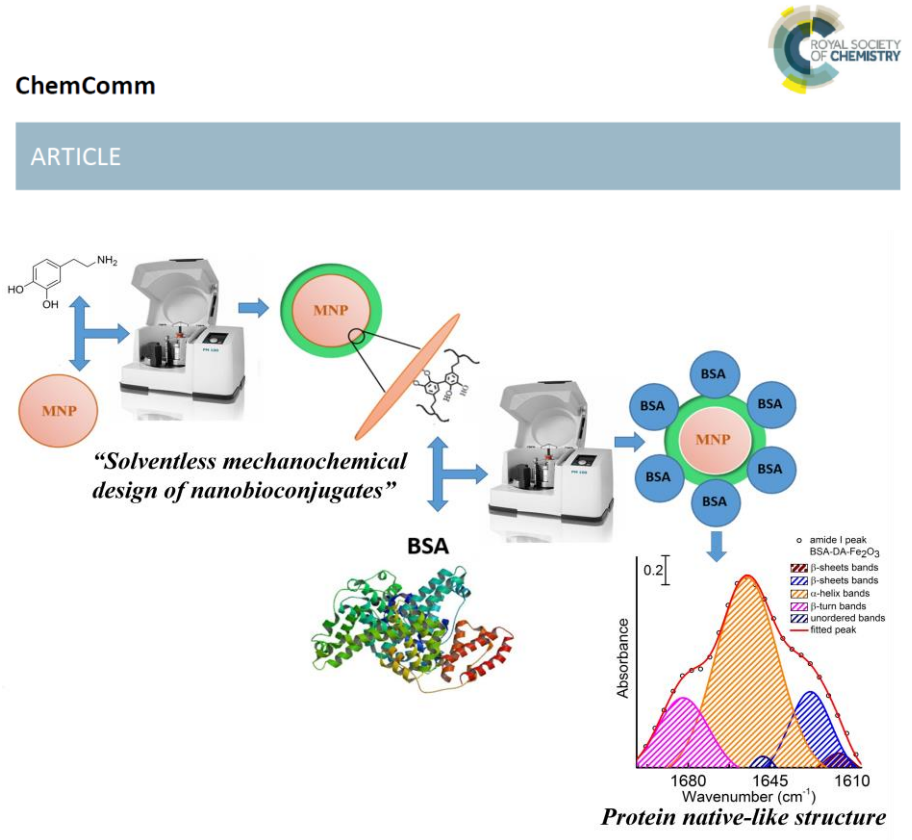

Daily Rodríguez-Padrón; Alain R. Puente Santiago; Alina M. Balu; Antonio A. Romero Reyes; Rafael Luque Álvarez de Sotomayor. **2017**. Solventless mechanochemical preparation of novel magnetic bioconjugates. **Chemical Communications**. 53. 7635-7637. 10.1039/C7CC03975A. IF: 6.319.

Solventless mechanochemical preparation of novel magnetic bioconjugates

Daily Rodríguez-Padrón[a+], Alain R. Puente-Santiago[b+], Alina M. Balu[a], Antonio A. Romero[a], Rafael Luque[a]*

[a]*Departamento de Química Orgánica, Grupo FQM-383, Universidad de Cordoba, Campus de Rabanales, Edificio Marie Curie (C-3), Ctra Nnal IV-A, Km 396, E14014, Cordoba (Spain), e-mail: q62alsor@uco.es*

[b]*Departamento de Química Física, Universidad de Cordoba, Campus de Rabanales, Edificio Marie Curie (C-3), Ctra Nnal IV-A, Km 396, E14014, Cordoba*

A solventless mechanochemical approach was employed to obtain a bioconjugate (BSA-DA-Fe_2O_3) based on bovine serum albumin (BSA) and dopamine (DA) coated iron oxide magnetic nanoparticles. UV-vis measurements of the obtained material showed a distinctive peak at 280 nm which, together with the presence of N on the surface of the nanomaterial (band at 400 eV in the XPS spectrum) and zeta potential measurements, confirmed the successful immobilization of the protein. Adittionally, the presence of two bands at 1652 and 1545 cm^{-1} in the FT-IR spectra of both, BSA and BSA-DA-Fe_2O_3 and steady-state fluorescence analysis validated that the protein preserved its native-like structure after the mechanochemical milling process. Also the functionalized MNPs preserved its magnetic properties as have been demostrated by the magnetic susceptibility value.

Introduction

Bio-modified magnetic nanomaterials have gained increased attention in recent years owing to the integration of their unique physical properties (e.g. high surface area, easy separation under magnetic external fields, etc.) with their biological functions, giving rise to a wide range of hybrid supramolecular assemblies.[1, 2] These bio-conjugates possess several biomedical applications including

the purification of biomolecules, cell separation, immunoassay, magnetic resonance imaging and drug delivery.[3-7] In this regard, iron oxide nanoparticles as magnetic carriers have demonstrated a better performance due to their good biocompatibility and low toxicity in living organisms.[8, 9]

Surface functionalisation of magnetic nanoparticles (MNPs) with biomolecules has been achieved using non-covalent attachment (e.g. electrostatic, van der Waal forces and hydrophobic interactions),[10-12] encapsulation[13] and covalent conjugation to surface ligands.[14-16] Most of these strategies have been traditionally carried out in solution and often the successful attachment and the stability binding of the species are highly influenced by the environmental conditions (pH, ionic strength, biomolecule concentration among others).[16]

On the other hand, mechanochemical milling processes have been reported for the synthesis of different types of nanomaterials, in order to simplify their preparation, reducing both reaction times and circumventing solvent issues. [17-19]

In addition, mechanochemical protocols have been used to bind monosaccharides at the surfaces of MNPs. [18] However, this procedure has not been described before for the synthesis of protein functionalized MNPs.

Herein we report for the first time a facile, rapid and solvent free two-step mechanochemical synthesis of a hybrid protein-MNPs assembly (Scheme 1) based on non-covalent interactions of bovine serum albumin with iron oxide magnetic nanoparticles coated by dopamine (DA) as robust anchor.

Bovine serum albumin and dopamine hydrochloride (DA-HCl), along with Fe_2O_3 magnetic nanoparticles were employed to obtain a novel bio-modified nanomaterial by mechanochemical milling processes. The Fe_2O_3 MNP was prepared using a ratio 2:1 carbon source (lignocellulosic biomass)/metal precursor (ammonium ferric citrate, $(NH_4)_5[Fe(C_6H_4O_7)_2]\cdot 2H_2O$), in a ball mill (Retsch PM100 ball mill model), at 350 rpm for 10 min. The resulting material was oven dried at 100 °C for 24 h and slowly heated up (1 °C/min) to 300 °C.

Afterwards, 500 mg of the synthetized Fe_2O_3 nanomaterial were mixed with 125 mg of DA-HCl previously solved in 600 µL of ultrapure water. The mixture was milled at 200 rpm for 10 min in the ball mill, giving rise to DA-Fe_2O_3.[20] The synthesis of BSA-DA-Fe_2O_3 was subsequently carried out by grinding a dispersion of 100 mg of BSA in 600 µL of NaH_2PO_4 buffer (pH=7) together with DA-Fe_2O_3 under identical grinding conditions. The obtained BSA-DA-Fe_2O_3 was washed five times with ultrapure water and finally oven dried at 30 °C for 24h.

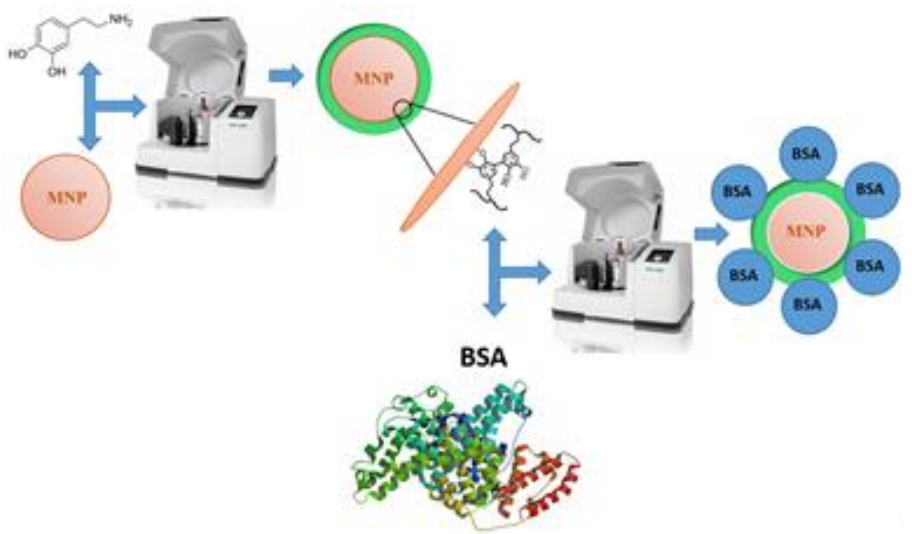

Scheme 1. Overview of the synthesis of the BSA-DA-Fe_2O_3 bio-modified material.

Results and discussion

BSA-DA-Fe_2O_3 bio-modified material was successfully prepared following the two mechanochemical steps depicted in Scheme 1. Figure 1 displays the TEM images of the Fe_2O_3 nanoparticles and the obtained bioconjugate. Both materials show a narrow particle size distribution-average. It can be observed an increment in the particle size after the protein functionalization from (5±1) nm to (8±1) nm, together with a tendency to form agglomerates most likely due to the Van der Waals interactions between neighbouring BSA moieties. The dynamic light scattering data of BSA-DA-Fe_2O_3 nanobioconjugates (See Figure 2a) reveal a considerable degree of

agglomeration with an average hydrodynamic size of 162 nm indicating that in aqueous suspension the disperse units are formed by approximately 50-60 individual particles. Notably, the zeta potential of DA-Fe_2O_3 was significantly decreased from 4.9 mV to -23.7 mV after coating with BSA molecules. (See Figure 2b, c) These findings are in accordance with the negative net electrical charge (-22.5 mV) of the BSA at 10 mM of NaCl (pH=7)[21] and confirmed both the successful immobilization of the BSA on the DA-Fe_2O_3 surfaces and the colloidal stability of the nanobioconjugates.

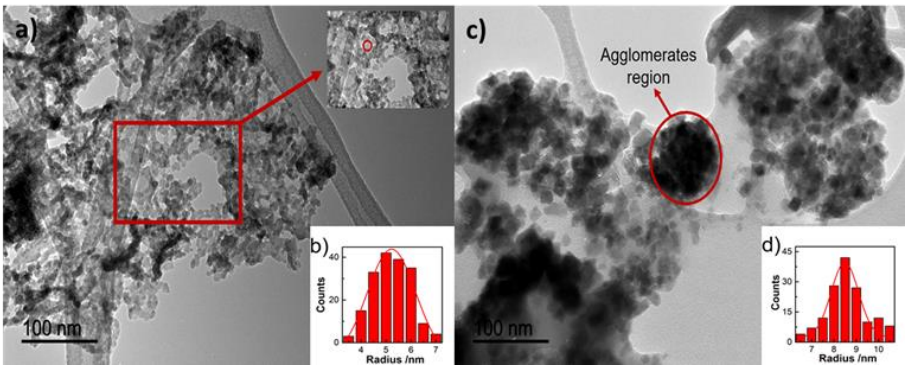

Figure 1. a) TEM image and b) size distribution based on TEM of Fe_2O_3 (180 particles), c) TEM image and d) size distribution based on TEM (180 particles) of the BSA-DA-Fe_2O_3**.**

The structure and arrangement of the Fe_2O_3 and BSA-DA-Fe_2O_3 materials had been studied by X-ray Diffraction analysis. The samples can be indexed to two phases, namely: maghemite and hematite (Fe_2O_3), with a clear appearance of the amorphous phase after the functionalization. (See Figure S1, ESI†)

UV–vis spectroscopy was used to evaluate the BSA successful immobilisation on the DA-Fe_2O_3 nanoparticles. A characteristic adsorption peak at 280 nm is observed (Figure S2c), similar to that observed in the UV-vis spectrum of BSA dissolved at the same buffer conditions.[22] This band has been attributed to the adsorption of tryptophan and tyrosine aminoacids.[23] The UV-vis spectra of DA and DA-Fe_2O_3 was also obtained (See Figure S2, ESI† for UV-vis spectra). Additionally, fluorescence emission analysis of BSA-DA-Fe_2O_3 nanobioconjugates was performed (See Figure S3, ESI†).

Figure 3a displays the FT-IR spectra of the BSA and the BSA-DA-Fe_2O_3 nanobioconjugates respectively. The characteristic amide I and II bands of proteins provided detailed information on the secondary structure of polypeptide chains.[24] The amide I band signal is characteristic from C=O stretching vibrations of peptide linkages. Comparably, amide II resulted from a combination of N–H in plane bending and C–N stretching vibrations of the peptide groups. The amide I and II of the BSA immobilised on the magnetic nanoparticles surfaces appeared at 1652 cm^{-1} and 1545 cm^{-1} respectively, essentially at the same wavelengths as those of free BSA. The contents of the different secondary structures are similar in both free BSA and BSA-DA-Fe_2O_3 (Figure 3b, table S1, ESI†), especially the α-helix and β-sheets contents, which strongly supported that BSA retain its structural features after the immobilization step.

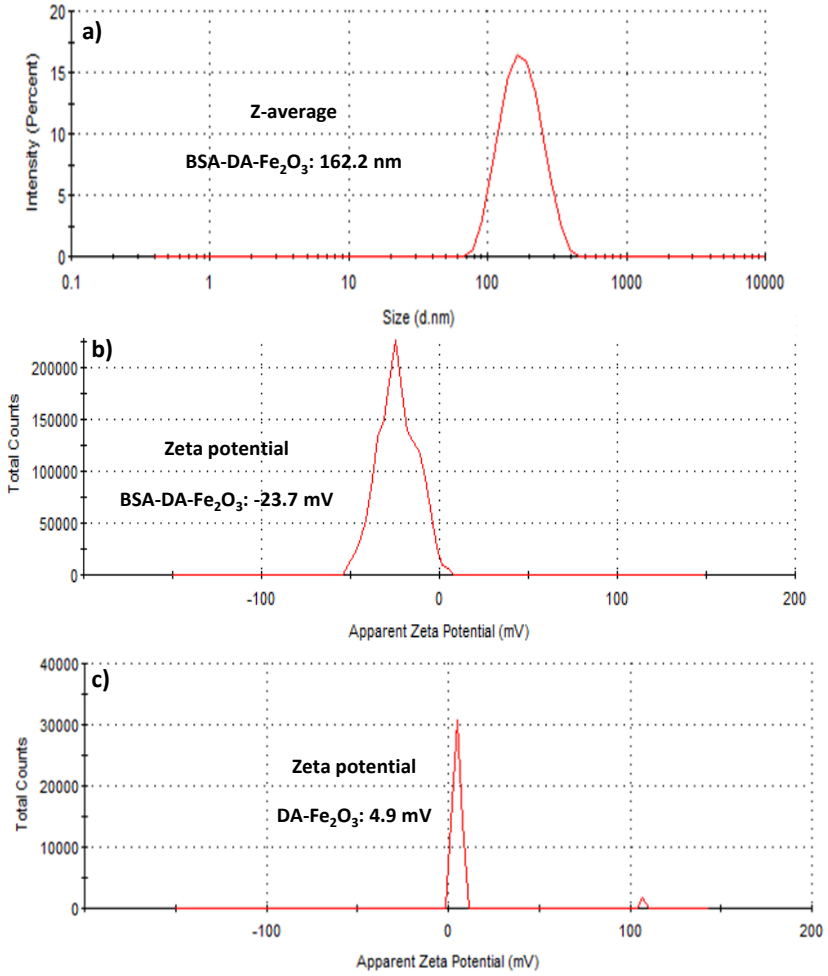

Figure 2. A Dynamic light scattering data of BSA-DA-Fe_2O_3 nanobioconjugates, B and C: zeta potential of BSA-DA-Fe_2O_3 and DA-Fe_2O_3 conjugates, respectively.

XPS analysis of the BSA-DA-Fe_2O_3, DA-Fe_2O_3 and Fe_2O_3 materials was performed to investigate the chemical composition of the nano-bioconjugate surface (See Figure 4, S4, S5, ESI† for all XPS spectra). The significant photoelectron band of N 1s at 403 and 402 eV for the DA-Fe_2O_3 and BSA-DA-Fe_2O_3 nanoconjugates, respectively, further confirmed the successful functionalization of the surface of the magnetic iron oxide nanoparticles. Additionally, C 1s XPS spectrum of BSA-DA-Fe_2O_3 (Figure 4b) exhibited three different contribution at 284.5, 285.8 and 287.6 eV,

associated to C-C/C=C, C-N and C-O, respectively mainly from the polypeptide chain of the immobilised protein. The peak at 401.1 eV in the BSA-DA-Fe_2O_3 spectrum can be attributed to the N from amino groups while the peak at 402.9 eV can be attributed to the N in the pyrrolic groups of the protein (Figure 4c).[25]

Furthermore, the XPS survey of the parent MNP (see Figure 4a, light green spectrum) displayed the Fe 2p bands at 714.2 and 727.9 eV respectively, indicating the presence of Fe^{3+} species on the iron oxide surface.[26, 27] Interestingly, these bands cannot be clearly visualised in the nanoconjugates spectra, which may indicate that the protein is fully covering the MNPs surface.

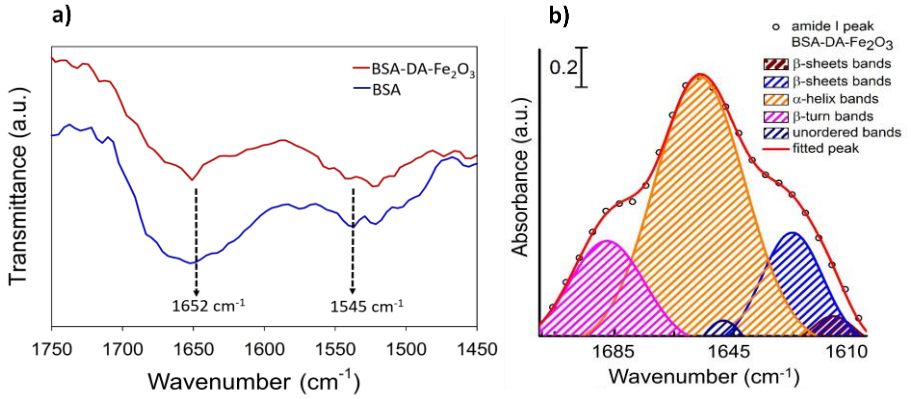

Figure 3. a) FT-IR spectra of BSA and BSA-DA-Fe_2O_3, b) Deconvoluted FT-IR spectrum for BSA-DA-Fe_2O_3 nanobioconjugates in the amide I region.

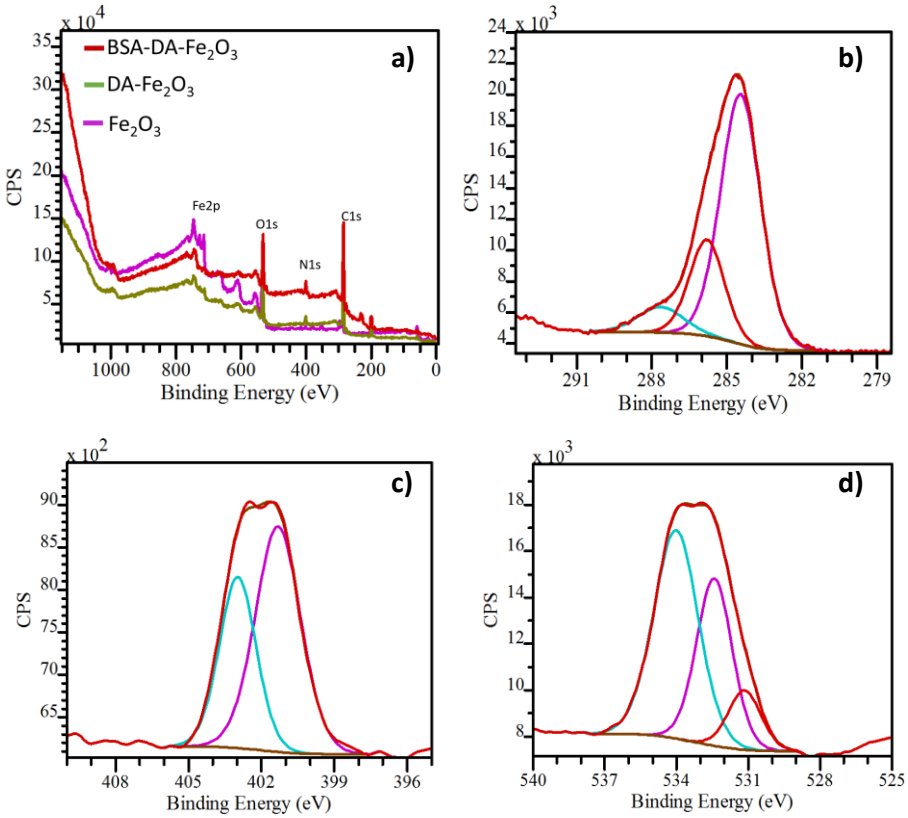

Figure 4. a) XPS survey of BSA-DA-Fe_2O_3 nanobioconjugates and Fe_2O_3 nanoparticles. Deconvoluted high-resolution XPS spectra of BSA-DA-Fe_2O_3 for b) C 1s, c) N 1s and d) O 1s.

The magnetic susceptibilities measured for both Fe_2O_3 nanoparticles and BSA-DA-Fe_2O_3 resulted in similar values, with a slight reduction for the bio-modified nanomaterial. In any case, the synthesized bioconjugates exhibit interesting magnetic properties after the mechanochemical synthesis for further applications. (Table S2. ESI†) The three materials were additionally characterized by TG-DTA measurements (See Fig. S6, ESI†) and N_2 absorption-desorption isotherms analysis. (See Fig. S7, ESI†). These findings also support the proposed presence of BSA on BSA-DA-Fe_2O_3 nanobioconjugates.

Conclusions

The synthesis of novel biofunctionlised magnetic nanomaterials was conducted using an environmentally friendly, simple, innovative and effective mechanochemical protocol. XPS, FT-IR, DLS, Steady-state fluorescence measurements and UV-vis experiments demonstrated the successful immobilisation of the protein on the surface of MNPs. Importantly, BSA molecules retained their native-like properties after the mechanochemical synthesis. The preservation of the magnetic characteristics after the functionalisation, together with the strong affinity of BSA to a variety of organic molecules, open a number of possibilities in the design of BSA-DA-Fe_2O_3 supramolecular assemblies as nanocarriers for biomedical applications to be reported in due course.

Acknowledgments

Rafael Luque gratefully acknowledges support from Consejeria de Ciencia e Innovacion, Junta de Andalucia for funding project P10-FQM-6711 as well as Spanish MINECO for funding Project CTQ2016-78289-P.

References

1. L. H. Wu, A. Mendoza-Garcia, Q. Li and S. H. Sun, *Chem. Rev.*, 2016, **116**, 10473.
2. K. E. Sapsford, W. R. Algar, L. Berti, K. B. Gemmill, B. J. Casey, E. Oh, M. H. Stewart and I. L. Medintz, *Chem. Rev.*, 2013, **113**, 1904.
3. P. C. Lin, C. C. Yu, H. T. Wu, Y. W. Lu, C. L. Han, A. K. Su, Y. J. Chen and C. C. Lin, *Biomacromolecules*, 2013, **14**, 160-168.
4. L. H. Reddy, J. L. Arias, J. Nicolas and P. Couvreur, *Chem. Rev.*, 2012, **112**, 5818.
5. C. Sun, J. S. H. Lee and M. Q. Zhang, *Adv. Drug Delivery Rev.*, 2008, **60**, 1252.
6. J. H. Gao, H. W. Gu and B. Xu, *Acc. Chem. Res*, 2009, **42**, 1097.
7. O. Veiseh, J. W. Gunn and M. Q. Zhang, *Adv. Drug Delivery Rev.*, 2010, **62**, 284.
8. N. Lee and T. Hyeon, *Chem. Soc. Rev.*, 2012, **41**, 2575.
9. M. A. Malvindi, V. De Matteis, A. Galeone, V. Brunetti, G. C. Anyfantis, A. Athanassiou, R. Cingolani and P. P. Pompa, *Plos One*, 2014, **9**, e85835.

10. R. X. Gao, X. R. Mu, Y. Hao, L. L. Zhang, J. J. Zhang and Y. H. Tang, *J. Mater. Chem. B*, 2014, **2**, 1733.
11. K. Ulbrich, K. Hola, V. Subr, A. Bakandritsos, J. Tucek and R. Zboril, *Chem. Rev.*, 2016, **116**, 5338.
12. S. Rana, Y. C. Yeh and V. M. Rotello, *Curr. Opin. Colloid Interface Sci.*, 2010, **14**, 828.
13. A. R. Herdt, B. S. Kim and T. A. Taton, *Bioconjugate Chem.*, 2007, **18**, 183.
14. H. W. Gu, K. M. Xu, C. J. Xu and B. Xu, *Chem. Commun.*,**9** 2006, 941-949.
15. C. J. Xu, K. M. Xu, H. W. Gu, X. F. Zhong, Z. H. Guo, R. K. Zheng, X. X. Zhang and B. Xu, *J. Am. Chem. Soc.*, 2004, **126**, 3392.
16. J. K. Xu, J. J. Sun, Y. J. Wang, J. Sheng, F. Wang and M. Sun, *Molecules*, 2014, **19**, 11465.
17. K. C. Mei, Y. Guo, J. Bai, P. M. Costa, H. Kafa, A. Protti, R. C. Hider and K. T. Al-Jamal, *ACS Appl. Mater. Interfaces*, 2015, **7**, 14176.
18. D. D. Herea, H. Chiriac, N. Lupu, M. Grigoras, G. Stoian, B. A. Stoica and T. Petreus, *Appl. Surf. Sci.*, 2015, **352**, 117.
19. J. Ding, T. Tsuzuki and P. G. McCormick, *J. Mater. Sci.*, 1999, **34**, 5293.
20. M. Ojeda, A. M. Balu, V. Barron, A. Pineda, A. G. Coleto, A. A. Romero and R. Luque, *J. Mater. Chem A*, 2014, **2**, 387.
21. A. Salis, M. Bostrom, L. Medda, F. Cugia, B. Barse, D. F. Parsons, B. W. Ninham and M. Monduzzi, *Langmuir*, 2011, **27**, 11597.
22. L. Z. Zhao, Y. S. Zhao, H. H. Teng, S. Y. Shi and B. X. Ren, *J. Appl. Spectrosc.*, 2014, **81**, 719.
23. C. N. Pace, F. Vajdos, L. Fee, G. Grimsley and T. Gray, *Protein Sci.*, 1995, **4**, 2411.
24. Y. Q. Wu, K. Murayama, B. Czarnik-Matusewicz and Y. Ozaki, *Appl. Spectrosc.*, 2002, **56**, 1186.
25. K. Jiang, S. Sun, L. Zhang, Y. Lu, A. G. Wu, C. Z. Cai and H. W. Lin, *Angew. Chem. Int. Ed.*, 2015, **54**, 5360.
26. Z. Wu, W. Li, P. A. Webley and D. Zhao, *Adv. Mater.*, 2012, **24**, 485.
27. T. Yamashita and P. Hayes, *Appl. Surf. Sci.*, 2008, **254**, 2441.

Supporting Information

Solventless mechanochemical preparation of novel magnetic bioconjugates

Daily Rodriguez-Padrón, Alain R. Puente-Santiago, Alina M. Balu, Antonio A. Romero, Rafael Luque*

The X-ray diffraction patterns of both Fe_2O_3 and BSA-DA-Fe_2O_3 nanomaterials were collected using the D8 Advanced Diffractometer (Bruker AXS) with the Lynxeye detector, at room temperature. TEM images were recorded in a FEI Tecnai G^2 system, equipped with a CCD ("charge coupling device") camera. Previously, the sample was dispersed in ethanol and transferred to a copper grid. UV-visible spectra were collected in a Jasco UV-visible-NIR (model V-570) spectrometer.

Particle size distributions and zeta potential of DA functionalized Fe_2O_3 MNPs and BSA-DA-Fe_2O_3 nanobioconjugate were analyzed using Zetasizer Nano ZSP (Malvern Instruments Ltd.,UK) instrument. All samples were diluted in 10 mM of KNO_3 and measurements were recorded in triplicate (n = 3) at 25 °C.

FTIR measurements were performed on the ABB MB3000 infrared spectrophotometer, equipped with an ATR PIKE MIRacle™ sampler, a window of ZnSe, and 256 scans at a resolution of 8 cm^{-1}. The Horizon MBTM software was employed for the spectra acquisition. During the measurements, the sample was purged with a dehydrated and deoxygenated nitrogen flow (20 mL min^{-1}).

Steady-state fluorescence measurements were carried out on the FLS920 Fluorimeter (Edinburgh Instrument Ltd, Livingston, UK).

XPS analysis was conducted using an ultrahigh vacuum (UHV) multipurpose surface analysis system SpecsTM. The analysis was carried out using a conventional X-ray source (XR-50, Specs, Mg-Kα, hv=1253.6 eV, 1 eV = 1.603 x 10^{-19} J) at pressures <10^{-10} mbar and in a "stop and go" mode. The sample was left overnight under vacuum (<10^{-6} Torr). Finally, spectra were acquired at room temperature (pass energy: 25 and 10 eV, step size: 1 and 0.1 eV, respectively) with the Phoibos 150-MCD energy detector. The deconvolution of the obtained curves was accomplished

with XPS CASA program. The magnetic susceptibility measurements were performed in a Bartington MS-2 instrument. Nitrogen adsorption measurements were carried out in the Micromeritics ASAP 2000 instrument. Moreover, thermogravimetric analysis was accomplished using the System Setaram Setsys 12 TGA instrument.

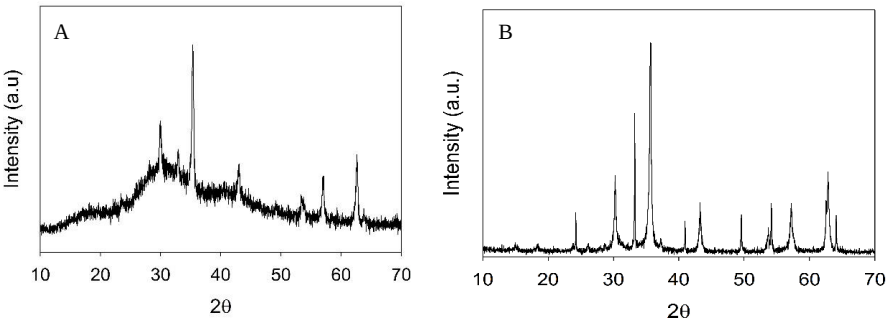

Figure S1. X-ray diffraction patterns of A: BSA-DA-Fe_2O_3 and B: Fe_2O_3.

The XRD pattern of Fe_2O_3 nanoparticles shows a mixture of two phases: maghemite and hematite. In the case of maghemite and magnetite (Fe_3O_4) phases, it is very difficult to clearly distinguish by XRD analysis since these two phases possess a similar XRD pattern. However, the absence of Fe^{2+} species (see XPS analysis) and the reddish-like colour are consistent with a maghemite magnetic phase.

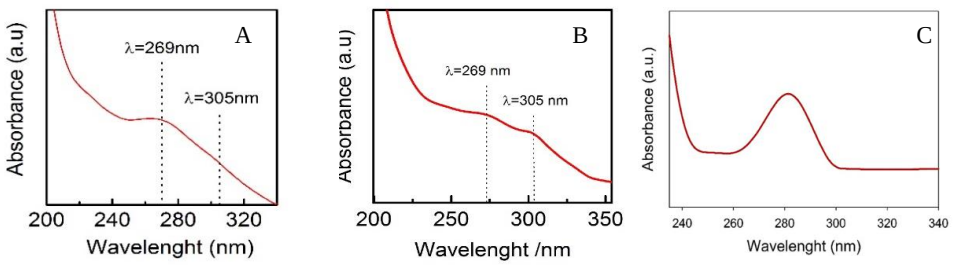

Figure S2. UV-vis spectra of A: DA, B: DA-Fe_2O_3, C: BSA-DA-Fe_2O_3 (1 mg/ml in 0.05 M PBS pH=7)

The UV-vis spectra of DA and DA-Fe_2O_3 was obtained. The main peak around 269 nm, (Q. Wei, F. L. Zhang, J. Li, B. J. Li and C. S. Zhao, Polymer Chemistry, 2010, 1, 1430-1433) in both cases, together with the not appearance of a band at 350 nm corroborate the successful

immobilization of the protein and that the attachment of the BSA to DA-Fe_2O_3 nanoconjugate through non-covalent interactions.

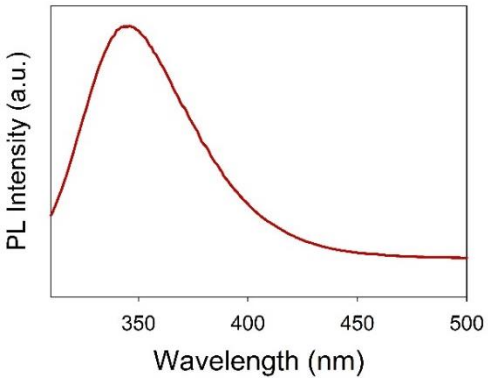

Figure S3. Fluorescence emission spectra of BSA-DA-Fe_2O_3 nanobioconjugates. (Excitation wavelength = 295 nm)

The significant band centered at 345 nm can be associated to native BSA, which is consistent with the fact that there are no changes in the environment of the tryptophan residues and therefore that BSA retain its structural features after the immobilization step. [E. L. Gelamo, M. Tabak, (2000). *Spectrochimica Acta Part A: Molecular and Biomolecular Spectroscopy*, **2000**, *56*, 2255-2271.]

Table S1. Conformational Analysis of BSA-DA-Fe_2O_3. Structural Percent values are given.

Secondary structure	**Native BSA pH=7.4***	**BSA-DA-Fe_2O_3**
α-helix	68%	67%
β-sheet	20%	18%
β-turn	5%	13%
unordered	4%	2%
Side chain moeties	3%	-

*Values reported in literature [Journal of Colloid and Interface Science 493 (2017) 334–341]

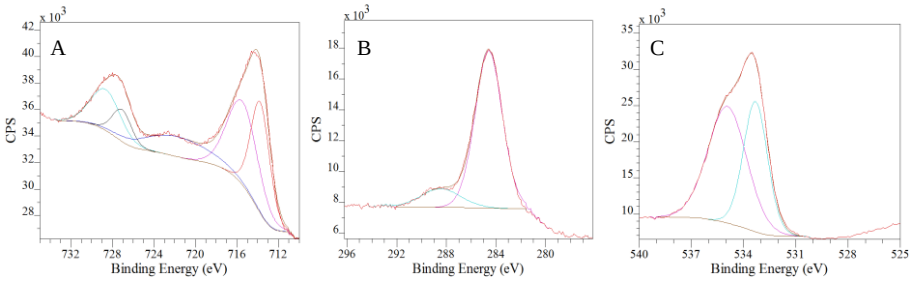

Figure S4. Deconvoluted high-resolution XPS spectra of Fe_2O_3 for a) Fe 2p, b) C 1s and c) O 1s.

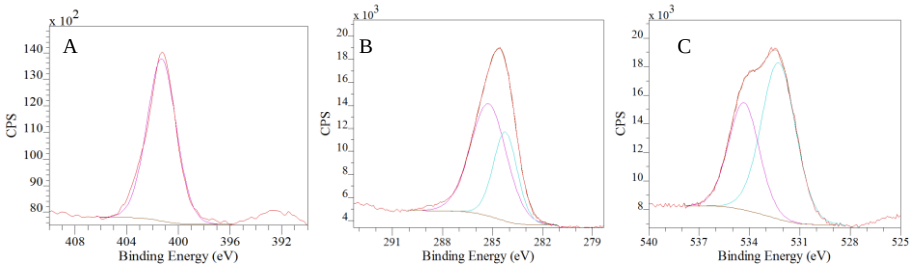

Figure S5. Deconvoluted high-resolution XPS spectra of DA-Fe_2O_3 for a) N 1s, b) C 1s and c) O 1s.

The peak at 401.1 eV can be attributed to the N from amino groups of the dopamine. These results are an evidence of the effective functionalization of the Fe_2O_3 nanoparticles with dopamine.

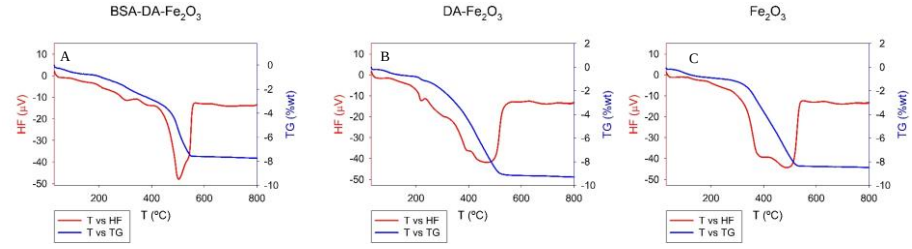

Figure S6. ATG of the a) BSA-DA-Fe_2O_3, b) DA-Fe_2O_3 and c) Fe_2O_3 nanostructures.

The first weight loss at 100 °C in the three materials: BSA-DA-Fe_2O_3, DA-Fe_2O_3, Fe_2O_3 can be correlated to the presence of water in the samples. From 220 °C and 350 °C, a progressive weight loss was observed, that is

more marked for the BSA-DA-Fe_2O_3 nanoconjugate and can be associated to the non-oxidative decomposition of organic species in the materials.

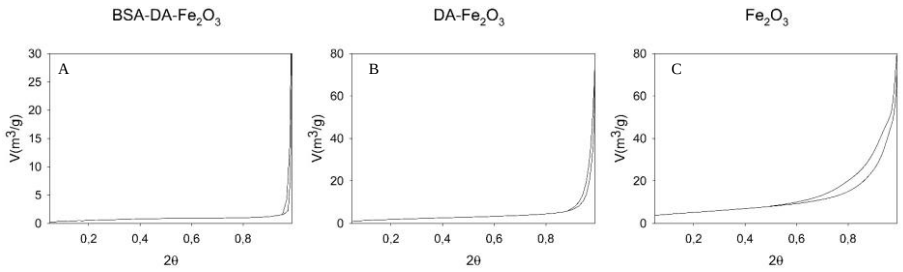

Figure S7. Adsorption-desorption isotherm of the BSA-DA-Fe_2O_3, DA-Fe_2O_3 and Fe_2O_3 nanostructures.

As was expected, the surface area values of the Fe_2O_3, DA-Fe_2O_3 and BSA-DA-Fe_2O_3 nanomaterials were found around 20, 7, and 2 m^2 / g, respectively, lower after the functionalization. The obtained surface area of the MNPs is satisfying, taking into account its preparation methodology.

Table S2. Magnetic susceptibility of the Fe_2O_3 and BSA-DA-Fe_2O_3.

Material	Magnetic susceptibility (10^{-6} m^3Kg^{-1})
Fe_2O_3	282
BSA-DA-Fe_2O_3	254

2.4. Mechanochemical design of hemoglobin-funtionalised magnetic nanomaterials for energy storage devices

Once the synthetic strategy was designed, we move forward to the use of such methodology for the preparation of a new bioconjugate based, in this case, on hemoglobin and cobalt oxide magnetic nanoparticles. The obtained sample was fully characterized and employed in the construction of a bioinspired energy storage device with excellent long cycle life.

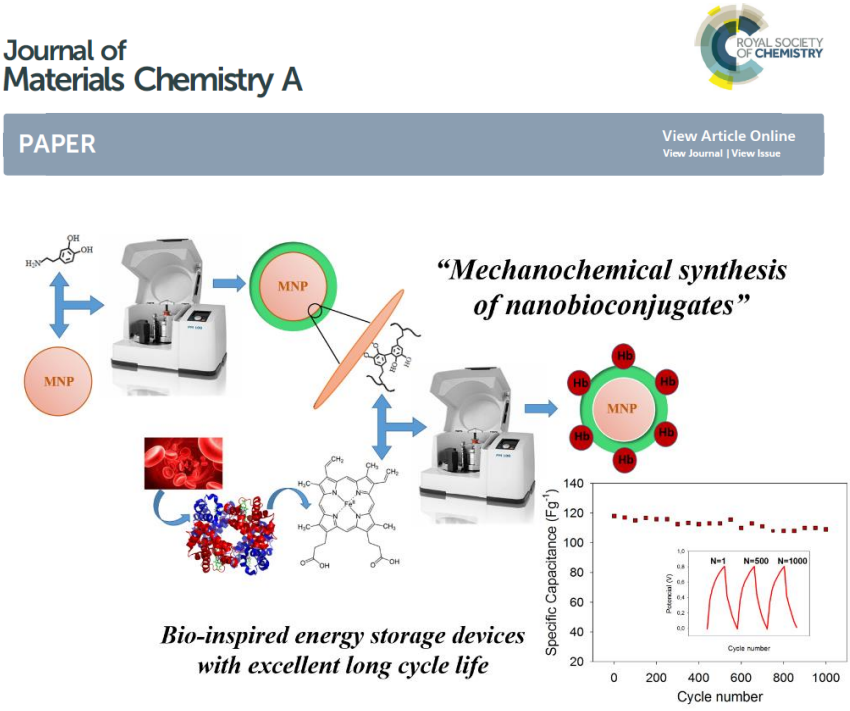

Daily Rodríguez-Padrón; Alain R. Puente Santiago; Alvaro Caballero; Almudena Benítez; Alina M. Balu; Antonio A. Romero Reyes; Rafael Luque Álvarez de Sotomayor. **2017**. Mechanochemical design of hemoglobin-functionalised magnetic nanomaterials for energy storage devices. **Journal of Materials Chemistry A**. 5. 16404-16411. 10.1039/C7TA04135G. IF: 9.931.

Mechanochemical design of hemoglobin-functionalised magnetic nanomaterials as energy storage devices

Daily Rodríguez-Padrón[a], Alain R. Puente-Santiago[b], Alvaro Caballero[c], Almudena Benítez[c], Alina M. Balu[a], Antonio A. Romero, Rafael Luque[a]*

[a]*Departamento de Química Orgánica, Grupo FQM-383, Universidad de Cordoba, Campus de Rabanales, Edificio Marie Curie (C-3), Ctra Nnal IV-A, Km 396, E14014, Cordoba (Spain), e-mail: q62alsor@uco.es*

[b]*Departamento de Química Física, Universidad de Cordoba, Campus de Rabanales, Edificio Marie Curie (C-3), Ctra Nnal IV-A, Km 396, E14014, Cordoba*

[c]*Departamento de Química Inorgánica e Ingeniería Química, Campus de Rabanales, Edificio Marie Curie (C-3), Ctra Nnal IV-A, Km 396, E14014, Cordoba*

Abstract

A bio-modified nanomaterial based on horse hemoglobin (Hb) and cobalt oxide magnetic nanoparticles (Co_3O_4 MNPs) was synthesized using a simple solventless mechanochemical dry milling step. Dopamine (DA) was employed as a robust scaffold to design the stable nanostructures. The nitrogen band (400 eV) in the XPS spectrum, together with zeta potential measurements support the presence of Hb in the obtained nanostructure. Additionally, the amide I and amide II bands at 1654 cm^{-1} and 1545 cm^{-1} in the FT-IR spectrum suggest that Hb does not undergo changes in its secondary structure. This assumption was also confirmed by Resonance Raman spectroscopy. TEM images reveals a homogeneous distribution of the Hb-DA-Co_3O_4, with a particle diameter of 10.1±0.2 nm. Functionalised materials exhibited a relevant magnetism, preserved upon functionalisation. The functionalised Hb-DA-Co_3O_4 nanocomposite was successfully employed in the design of a supercapacitor (specific capacitance average: 115 Fg^{-1}) with excellent cycling durability, over 94% specific capacitance retained after 1000 cycles.

Introduction

Bio-modified magnetic nanoparticles have attracted significant attention in the past decade.[1-3] A wide range of novel nanomaterials have been designed taking advantage of the unique properties of magnetic nanoparticles, which can be easily manipulated and separated from the bulk solution by a magnetic field gradient. This behaviour opened exciting opportunities in many areas of biotechnology, biosensing and biomedicine such as enzyme immobilization,[4, 5] nucleic acid detachment,[6, 7] protein adsorption and purification,[8, 9] cell sorting[10, 11] and drug delivery.[12, 13]

Various strategies have been developed to functionalize biological molecules on magnetic nanoparticle surfaces. One successful strategy involves the covalent binding of small molecules to MNPs surfaces to provide specific functional groups that can favour further coordination of biomolecules including DNA, antibodies, enzymes and proteins.[14] Dopamine (was frequently employed as a versatile and robust scaffold to immobilize biomolecules on MNPs[15, 16] due to the good stability of the resulting nanostructures, simplicity in linkages and the ability to restructure under-coordinated Fe surface sites back to a bulk-like lattice structure with an octahedral geometry for oxygen-coordinated iron.[17] Nevertheless, nearly all reported synthetic methods have been conducted in aqueous phase and/or solution with inherent drawbacks including negative solvent effects and lack of control over surface chemistry.

In order to simplify the synthesis of bio-modified magnetic nanoparticles, reducing both reaction times and circumventing solvent issues, mechanochemical processes offers a valuable alternative to traditional routes.[18] This simple, inexpensive, reproducible and greener methodology has been demonstrated to be highly useful for the design of a range of advanced nanomaterials.[19-21] Interestingly, mechanochemistry has not been reported to date for the preparation of bio-conjugates based on proteins and magnetic nanoparticles.

In this sense, Hemoglobin (Hb) is an excellent candidate to be used in mechanochemical synthesis due to its robustness, commercial

availability, moderate cost and known well documented structure.[22] This protein possesses a quaternary structure that contains four polypeptide chains (globin chains) and one heme group bound to each of the globin chains which can store and transport oxygen in muscle cells in vertebrate animals.[23]

Metalloproteins such as c-type cytochrome immersed in an electrically conductive matrix of microbial biofilms has been proven to act as pseudo-capacitors.[24] The redox groups of the cytochrome give rise to fast surface redox reactions[25] which can provide high electron storage capacity and high specific capacitances to the biofilm. These preliminary results opened innovative possibilities for capacitors design which have attracted interest in energy storage since supercapacitors have the potential to complement or replace batteries.

Inspired by such original approach, our research group proposes herein the first mechanochemical strategy that combines magnetic nanomaterials with proteins towards the design of a novel bio-inspired supercapacitor under dry milling using dopamine as a robust linker. The concept of the proposed methodology is depicted in Scheme 1.

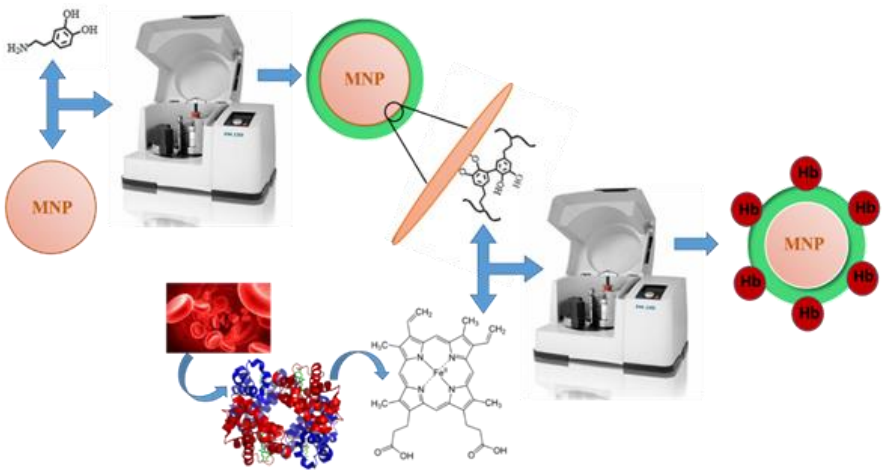

Scheme 1 Overview of the preparation of the Hb-DA-Co_3O_4 bio-modified material

Experimental part

Synthesis of bio-modified magnetic nanoparticles: Hb-DA-Co_3O_4

Horse hemoglobin (Hb) and dopamine hydrochloride (DA-HCl), together with pre-synthesized Co_3O_4 magnetic nanoparticles (MNPs) were utilised to develop a new bio-modified nanomaterial by mechanochemical milling processes. In a first step, 125 mg of DA-HCl was solved in 600 µL of ultrapure water and added to 500 mg of MNPs. This mixture was milled in a Retsch PM100 ball mill under typical optimized conditions from previous work of the group (i.e. 200 rpm, 10 min),[26] resulting in DA-Co_3O_4. The synthesis of Hb-DA-Co_3O_4 was subsequently conducted by milling a dispersion of 100 mg of Hb in 600 µL of NaH_2PO_4 buffer (pH=7) together with DA-Co_3O_4 under identical grinding conditions. Hb-DA-Co_3O_4 obtained after milling was washed five times with ultrapure water to remove any weakly physisorbed protein and finally oven dried at 30ºC for 24h.

Material Characterization

Hb-DA-Co_3O_4 bio-modified material was characterized by X-ray Photoelectronic Spectroscopy (XPS), Transmission Electronic Microscopy (TEM), Dynamic Light Scattering (DLS), Fourier Transform-Infrared Spectroscopy (FT-IR) and Raman spectroscopy, in order to prove the protein immobilization on MNPs.

The X-ray diffraction patterns of both, Co_3O_4 MNPs and Hb-DA-Co_3O_4 bioconjugate were collected using the D8 Advanced Diffractometer (Bruker AXS) with the Lynxeye detector, at room temperature. The 2θ scan range was from 10° to 70°, with a step size of 0.02° and a counting time of 0.2 second for phase identification and 1 second for phase quantification. Phase identifications were conducted using the Bruker Diffrac-plus EVA software, supported by the Powder Diffraction File (PDF) database of the International Centre for Diffraction Data (ICDD).

XPS analysis was conducted at the Central Service of Research Support (SCAI) of the University of Cordoba, using an ultrahigh vacuum (UHV) multipurpose surface analysis system SpecsTM. The experiment was carried out at pressures $<10^{-10}$ mbar, using a conventional X-ray source (XR-50, Specs, Mg-Kα, hv=1253.6 eV, 1 eV = 1.603×10^{-19} J) in a "stop and

go" mode. The sample was deposited on a sample holder using a double-sided adhesive tape, and afterwards evacuated overnight under vacuum (<10^{-6} Torr). Spectra were collected at room temperature (pass energy: 25 and 10 eV, step size: 1 and 0.1 eV, respectively) with the Phoibos 150-MCD energy detector. The XPS CASA program was employed for deconvolution of the obtained curves.

FTIR spectra were recorded on an infrared spectrophotometer (ABB MB3000 with Horizon MBTM software), equipped with an ATR PIKE MIRacleTM sampler, a window of ZnSe, and 256 scans at a resolution of 8 cm^{-1}. During the measurements the sample was purged with a dehydrated and deoxygenated nitrogen flow (20 mL min^{-1}). Spectra were recorded at room temperature in a 4000-600 cm^{-1} wavenumber range. UV-visible absorption spectra were performed on the Jasco UV-visible-NIR (model V-570) spectrophotometer.

Raman measurements were carried out on a XploRA PLUS Raman spectrometer with a 532 nm excitation laser, a standard spectral resolution of 8 cm^{-1}, and a step mapping stage of 0.1 μm with SWIFT™ imaging. The LabSpec Spectroscopy Suite software was used to obtain the spectra.

TEM analysis was performed in the FEI Tecnai G^2 system, equipped with a CCD ("charge coupling device") camera. The sample was dispersed in ethanol and directly deposited on a copper grid, previous to analysis.

Particle size distributions and zeta potential of DA-Co_3O_4 and Hb-DA-Co_3O_4 bioconjugate were analyzed using Zetasizer Nano ZSP (Malvern Instruments Ltd.,UK) instrument. The samples were previously diluted in 10 mM of KNO_3 and the measurements were recorded in triplicate (n = 3) at 25 °C.

Thermogravimetric analysis was accomplished by simultaneous TG-DTA measurements using a Setaram Setsys 12 TGA thermobalance. Samples were heated at a rate of 10 °C min^{-1} under nitrogen atmosphere (40 mL min^{-1}) in the 50–1000 °C temperature range.

The magnetic susceptibility of both Hb-DA-Co_3O_4 and Co_3O_4 materials was evaluated at room temperature and at low frequency (470 Hz), employing a Bartington MS-2 instrument.

Electrochemical experiments

Cyclic voltammetry (CV) measurements were performed in a Potenciostat/Galvanostat Autolab (Solartron1286), 5 sequential cycles were programmed at scan rates of 100 mV/s in a potential window of -0.5–0.7 V. A two-electrode configuration consisting of Hb-DA-Co_3O_4 nanocomposite as working electrode and a Pt foil as counter electrode was used.

The charging/discharging measurement was carried out through chronopotentiometry analysis (CP) at a scan rate of 30 Ag^{-1} in a voltage range of 0-0.8 V using a multichannel potentiostat–galvanostat system (Arbin BT2000). The specific capacitance of the Hb-DA-Co_3O_4 electrodes was calculated from the galvanostatic discharging curves by:

$$C_m = \frac{I \cdot \Delta t}{\Delta E \cdot m} \qquad \text{(equation 1)}$$

where C_m is the specific capacitance of the supercapacitor, I is the current of the charge–discharge, ΔE is the potential range, Δt is the discharging time period in seconds, and the m is the mass load of active materials.

Results and discussion

Hb-DA-Co_3O_4 bio-modified nanomaterial was characterized using several techniques including magnetic susceptibility measurements. The structure and arrangement of the Hb-DA-Co_3O_4 and Co_3O_4 nanomaterials has been investigated by X-ray Diffraction measurements. The diffraction peaks of both samples can be indexed to the spinel Co_3O_4 phase, with the appearance of an amorphous phase after the functionalization. (See Fig. S1, ESI†)

A comparison between Hb-DA-Co_3O_4, DA-Co_3O_4 and the parent Co_3O_4 MNPs by X-ray photoelectron spectroscopy indicated the presence of Co^{3+} species in the three materials from the Co2p peak around 788.0 eV. Importantly, the presence of nitrogen (N1s∼401.0 eV) on the surface of Hb-DA-Co_3O_4 and DA-Co_3O_4 was clearly visualised in the survey XPS spectrum (See Fig. 1a, Fig. S2, S3 ESI†), absent in MNPs. Figure 1c shows two peaks at 400.1 and 402.4 eV in the Hb-DA-Co_3O_4 spectrum, that can be attributed to the N from amino groups and N in the porphyrinic groups of the protein, respectively.[27] This is a clear indication of the presence of

the protein on the surface of the MNPs after mechanochemical functionalisation. Additional bands corresponding to C1s (285.0 eV) and O1s (531.9 eV) also appear in the spectra of the materials, being evidently higher for Hb-DA-Co_3O_4. Specifically, the deconvoluted high-resolution XPS spectrum of C 1s (Fig. 1b) exhibited three different contribution at 284.6, 286.1 and 288.0 eV, associated to C-C/C=C, C-N and C-O from the protein chain, respectively. These findings further supported the presence of Hb in the obtained bio-conjugated nanostructure.

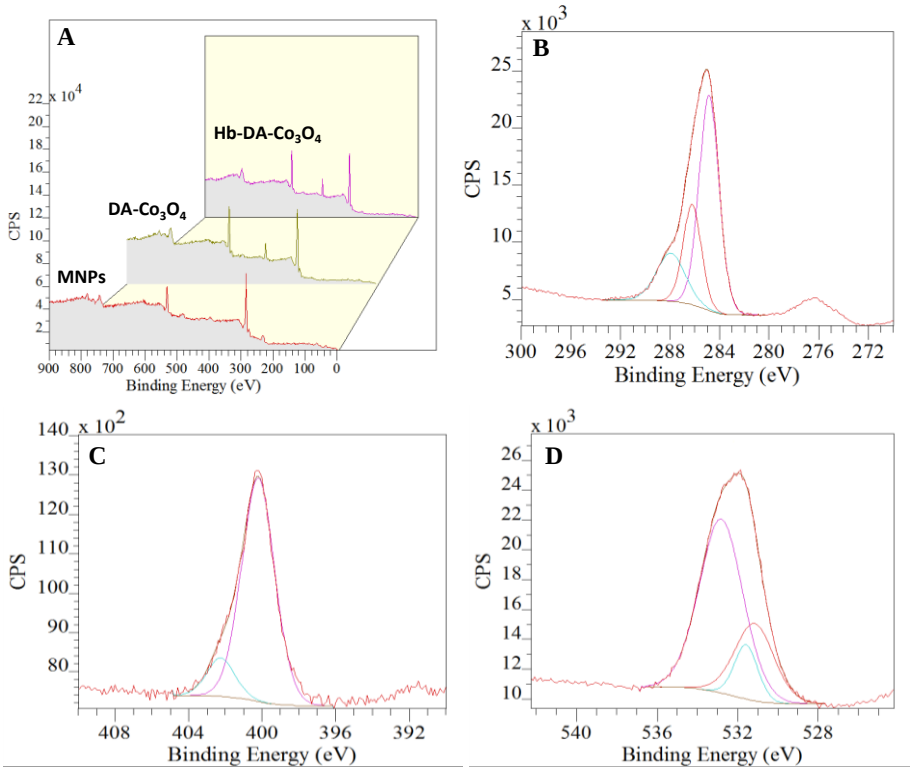

Figure 1. a. XPS survey of Hb-DA-Co_3O_4, DA-Co_3O_4 and Co_3O_4 MNPs. Deconvoluted high-resolution XPS spectra of Hb-DA-Co_3O_4 for b) C 1s, c) N 1s and d) O 1s

The conformation of immobilized Hb on the surface of MNPs was examined by FT-IR. The successful functionalisation of the surface could be confirmed by the presence of amide I and amide II bands from Hb at 1654 cm^{-1} and 1545 cm^{-1}, respectively (Fig. 2.A). The former band (1700–

1600 cm^{-1}) can be attributed to the C=O stretching vibration of peptide linkages in the backbone of the protein, while the latter (1620–1500 cm^{-1}) results from the combination of N-H bending and C–N stretching. Amide I and II bands observed in the spectra of Hb-DA-Co_3O_4 are substantially at the same wavelength of those obtained for Hb in solution (1650 cm^{-1} and 1540 cm^{-1}), suggesting that Hb does not undergo any structural changes in its secondary structure, with a preserved native-like structure after the mechanochemical milling process, as expected due to the mild milling conditions (200 rpm, 10 min). Functionalisation experiments run at longer milling times (30 mins) do not seem to induce changes in the protein structure. This hypothesis was also corroborated by UV-vis measurments. Adittionally, the UV-vis spectrum of DA-Co_3O_4 was also obtained. (See Fig. S4, ESI†)

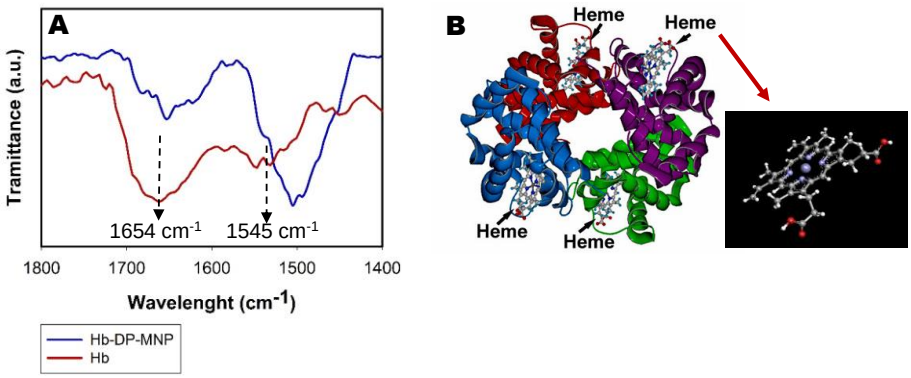

Figure 2. A: FT-IR spectra of the Hb-DA-Co_3O_4 and Hb; B: Structure of horse hemoglobin.

Fig. 3 display a representative RR spectrum of the hybrid nanomaterial at 532 nm. It can be observed four prominent peaks located at 476, 515, 614 and 684 cm^{-1}, which correspond to E_g, $F_{2g}^{(2)}$,$F_{2g}^{(1)}$ and O_h^7 Raman active modes of the inorganic core formed by the spinel Co_3O_4. [28-30] The bands in the frequency range of 1300-1600 cm^{-1} show the typical vibrations of the hemoglobin porphyrin macrocycles tied to MNPs surfaces.[31-34] The ν_4 oxidation state vibration marker band at 1371 cm^{-1} reveals that the irons of heme groups are mainly in the ferric state.[31] The ν_2 vibrational mode which is sensitive to the spin state of the iron atom is observed at 1585

cm^{-1}, indicating that the redox groups of the proteins are in a six-coordinated low spin configuration (6cLS).[34] Both methodologies (FT-IR, and Raman measurements) were generally in good agreement, supporting the validity of our assumption on preserved native protein structure after the synthetic process.

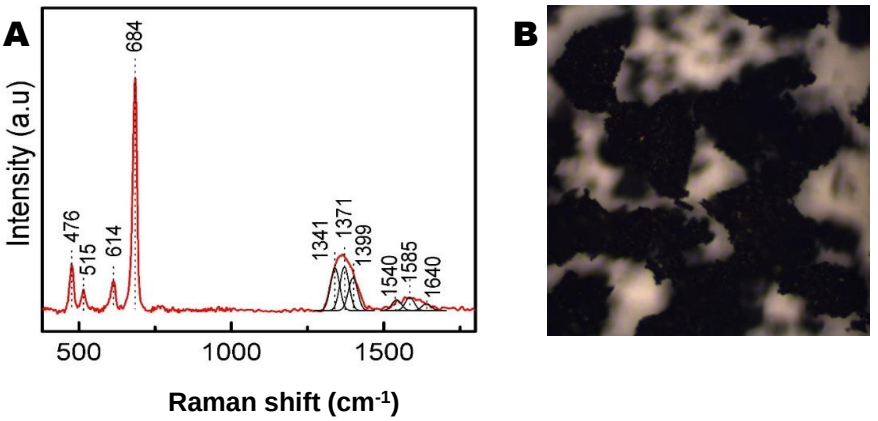

Figure 3. A: Raman spectrum. Excitation at λ=532nma and B: Raman images of Hb-DA-Co_3O_4 nanoparticles

The morphology of both parent MNPs and Hb-DA-Co_3O_4 nanomaterials was determined by TEM analysis. TEM micrographs depict a homogeneous distribution of the magnetic nanoparticles for both materials with a mean diameter of 10.1±0.2 nm. In the case of Hb-DA-Co_3O_4, the magnetic nanoparticles could be entrapped by the protein, with a significant tendency to form agglomerates that can be observed (Fig. 4), being also an evidence of the aggregation of Hb on the surface of the nanomaterials.

The dynamic light scattering data of Hb-DA-Co_3O_4 conjugate (See Fig. 5a) displayed an appreciable degree of agglomeration with an average hydrodynamic size of 177 nm. After the protein functionalization, the zeta potential of DA-Co_3O_4 decrease from 4.9 mV to -1.8 mV. (See Fig. 5b, S5 ESI†), which is in agreement with the zeta potential of the Hb in solution and confirm the successful anchorage of the protein on the MNPs surfaces.[35, 36]

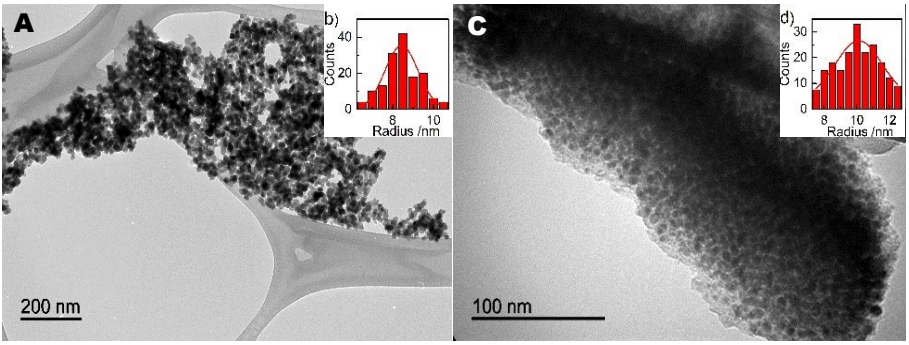

Figure 4. TEM images of **A**: MNPs, **C**: Hb-DA-Co_3O_4, Particle distribution of **B**: MNPs, **D**: Hb-DA-Co_3O_4 Hb-DA-Co_3O_4.

Thermogravimetric analysis was performed to investigate the desorption-calcination of both materials: A) MNPs and B) Hb-DA-Co_3O_4 (Fig. 6). The first weight loss at 100 ºC in both, MNPs and Hb-DA-Co_3O_4 (endothermic-TDA signal) can be correlated to the presence of water in the materials. From 220 ºC and 250 ºC for MNPs and Hb-DA-Co_3O_4 respectively, a progressive weight loss was observed, that can be assigned to the non-oxidative decomposition of organic species present in the materials. Interestingly, DTA experiments of Hb-DA-Co_3O_4 clearly exhibited two sharp endothermic bands at 270 and 320 ºC, corresponding to the decomposition of the protein in the material. Comparably, no bands could be observed in this range despite a similar TG mass loss profile. These findings also support the proposed presence of Hb on Hb-DA-Co_3O_4.

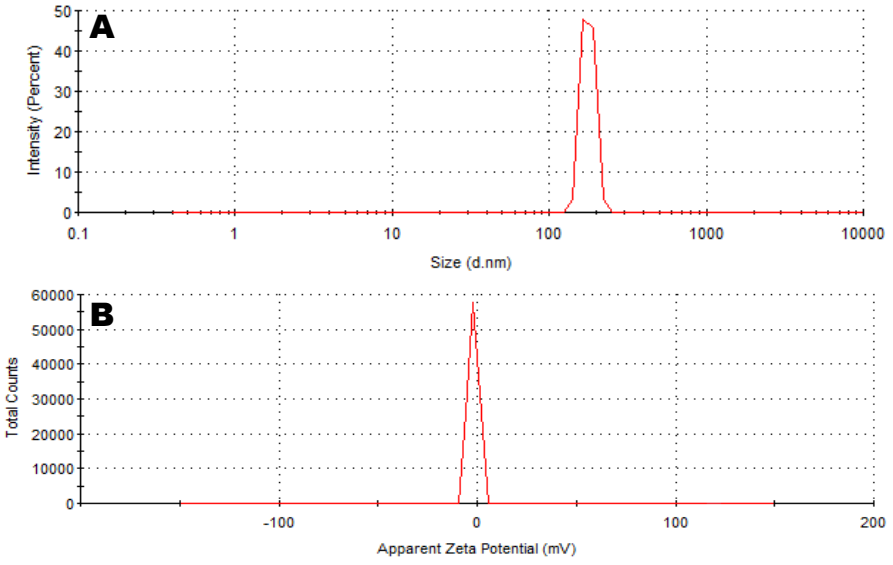

Figure 5. A Dynamic light scattering data and **B** zeta potential of Hb-DA-Co_3O_4 nanobioconjugates.

The magnetic susceptibilities measured for both MNPs and Hb-DA-Co_3O_4 resulted in similar values, with a slightly lower value for the bio-modified nanomaterial (Table 1). The observed loss could be both attributed to the protein loading after functionalisation as well to the functionalised material itself. In any case, without any considerable loss of magnetism after the synthetic process, both materials feature attractive properties for magnetic separation and manipulation in view of potential applications.

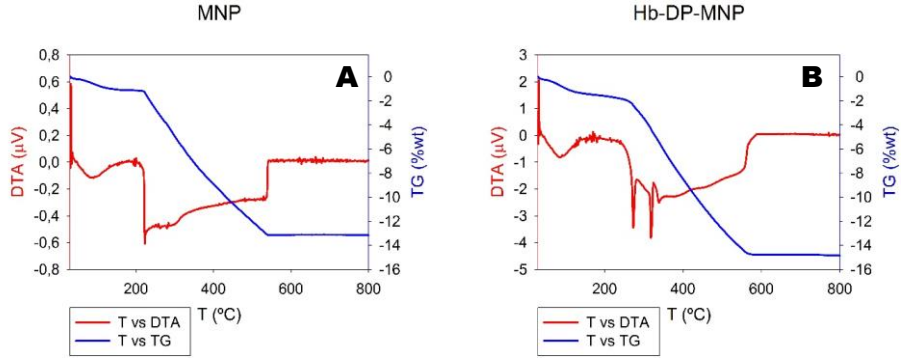

Figure 6. ATG of the **A**: MNPs, **B**: Hb-DA-Co_3O_4

Table 1 Magnetic susceptibility of the Hb-DA-Co_3O_4 and MNPs

Material	Magnetic susceptibility (10^{-6} m^3Kg^{-1})
MNPs	370
Hb-DA-Co_3O_4	357

Electrochemical analysis

The cyclic voltammograms (CV) of A) MNPs, B) DA-Co_3O_4 and C) Hb-DA-Co_3O_4 nanocomposites in 0.1M PBS at a scan rate of 100 mV/s are depicted in Fig. 7. No redox peaks were observed for MNPs and DA-Co_3O_4 as expected (Fig. 7a, 7b), indicating a non-electroactive behaviour of both nanostructured materials. Comparably, cyclic voltammograms of Hb-DA-Co_3O_4 nanocomposite (Fig. 7c) showed two well-defined redox peaks located at 0.007 V and -0.097 V vs Ag/AgCl respectively. These results can be associated with the Hb-heme Fe (III)/Fe (II) redox couple[37, 38] and suggest that a fraction of Hb immobilized on MNPs surface adopted an active electron transfer (ET) orientation. The cyclic voltammetry of Hb-DA-Co_3O_4 was consistent with a pseudocapacitance behavior where the charge and discharge processes are associated with oxidation and reduction peaks,[39, 40] whereas the voltammogran of MNPs displayed a rectangular shape, typical of a pure electrostatic capacitor.[41]

The presence of pseudocapacitance in Hb-DA-Co_3O_4 was also evidenced in galvanostatic charge and discharge cycling profiles (Fig. 8). The nanocomposite clearly deviated from the triangular shape of an ideal capacitor in which the electrostatic charge is accumulated in the double layer of the electrolyte-electrode interface.[42] A significant hump in the charge branch of the cycles was observed, in agreement with the expected pseudocapacitance behaviour of redox molecules.[40, 42, 43] The galvanostatic measurments of DA-Co_3O_4 were also performed (See Fig. S6, ESI†). The obtained results indicate that the observed pseudocapacitance is due to the electron exchange at the redox groups of the electroactive hemoglobins immobilized on the DA-Co_3O_4 surfaces.

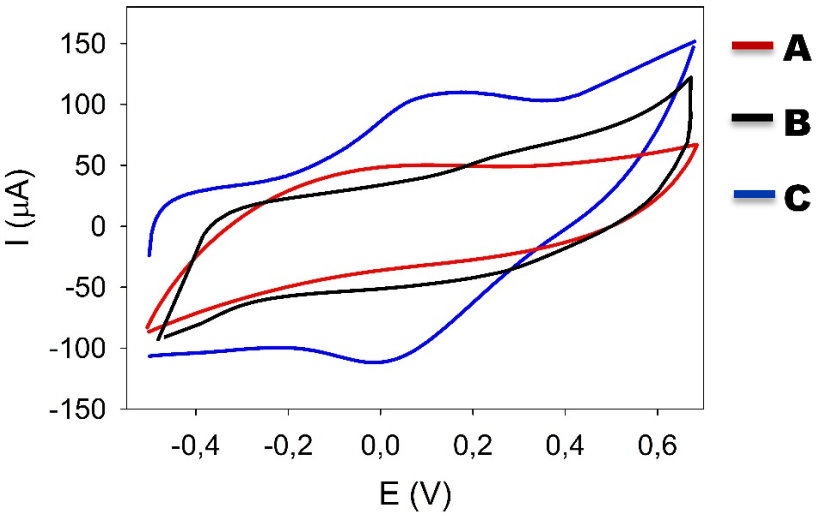

Figure 7. Representative cyclic voltammograms of A: MNPs, B: DA-Co_3O_4 and C: Hb-DA-Co_3O_4 nanocomposites at the scan rate of 100 mV/s in 0.1 M PBS pH=7

Hb-DA-Co_3O_4 possessed an average of specific capacitance of 115 Fg^{-1}, certainly comparable with reported synthetic supercapacitors[44, 45] and with the specific capacitance reported for a supercapacitor based on c-type cytochromes using conductive nanostructured networks of living bacteria[24] (Table 2). Importantly, it should be point out that the specific capacitance of a Hb film have been reported to be 12.18 F/g,[46] which is 10 times lower that the one that we reported on this manuscript. This finding strongly confirmed the successful described biosupercapacitor design. Although other nanomaterials provide higher capacitance values such as carbon nanotubes (CNTs) based networks materials (100-350 Fg^{-1}), metal oxide-carbon hybrid structures (200-700 Fg^{-1}) and conductive polymers (200-1000 Fg^{-1});[47] they have several drawbacks based mainly in the high cost, tedious fabrication steps, and difficult scale up.

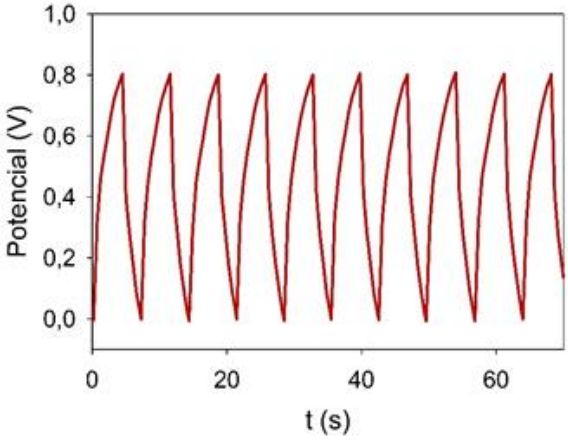

Figure 8. Galvanostatic charge and discharge profile of Hb-DA-Co_3O_4, at a current density of 30Ag^{-1} in 0.5 M KOH aqueous solution.

Table 2. Specific capacitance of supercapacitors reported in literature.

Supercapacitor configuration	Intensity (mA)	Range of potential	Scan rate	Specific Capacitance (Fg^{-1})	Reference
c-cytochromes on a microbial film	1	0-0.8	-	110[a]	24
Fe_3O_4 nanocrystals graphene composites	-	-	100mV/s	88[b]	41
graphene/MnO_2/ACN asymmetric	-	-	1mV/s	113.5[b]	42
Hb-DA-Co_3O_4	0.5	0-0.8	30Ag^{-1}	115[a]	This work

[a] Specific capacitance obtained from galvanostatic curves and [b] Specific capacitance obtained from CV curves.

The specific capacitance of Hb-DA-Co_3O_4 as a function of the number of cycles has also been represented in Fig. 9. Approximately 94% (110 Fg^{-1}) of the initial specific capacitance (118 Fg^{-1}) could be measured after 1000 cycles, further demonstrating the high stability of the designed bio-nanocomposite and its excellent properties as a high-performance supercapacitor.

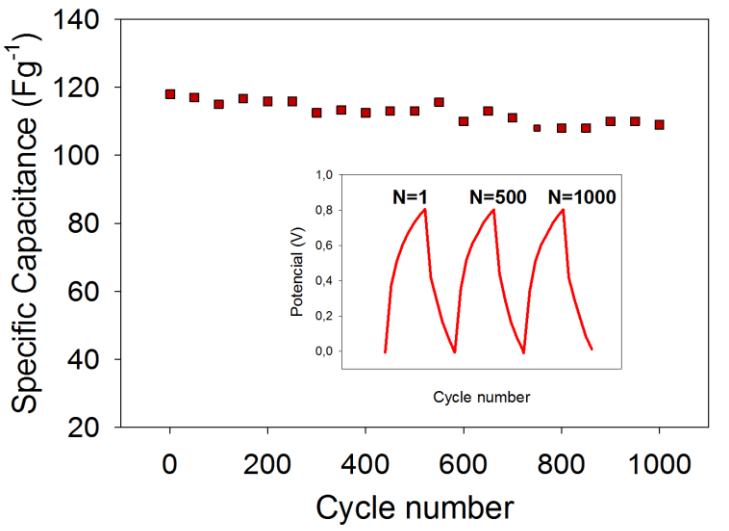

Figure 9. Cycling behaviour of Hb-DA-Co_3O_4 nanocomposite at a current density of 30Ag^{-1} in 0.5 M KOH aqueous solution. Inset: Different cycles of galvanostatic charge-discharge curves.

Conclusions

The design of a bio-inspired protein-functionalised magnetic nanomaterial containing horse hemoglobin, dopamine and a Co nanoferrite as support was successfully accomplished using a mechanochemical approach. The proposed dry milling functionalisation was proven to be a simple, environmentally friendly and effective alternative methodology for the preparation of bio-modified materials for various applications. The incorporation of the protein on the surface of the Co-containing nanostructures was confirmed by XPS, DLS, FT-IR, Raman spectroscopy and TG/DTA, with fully preserved protein structure after the milling process. A novel and durable supercapacitor based could also be developed based on the obtained Hb-DA-Co_3O_4 nanocomposite. The assembled supercapacitor could be reversibly cycled in the voltage region of 0-0.8 V, exhibiting a maximum specific capacitance of 118 Fg^{-1} at a scan rate of 30 Ag^{-1}. Additionally, the supercapacitor device showed

an excellent long cycle life along with 94% specific capacitance retained after 1000 cycles. We envisaged the proposed system and further modifications currently under investigation in our laboratories to pave the way to further developments of environmentally friendly and affordable bio-inspired energy storage devices for practical applications.

Acknowledgments

Rafael Luque gratefully acknowledges support from Consejeria de Ciencia e Innovacion, Junta de Andalucia for funding project P10-FQM-6711 as well as Spanish MINECO for funding Project CTQ2016-78289-P.

References

1. Y. Pan, X. W. Du, F. Zhao and B. Xu, *Chem. Soc. Rev.*, 2012, **41**, 2912.
2. S. Laurent, D. Forge, M. Port, A. Roch, C. Robic, L. V. Elst and R. N. Muller, *Chem. Rev.*, 2008, **108**, 2064.
3. K. Ulbrich, K. Hola, V. Subr, A. Bakandritsos, J. Tucek and R. Zboril, *Chem. Rev.*, 2016, **116**, 5338.
4. G. D. Liu, Y. H. Lin, V. Ostatna and J. Wang, *Chem. Commun.*, 2005, **27**, 3481.
5. D. Sarauli, C. Wettstein, K. Peters, B. Schulz, D. Fattakhova-Rohlfing and F. Lisdat, *ACS Catal.*, 2015, **5**, 2081.
6. P. R. Levison, S. E. Badger, J. Dennis, P. Hathi, M. J. Davies, I. J. Bruce and D. Schimkat, *J. of Chromatogr. A*, 1998, **816**, 107.
7. M. Uhlen, *Nature*, 1989, **340**, 733.
8. X. P. Jia, M. L. Xu, Y. Z. Wang, D. Ran, S. Yang and M. Zhang, *Analyst*, 2013, **138**, 651.
9. Z. W. Xia, Z. A. Lin, Y. Xiao, L. Wang, J. N. Zheng, H. H. Yang and G. N. Chen, *Biosensors & Bioelectronics*, 2013, **47**, 120.
10. T. J. Yoon, K. N. Yu, E. Kim, J. S. Kim, B. G. Kim, S. H. Yun, B. H. Sohn, M. H. Cho, J. K. Lee and S. B. Park, *Small*, 2006, **2**, 209.
11. R. Di Corato, N. C. Bigall, A. Ragusa, D. Dorfs, A. Genovese, R. Marotta, L. Manna and T. Pellegrino, *ACS Nano*, 2011, **5**, 1109.
12. J. Kim, H. S. Kim, N. Lee, T. Kim, H. Kim, T. Yu, I. C. Song, W. K. Moon and T. Hyeon, *Angew. Chem. Int. Ed.*, 2008, **47**, 8438.

13. O. Veiseh, J. W. Gunn and M. Q. Zhang, *Adv. Drug Delivery Rev.*, 2010, **62**, 284.
14. R. A. Bohara, N. D. Thorat and S. H. Pawar, *RSC Adv.*, 2016, **6**, 43989.
15. W. H. Zhou, C. H. Lu, X. C. Guo, F. R. Chen, H. H. Yang and X. R. Wang, *J. Mater. Chem.*, 2010, **20**, 880.
16. C. J. Xu, K. M. Xu, H. W. Gu, R. K. Zheng, H. Liu, X. X. Zhang, Z. H. Guo and B. Xu, *J. Am. Chem. Soc.*, 2004, **126**, 9938.
17. T. Rajh, L. X. Chen, K. Lukas, T. Liu, M. C. Thurnauer and D. M. Tiede, *J. Phys. Chem. B*, 2002, **106**, 10543.
18. T. Tsuzuki and P. G. McCormick, *J. Mater. Sci.*, 2004, **39**, 5143.
19. C. C. Koch, *Nanostructured Mater.*, 1993, **2**, 109.
20. J. Ding, Y. Shi, L. F. Chen, C. R. Deng, S. H. Fuh and Y. Li, *J. Magn. Magn. Mater.*, 2002, **247**, 249.
21. J. Ding, T. Tsuzuki and P. G. McCormick, *J. Mater. Sci.*, 1999, **34**, 5293.
22. M. L. Verma, C. J. Barrow, J. F. Kennedy and M. Puri, *Int. J. Biol. Macromol.*, 2012, **50**, 432.
23. H. Y. Gu, A. M. Yu and H. Y. Chen, *J. Electroanal. Chem.*, 2001, **516**, 119.
24. N. S. Malvankar, T. Mester, M. T. Tuominen and D. R. Lovley, *ChemPhysChem*, 2012, **13**, 463.
25. L. L. Zhang and X. S. Zhao, *Chem. Soc. Rev.*, 2009, **38**, 2520.
26. M. Ojeda, A. M. Balu, V. Barron, A. Pineda, A. G. Coleto, A. A. Romero and R. Luque, *J. Mater. Chem A*, 2014, **2**, 387.
27. K. Jiang, S. Sun, L. Zhang, Y. Lu, A. G. Wu, C. Z. Cai and H. W. Lin, *Angew. Chem. Int. Ed.*, 2015, **54**, 5360-5363.
28. Y. Lou, L. Wang, Y. H. Zhang, Z. Y. Zhao, Z. G. Zhang, G. Z. Lu and Y. Guo, *Catalysis Today*, 2011, **175**, 610.
29. Q. Liu, L. C. Wang, M. Chen, Y. Cao, H. Y. He and K. N. Fan, *Journal of Catalysis*, 2009, **263**, 104.
30. L. J. Dai, M. Liu, Y. Song, J. J. Liu and F. Wang, *Nano Energy*, 2016, **27**, 185.
31. T. G. Spiro, J. D. Stong and P. Stein, *J. Am. Chem. Soc.*, 1979, **101**, 2648.
32. M. Feng and H. Tachikawa, *J. Am. Chem. Soc.*, 2008, **130**, 7443.

33. B. R. Wood, M. Asghari-Khiavi, E. Bailo, D. McNaughton and V. Deckert, *Nano Lett.*, 2012, **12**, 1555.
34. G. Kalaivani, A. Sivanesan, A. Kannan, N. S. V. Narayanan, A. Kaminska and R. Sevvel, *Langmuir*, 2012, **28**, 14357.
35. M. Mahato, P. Pal, B. Tah, M. Ghosh and G. B. Talapatra, *Colloids Surf., B*, 2011, **88**, 141-149.
36. I. Sur, D. Cam, M. Kahraman, A. Baysal and M. Culha, *Nanotechnology*, 2010, **21**.
37. N. Zheng, X. Zhou, W. Y. Yang, X. J. Li and Z. B. Yuan, *Talanta*, 2009, **79**, 780.
38. L. S. Xuan Xu, Qiquin Seng, Xiadong Cao and Cheng Yao, *Electroanalysis*, 2016, **28**, 1.
39. Z. Gonzalez, B. Ferrari, A. J. Sanchez-Herencia, A. Caballero and J. Morales, *Electrochimica Acta*, 2016, **211**, 110.
40. Y. X. Xu, Z. Y. Lin, X. Q. Huang, Y. Wang, Y. Huang and X. F. Duan, *Adv. Mater.*, 2013, **25**, 5779.
41. S. Roldan, Z. Gonzalez, C. Blanco, M. Granda, R. Menendez and R. Santamaria, *Electrochimica Acta*, 2011, **56**, 3401.
42. S. Roldan, C. Blanco, M. Granda, R. Menendez and R. Santamaria, *Angew. Chem. Int. Ed.*, 2011, **50**, 1699.
43. B. E. Conway, *Electrochemical Supercapacitors:Scientific Fundamentals and Technological Applications*, Kluwer/Plenum, New York, **1999**.
44. B. J. Li, H. Q. Cao, J. Shao, M. Z. Qu and J. H. Warner, *J. Mater. Chem.*, 2011, **21**, 5069.
45. Z. J. Fan, J. Yan, T. Wei, L. J. Zhi, G. Q. Ning, T. Y. Li and F. Wei, *Adv. Funct. Mater.*, 2011, **21**, 2366.
46. M. Khairy and S. A. El-Safty, *Journal of Energy Chemistry*, 2015, **24**, 31-38.
47. H. Jiang, P. S. Lee and C. Z. Li, *Energy Environ Sci*, 2013, **6**, 41.

Supporting Information

Mechanochemical design of hemoglobin-functionalised magnetic nanomaterials as energy storage devices

Daily Rodriguez-Padrón, Alain R. Puente-Santiago, Alina M. Balu, Antonio A. Romero, Rafael Luque*

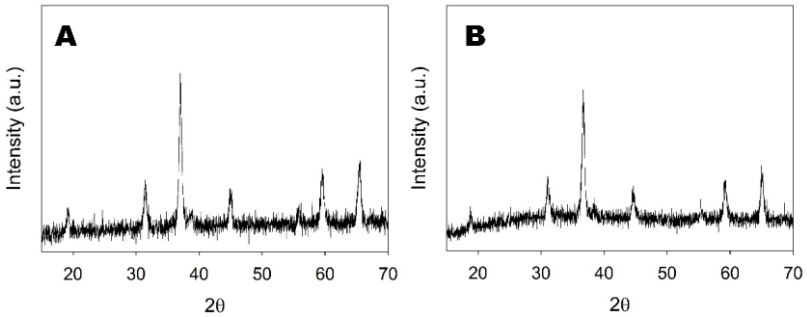

Figure S1. XRD patterns of A: Co_3O_4 MNPs and B: Hb-DA-Co_3O_4.

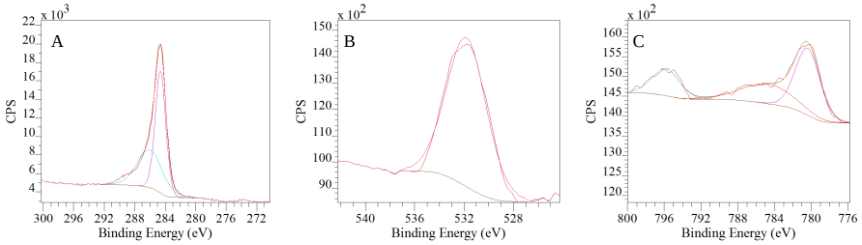

Figure S2. Deconvoluted high-resolution XPS spectra of Co_3O_4 for a) C 1s, b) O 1s and c) Co 2p.

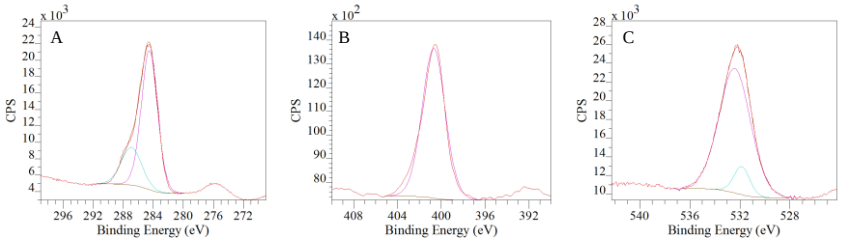

Figure S3. Deconvoluted high-resolution XPS spectra of DA-Co_3O_4 for a) C 1s, b) N 1s and c) O 1s.

The band at 400.5 eV in the XPS spectrum (Fig. S3. b) of DA-Co_3O_4, which can be attributed to the N from amino groups, together with the main peak in the UV-vis spectrum (Fig. S4.b) around 269 nm (Q. Wei, F. L. Zhang, J. Li, B. J. Li and C. S. Zhao, Polymer Chemistry, 2010, 1, 1430-1433) corroborate the successful funtionalization of the Co_3O_4 MNPs with dopamine.

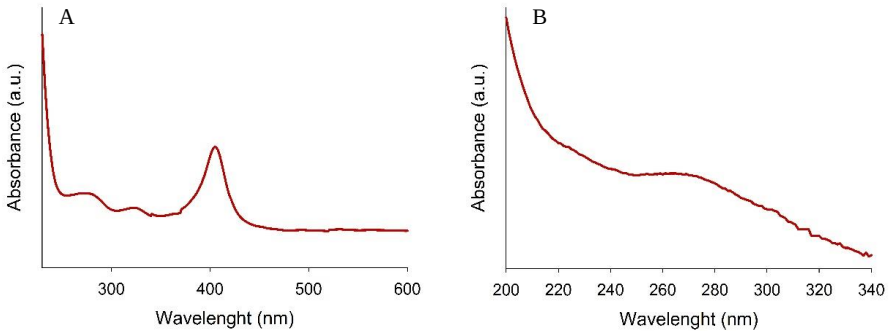

Figure S4. a UV-vis spectrum of Hb after mechanochemical milling process (200 rpm, 30 min), **b** UV-vis spectrum of DA-Co_3O_4.

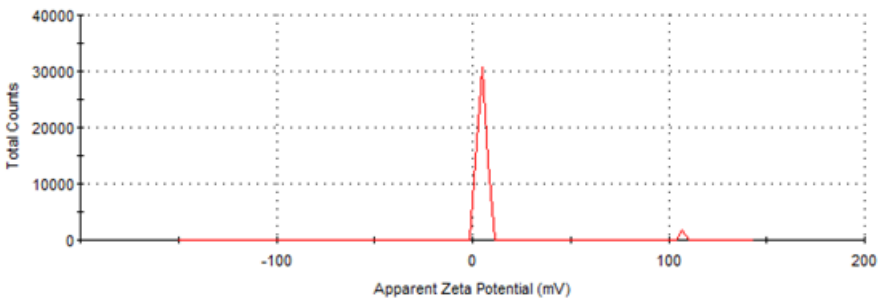

Figure S5. Zeta potential of DA-Co_3O_4 nanobioconjugates.

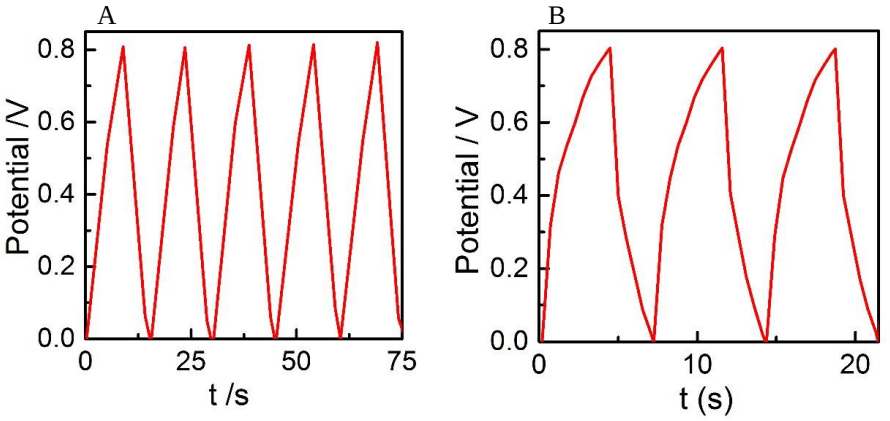

Figure S6. Galvanostatic charge and discharge profile of A: DA-Co_3O_4 and B: Hb-DA-Co_3O_4, at a current density of $30Ag^{-1}$ in 0.5 M KOH aqueous solution.

The galvanostatic measurements of DA-Co_3O_4 nanomaterial show a specific capacitance of just 0.5 Fg^{-1}. The galvanostatic charge and discharge curves of the DA-Co_3O_4, (**Fig. S6 A**) clearly possess the triangular shape of an ideal capacitor and differs from the corresponding to the Hb-DA-Co_3O_4, (**Fig. S6 B**) which display a significant hump in the charge branch, in accordance with the expected behaviour of redox molecules.

2.5. Highly efficient direct oxygen electro-reduction by partially unfolded laccases immobilized on waste-derived magnetically separable nanoparticles

Following the previously developed mechanochemical protocol, a novel bioconjugate based on laccase, iron oxide nanoparticles and dopamine as anchor was subsequently prepared. A full characterization of the material was performed, revealing that for proteins with less α-helice content, such as LAC, certain denaturalization was observed by using the mechanochemical strategy. Noteworthy, the shown structural changes could become a favorable factor for the eletrocatalytic response of the enzyme, as confirmed by using the synthesized bioconjugate in the electrocatalytic reduction of oxygen.

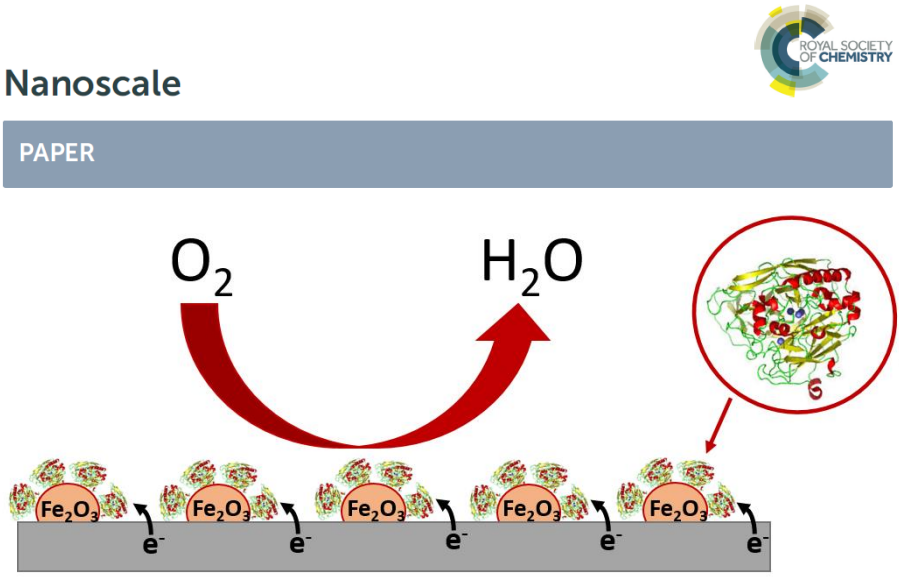

Daily Rodríguez-Padrón; Alain R. Puente Santiago; Alvaro Caballero; Alina M. Balu; Antonio A. Romero Reyes; Rafael Luque Álvarez de Sotomayor. **2018**. Highly efficient direct oxigen electro-reduction by partially unfolded laccases immobilized on waste-derived magnetically separable nanoparticles. **Nanoscale**. 10. 3961-3968. 10.1039/C8NR00512E. IF: 7.367.

Highly efficient direct oxygen electro-reduction by partially unfolded laccases immobilized on waste-derived magnetically separable nanoparticles

Daily Rodríguez-Padrón[a], Alain R. Puente-Santiago[a]*, Alvaro Caballero[b], Alina M. Balu[a], Antonio A. Romero, Rafael Luque[a]*

[a]*Departamento de Química Orgánica, Grupo FQM-383, Universidad de Córdoba, Campus de Rabanales, Edificio Marie Curie (C-3), Ctra Nnal IV-A, Km 396, E14014, Córdoba (Spain), e-mail: q62alsor@uco.es, apuentesantiago@gmail.com*

[b]*Departamento de Química Inorgánica e Ingeniería Química, Campus de Rabanales, Edificio Marie Curie (C-3), Ctra Nnal IV-A, Km 396, E14014, Córdoba*

A biocatalytic system based on laccase functionalized waste-derived iron oxide nanoparticles (LAC-DA-Fe_2O_3) was designed by a mechanochemical approach and employed in the electrocatalytic reduction of oxygen. Full characterization of the obtained bioconjugates revealed that the protein adopted a partially unfolded state. The mentioned configuration, together with the geometry coordination changes along the T1 center can be further related to a high bioelectrocatalytic response. A current density up to 2.9 mA/cm^2 has been achieved, which is among the highest values reported in literature for laccase functionalized nanomaterials.

Introduction

Electronic wiring of metalloenzymes for the design of electrocatalytic nanobiomaterials with applications in biosensing,[1, 2] bioreactors[3, 4] and bioenergy conversion,[5, 6] has been one of the most preeminent topics in the field of bioelectronics over the last decades. Particularly, the effective plugging of redox enzymes to electrodes becomes a crucial factor for the development of highly efficient enzymatic fuel cells. In this sense, the direct electron transfer (DET) and in turn the bioelectrocatalytic activity

of the metalloenzymes are directly tuned by the conformation and/or orientation states that they adopt upon immobilization over different nanomaterials.[7, 8] Numerous approaches have been developed to achieve an efficient electrochemical communication between an immobilized enzyme and the electrode. These include adsorption on nanostructured carbonaceous or gold electrodes,[9, 10] co-immobilization of enzymes with conductive polymers (*molecular cables*),[11, 12] conductive wiring by graphene or carbon nanotubes (CNTs), carbon or iron oxide nanoparticles,[13-15] covalent anchorage by crosslinkers, pyrene derivatives or self-assembled monolayers (SAMs),[16-18] encapsulation or entrapment of enzymes in polymers,[19, 20] addition of redox mediators to shuttle electrons between redox active site of enzymes and electrodes[21] and most recently the use of conductive protein bionanowires as redox mediators.[22]

Multicopper oxidases (MCO) have been widely investigated since they can catalyze the four-electron reduction of O_2 to H_2O at low overpotentials.[23] Among them, laccases have been widely used as biocathodes in enzymatic biofuel cells due to their interesting advantages including high catalytic rates, resistance to contamination and relatively low cost.[24-26] Laccases from fungus or plants comprise an anti-parallel β-sheet barrel with a hydrophobic core. They utilize an electron shuttling Type 1 Cu (T1) site in conjunction with a mononuclear Type 2 (T2) and a binuclear Type 3 (T3) site, arranged in a trinuclear copper cluster (TNC), to reduce O_2 to H_2O. Primary electron acceptor (T1) is located about 6.5 Å underneath the protein surface, while T2/T3 cluster is about 12 Å deeply buried in the three-dimensional structure (Scheme 1).[27]

Biological activities of enzymes are well known to be closely related to their three dimensional structures. A proper unfolding of proteins to a most exposure intermediate states can greatly promote their bioelectrocatalytic function despite conformational changes of metalloenzymes usually lead to a loss of the bioelectrocatalytic activity.[28, 29-32]

In this work, the direct wiring of a laccase from Aspergillus sp. was conducted on waste-derived magnetically separable iron oxide

nanoparticles using a mechanochemical approach[33] in order to profit from inherent advantages of magnetic nanoparticles as nanoscaffolds.[34-36] The synthesized nanobioconjugates exhibit excellent electron transfer rates and low-overpotential for the direct bioelectrocatalytic reduction of oxygen. To the best of our knowledge, the highly efficient electrocatalytic behavior of laccase is unprecedentedly linked to a partially unfolded conformation of the enzyme upon immobilization at the nanoparticles surface.

Scheme 1. Schematic illustration of Laccase.

Experimental part

Synthesis of Laccase functionalized magnetic nanoparticles: LAC-DA-Fe_2O_3

LAC-DA-Fe_2O_3 was synthesized by a mechanochemical milling processes employing Laccase from Aspergillus sp. (LAC), dopamine hydrochloride (DA-HCl), and Fe_2O_3 magnetic nanoparticles (MNPs). The employed protocol has been already reported by our group for the design of protein based bioconjugates.[33] Fe_2O_3 MNPs were previously synthetized using $Fe(NO_3)_3 \cdot 9H_2O$ as iron precursor and orange peel waste as carbon source in a ratio 1:2. The mentioned materials were milled in a ball mill (Retsch

PM100 ball mill model), at 350 rpm for 15 min, employing a 125 mL reaction chamber and eigthteen 10 mm stainless steel balls. Subsequently, the material was oven dried at 100 °C for 24 h, and finally heated up (1 ºC/min) to 300 °C under air and kept at that temperature for 30 min.

Material Characterization

LAC-DA-Fe_2O_3 bioconjugates were characterized by Fourier Transform-Infrared Spectroscopy (FT-IR), UV-vis and Fluorescence Spectroscopies, Electronic Paramagnetic Spectroscopy (EPR), X-ray Photoelectronic Spectroscopy (XPS), Transmission Electronic Microscopy (TEM), Thermogravimetric analysis (TGA-DTA) and Dynamic Light Scattering (DLS) and Zeta-Potential measurements, in order to obtain a full information of the protein configuration after the immobilization process.

X-ray diffraction analysis was performed for both, Fe_2O_3 MNPs and LAC-DA-Fe_2O_3 bioconjugates using the D8 Advanced Diffractometer (Bruker AXS) with the Lynxeye detector, at room temperature. X-ray diffraction patterns were obtained in a 2θ scan range from 10° to 70°, with a step size of 0.02°. Phase identifications were carried out using the Bruker Diffrac-plus EVA software, supported by the Powder Diffraction File (PDF) database of the International Centre for Diffraction Data (ICDD). The magnetic susceptibility of both LAC-DA-Fe_2O_3 and Fe_2O_3 MNPs materials was measured on the Bartington MS-2 instrument at room temperature and at low frequency (470 Hz).

FT-IR spectra were acquired on the ABB MB3000 infrared spectrophotometer, equipped with an ATR PIKE MIRacleTM sampler, a window of ZnSe, and 256 scans at a resolution of 16 cm^{-1}. Spectra were recorded at room temperature in a 4000-600 cm^{-1} wavenumber range, using the Horizon MBTM software. During the measurements, the sample was purged with a nitrogen flow (20 mL min^{-1}, dehydrated and deoxygenated). The amide I band was treated by a fitting procedure, having a linear baseline between 1700 and 1500 cm^{-1}. Component peaks were fitted with Gaussian band profiles. Peak positions were estimated from literature.[7, 37]

UV measurements at different potentials were carried out at room temperature in a three-electrode spectroelectrochemical cell using Princeton Applied Research 263A potentiostat coupled with a Shimadzu UV 1603 spectrophotometer. A three-electrode cell with a laccase/Ni electrode as working electrode, a platinum wire auxiliary electrode, and an Ag/AgCl (3M, KCl) as reference electrode were used. EPR experiments were accomplished on the Bruker ESP-380 spectrometer equipped with an Oxford Instrument ESR-900 continuous-flow helium cryostat.

XPS studies were performed employing an ultrahigh vacuum (UHV) multipurpose surface analysis system SpecsTM with the Phoibos 150-MCD energy detector. Prior to the analysis, the sample was evacuated overnight under vacuum ($<10^{-6}$ Torr). The experiment was accomplished at pressures $<10^{-10}$ mbar, using a conventional X-ray source (XR-50, Specs, Mg-Kα, hv=1253.6 eV, 1 eV = 1.603×10^{-19} J) in a "stop and go" mode. The deconvolution of the obtained curves and element quantification was carried out using the XPS CASA program.
TEM images were recorded on the FEI Tecnai G^2 system, equipped with a CCD ("charge coupling device") camera. Previously, the samples were dispersed in ethanol and deposited on a copper grid. Thermogravimetric analysis was accomplished on the Setaram Setsys 12 TGA thermobalance. Samples were heated at a rate of 10 °C min^{-1} under nitrogen atmosphere (50 mL min^{-1}) in a 30–800 °C temperature range.
Particle size distributions and zeta potential were analyzed using Zetasizer Nano ZSP (Malvern Instruments Ltd.,UK) instrument. Samples was dispersed in 10 mM of KNO_3 and the measurements were recorded in triplicate (n = 3) at 25 °C.

Electrochemical experiments
CV and chonoamperometric experiments were performed in a three-electrode electrochemical cell using a Potentiostat/Galvanostat Autolab (Solartron1286). Working electrodes were constructed by pressing LAC-DA-Fe_2O_3 nanobioconjugates on Ni foam surfaces with a geometrical area of 0.3 cm^2, Pt wire was used as counter electrodes and Ag/AgCl (3 M, KCl) as reference electrode.

Results and discussion

A full characterization of LAC-DA-Fe_2O_3 was accomplished in order to confirm the successful functionalization of the iron oxide magnetic nanoparticles (MNPs), as well as the conformation of the protein in the synthesized bioconjugates. XRD patterns of MNPs displayed a mixture of two main crystalline phases, namely maghemite and hematite (Figure S1B, ESI†), in accordance with the observed magnetic properties of the material (Table S1, ESI†). LAC-DA-Fe_2O_3 showed a similar structure and arrangement, with the presence of the above mentioned phases. However, a slightly loss of crystallinity could be appreciated after milling, which can be attributed to the presence of the protein in the bioconjugates structure (Figure S1A, ESI†).

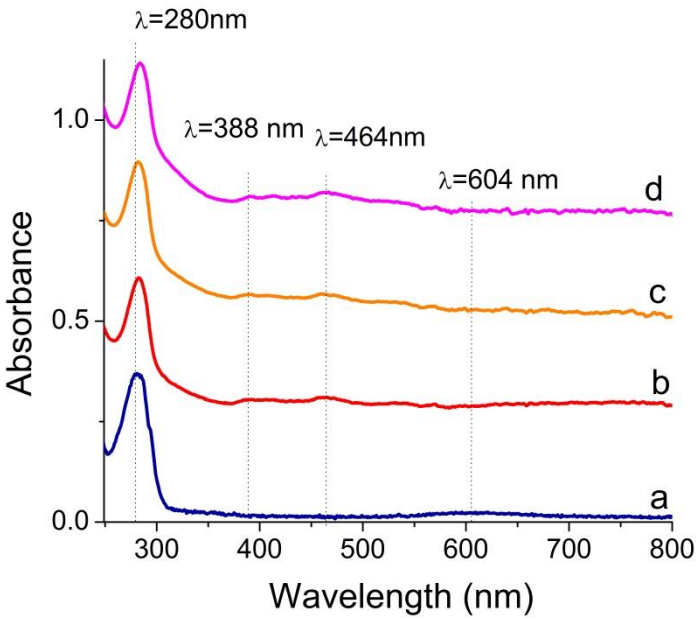

Figure 1. UV-vis spectra for a) free laccase (no oxygen atmosphere) and b) LAC-DA-Fe_2O_3 at open circuit, c) LAC-DA-Fe_2O_3 at 0.2V and d) LAC-DA-Fe_2O_3 at -0.4 V under oxygen purging. PBS 0.1M pH=6.

Remarkable spectral changes associated to the aerobic reduction of oxygen have been observed between the free laccase (in solution) with respect to the immobilized laccase on the magnetic nanoparticles

surfaces (Figure 1. a, b). The spectra show a significant decrease of the band at 600 nm assigned to the Cu (T1) redox center[38], with the concomitant appearance of extra bands at 364 and 464 nm. These spectral changes have been ascribed to the conformational state of partially reduced laccases upon the catalytic reduction of O_2 molecules, which involves structural changes around the coordination geometry of at least one of the copper centers, most likely on type I copper. [39-41] Interestingly, the spectra of the nanobioconjugates remain unaltered at large overpotentials (Figure 1. c, d) suggesting that the immobilized enzymes hold an irreversible configuration i.e. "*frozen*" state. The shifts in the 280 nm adsorption band of immobilized laccases can be attributed to significant conformational changes in the environment of the tryptophan and tyrosine aminoacids. Additionally, UV-Vis spectra of Fe_2O_3 and DA-Fe_2O_3 have been performed (Figure S2, ESI†). The absorption spectrum of Fe_2O_3, did not displayed any significant band in the 250-700 nm wavelength range. On the other hand, dopamine coated MNPs, shows a characteristic absorption peak at 260 nm, which is an accordance with the spectrum obtained for dopamine. Furthermore the band at 294 nm, in the commercial dopamine, displayed a slightly blue shift to 289 nm, which could be associated to changes after the immobilization process.

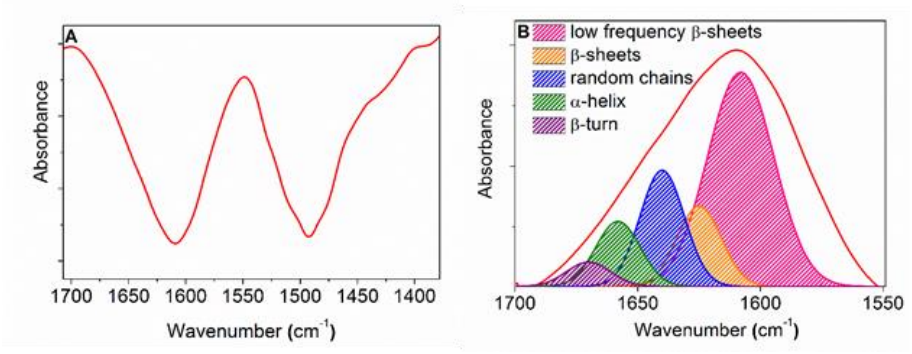

Figure 2. A FT-IR spectrum of LAC-DA-Fe_2O_3 and **B** Deconvoluted FT-IR spectrum of LAC-DA-Fe_2O_3 nanobioconjugates in the amide I region.

FT-IR analysis strongly support the successful functionalization of MNPs. This conclusion can be inferred from bands at 1609 cm^{-1} and 1493 cm^{-1},

related to amide I and amide II groups from laccase, respectively (Figure 2.A). The band at 1609 cm^{-1} can be associated to the C=O stretching vibration from carbonyl groups of the peptide bonds of the protein, while the band of amide II corresponds to the combination of C–N stretching and N-H bending. The conformation of laccase on the surface of MNPs was also investigated by the analysis of the deconvoluted FT-IR spectrum of the amide I region, which is very sensitive to secondary structures. Five types of secondary structures could be resolved upon deconvolution. Low-frequency β-sheets (1607 cm^{-1}, 52%), β-sheets (1624 cm^{-1}, 14%), random coils (1640 cm^{-1}, 19%), α-helices (1658 cm^{-1}, 10%), β-turns (1670 cm^{-1}, 4%), shown in Figure 2B. Compared to the commercial free laccase, laccase immobilized on MNPs were found to possess a larger low-frequency β-sheet content (Table 1). A larger contribution of these peaks suggests that such immobilized laccases underwent a partial unfolding induced by the mechanochemical functionalization step on MNPs, in good agreement with UV-vis spectra results.

The IR spectra of DA and DA-Fe_2O_3 were also obtained and they are reported in Figure S3, ESI†. Both materials displayed similar IR spectra, suggesting the successful attachment of the dopamine on the surface of the magnetic nanoparticles. A series of absorbance peaks, in the region between 1470 and 1620 cm^{-1}, was observed which can be ascribed to the stretching vibration of the polycyclic aromatic ring of dopamine. Particularly, the presence of phenolic C–O stretching vibration, was inferred from the absorption peak at 1287 cm^{-1}. Both spectra revealed the presence of two peaks at 2956 and 3036 cm^{-1}, associated to the stretching vibration of the C–H bond. Furthermore, the bands at 3344 and 3206 cm^{-1} can be attributed to N-H and O-H stretching vibration, respectively.[42]

Fluorescence spectra have emerged as an useful tool to investigate the conformational changes of the enzymes at different binding scenarios. Fluorescence emission of laccase is originated by its intrinsic fluorophores (e.g. tryptophan (Trp), tyrosine (Tyr) and phenylalanine (Phe) residues. Each monomeric laccase contains seven Trp and fifteen Tyr residues,[27] which are mainly located in the hydrophobic interior core of the protein tertiary structure. Interestingly, the wavelength at the maximum emission of the LAC-DA-Fe_2O_3 bioconjugates in water solution underneath a large shift in comparison with the free laccase in the same

conditions (See Figure S4, ESI†), which have been associated to a change in the nanoenvironment polarity of the Tryptophan residues as a consequence of the unfolding of the enzymes.[43, 44] Bearing in mind the partial unfolding of the immobilized laccase, is conceivable to think that the possible modifications in the typical features of the fluorophores environment such as polarity, the nearest groups or even the coordination state may strongly affect the fluorescence of the native form.

Table 1. Conformational analysis of LAC-DA-Fe_2O_3. Structural Percent values are given.

Secondary structure	**Native Laccase[28]**	**LAC-DA-Fe_2O_3(*)**
Low-frequency β-sheet	17 ± 4.0	52 ± 3.9
β-sheet	33 ± 3.0	14 ± 1.8
Random coils	13 ± 0.8	19 ± 0.9
α-helix	18 ± 2.0	10 ± 1.5
β-turn	19 ± 4.8	5 ± 0.5

*The conformational analysis of the immobilized laccase was obtained by the average of the amide I peak fitted components of 6 different samples.

XPS analysis indicated the presence of C, N and O on the surface of the obtained bioconjugates (Figure 3.A). In particular, the clear presence of nitrogen (N1s~400.1 eV) strongly confirmed the successful protein immobilization.[45] Such N 1s spectrum can be deconvoluted into two peaks at 399.9 and 401.5 eV, corresponding to N from the peptide bonds and pyrimidinic groups of the protein, respectively (Figure 3.C).[46] The peak at 284.6 eV, associated to C1s, displayed three different contributions suggesting the presence of C-C/C=C, C-N and C-O at 284.3, 285.7 and 288.1 eV, respectively, mainly from the polypeptide chain of the immobilized protein (Figure 3.B). In addition, the band at 531.8 eV in the XPS spectrum, related to the O1s, presented two contributions, attributed to the of C-O and Fe-O bonds in the bioconjugates (Figure 3.D). The elemental quantification of LAC-DA-Fe_2O_3 revealed a 74%, 7% and

19% for C, N, and, O, respectively. Component quantification of the three C, N, and, O regions in the XPS spectrum have been also reported in Table S2, ESI†.

XPS analysis of DA-Fe_2O_3 and Fe_2O_3 was additionally performed (Figure S5, S6, ESI†). XPS spectrum of DA-Fe_2O_3 revealed the presence of a peak at 401.1 eV, which can be associated to the nitrogen from the amino group of dopamine. Additionally, it was found the presence of carbon and oxygen in the sample, as can be inferred from the bands at 284.6 and 532.6 eV, respectively. These results, together with the UV-vis data, confirmed the successful functionalization of the magnetic nanoparticles with dopamine.

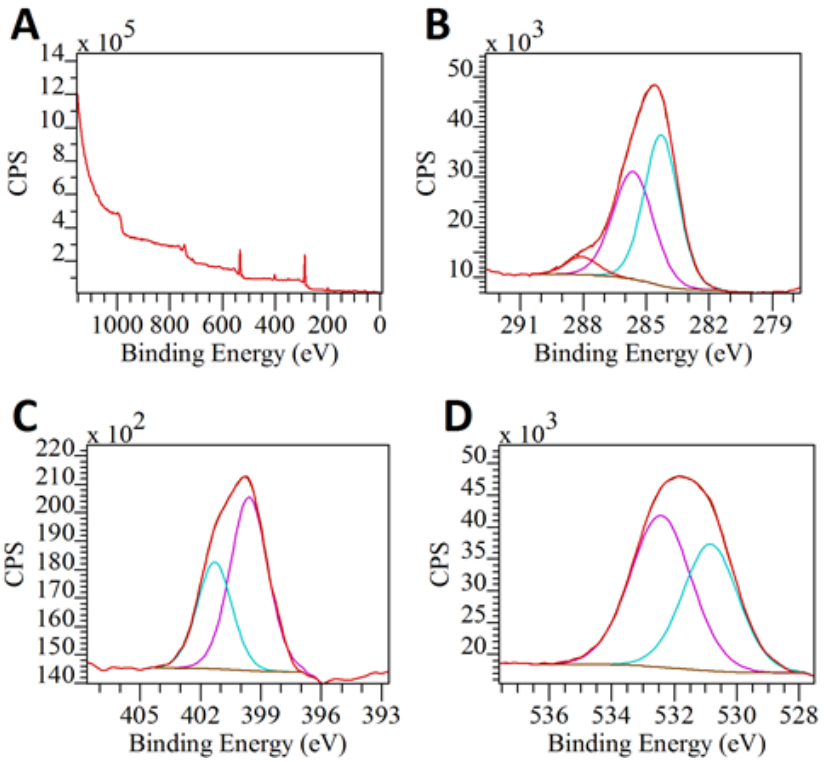

Figure 3. A. XPS survey of LAC-DA-Fe_2O_3. Deconvoluted high-resolution XPS spectra of LAC-DA-Fe_2O_3 for **B.** C 1s, **C.** N 1s and **D.** O 1s.

EPR measurements were accomplished for the magnetic characterization of LAC-DA-Fe_2O_3 bioconjugates (Figure S7, ESI†). EPR band at 165 mT

confirmed the presence of iron oxide magnetic nanoparticles in the investigated sample. Besides, laccase possess three types of Cu atoms, called T1, T2 and T3, being the latest EPR silent. EPR spectrum of this enzyme is characterized by a parallel and a perpendicular region.[47] In the EPR spectrum of LAC-DA-Fe_2O_3 bioconjugates, T1 and T2 signals in the perpendicular region are completely overlapped at 337 mT, while the parallel region cannot be clearly distinguish in the spectrum. These results also indicated that iron oxide MNPs were successfully functionalized with the laccase.

TEM micrographs displayed a narrow particle size distribution-average for both MNPs [(8.7±0.2) nm] and LAC-DA-Fe_2O_3 bioconjugates [(9.9±0.2) nm] (Figure S8, ESI†). The slight increase in particle size, together with clear visualization of agglomerated regions further confirmed the protein functionalization on MNPs. The observed agglomeration can be attributed to the Van der Waals interactions between laccase units.

The thermal stability of LAC-DA-Fe_2O_3 conjugates was subsequently investigated by Thermogravimetric analysis. Figure S9, ESI† illustrates that the bioconjugates exhibited a weight loss of 6.8 wt % from RT to 800ºC, due to the presence of organic compounds in the material. Degradation started at 100 ºC owing to the presence of unbounded/physisorbed water, followed by a progressive weight loss was observed from 240 ºC and 520 ºC ascribed to the non-oxidative decomposition of the enzyme present in LAC-DA-Fe_2O_3. Additionally, DTA measurements displayed two endothermic bands at 295 and 434 ºC associated to a degradation of the laccase in the material.[48] Thermogravimetric analysis was additionally performed for DA-Fe_2O_3 and Fe_2O_3 nanomaterials (Figure S9, ESI†). A significant weight loss from 220 ºC was observed for DA-Fe_2O_3, being associated to the presence of an endothermic-DTA signal. This weight loss can be correlated to the non-oxidative decomposition of dopamine present in the material. Interestingly, DTA experiments of Fe_2O_3 clearly did not exhibit any endothermic band in this range despite a similar TG mass loss profile.

Dynamic light scattering studies of LAC-DA-Fe_2O_3 bioconjugates pointed to an average hydrodynamic size of 130 nm (See Figure

4.A), in good agreement with a certain degree of agglomeration, most likely due to the Van der Waals interactions between protein moieties. The zeta potential for LAC-DA-Fe_2O_3 material was -22 mV (See Figure 4.B), within the range of the expected value for a stable bioconjugate colloidal solution,[49] again confirming the immobilization of laccase on the iron oxide MNPs surface. Dynamic light scattering and zeta potential studies were also performed for DA-Fe_2O_3 and Fe_2O_3, obtaining an average hydrodynamic size of 121 and 106 nm, respectively. The zeta potential of DA-Fe_2O_3 and Fe_2O_3 material was -4.9 and -9 mV, respectively (Figure S10, S11, ESI†).

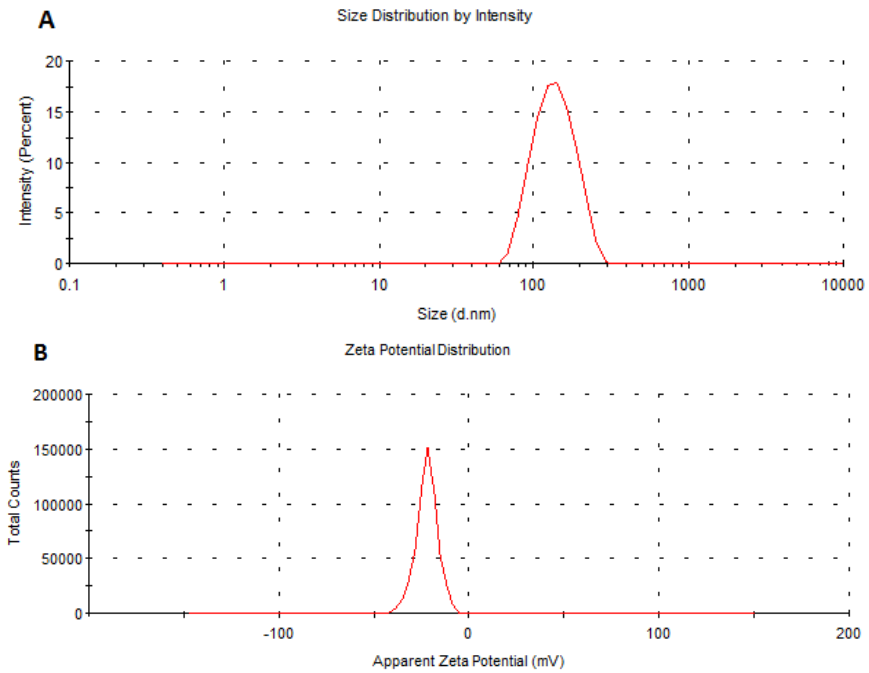

Figure 4. A. Dynamic light scattering data and B. zeta potential of LAC-DA-Fe_2O_3 nanobioconjugates.

Figure 5 display the typical voltammograms of Fe_2O_3 -NPs and DA-Fe_2O_3 NPs in the presence and absence of O_2 together with the LAC-DA-Fe_2O_3 in N_2 atmosphere. At pH=6 PBS, Fe_2O_3 NPs and DA- Fe_2O_3 NPs did not show any redox responses in the presence and in the absence of O_2

respectively. These findings are in good agreement with the electrochemistry of iron oxide nanoparticles based electrodes reported in others works.[50, 51]

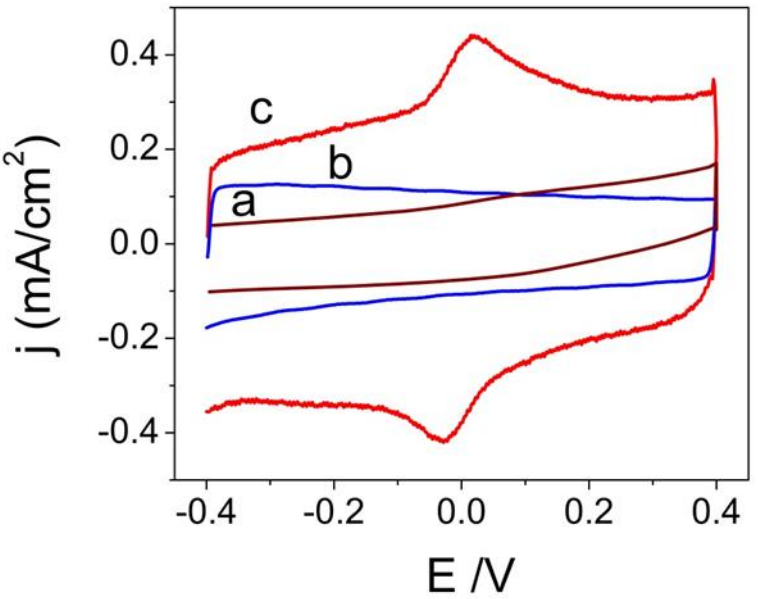

Figure 5. Representative cyclic voltammograms of a) Fe_2O_3 -NPs in the presence and absence of O_2, b) DA- Fe_2O_3 NPs in the presence and absence of O_2 and c) LAC-DA-Fe_2O_3 bioconjugates after purged with N_2 during 15 min. 0.1 M PBS pH=6 scan rate: 0.01 V/s.

Importantly, the voltammogram for the LAC- DA-Fe_2O_3 shows a pair of well-defined and stable redox peaks, which is attributed to the direct electron transfer (DET) between the T1 redox center of the immobilized laccase and the electrode surface. The anodic peak (E_a) and cathodic peak (E_b) are located at 0.44 and -0.41 (vs Ag/AgCl 3 M KCl) respectively. Additionally, the formal potential (Eº') of the bioconjugates was calculated from the average of the cathodic and anodic peak potentials and the value obtained was 0.015V (vs Ag/AgCl, 3M, KCl). This value is quite far compared with the values of 0.16V and 0.22 V (vs Ag/AgCl, 3M, KCl) obtained for the Eº' of the laccases in the literature at different pH conditions.[52-54] It is well-known that there are several factors that can

affect the redox potential of metalloproteins such as changes on the electrostatic potential in the proximities of the redox groups, different orientations and conformational or/and structural changes involving the redox center and its surroundings.[55, 56] Taking in account the spectroscopic results, the efficiency of the ET enzyme function was linked to both the partial unfolding of the laccases and the structural changes along the T1 redox center, which can greatly reduce the spatial hindrance between the buried copper sites and nanoparticles surfaces improving the electronic communication between the enzyme and the electrode surface.

The catalytic behavior of LAC-DA-Fe_2O_3 bioconjugates was subsequently investigated in the electroreduction of oxygen (Scheme 2). Figure 6 A represents cyclic voltammogramns of laccase and laccase functionalized MNPs deposited onto Ni foam electrodes in 0.1 M PBS pH=6 under constant oxygen flow. A poor electrocatalytic activity was observed for laccase immobilized over Ni foam electrodes. We believe that the lack of efficient ET orientation of laccase on Ni electrodes is responsible to the observed low bioelectrocatalytic responses. Comparably, literature reports disclosed higher current densities (up to 0.5 mA/cm^2) toward the electrocatalytic reduction of O_2 to H_2O when laccases are covalently bound to graphite electrodes[57].

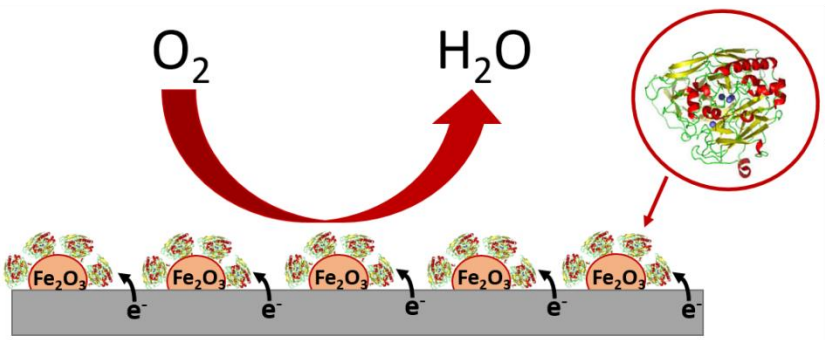

Scheme 2. Overview of the direct bioelectrocatalytic reduction of oxygen by LAC-DA-Fe_2O_3 nanobioconjugates.

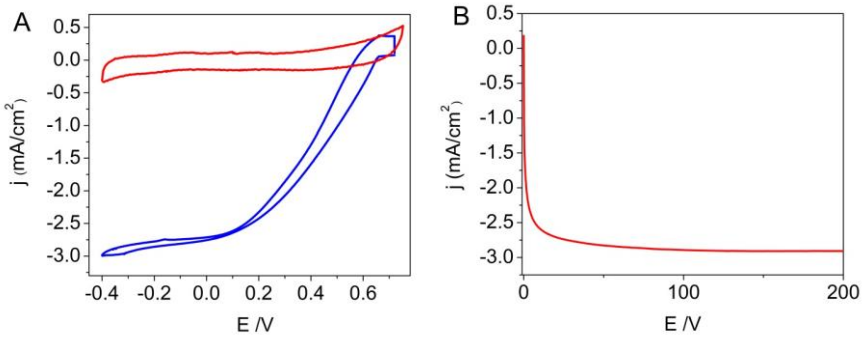

Figure 6. A. Cyclic voltammograms of laccase free (red line) and LAC-DA-Fe_2O_3 (blue line) under oxygen purging (0.1M PBS pH=6 scan rate: 0.01 V/s) **B.** Chronoamperometric response for LAC-DA-Fe_2O_3 nanobioconjugates performed at 0.35V (vs Ag/AgCl) in 0.1M PBS at pH=6 under oxygen purging.

Nevertheless, immobilized laccases on MNPs exhibited a classic sigmoidal waveshape with a remarkable electrocatalytic current. Cathodic currents in oxygenated solutions with an onset potential of +0.66 V (vs. Ag/AgCl) are close to the formal reduction potential of Cu (T1) redox center of fungal laccases +0.78 (vs NHE),[58] confirming the highly efficient DET between the laccases attached to MNPs and the electrodes without redox mediators. The mechanism of the electroreduction of O_2 by multicopperoxidase enzymes is similar to a ping-pong ET scheme in which four electrons are sequentially taken up from reducing substrates by the T1 center and shuttle 13 Å away to a trinuclear copper center, where the oxygen reduction takes place.[27] Small shifts in the redox potential of T1 center (≈ 60 mV) could be ascribed to structural changes involving redox centers and surroundings,[56] consistent with results obtained by UV measurements.

Along with cyclic voltammetry, chronoamperometric experiments were performed at 0.35 V for laccase-functionalized MNPs bioelectrodes (Figure 6B). The bioelectrodes exhibited stable electrocatalytic currents with a maximun electrocatalytic current of 2.9 mA/cm^2, similar to values reported for supramolecular assemblies with highly conductive nanomaterials such as carbon nanotubes and gold nanoparticles.[13, 59] Bearing in mind the spectroscopic results, we propose that the partial

unfolding of the laccases and the geometry coordination changes along the T1 center can greatly reduce the spatial hindrance between the buried copper sites and nanoparticles surfaces favoring the adoption of an effective ET configuration in the laccase which is responsible for the observed improvement of the bioelectrocatalytic currents.

Conclusions

A mechanochemically designed laccase/waste-derived magnetic iron oxide nanoparticle was successfully synthesized. This bioconjugate could effectively achieve a highly efficient direct electroreduction of oxygen, displaying displayed a maximum electrocatalytic current of 2.9 mA/cm^2, one of the highest values reported in literature for the above mentioned reaction catalyzed by multicopperoxidases. The observed high efficiency of LAC-DA-Fe_2O_3 was associated to conformational and structural changes in the immobilized laccase, as supported by UV-vis, FT-IR and Fluorescence spectroscopic measurements. This work represents a breakthrough in the bioelectrocatalytic scientific community, illustrating the importance of flexibility and dynamics in the structure of enzymes for their function and paves the way for additional opportunities in the design of novel biodevices with high-performance DET.

Acknowledgments

Rafael Luque gratefully acknowledges support from MINECO (project CTQ2016-78289-P) cofinanced with FEDER funds. Special thanks go to Filipe Folgosa, Smilja Todorovic, Celia M. Silveira for help with EPR and UV-vis experiments.

References:

1. Y. Xiao, F. Patolsky, E. Katz, J. F. Hainfeld and I. Willner, *Science*, 2003, **299**, 1877-1881.
2. F. Patolsky, Y. Weizmann and I. Willner, *Angew. Chem. Int. Edit.*, 2004, **43**, 2113-2117.
3. I. Mazurenko, M. Etienne, G. W. Kohring, F. Lapicque and A. Walcarius, *Electrochim. Acta*, 2016, **199**, 342-348.

4. O. Yehezkeli, R. Tel-Vered, S. Reichlin and I. Willner, *ACS Nano*, 2011, **5**, 2385-2391.
5. J. A. Cracknell, K. A. Vincent and F. A. Armstrong, *Chem. Rev.*, 2008, **108**, 2439-2461.
6. S. C. Barton, J. Gallaway and P. Atanassov, *Chem. Rev.*, 2004, **104**, 4867-4886.
7. P. Roach, D. Farrar and C. C. Perry, *J. Am. Chem. Soc.*, 2005, **127**, 8168-8173.
8. J. Masa and W. Schuhmann, *Nano Energy*, 2016, **29**, 466-475.
9. S. Rubenwolf, O. Strohmeier, A. Kloke, S. Kerzenmacher, R. Zengerle and F. von Stetten, *Biosens. Bioelectron.*, 2010, **26**, 841-845.
10. H. J. Qiu, C. X. Xu, X. R. Huang, Y. Ding, Y. B. Qu and P. J. Gao, *J. Phys. Chem. C*, 2008, **112**, 14781-14785.
11. M. T. Meredith and S. D. Minteer, *Annu. Rev. Anal. Chem., Vol 5*, 2012, **5**, 157-179.
12. P. Mishra, G. Lakshmi, S. Mishra, D. K. Avasthi, H. C. Swart, A. P. F. Turner, Y. K. Mishra and A. Tiwari, *Nano Energy*, 2017, **39**, 601-607.
13. N. Lalaoui, P. Rousselot-Pailley, V. Robert, Y. Mekmouche, R. Villalonga, M. Holzinger, S. Cosnier, T. Tron and A. Le Goff, *ACS Catal.*, 2016, **6**, 1894-1900.
14. N. Lalaoui, A. Le Goff, M. Holzinger, M. Mermoux and S. Cosnier, *Chem. Eur. J.*, 2015, **21**, 3198-3201.
15. A. Kaushika, R. Khan, P. R. Solanki, P. Pandey, J. Alam, S. Ahmad and B. D. Malhotra, *Biosens. Bioelectron.*, 2008, **24**, 676-683.
16. J. Martinez-Ortiz, R. Flores and R. Vazquez-Duhalt, *Biosens. Bioelectron.*, 2011, **26**, 2626-2631.
17. F. Giroud and S. D. Minteer, *Electrochem commun.*, 2013, **34**, 157-160.
18. R. K. Shervedani and A. Amini, *Bioelectrochemistry*, 2012, **84**, 25-31.
19. C. M. Moore, N. L. Akers, A. D. Hill, Z. C. Johnson and S. D. Minteer, *Biomacromolecules*, 2004, **5**, 1241-1247.
20. S. A. Merchant, T. O. Tran, M. T. Meredith, T. C. Cline, D. T. Glatzhofer and D. W. Schmidtke, *Langmuir*, 2009, **25**, 7736-7742.

21. P. Kavanagh and D. Leech, *Phys. Chem. Chem. Phys.*, 2013, **15**, 4859-4869.
22. L. Altamura, C. Horvath, S. Rengaraj, A. Rongier, K. Elouarzaki, C. Gondran, A. L. B. Macon, C. Vendrely, V. Bouchiat, M. Fontecave, D. Mariolle, P. Rannou, A. Le Goff, N. Duraffourg, M. Holzinger and V. Forge, *Nat. Chem.*, 2017, **9**, 157-163.
23. A. Zebda, C. Gondran, A. Le Goff, M. Holzinger, P. Cinquin and S. Cosnier, *Nat. Commun.*, 2011, **2**, 1-6.
24. L. Brunel, J. Denele, K. Servat, K. B. Kokoh, C. Jolivalt, C. Innocent, M. Cretin, M. Rolland and S. Tingry, *Electrochem commun.*, 2007, **9**, 331-336.
25. Y. Chen, P. P. Gai, J. R. Zhang and J. J. Zhu, *J. Mater. Chem. A*, 2015, **3**, 11511-11516.
26. D. Selloum, A. Abou Chaaya, M. Bechelany, V. Rouessac, P. Miele and S. Tingry, *J. Mater. Chem. A*, 2014, **2**, 2794-2800.
27. K. Piontek, M. Antorini and T. Choinowski, *J. Biol. Chem.*, 2002, **277**, 37663-37669.
28. F. Wu, L. Su, P. Yu and L. Q. Mao, *J. Am. Chem. Soc.*, 2017, **139**, 1565-1574.
29. O. A. Sytina, D. J. Heyes, C. N. Hunter, M. T. Alexandre, I. H. M. van Stokkum, R. van Grondelle and M. L. Groot, *Nature*, 2008, **456**, 1001-U1089.
30. E. Z. Eisenmesser, D. A. Bosco, M. Akke and D. Kern, *Science*, 2002, **295**, 1520-1523.
31. O. Flomenbom, K. Velonia, D. Loos, S. Masuo, M. Cotlet, Y. Engelborghs, J. Hofkens, A. E. Rowan, R. J. M. Nolte, M. Van der Auweraer, F. C. de Schryver and J. Klafter, *Proc. Nat. Acad. Sci. U. S. A*, 2005, **102**, 2368-2372.
32. H. Wu, S. H. Fan, W. Y. Zhu, Z. Dai and X. Y. Zou, *Biosens. Bioelectron.*, 2013, **41**, 589-594.
33. D. Rodriguez-Padron, A. R. Puente-Santiago, A. M. Balu, A. A. Romero and R. Luque, *Chem. Comm.*, 2017, **53**, 7635-7637.
34. L. M. Rossi, A. D. Quach and Z. Rosenzweig, *Anal. Bioanal. Chem.*, 2004, **380**, 606-613.
35. D. F. Cao, P. L. He and N. F. Hu, *Analyst*, 2003, **128**, 1268-1274.

36. V. Polshettiwar, R. Luque, A. Fihri, H. Zhu, M. Bouhrara and J.-M. Bassett, *Chem. Rev.*, 2011, **111**, 3036-3075.
37. F. N. Fu, D. B. Deoliveira, W. R. Trumble, H. K. Sarkar and B. R. Singh, *Appl. Spectrosc.*, 1994, **48**, 1432-1441.
38. L. L. Kiiskinen, L. Viikari and K. Kruus, *Appl. Microbiol. Biotechnol.*, 2002, **59**, 198-204.
39. M. Goldberg, O. Farver and I. Pecht, *J. Biol. Chem.*, 1980, **255**, 7353-7361.
40. H. W. Huang, G. Zoppellaro and T. Sakurai, *J. Biol. Chem.*, 1999, **274**, 32718-32724.
41. O. Farver, M. Goldberg and I. Pecht, *Eur. J. Biochem.*, 1980, **104**, 71-77.
42. M. Y. Liu, J. Z. Ji, X. Y. Zhang, X. Q. Zhang, B. Yang, F. J. Deng, Z. Li, K. Wang, Y. Yang and Y. Wei, *J. Mater. Chem. B*, 2015, **3**, 3476-3482.
43. X. C. Li, P. Yu, L. F. Yang, F. Y. Wang and L. Q. Mao, *Anal. Chem.*, 2012, **84**, 9416-9421.
44. P. Durao, I. Bento, A. T. Fernandes, E. P. Melo, P. F. Lindley and L. O. Martins, *J. Biol. Inorg. Chem.*, 2006, **11**, 514-526.
45. D. Rodriguez-Padron, A. R. Puente-Santiago, A. Caballero, A. Benitez, A. M. Balu, A. A. Romero and R. Luque, *J. Mat. Chem. A*, 2017, **5**, 16404-16411.
46. K. Jiang, S. Sun, L. Zhang, Y. Lu, A. G. Wu, C. Z. Cai and H. W. Lin, *Angew. Chem. Int. Edit.*, 2015, **54**, 5360-5363.
47. R. Pogni, M. C. Baratto, A. Sinicropi and R. Basosi, *Cell. Mol. Life Sci.*, 2015, **72**, 885-896.
48. D. Songurtekin, E. E. Yalcinkaya, D. Ag, M. Seleci, D. O. Demirkol and S. Timur, *Appl. Clay Sci.*, 2013, **86**, 64-69.
49. A. Salis, M. Bostrom, L. Medda, F. Cugia, B. Barse, D. F. Parsons, B. W. Ninham and M. Monduzzi, *Langmuir*, 2011, **27**, 11597-11604.
50. H. L. Zhang, X. Z. Zou, G. S. Lai, D. Y. Han and F. Wang, *Electroanalysis*, 2007, **19**, 1869-1874.
51. G. Zhao, J. J. Xu and H. Y. Chen, *Electrochem commun.*, 2006, **8**, 148-154.
52. D. W. Li, L. Luo, Z. Y. Pang, L. Ding, Q. Q. Wang, H. Z. Ke, F. L. Huang and Q. F. Wei, *ACS Appl. Mater. Interfaces*, 2014, **6**, 5144-5151.

53. D. Brondani, B. de Souza, B. S. Souza, A. Neves and I. C. Vieira, *Biosens. Bioelectron.*, 2013, **42**, 242-247.
54. M. Frasconi, H. Boer, A. Koivula and F. Mazzei, *Electrochim. Acta*, 2010, **56**, 817-827.
55. J. Zhou, J. Zheng and S. Y. Jiang, *J. Phys. Chem. B*, 2004, **108**, 17418-17424.
56. L. L. Xue, Y. H. Wang, Y. Xie, P. Yao, W. H. Wang, W. Qian, Z. X. Huang, J. Wu and Z. X. Xia, *Biochemistry*, 1999, **38**, 11961-11972.
57. C. Vaz-Dominguez, S. Campuzano, O. Rudiger, M. Pita, M. Gorbacheva, S. Shleev, V. M. Fernandez and A. L. De Lacey, *Biosens. Bioelectron.*, 2008, **24**, 531-537.
58. A. Christenson, N. Dimcheva, E. E. Ferapontova, L. Gorton, T. Ruzgas, L. Stoica, S. Shleev, A. L. Yaropolov, D. Haltrich, R. N. F. Thorneley and S. D. Aust, *Electroanalysis*, 2004, **16**, 1074-1092.
59. N. Lalaoui, R. David, H. Jamet, M. Holzinger, A. Le Goff and S. Cosnier, *ACS Catal.*, 2016, **6**, 4259-4264.

Supporting Information

Highly efficient direct oxygen electro-reduction by partially unfolded laccases immobilized on waste-derived magnetically separable nanoparticles

Daily Rodríguez-Padrón[a], Alain R. Puente-Santiago[a]*, Alvaro Caballero[b], Alina M. Balu[a], Antonio A. Romero, Rafael Luque[a]*

Abstract

A biocatalytic system based on laccase functionalized iron oxide nanoparticles (LAC-DA-Fe_2O_3) was designed by a mechanochemical approach and applied to the electrocatalytic reduction of oxygen. The full characterization of the obtained bioconjugates was performed; in particular, the spectroscopy characterization by UV-vis and FT-IR revealed that the protein adopted a partially unfolded state. The mentioned configuration, together with the geometry coordination changes along the T1 center can be further related to a high bioelectrocatalytic response. A current density up to 2.9 mA/cm^2 has been achieved, which is among the highest values reported in the literature for laccase functionalized nanomaterials.

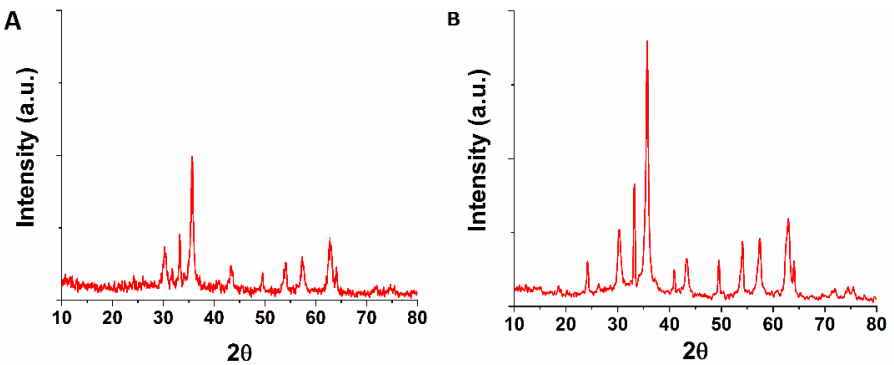

Figure S1. X-ray diffraction patterns of A: LAC-DA-Fe_2O_3 and B: Fe_2O_3.

Table S1. Magnetic susceptibility of the Fe_2O_3 and LAC-DA-Fe_2O_3.

Material	Magnetic susceptibility (10^{-6} m^3Kg^{-1})
Fe_2O_3	250
LAC-DA-Fe_2O_3	236

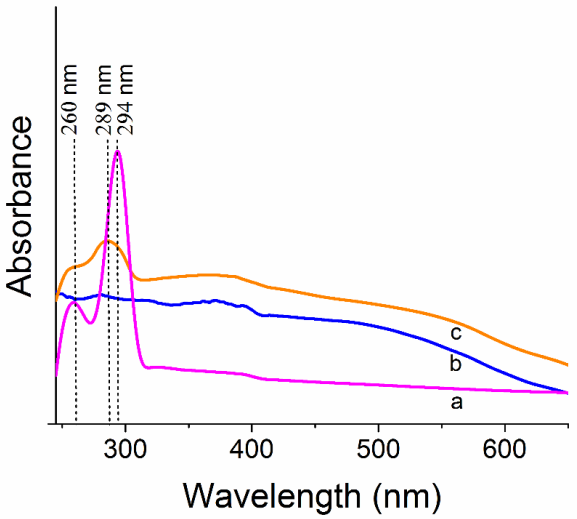

Figure S2. UV-vis spectra for DA-Fe_2O_3 (orange line), Fe_2O_3 (blue line) and DA (pink line).

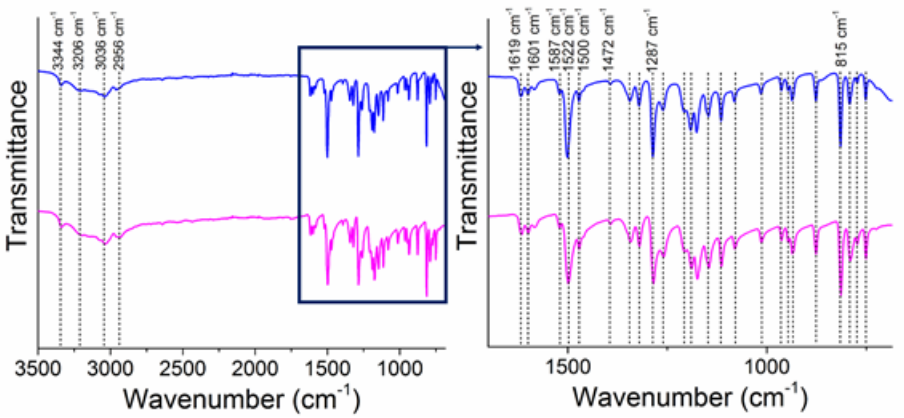

Figure S3. FT-IR spectra for DA-Fe_2O_3 (pink line) and commercial DA (blue line).

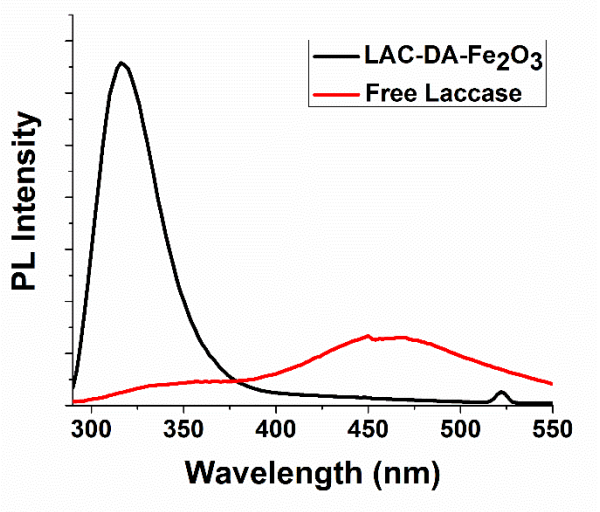

Figure S4. Fluorescence emission spectra of LAC-DA-Fe_2O_3 nanobioconjugates (black line) and free laccase from Aspergillus sp. (red line). Excitation wavelength = 260 nm.

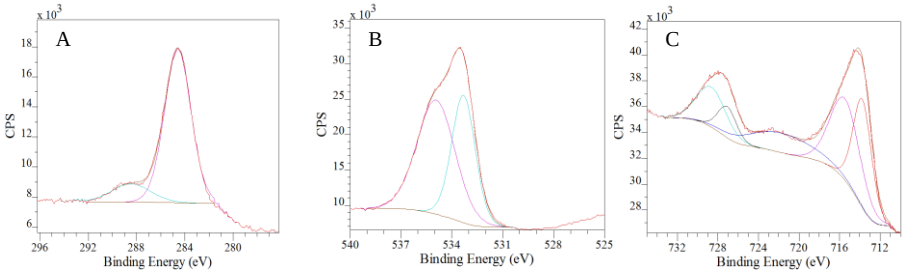

Figure S5. Deconvoluted high-resolution XPS spectra of Fe_2O_3 for a) C 1s, b) O 1s and c) Fe 2p.

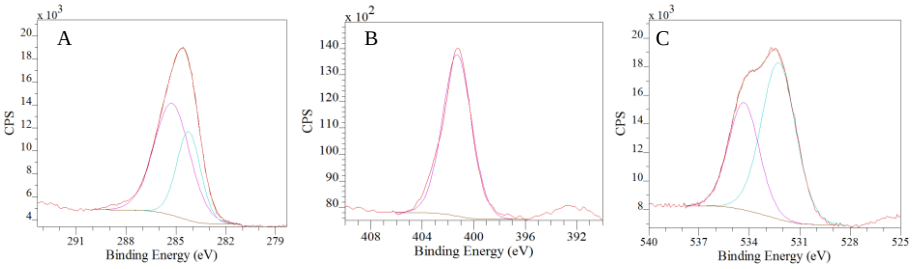

Figure S6. Deconvoluted high-resolution XPS spectra of DA-Fe_2O_3 for a) C 1s, b) N 1s and c) O 1s

Table S2. Components quantification in the C1s, N1s and O1s XPS regions.

Material	C-C (%)	C-N (%)	C-O (%)
LAC-DA-Fe_2O_3	50.3	44.2	5.5
	$N_{PEPTIDE\ BONDS}$ (%)	**$N_{PIRIMIDINIC\ GROUPS}$ (%)**	
	50.3	44.2	
	O-C (%)	**O-Fe (%)**	
	57.5	42.5	

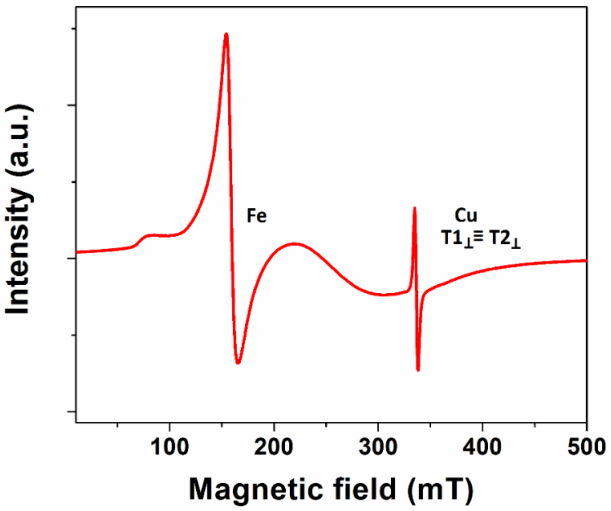

Figure S7. EPR spectra of LAC-DA-Fe_2O_3 nanobioconjugates.

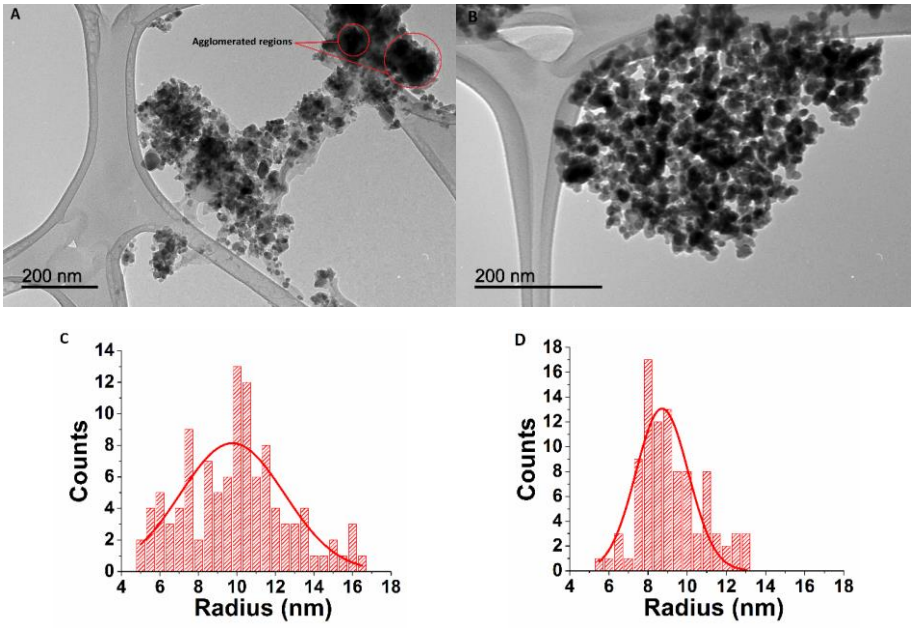

Figure S8. TEM image of the A: LAC-DA-Fe_2O_3 and B: Fe_2O_3 nanoparticles. Size distribution based on TEM of C: LAC-DA-Fe_2O_3 (100 particles) and D: Fe_2O_3 (100 particles).

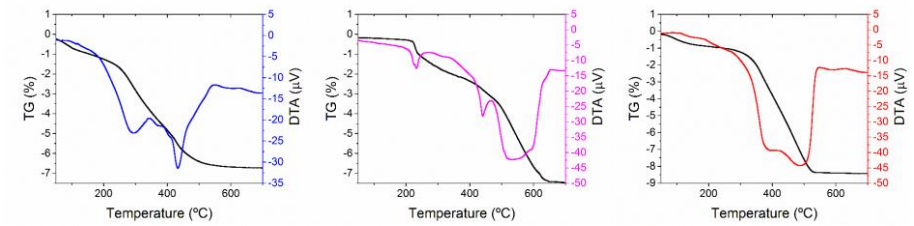

Figure S9. TG-DTA of LAC-DA-Fe_2O_3 (blue line), DA-Fe_2O_3 (pink line), Fe_2O_3 (red line) nanomaterials.

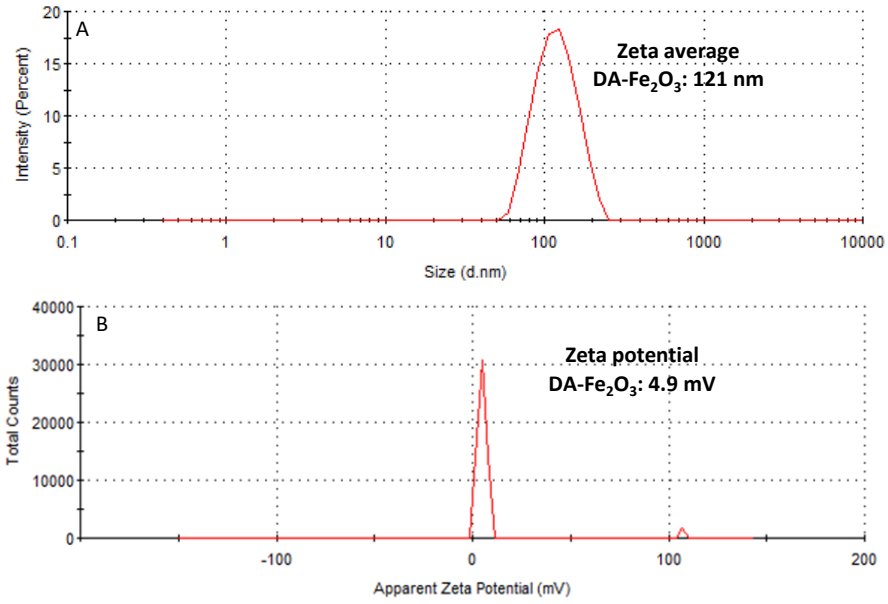

Figure S10. A. Dynamic light scattering data and **B.** zeta potential of DA-Fe_2O_3.

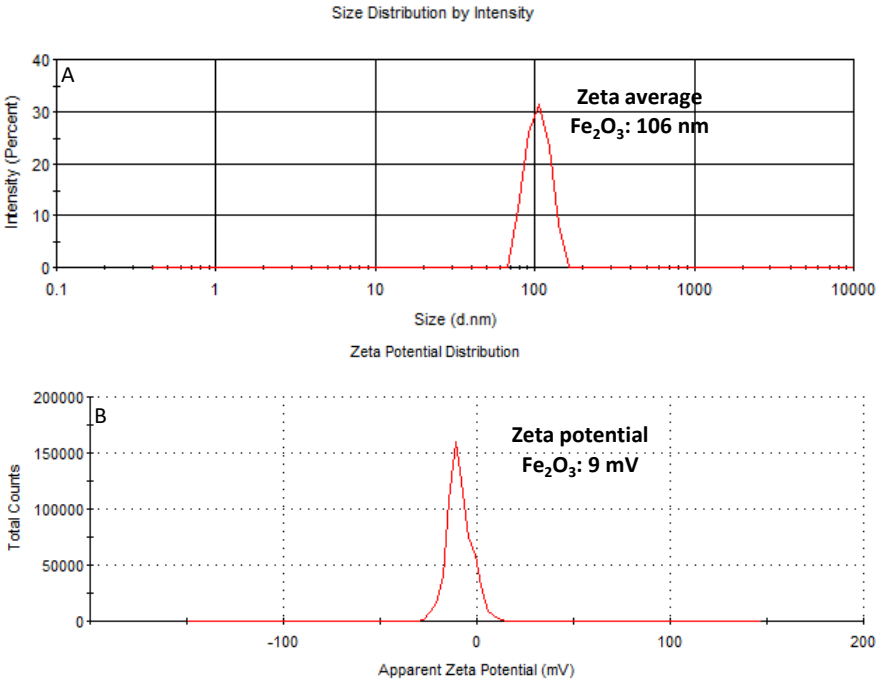

Figure S11. A. Dynamic light scattering data and **B.** zeta potential of Fe_2O_3.

Capítulo 3

3. Mechanochemically synthesized materials as catalyst for the preparation of fluorescent carbon-based nanoparticles

3.1. Hypothesis

Quantum dots (QDs) are multicolor emissive materials, being broadly employed in recent years. However, such type of nanoparticles possesses some inherent disadvantages mostly associated with their high toxicity. In this regard, fluorescent carbon based nanoparticles, such as carbon quantum dots (CQDs), have attracted the attention of the scientific community in recent years, as an attractive alternative to QDs. CQDs have been well-recognized by their low/non-toxic features and biocompatible properties, being excellent candidates for their use for *in-vivo* applications including cell imaging, drug delivery, visible light bactericidal activity and chemical-sensors, among others. Additionally, CQDs could be also used as photocatalytic materials for pollutants degradation, in solar devices and for photo/electrochemical water splitting. Besides the advantages from an environmental point of view, a remarkable aspect for the development of CQDs is the cost-effectiveness of the preparation protocol. In this sense, catalysis, as a key factor for sustainable chemistry, could reduce reaction times and enable the use of mild temperature conditions. Considering as well, the sustainability of the catalyst preparation procedure, mechanochemical protocols could be used, taken advantage of their feasibilities.

3.2. Objectives

Iron containing materials will be synthesized employing a mechanochemical strategy. In a first case, a nanobioconjugate based on iron oxide magnetic nanoparticles and hemoglobin will be prepared following the above described protocol. On the other hand, another iron

containing material will be synthesized by using a milling procedure, in this case, iron oxide nanoparticles supported on a porous silicate (SBA-15). The prepared materials will be employed for the synthesis of fluorescent carbon-based nanoparticles, following a top-down and a bottom-up strategies. for the iron oxide supported materials and for the iron containing bioconjugate, respectively. A full characterization of the fluorescent materials will be performed by studying their optical, electronic and morphological properties.

3.3. Synthesis of carbon-based fluorescent polymers driven by catalytically active magnetic bioconjugates

Within this doctoral thesis, it was also explored the use of nanobioconjugates, prepared by mechanochemical protocols, for the synthesis of fluorescent carbon-based materials, using a bottom-up methodology. In this case, a nanobioconjugate based on Hb and iron oxide magnetic nanoparticles was prepared using a mechanochemical procedure as previously described. The obtained material was fully characterized and employed in the oxidative polymerization of phenylenediamines. Remarkably, the use of this catalytic system allows the use of room temperature conditions. The obtained carbon based samples displayed an interesting morphology and fluorescent behaviour.

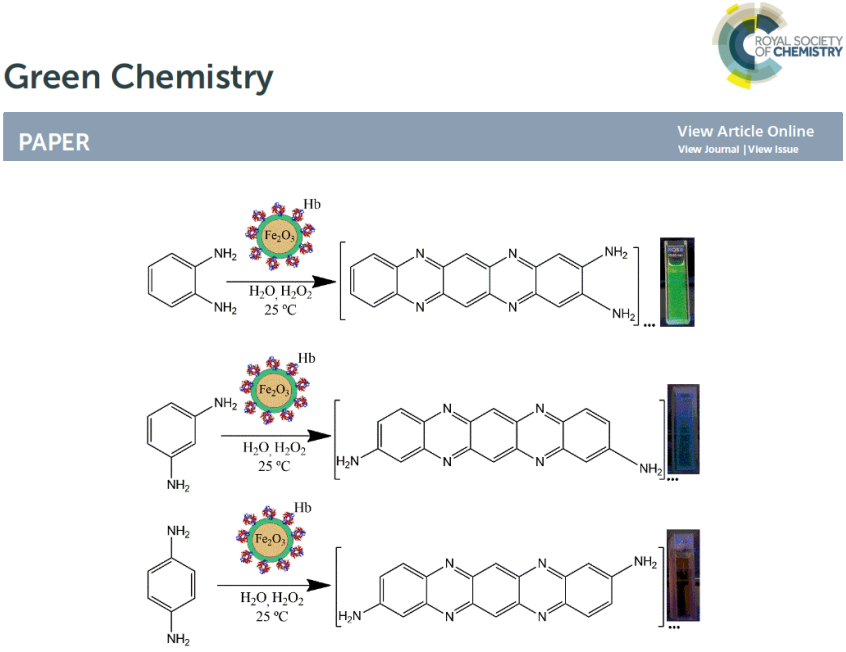

Daily Rodríguez-Padrón; Alexander Jodlowski; Gustavo De Miguel; Alain Puente Santiago; Alina M. Balu; Rafael Luque. **2018**. Synthesis of carbon-based fluorescent polymers driven by catalytically active magnetic bioconjugates. **Green Chemistry**. 20. 225-229. 10.1039/C7GC03295A. IF: 9.125.

Synthesis of carbon-based fluorescent polymers driven by catalytically active magnetic bioconjugates

Daily Rodríguez-Padrón,[a] Alexander D. Jodlowski ,[b] Gustavo de Miguel,[b] Alain R. Puente-Santiago,[a]* Alina M. Balu,[a] Rafael Luque [a]*

[a.]*Departamento de Química Orgánica, Grupo FQM-383, Institute of Fine Nanochemistry, Universidad de Cordoba, Campus de Rabanales, Edificio Marie Curie (C-3), Ctra Nnal IV-A, Km 396, E14014, Cordoba (Spain), e mail: q62alsor@uco.es, apuentesantiago@gmail.com*

[b.]*Departamento de Química Física, Institute of Fine Nanochemistry, Universidad de Cordoba, Campus de Rabanales, Edificio Marie Curie (C-3), Ctra Nnal IV-A, Km 396, E14014, Cordoba*

Bioconjugates based on a redox protein and iron oxide magnetic nanoparticles were employed in the catalytic polymerization of *ortho*, *meta* and *para* substituted phenylenediamines at room temperature for the synthesis of carbon-based fluorescent polymers. UV-Vis absorption measurements of the three obtained products displayed a red shift compared to starting materials. These results together with the FT-IR and XPS analysis confirm the successful formation of the polymers. In particular, the component quantification in the C1s XPS spectra revealed the high proportion of C-N bonds, associated to the oxidative polymerization of the precursors. MALDI-TOF MS analysis was performed in order to determine the molecular weights of the products. The synthesized poly-oPDA, poly-mPDA and poly-pPDA resulted to have a highly green, blue and red fluorescence, respectively. The reusability of the biocatalyst and the effect of the pH were investigated in the reaction for the *ortho* isomer. The biocatalytic system displayed optimum results when the pH was below the enzyme isoelectric point (pI).

Introduction

The development of nanotechnology-inspired biocatalytic systems have gained a lot of interest in the last years due to their importance for the design of biosensors,[1,2] bioelectronic devices[3,4] or biofuel cells.[5, 6] Particularly, the use of magnetic nanoparticles (MNPs) as versatile nanoscalfolds to immobilized enzymes has been widely used to design novel bioreactors which show high catalytic yields in different types of processes.[7-9] Advantageously, they allow the use of an external magnetic field to retrieve the catalysts and subsequently reuse them in multiple reactions.[10,11]

Among the enzyme-catalyze reactions reported in the literature, oxidative polymerization of aromatic diamines has been scarcely studied. A pioneering work reported a horseradish peroxidase (HRP) catalyzing, in the presence of hydrogen peroxide, the oxidation of aromatic diamines by an oxidative free-radical coupling mechanism.[12,13] Successful attempts using others heme-containing proteins have also been achieved. Tsutomu and coworkers developed a nanostructural environment catalytically activated system based on cytochrome C solubilized in reverse micelles for the oxidative catalysis of the *o*-phenylenediamine (*o*-PDA).[14] In addition, Yimin Zhu et al. have synthesized a trimer from the oxidative polymerization of the *o*-PDA catalyzed by cytochrome C and H_2O_2.[15] The mechanism of these metalloenzyme-catalyzed oxidative polymerizations is based on the oxidation of the metalloenzymes by H_2O_2 to obtain a metalloprotein-oxygen complex, which subsequently reacts with an aromatic diamine monomer to form a monomer radical and a Hb-OH compound (Complex II). The monomer radical is formed also by the reaction between the Hb-OH compound and monomer, allowing the regeneration of the enzyme (Scheme S1, ESI†).[16]

The facile and environmentally friendly synthesis of carbon-based fluorescence nanoparticles still remains a significant challenge.[17] The unique optical and low/non-toxic properties of these nanomaterials can be further applied to construct optoelectronic devices.[18, 19] Herein, our research group has designed for the first time a one-step synthesis at room temperature of highly luminescence carbon based polymers via biocatalytic activity of

magnetic nanobioconjugates (Scheme 1). As a consequence, novel fluorescent polymers have been synthesized by the oxidative polymerization of *o*-PDA, *m*-PDA and *p*-PDA precursors using a hybrid redox protein-MNPs assembly based on hemoglobin immobilized on dopamine (DA) coated Fe_2O_3 nanoparticles (Hb-DA-Fe_2O_3).

Materials and methods

The synthesis of the biocatalyst was carried out by mechanochemical milling processes using horse hemoglobin (Hb) and dopamine hydrochloride (DA-HCl), together with pre-synthesized Fe_2O_3 magnetic nanoparticles (MNPs). The nanobiocatalyst has been broadly characterized by XRD, XPS, DLS,

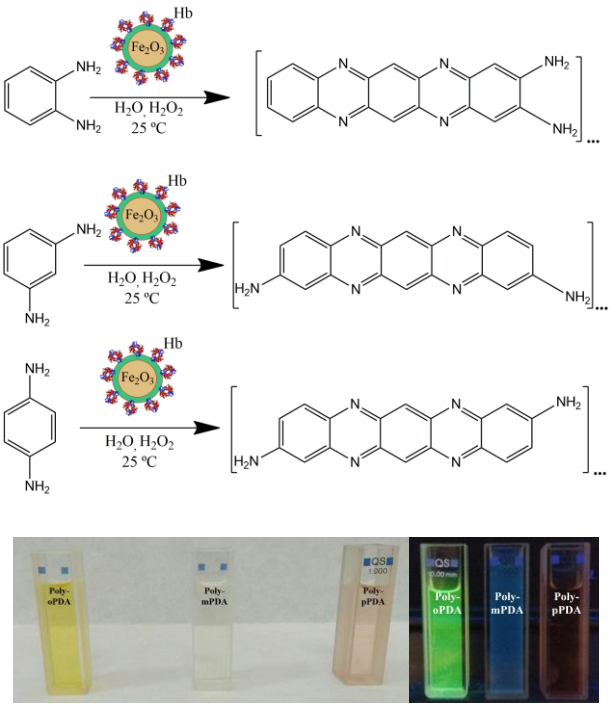

Scheme 1. Overview of the oxidative catalysed polymerization of phenylenediamines. Bottom images correspond to the corresponding poly *o*, *m* and *p*PDA (left image) and UV-irradiated (365 nm), respectively.

UV-Vis, IR spectroscopy and TEM (Figure S1-S5, ESI†). Additionally, magnetic susceptibility measurements were performed, confirming the interesting magnetic properties of the nanobioconjugates (Table S1, ESI†). This synthetic protocol has been previously reported by our group for the successful preparation of nanobioconjugates.[20] Subsequently, a simple protocol has been developed for the synthesis of fluorescent nanomaterials based on *o*-PDA, *m*-PDA and *p*-PDA. The polymerization reaction was carried out at room temperature for 24 h using 544 mg of each isomer respectively, 60 μL of H_2O_2, 50 mg of the catalyst and 8 mL of H_2O as solvent. The samples were purified by silica gel column chromatography with gradient elution using ethyl acetate and cyclohexane as eluents. Finally, the products were dried via rotaevaporation. The three poly-*o*PDA, poly-*m*PDA and poly-*p*PDA were obtained in 26, 10 and 11wt% yields, respectively. A full characterization of the materials was performed by TEM, MALDI-TOF MS, FT-IR, XPS, ^{13}C-NMR, UV-Vis Absorption and Fluorescence spectroscopies.

Results and discussion

The morphology of the synthesized polymers was determined by TEM analysis. The micrographs (Figure S6, ESI†) depict a homogeneous distribution with a mean radius around 12 nm. Figure 1 displays the UV-Vis absorption spectra of the three obtained products with characteristic absorption peaks at 422, 346 and 525 nm for the poly-*o*PDA, poly-*m*PDA and poly-*p*PDA, respectively.

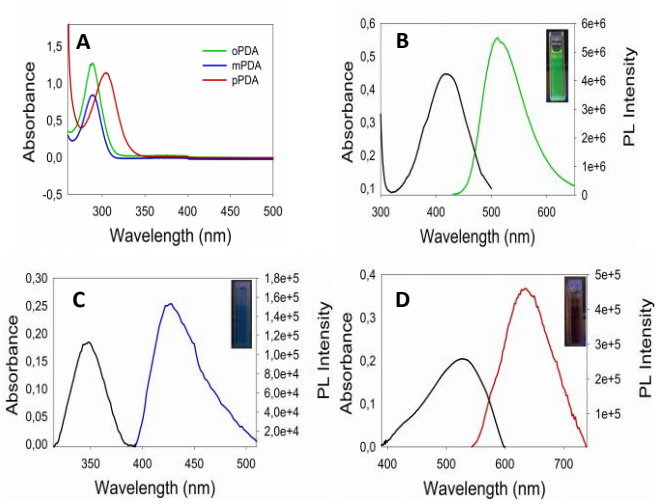

Figure 1. A: UV-Vis absorption spectra of the *o*PDA, *m*PDA and *p*PDA precursors in 0.2 g/mL aqueous solution, UV-Vis and Fluorescence Emission spectra of B: poly- *o*PDA, C: poly- *m*PDA and D: poly- pPDA from a starting material concentration of 0.07 g/ml.

These absorption signals are significantly different than those of the corresponding starting materials (Figure 1A) indicating the formation of π-conjugated systems in the polymerization process. The absorption bands can be ascribed to n→π* electronic transitions suggesting the formation of carbon based nanomaterials with smaller electronic bandgaps than the phenylenediamines.[21] The fluorescence spectra of the obtained polymers were measured to study in detail their Photoluminescence (PL) properties (Figure 1). Interestingly, the products displayed different emission maxima at 520, 425, 638 nm for the poly-*o*PDA, poly-*m*PDA and poly-*p*PDA, respectively (under a single excitation wavelength of 365 nm). Additionally, the emission spectra of the Hb-DA-Fe_2O_3 bionanocatalyst were registered for comparison (Figure S7, ESI†). The PL lifetimes of the poly-*o*PDA, poly-*m*PDA and poly-*p*PDA were measured showing a mono-exponential profiles with lifetimes of 1.78±0.1 (λ_{em} =402), 2.04±0.1 (λ_{em} =372) and 0.6±0.1 ns (λ_{em} =440), respectively. Additionally, fluorescence quantum yields (QY) of 5, 2 and 0.01% were obtained for the poly-*o*PDA, poly-*m*PDA and poly-*p*PDA, respectively (Table S2, ESI†). In particular, the poly-*o*PDA resulted to be

a potential candidate for its use in the future development of optoelectronic devices, with a quantum yield in solution similar to others reported in the literature for this kind of compounds.[22]

The infrared spectra of the poly-*o*PDA, poly-*m*PDA and poly-*p*PDA showed characteristic bands between 3200-3450 cm^{-1}, which can be attributed to the N–H stretching vibrations of the -NH_2 groups (Figure 2). The signal at 1500-1510 cm^{-1} is associated to the C=C stretching vibration. Significantly, peaks appeared at about 1330-1339 cm^{-1} can be attributed to the aliphatic C-N= stretching vibrations, which imply the intermolecular cyclization of the *o*-PDA, *m*-PDA and *p*-PDA precursors. Additionally, bands in the range of 830-870 cm^{-1} can be linked to a ring hydrogen deformation vibration isolation.[23, 24]

XPS analysis indicated the presence of C, N and O in the three obtained polymers (Figure S8, ESI†). The elemental quantification was performed and it is reported in Table 1 displaying similar percentages for each element in the three products.

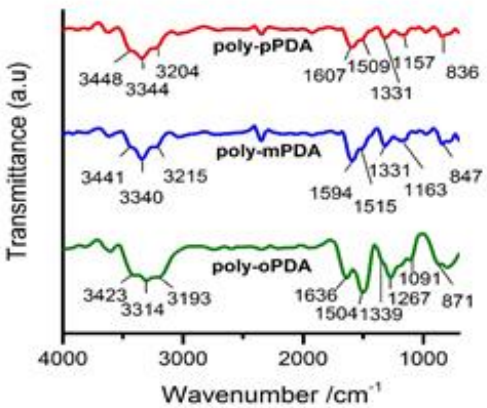

Figure 2. FT-IR spectra of poly- *o*PDA, poly- *m*PDA and poly- *p*PDA.

Table 1. Elemental quantification of poly-*o*PDA, poly-*m*PDA and poly-*p*PDA.

Product	C (%)	N (%)	O (%)
Poly-oPDA	74.90	11.93	13.17
Poly-mPDA	78.72	12.73	8.55
Poly-pPDA	74.49	8.24	17.26

The deconvoluted C 1s XPS spectra exhibited three different contributions associated to the presence of C-C/C=C (aromatic carbon), C-N and C-O (carboxylate). Noticeably, the component quantification in this region reveals a high percent of C-N bonds (Table S3, ESI†). This result strongly supports the successful polymerization of the precursor materials and corroborates the IR results. In addition, the N 1s spectra, can be deconvoluted in two peaks, corresponding to the pyrimidinic and amino groups (Figure 3).These results are in good agreement with other reported in the literature for similar materials, taking into account the different synthetic metodologies.[21] Additionally, ^{13}C-NMR characterization was performed for the three solid products, displaying a signal above 140 ppm, that can be ascribed to C=N in the quinoid units of the polymers.[25] The peaks at ≈125-128 ppm are ascribed to the carbon in the C-H bonds and the peaks between 110-119 ppm can be assigned to the nitrogen-bonded carbon (C-NH) in the benzoic units. (Figure S9, ESI†).

The three products of the polymerization of *ortho*, *meta* and *para* substituted phenylenediamines were analized by MALDI-TOF MS under positive ion mode. The poly-*o*PDA spectrum revealed the presence of four oligomers: $C_{12}H_{10}N_4$, $C_{24}H_{14}N_8$, $C_{30}H_{16}N_{10}$, $C_{36}H_{18}N_{12}$. Furthermore, the poly-mPDA displayed a similar polymer weight distribution with the presence of $C_{18}H_{12}N_6$, $C_{24}H_{14}N_8$, $C_{36}H_{18}N_{12}$ as can be observed in the respective mass spectra (Figure 4). In particular, the poly-*p*PDA spectrum showed the only presence of the corresponding trimer $C_{18}H_{12}N_6$.

During the polymerization reaction, several samples were taken every 2 hours and characterized by UV-Vis absorption spectroscopy. As can be

observed in Figure 5A, the absorbance and therefore the product concentration did not change considerably after 4h.

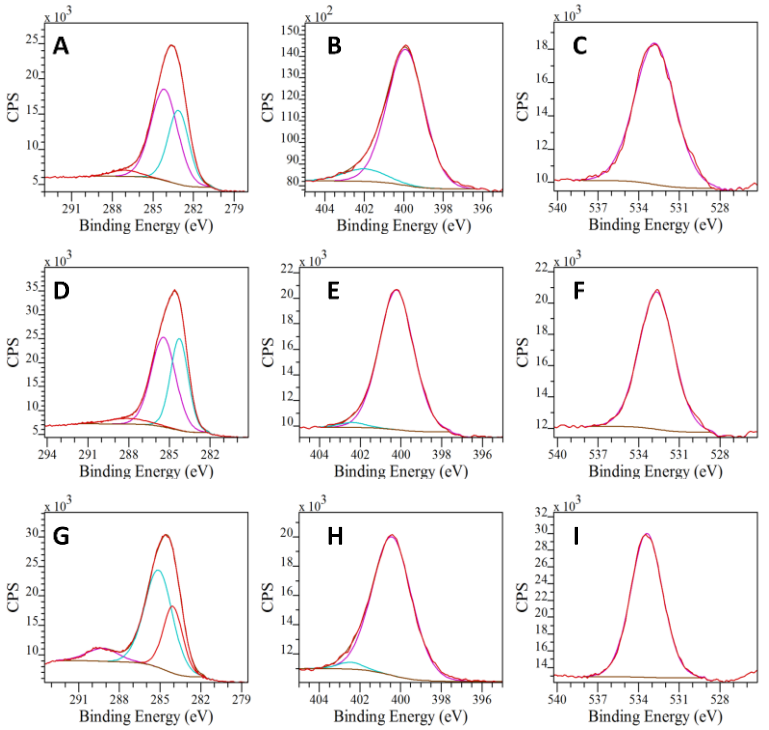

Figure 3. Deconvoluted XPS spectra of poly- *o*PDA for A: C1s, B: N1s and C: O1s, poly- *m*PDA for D: C1s, E: N1s and F: O1s and poly- *p*PDA for G: C1s, H: N1s and I: O1s.

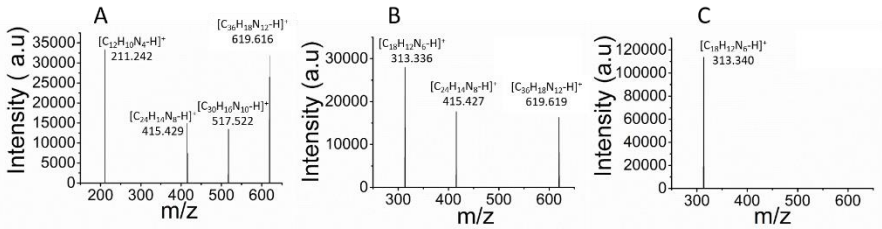

Figure 4. MALDI-TOF MS analysis of A: poly- *o*PDA, B: poly- *m*PDA and C: poly- *p*PDA.

Moreover, the reusability of the catalyst was studied for the oxidative polymerization of the *ortho* isomer. After the first use, the catalyst was recovered by a magnet, washed several times with H_2O, and let it dry at

30°C for 48 h. Once the catalyst was dry, the reaction was repeated in the same conditions. It was observed a decrease in the intensity of the emission and excitation spectra, which can be attributed to the absorption of organic species on the surface of the biocatalytic system (Figure 5B). This assumption was corroborated by FT-IR spectroscopy, which revealed a similar spectrum compared with the obtained for the poly-*o*PDA (Figure S10, ESI†). XPS quantification of the Hb-DA-MNP after the reaction showed a N/Fe ratio of 98 which is 3 times higher than the one obtained for the Hb-DA-MNP before the reaction (Figure S11, Table S4, ESI†). In addition, UV-Vis analysis also confirmed the presence of the polymer in the catalyst (Figure S11, ESI†). Although, the intensity of the emission and excitation spectra decreases after the second use, the Hb-DA-Fe_2O_3 can be reused in the polymerization of *o*-PDA. These results together with the magnetic properties of this material, which allow its easy separation and manipulation, make it a good option as catalyst for the polymerization of phenylenediamines. Remarkably, this work could represent a breakthrough in the scientific community and the beginning of novel environmentally friendly protocols for the synthesis of carbon based fluorescence nanomaterials.

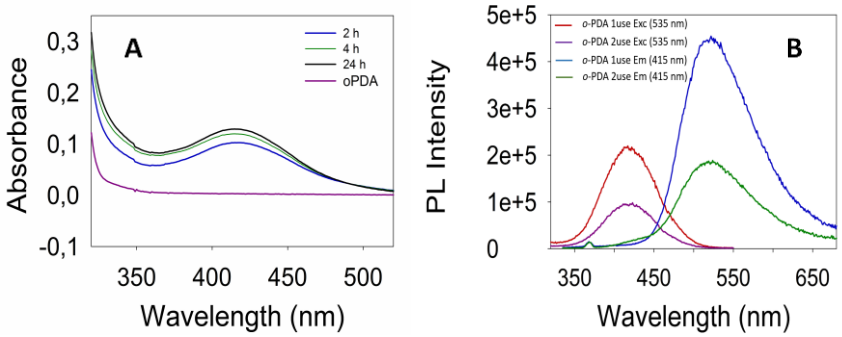

Figure 5. UV-Vis spectra of A: samples taken each 2 h from polymerization of *o*PDA, B: Emission and excitation spectra of the first and second use of the Hb-DA-Fe_2O_3 in the polymerization of *o*PDA.

It is well-known that all enzymes-coated NPs show a striking pH-dependent colloidal stability properties.[26-29] As a consequence, Z-potential measurements at different pH values have been performed in order to determine the pI of the Hb-DA-Fe_2O_3 (Figure

6 A). At low pHs values the Z-potential exhibit positive values between 7-9 mV and slowly changes to negative values at higher pHs, which give rise to a pI=7.3. Accordingly, in the pH range around the pI, the nanobioconjugates become unstable and start agglomerating and maintain a good colloidal stability properties at pH>pI, pH<pI. UV measurements (figure 6B) reveal a significant enhancement of the absorbance in the poly-*o*PDA synthesized at pH=4, while the absorbance when the reaction was carried out at pH=7 and pH=8, which are close to the pI, decrease significantly. Consequently, the catalytic yields in the polymerization are directly influenced by the colloidal stability of the nanobioconjugates and in turn by the pH environment. Also, it is worth to note that a red shift occurs in the maximum absorption at pH=4 indicating that the conjugation in the poly-*o*PDA structure is extended at low polymerization pH values.[30]

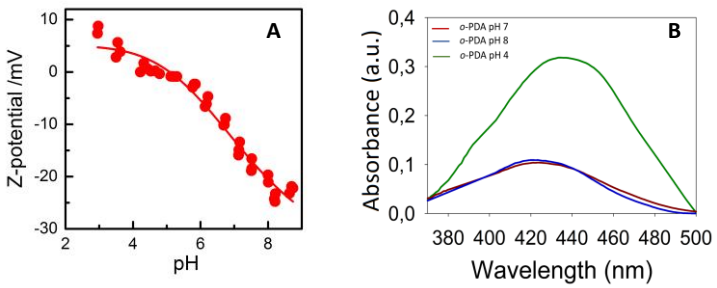

Figure 6. A: Z-potential titration curve of the nanobioconjugates. B: UV-Vis spectra of the polymerization of *o*PDA at different pHs values.

Conclusions

In summary, the Hb-DA-Fe_2O_3 biocatalyst turned out to be a potential candidate for its use in the oxidative polymerization of phenylenediamines. The combination of the redox properties of the protein together with the magnetic characteristics of the nanoparticles, which facilitate its reusability, could lead to a wide range of applications in catalyzed oxidation reactions. Remarkably, the reaction was

performed at room temperature, being advantageous from an environmental point of view. The obtained polymers possess an interesting fluorescence behaviour, which could be further employed for the development of optoelectronic devices, which is currently under investigation in our research group.

Acknowledgments
R. Luque gratefully acknowledges MINECO for funding under project CTQ2016-78289-P.

References

1. M.Filice, J. M.Palomo, *ACS Catal.*, 2014, **4**, 1588.
2. I. Willner , B.Willner , *Nano Lett.*, 2010, **10**, 3805.
3. Y. Xiao; F.Patolsky , E.Katz ; J. F.Hainfeld , I.Willner , *Scienc*e, 2003, **299**, 1877.
4. M. Dagys, A. Laurynenas, D.Ratautas , J. Kulys , R. Vidziunaite, M.Talaikis , G. Niaura , L. Marcinkeviciene, R. Meskys , S. Shleev, *Energy Energy Environ. Sci.*, 2017, **10** , 498.
5. C. Zhao , P. Gai; R. Song , Y. Chen , J. Zhang , J.J. Zhu , *Chem. Soc. Rev.*, 2017, **46**, 1545.
6. J. Cheng, Y. Han , L. Deng , S. Guo, *Anal. Chem.* 2014, **86**, 11782.
7. A. K. Vahidi, Y.Yang, T. P. N. Ngo, Z. Li , *ACS Catal.*, 2015, **5**, 3157.
8. S. C. Corgie, P. Kahawong, X. Duan, D. Bowser, J. B. Edward, L. P.Walker, E. P. Giannelis, *Adv. Funct. Mater.*, 2012, **22**, 1940.
9. J. Garcia, Y. Zhang, H.Taylor, O. Cespedes, M. E. Webb, D. Zhou, *Nanoscale*, 2011, **3**, 3721.
10. V. Polshettiwar, R. Luque, A. Fihri, H. Zhu, M. Bouhrara, J. M. Bassett, *Chem. Rev.*, 2011, **111**, 3036.
11. Y. Pan, X. W. Du, F. Zhao, B. Xu, *Chem. Soc. Rev.*, 2012, **41**, 2912.
12. X. G. Li, M. R. Huang, W. Duan, Y. L. Yang, *Chem. Rev*., 2002, **102**, 2925.
13. H. P. Dai, Q. H. Wu, S. G. Sun, K. K. Shiu, *J. Electroanal. Chem.* ,1998, **456**, 47.
14. T. Ono, K. Kawakami, M. Goto, S. Furusaki, *J. Mol. Catal. B-Enzym.,* 2001, **11**, 955.

15. Y. M. Zhu, J. H. Li, Z. M. Liu, G. J. Cheng, S. J. Dong, E. K. Wang, *J. Mol. Catal. B-Enzym.*2001*,* **4** , 33.
16 D. Ichinohe, T. Muranaka, T. Sasaki, M. Kobayashi, H. Kise, *J. Polym. Sci., Part A: Polym. Chem.* 1998, **36,** 2593.
17. G. E. LeCroy, S.T. Yang, F.Yang, Y.Liu, K. A. S. Fernando, C. E.Bunker, Y.Hu, P. G. Luo, Y.P. Sun, *Coord. Chem. Rev.*, 2016, **320**, 66.
18. F. L. Yuan, Z. B. Wang, X. H. Li, Y. C. Li, Z. A. Tan, L. Z. Fan, S. H.Yang, *Adv. Mater.*,2017, **29**, 516.
19. H. Choi, S. J. Ko, Y.Choi, P.Joo, T. Kim, B. R. Lee, J. W. Jung, H. J.Choi, M.Cha, J. R. Jeong, I. W. Hwang, M. H. Song, B. S. Kim, J. Y. Kim, *Nature Photonics*, 2013, **7**, 732.
20. D. Rodriguez-Padron, A. R. Puente-Santiago, A. M. Balu, A. A. Romero, R.Luque, *Chem. Commun.*, 2017, **53**, 7635.
21. K. Jiang, S. Sun, L. Zhang, Y. Lu, A. Wu, C. Cai, H. Lin, *Angew. Chem. Int. Ed.*, 2015, **54**, 5360.
22 C. Gu, N. Huang, Y. Wu, H. Xu, D. Jiang, *Angew. Chem. Int. Ed.*, 2015, **54**, 11540.
23. N. Kannapiran, A. Muthusamy, P. Chitra, S. Anand, R.Jayaprakash, *J. Magnetism Magnetic Mater.*, 2017, **423**, 208.
24. K. R. Das, M. J.,Antony, *Polymer*, 2016, **87**, 215.
25 I. Amer, D. A. Young, *Polymer*, 2013, **54**, 505.
26. M.Chanana, M. A. Correa-Duarte, L. M.Liz-Marzan, *Small*, 2011, **7**, 2650.
27. M. S.Strozyk, M.Chanana, I. Pastoriza-Santos, J.Perez-Juste, L. M. Liz-Marzan, *Adv. Funct. Mater* ,2012, **22**, 1436.
28. I.Dewald, O. Isakin, J.Schubert, T.Kraus, M.Chanana, *J. Phys. Chem. C*, 2015, **119**, 25482.
29. J. Y. Zhang, A. R. Zhu, T.Zhao, L.Wu, P.Wu, X. D. Hou, *J. Mater. Chem. B*, 2015, **3**, 5942.
30. I. Losito, E. De Giglio, N. Cioffi, C. Malitesta, *J. Mater. Chem.,*2001, **11**, 1812.

Supporting Information

Synthesis of carbon-based fluorescent polymers driven by catalytically active magnetic bioconjugates

Daily Rodríguez-Padrón,[a] Alexander D. Jodlowski,[b] Gustavo de Miguel,[b] Alain R. Puente-Santiago,[a]* Alina M. Balu,[a] Rafael Luque [a]*

[a.] *Departamento de Química Orgánica, Grupo FQM-383, Institute of Fine Nanochemistry, Universidad de Cordoba, Campus de Rabanales, Edificio Marie Curie (C-3), Ctra Nnal IV-A, Km 396, E14014, Cordoba (Spain), e mail: q62alsor@uco.es, apuentesantiago@gmail.com*

[b.] *Departamento de Química Física, Institute of Fine Nanochemistry, Universidad de Cordoba, Campus de Rabanales, Edificio Marie Curie (C-3), Ctra Nnal IV-A, Km 396, E14014, Cordoba*

Bioconjugates based on a redox protein and iron oxide magnetic nanoparticles were employed in the catalytic polymerization of ortho, meta and para substituted phenylenediamines at room temperature for the synthesis of carbon-based fluorescent polymers. UV-visible absorption measurements of the three obtained products displayed a red shift compared to starting materials. These results together with the FT-IR and XPS analysis confirm the successful formation of the polymers. In particular, the component quantification in the C1s XPS spectra revealed the high proportion of C-N bonds, associated to the oxidative polymerization of the precursors. MALDI-TOF MS analysis was performed in order to determine the molecular weights of the products. The synthesized poly-oPDA, poly-mPDA and poly-pPDA resulted to have a highly green, blue and red fluorescence, respectively. The reusability of the biocatalyst and the effect of the pH were investigated in the reaction for the ortho isomer. The biocatalytic system displayed optimum results when the pH was below the enzyme isoelectric point (pI).

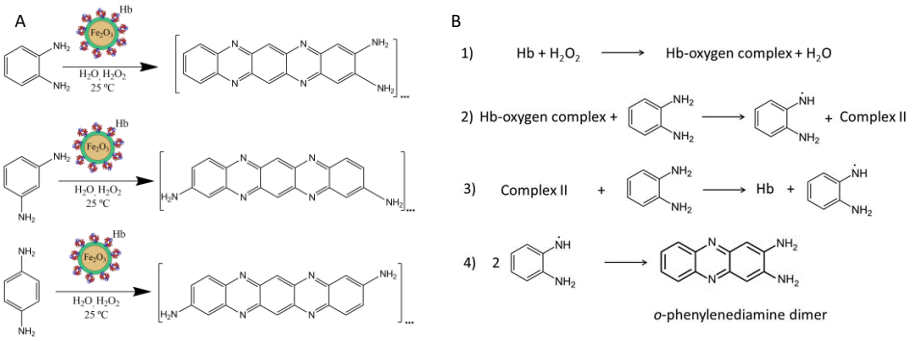

Scheme 1. A: Overview of the oxidative catalysed polymerization of phenylenediamines. **B:** First cycle of the oxidative polymerization mechanism of phenylenediamines driven by Hb-DA-Fe_2O_3 nanobioconjugates and H_2O_2.

Experimental Procedures

Materials:

Reagent grades of o-, m-, p-phenylenediamines, hemoglobin and dopamine hydrochloride were purchased from Sigma-Aldrich. All chemicals were used as received without further purification unless otherwise specified. Deionized (DI) water was used throughout this study.

Characterizations:

The obtained product was characterized by Transmission Electronic Microscopy (TEM), Matrix-assisted laser desorption/ionization time-of-flight mass spectrometry (MALDI-TOF MS), Fourier Transform-Infrared Spectroscopy (FT-IR), Nuclear Magnetic Resonance (NMR), UV-vis spectroscopy, steady-state and time-resolved fluorescence spectroscopy, in order to identify its structure and morphology.

TEM images were taken in the FEI Tecnai G2 system, equipped with a CCD ("charge coupling device") camera. The product was dispersed in ethanol for 1 h by ultrasound and directly deposited on a copper grid, previous to analysis.

MALDI-TOF MS analyses were performed on a 4800 Proteomics Analyzer, Applied Biosystems. The spectra acquisition was carried out automatically and the extraction delay time was optimized to 180 ns. The measurements were performed in positive ionization reflection mode in a mass/charge range (m/z) of 100 to 1500 Da.

FT-IR measurements were carried out on the ABB MB3000 infrared spectrophotometer (with Horizon MBTM software), provided with an ATR PIKE MIRacleTM sampler, a window of ZnSe, and 256 scans at a resolution of 8 cm-1. Spectra were obtained in a 4000-600 cm-1 wavenumber range. During the acquisition, the obtained polimer was purged with a dehydrated and deoxygenated nitrogen flow (20 mL min-1). Additionally, 13C-NMR spectra were accomplished in the Bruker Avance III HD 400 WB equipped with a 4 mm CP / MAS probe.

UV-visible absorption spectra were performed on the Cary 100 Bio UV-visible spectrophotometer. Steady-state and time-resolved fluorescence analysis were acquired on the FLS920 Fluorimeter (Edinburgh Instrument Ltd, Livingston, UK). The determination of the quantum yields was carried out employing coumarin 153, 9,10-diphenyl-antracene and tetraphenyl porphyrin as references for the poly-*o*PDA, poly-*m*PDA and poly-*p*PDA, respectively.

XPS analysis was conducted using an ultrahigh vacuum (UHV) multipurpose surface analysis system SpecsTM. The analysis was carried out using a conventional X-ray source (XR-50, Specs, Mg-Kα) at pressures <10-10 mbar and in a "stopand go" mode. The sample was left overnight under vacuum (<10-6 Torr). Finally, spectra were acquired at room temperature (pass energy: 25 and 10 eV, step size: 1 and 0.1 eV, respectively) with the Phoibos 150-MCD energy detector. The deconvolution of the obtained curves was accomplished with XPS CASA program.

Results and Discussion

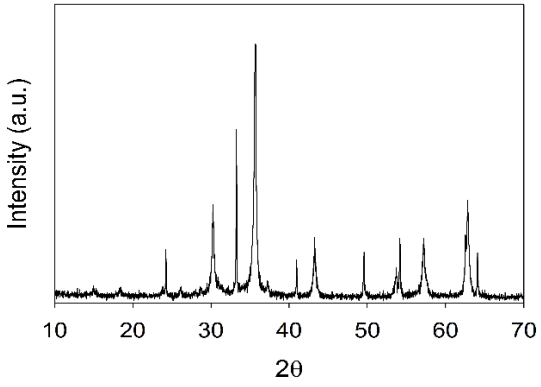

Figure S1. XRD patterns of Fe_2O_3

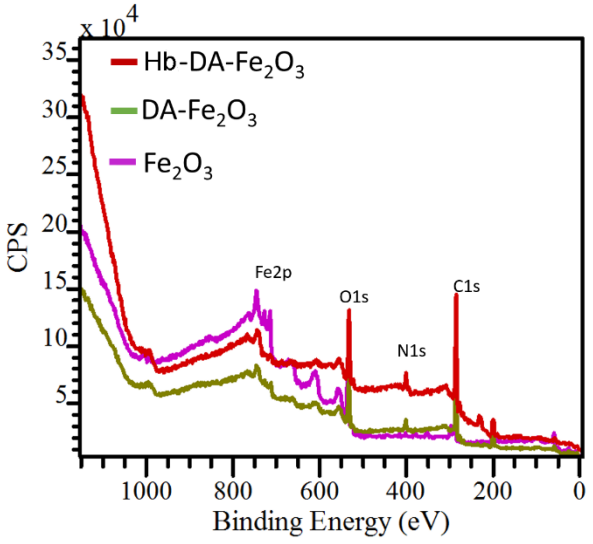

Figure S2. XPS spectra of Hb-DA-Fe_2O_3 nanobioconjugates, DA-Fe_2O_3 and Fe_2O_3 nanoparticles respectively.

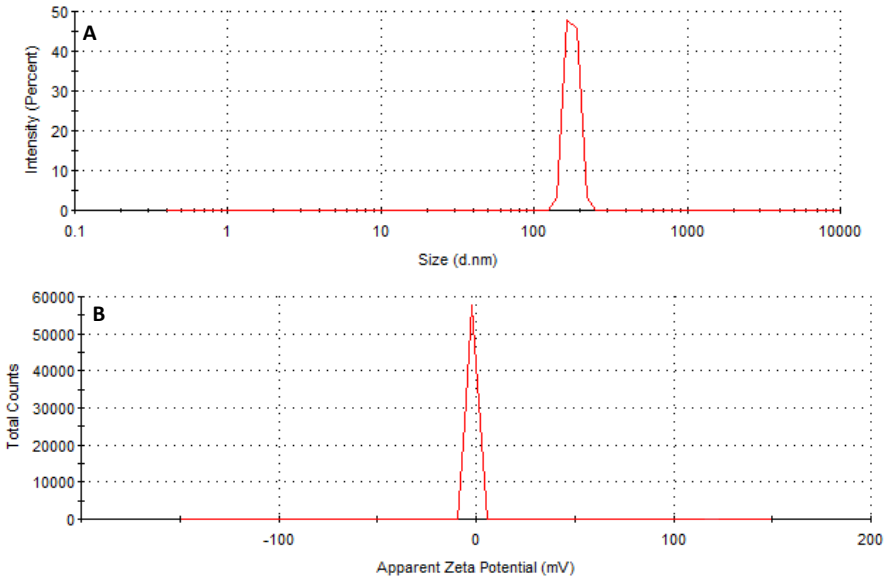

Figure S3. A: DLS and B: Z potential measurements of Hb-DA-Fe_2O_3 nanobioconjugates.

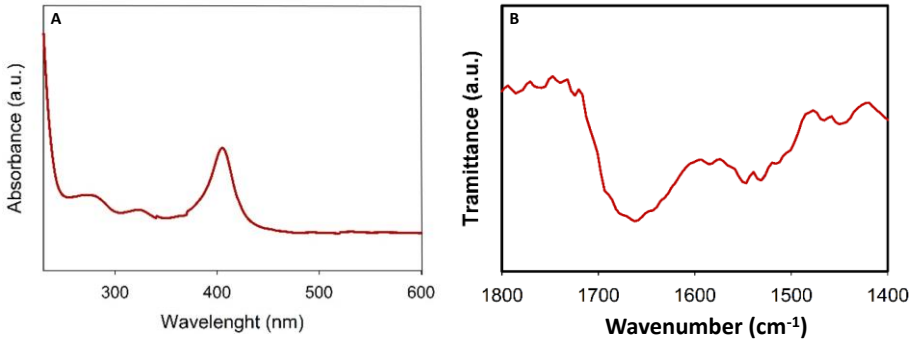

Figure S4. A: UV and B: FTIR measurements of Hb-DA-Fe_2O_3 nanobioconjugates.

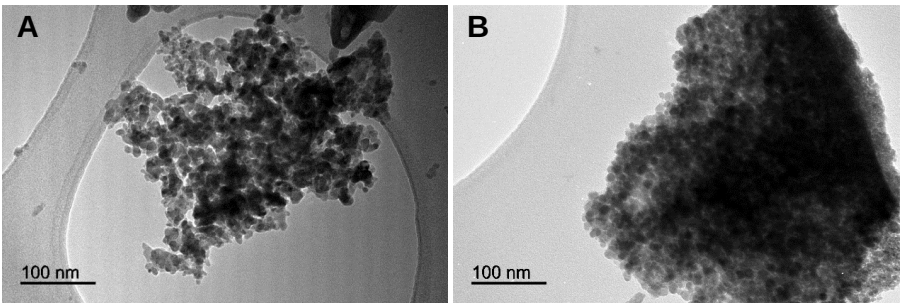

Figure S5. TEM images of A: Fe_2O_3 and B: Hb-DA-Fe_2O_3.

.**Table S1.** Magnetic Susceptibility measurements.

Material	**Magnetic susceptibility (10^{-6} m^3Kg^{-1})**
Fe_2O_3	282
Hb-DA-Fe_2O_3	267

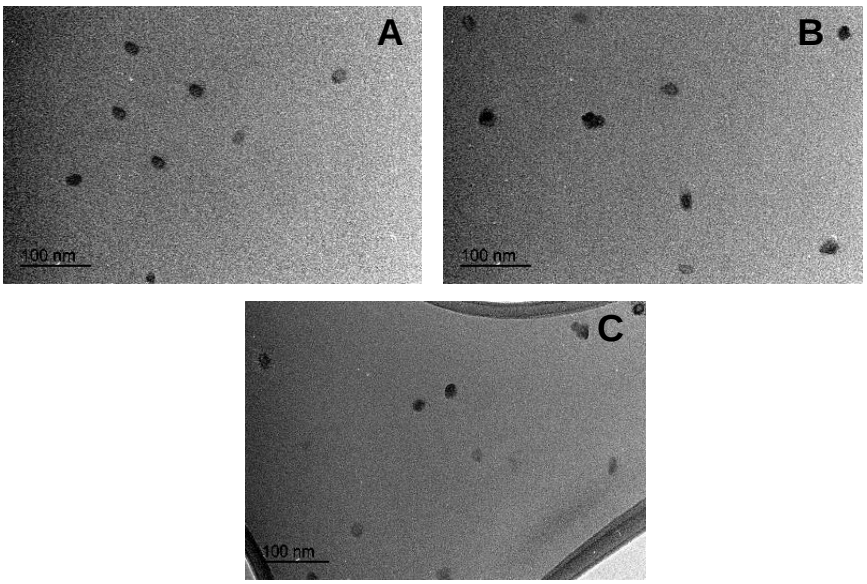

Figure S6. TEM images of A: poly-*o*PDA, B: poly-*m*PDA and C: poly-*p*PDA.

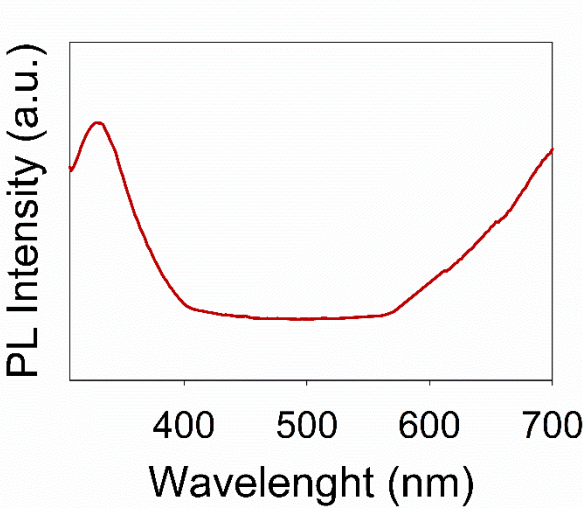

Figure S7. Fluorescence spectrum of the Hb-DA-Fe_2O_3 bionanocatalyst.

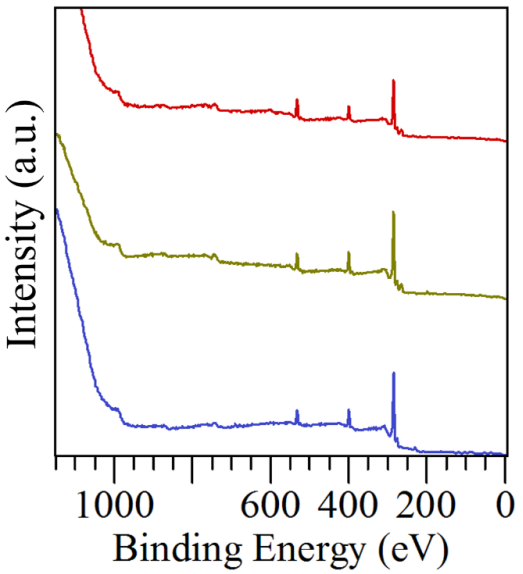

Figure S8. Survey XPS spectra of poly-*o*PDA, poly-*m*PDA and poly-*p*PDA.

Table S2. Quantum Yield of poly-*o*PDA, poly-*m*PDA and poly-*p*PDA.

Product	**λ_{exc} (nm)**	**λ_{ems} (nm)**	**Solvent**	**Reference**	**QY (%)**
Poly-*o*PDA	420	520	EtOH	Coumarin 153	5
Poly-*m*PDA	350	420	AcOEt	9,10-diphenyl-antracene	2
Poly-*p*PDA	512	638	H_2O	Tetraphenyl porphyrin	0.01

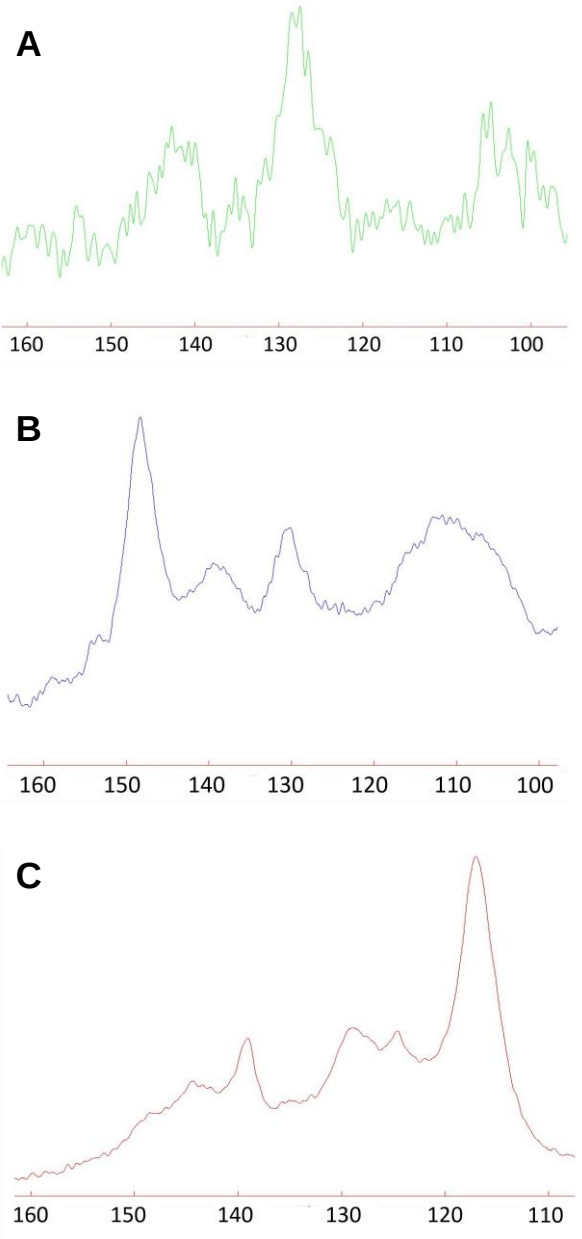

Figure S9. ^{13}C-NMR spectra of A: poly-*o*PDA, B: poly-*m*PDA and C: poly-*p*PDA.

Table S3. Components quantification in the C1s XPS spectrum region.

Product	C-C (%)	C-N (%)	C-O (%)
Poly-oPDA	38.04	55.00	6.96
Poly-mPDA	53.80	40.15	6.05
Poly-pPDA	30.36	62.05	7.59

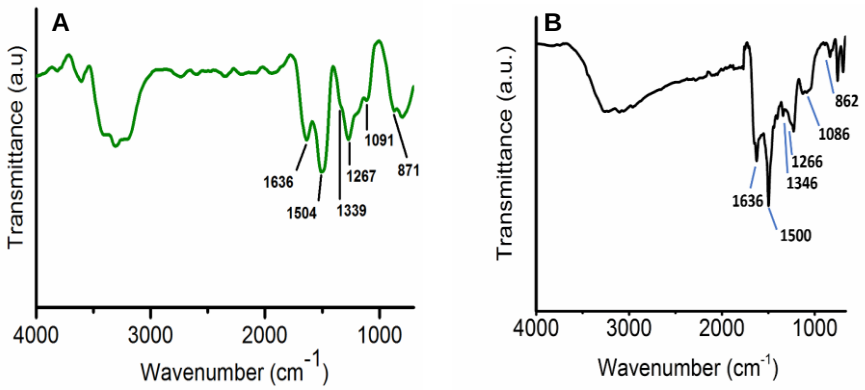

Figure S10. FT-IR spectra of A: poly-*o*PDA, B: Hb-DA-MNP after the first use.

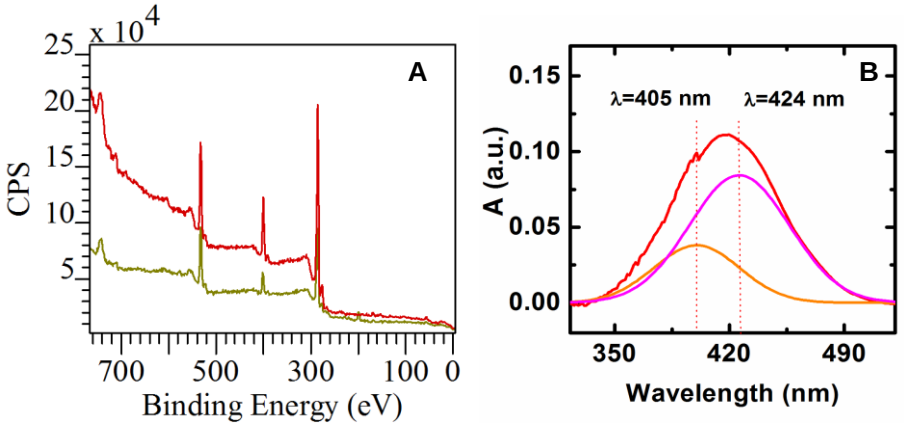

Figure S11. A: XPS spectra of Hb-DA-MNP before (green line) and after (red line) the first use. B: UV-Vis spectrum of Hb-DA-MNP after) the first use.

Table S4. Elemental quantification of Hb-DA-MNP and Hb-DA-MNP after the first use.

Product	C (%)	N (%)	O (%)	Fe (%)	N/Fe ratio
Hb-DA-MNP	68.90	10.47	20.18	0.44	34
Hb-DA-MNP (reused)	75.05	12.69	12.13	0.13	98

3.4. Catalyzed microwave-assisted preparation of carbon quantum dots from lignocellulosic residues

Mechanochemical protocols were employed for the preparation of an iron oxide supported silicate material. The synthesized sample was used as an acid catalyst for the preparation of carbon-based fluorescent nanoparticles. In this case, we moved forward from the previously described bottom-up strategy to a top-down protocol, employing a lignocellulosic residue as carbon source. Microwave assisted treatment was employed for the synthesis of the CQDs and a full multi-technique characterization analysis was carried out.

Daily Rodríguez-Padrón; Manuel Algarra; Luis Tarelho; Jorge Frade; Ana Franco; Gustavo de Miguel; Jose Jimenez, Enrique Rodriguez-Castellon; Rafael Luque. **2018**. Catalyzed microwave-assisted synthesis of Carbon Quantum dots from lignocellulosic residues. **ACS Sustainable Chemistry & Engineering**. *6*(6), 7200-7205. 10.1021/acssuschemeng.7b03848, IF: 6.14.

Catalyzed microwave-assisted preparation of Carbon Quantum dots from lignocellulosic residues

Daily Rodríguez-Padrón[□], Manuel Algarra[§,♱*] Luis A.C. Tarelho[■], Jorge Frade[◊], Ana Franco[□] Gustavo de Miguel[†], José Jiménez[§], Enrique Rodríguez-Castellón[§], Rafael Luque[□ϱ*]

[□]*Dept. Quimica Organica, Universidad de Córdoba. Edif. Marie Curie, Ctra Nal IV-A Km 396, E-14014, Córdoba, Spain. q62alsor@uco.es*

[§]*Dept. Inorganic Chemistry, Facultad de Ciencias, Universidad de Málaga, Campus de Teatinos s/n, 29071 Málaga, Spain.*

[♱] *Centro de Química da Madeira*

[□]*Dept. Environment & Planning. University of Aveiro. 3810-193 Aveiro, Portugal*

[◊]*Dept. Materials and Ceramic Engineering (DEMAC). University of Aveiro. 3810-193 Aveiro, Portugal*

[†]*Dept. Physical Chemistry, Univ. Córdoba. Edif. Marie Curie, Ctra N IVa Km 396, 14014, Córdoba, Spain.*

ϱPeoples Friendship University of Russia (RUDN University), 6 Miklukho-Maklaya Str., 117198, Moscow, Russia

A lignocellulosic residue from the pulp and paper industry (primary sludge) was employed to obtain carbon-based fluorescent nanomaterials. The unprecedented preparation of the Carbon Quantum Dots (CQDs) was carried out using a microwave-assisted reaction catalyzed by a solid acid catalyst, which induced the formation of CQDs. The obtained CDQs were fully characterized using a number of analytical techniques. HR-TEM images depicted particle sizes of average diameter value of 17.5 nm. UV-visible spectra displayed a characteristic peak at 325 nm associated with the formation of CQDs. Fluorescence measurements recorded at 360 nm (excitation wavelength) exhibited an emission band at ca. 435 nm. This emission signal turned out to be dependent on the excitation wavelength that further confirmed the presence of CQDs.

Keywords*: Lignocellulosic residue; Carbon Quantum Dots; Microwave; Acid catalyst; Photoluminiscent*

Introduction

Paper is one of the most important goods in society day life, currently manufactured using a pulp process from natural fibers from distinct types of forest plantations and/or with paper recovered from recycled fibers. Most papers comprise both long and short fibers, in varying proportions, depending on paper variety. The fiber morphology differs in each tree and thus gives different characteristics. The pulp and paper (P&P) industry transforms various types of lignocellulosic feedstocks into paper end-products influenced by the type of biomass feedstock and process applied, being present in distinct regions worldwide.[1-5] This industrial sector is characterized by the generation of significant amounts of solids, liquids and gaseous residual streams, despite of a recognized high level of process integration, which required further treatments before being discharged on the environment.

Portugal has an important industrial P&P sector, being the Kraft process the most widely employed (5 out of 6 industrial installations to transform the predominant wood species Eucalyptus globulus into pulp)[6]. The Kraft process for chemical pulping generates wastewater effluents that need to be accordingly treated. Typically, wastewater treatment includes primary and secondary processes.[1,2.7,8] Primary processes include physico-chemical steps that can include pH neutralization and a sedimentation or flotation (typically sedimentation in Portuguese P&P). Secondary processes involve a biologic treatment. A primary sludge rich in wood fibers is generally obtained (e.g., from pulp washing step, primary sedimentation) often also rich in $CaCO_3$ (e.g., from chemical recovery steps in the Kraft process).[8,9] This primary sludge is then de-watered for solids content in the 25 to 40 wt. % dry solids content range[9] via filter press.[8] This primary sludge is one of the most relevant waste feedstocks generated in the pulp and paper industry,[8,9] classified with code 030310 or 030311 when mixed with secondary sludge according to the European List of Waste.[10]

Common practices of primary sludge management include landfill, incineration and soil amendment in agriculture and forestry soils.[9] However, both sludge uses as soil amendment and especially in landfill sites have been recently subjected to strict limitations.[11] Sustainable strategies for environment management and preferable for the valorization of primary sludge are of high demand in the P&P industry sector. Interesting possibilities have been proposed to date for treatment/valorization of sludge in the context of bio-refinery products such as methane or hydrogen production via anaerobic digestion processes or ethanol via fermentation processes,[12,13] energy recovery using thermochemical conversion technologies,[14,15] design of adsorbents for water treatment[16] and valorization towards additives in construction materials.[8,9,17] These valorization strategies have a remarkable value from an environmental point of view due to their potential to deal with all different types of residues from the P&P industry. For instance, P&P residues are potentially suitable to be converted into high added-value carbon nanomaterials.[18]

In this sense, the conversion of such waste into photoluminiscent materials can further spark the interest of new applications in full-color displays, sensing, bio-imaging, light-emitting diodes and optoelectronic devices. In the past years, multicolor emissive materials including quantum dots (QDs), polymer dots, rare-earth based nanostructured materials, molecular nanomaterials, and organic fluorescent dyes emerged as promising materials for a number of applications.[19] Nonetheless, the majority of QDs possess an inherent disadvantage related to its high toxicity, which can limit their practical applications. Interestingly, CQDs represent an alternative to semiconductor QDs as new generation of carbon-based fluorescent nanomaterials because of their remarkable optical properties. Additionally, these materials exhibit a high solubility, chemical stability, and good possibilities for functionalization and low/nontoxic characteristics being heavy metal-free.[20-22] Considering their biocompatible properties, in vivo applications of CQDs, such as cell imaging, drug delivery, chemical-sensors and other emerging technologies,[23-29] or used as environmental tool for pollutant degradation, have increased considerably over the past years.[30]

Based on these premises, this contribution has been aimed to investigate a facile and sustainable microwave-assisted protocol, using a solid acid catalyst, for the valorization of a lignocellulosic residue from the P&P industry (WPP), in order to obtain CQDs with promising fluorescence properties. The proposed methodology is depicted in Figure 1. The work aims to provide a new strategy for the treatment/valorization of the sludge waste.

Figure 1. Schematic approach to obtain CQDs from WPP.

Experimental section

Synthesis of CQDs. Previous to the reaction, the lignocellulose residue, obtained from the paper industry from the Aveiro, North of Portugal was ground in a planetary mill (Emax ball mill model, Retsch), during 10 minutes at 900 rpm. Subsequently, the preparation of CQDs was carried out in a Microwave Ethos 1 model using 1 g of the milled WPP, 20 mL of dimethylformamide and 0.1 g of a solid acid catalyst, at 100 °C for 120 min. The final solution was left to cool down at room temperature, followed by centrifugation, filtration and drying under vacuum for 24 h, after which carbon-based fluorescence nanoparticles were obtained. CQDs were then subsequently characterized in detail. The selected solid acid catalyst was prepared under mechanochemical conditions from the dry milling of a porous silicate (Si-SBA-15) using a protocol previously reported by our group employing ($Fe(NO_3)_3 \times 9H_2O$) and propionic acid.[31]

Characterization. CQDs were fully characterised using various analytical techniques. High Resolution Electron Microscopy (HRTEM) imaged were recorded in a FEI Talos F200X microscope. X-ray diffraction patterns were registered in a D8 Advanced Diffractometer (Bruker AXS, room temperature) equipped with a Lynxeye detector. UV-visible absorption measurements were collected on a Cary 100 Bio UV-visible spectrophotometer. Time-resolved and steady-state fluorescence have also been carried out in a FLS920 Fluorimeter (Edinburgh Instrument Ltd, Livingston, UK). X-Ray Photoelectron Spectroscopy (XPS) measurements were recorded on a Physical Electronic PHI 5700 spectrometer utilizing Mg-K non-monochromatic radiation with a hemispherical multichannel detector (300 W, 15 kV and 1253.6 eV). Spectra were recorded using a 720 μm diameter circular analysis area, with a constant pass energy value at 29.35 eV. PHI ACESS ESCA-V6.0F software was employed for results analysis, further processed using MultiPak 8.2B package. Carbon C 1s signal (284.8 eV) was used as reference to determine the binding energy values, using Shirley-type background and Gauss-Lorentz curves. FT-IR analysis was performed on a ABB MB3000 infrared spectrophotometer, equipped a window of ZnSe, and 256 scans (16 cm^{-1} resolution) within a ATR PIKE MIRacle™ sampler. The Zetasizer Nano ZSP (Malvern Instruments Ltd.,UK) was employed to measure the zeta potential of CQDs, for which samples were diluted before analysis in 10 mM of KNO_3. All reagents were of analytical grade without further treatments.

Results and discussion

CQDs were obtained by a top-down approach from the lignocellulosic primary sludge, with concentrations of C (24.242 %) and H (2.826 %). Figure S1, ESI† showed the solid ^{13}C-NMR spectrum of the WPP in order to have an overview of the carbon content and its nature. Under the aforementioned reaction conditions, it was observed the formation of well dispersed nanoparticles with spherical regularity, corresponding to the CQDs (See TEM image, Figure 2). The average diameter of the obtained nanoparticles was 17.5 nm.

Remarkably, no nanoparticles could be observed when the WPP was treated in the absence of the solid acid catalyst (Figure S2, ESI†), indicating its crucial role in the microwave-assisted step to obtain CQDs. Importantly, these studies constitute an unprecedented approach for the preparation of CQDs using a heterogeneously catalyzed step. We believe the solid acid catalyst employed could promote an acidolytic cleavage of the lignocellulosic residue currently under in-depth investigation in our groups. The acidic properties of the solid acid catalyst were studied by DRIFT experiments. The catalyst displayed relevant acidic properties as evidenced from distinguishable strong bands observed at 1440 and 1620 cm^{-1}. These peaks correspond to Lewis acid sites (Figure S3, ESI†). This material still exhibited acidity features at increasing temperatures (200 and 300 ºC), with well-defined acidity bands that may hold additional promises in Lewis acid-catalyzed reactions. In addition, TEM images of the prepared catalyst are present in the supplementary material (Figure S4, ESI†).

The crystal structure of obtained CQDs was studied using powder XRD. Figure S5 (ESI†) clearly demonstrated a poor crystallinity of CQDs according to the broad peak centered at 24.4º, which could be assigned to the graphite (002) plane of disordered carbon.

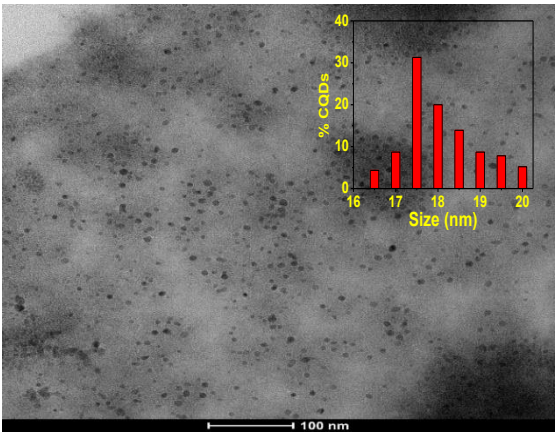

Figure 2. TEM micrographs of synthesized CQDs. Inset: particle size distribution (180 nanoparticles).

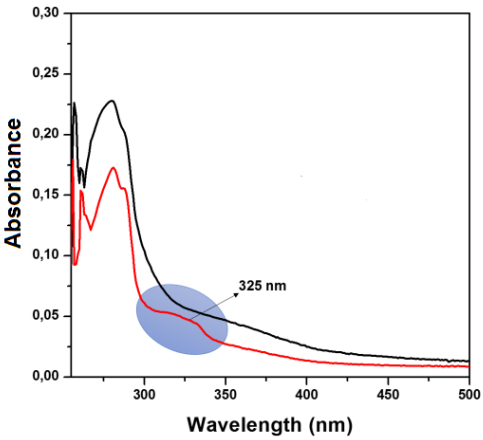

Figure 3. UV-visible spectra of CQDs (red line) and WPP treated in absence of catalyst (black line).

Figure 3 depicts the optical properties of CQDs and WPP (treated in absence of catalyst) as measured by UV spectroscopy. A weak and distinct broad band can be clearly visualized at 325 nm for WPP treated with the solid acid catalyst, corresponding to n-π* transitions of carbonyl/ hydroxyl moieties present on CQDs surface. The band at <300 nm could also be assigned to analogous features of conjugated C=C units corresponding to the carbon-core.[32,33] The obtained absorption spectrum was found to be almost identical to that obtained for fluorescent carbon dots when active carbon was used as the precursor.[22]

The fluorescence spectra of the obtained CQDs were measured in order to study in detail their Photoluminescence (PL) properties. A significant increase in fluorescence intensity ca. 75% was observed for the CQDs obtained at higher reaction times (30, 60 and 120 min, respectively, Figure S6, ESI†). This behavior could be associated to an increase in the concentration of the emissive species, indicating that the most efficient process, in terms of quantum yield, is the one performed for 120 min.

Figure 4A displays the fluorescence spectra of the CQDs in the reaction bulk at various excitation wavelengths (320 and 360 nm). The emission maximum did not change by varying the excitation wavelength, and therefore the quantum effect of CQDs cannot be clearly observed when the carbon nanoparticles are in the reaction bulk. In this regard, a filtered

and dried sample of synthesized CQDs was further excited at different excitation wavelengths (Figure 4B). Remarkably, the emission peaks of purified CQDs gradually shifted to shorter wavelengths at increasing excitation wavelengths (from 280 to 360 nm, Figure 4B), namely *anti*-Stokes photoluminescence. This wavelength-dependent emission behavior is usually detected in CQDs, supporting their formation.[33] These results also indicates the existence of different surface energy traps on the CQDs, which explain the fluorescence at shorter wavelengths. The observed multifluorescence bands are mainly originated from distinct states associated to the carbon-structure.[34]

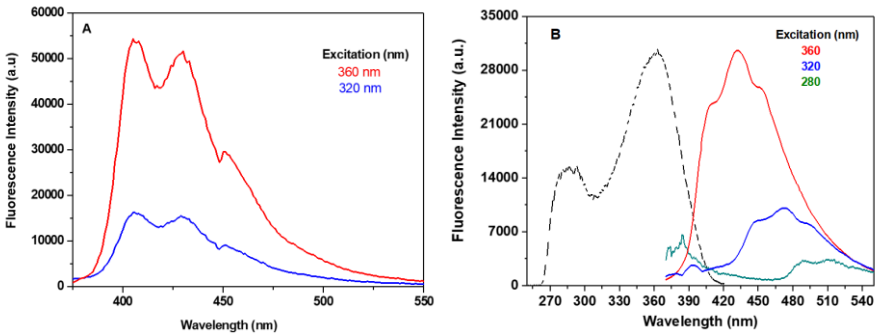

Figure 4. Emission spectra of **(A)** CQDs (reaction bulk) and **(B)** CQDs (filtered and dried) at different excitation wavelengths.

The quality of the CQDs obtained is associated to the full width of half maximum (FWHM), calculated as 73 nm, broader compared with the obtained with semiconductors QDs and similar to others previously reported CQDs,[35] which is influenced by its heterogeneous nature. To further investigate the luminescence dynamics within CQDs, the fluorescence lifetimes were derived from mono-exponential analysis of the experimental decays for CQDs solution. At the different reaction times and exciting at 372 nm, a similar lifetime of ~ 0.57 ns was obtained for all reaction times which indicate that a major emissive species is present in all the samples. Fluorescence lifetimes were also measured at three different emission wavelengths 410, 435 and 475 nm, corresponding to the three emission peaks. No significant changes in lifetimes (⍰= 0.57±0.02) were detected for the different emission wavelengths. These results further support the existence of the three peaks related to

vibrational progressions of the same electronic excited state. Time-resolved experiments were found to be in line with those of CQDs where radiative recombination was reported as principal deactivation mechanism.[36] Additionally, a fluorescence quantum yield (QY) of 2.7% was obtained for the CQDs, with this value probably depending on the effectiveness of the reaction (Table S1, ESI†). The observed luminescence emission yield is comparable with other reported in the literature for CQDs, which indicates the good performance of this synthetic route.[37]
The elemental composition of the prepared CQDs was obtained by XPS analysis (Figure S7, ESI†). XPS survey results pointed out oxygen, carbon and nitrogen content in the materials as illustrated in deconvoluted curves of these elements in Figure 5. In addition, characteristic bands at 684.9 and 598.5 eV, corresponding to fluorine, can be observed in the XPS spectrum, most likely due to presence of this element in the untreated waste. Furthermore, traces of Si were found on the surface of the CQDs, as can be inferred from the peaks at 154.5 and 103.3 eV. Nonetheless, Si just represent a 0.6 atomic %, which can be considered negligible compared to the other elements present in the obtained material. No Fe was found to be present. C1s XPS spectrum of the lignocellulosic residue was also obtained in order to compare it with the synthetized CQDs. The deconvoluted C 1*s* XPS spectrum of the residue (Figure 5A) showed four contributions at 290.33 eV (carbonate), 287.68 eV (C=O), 286.28 eV (C-OH) and 284.7 eV (C-C/C=C, graphitic, aromatic carbon), corresponding to the different C species.[38] On the other hand, the C 1*s* XPS spectrum of the CQDs was deconvoluted into bands at 284.6, 286.1 and 287.7 eV (Figure 5B), ascribed to C-C/C = C (graphitic and aromatic hydrocarbons), C-N/C=O and COO^- (carboxylate) bonds, respectively.

N 1*s* XPS spectrum shows two main bands at 400.0 eV and 402.0 eV (Figure 5C), revealing the existence of amine and its protonated groups.[39] Moreover, O1*s* spectrum displayed bands at 532.3 and 533.9 eV, related to the presence of C = O and H_2O, respectively (Figure 5D).[40]

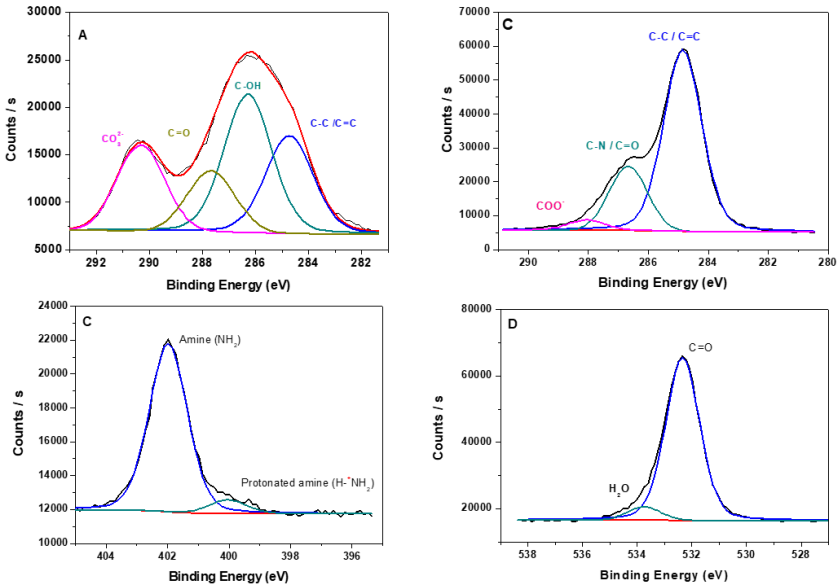

Figure 5. (**A**) High resolution C1s core level XPS spectrum for untreated WPP. High resolution (**B**) C1s, **C**) N1s and **D**) O1s core levels of CQDs.

The surface chemistry of the CQDs was studied using Infrarred spectroscopy (Figure S8, ESI†). FT-IR of CQDs displayed a wide peak at 3424 cm^{-1}, attributed to two main vibrational (stretching) contributions of O-H and N-H from hydroxyl and amine groups, respectively.[41] C-H stretching vibrational bands could be also visualized at 2934 cm^{-1}. Several additional vibrations ca. 1796, 1402 and 1040 cm^{-1} also correspond to carbonyl stretching, -$COCH_2$- bending and C-OH bonds, respectively.[42] Furthermore, 874 and 708 cm^{-1} bands related to torsion outside the plane of a carboxyl group and torsional vibrations of C-OH bonds, respectively. The FT-IR analysis suggested the presence of amino, hydroxyl and carboxylic/carbonyl moieties, strongly confirming the highly functionalized surface of the CQDs.

Zeta potential measurements were lastly carried out to provide further insights into chemical composition and structure of synthesized CQDs. CQDs exhibited a zeta potential of -14 mV (See Figure S9, ESI†), in good agreement with previous studies of stable

CQDs in colloidal solutions which further confirm the successful preparation of CQDs.

Conclusions

This contribution provides an unprecedented, effective and environmentally friendly valorization of a pulp and paper-derived lignocellulosic waste to fluorescent carbon dots (CQDs). The proposed microwave-assisted catalyzed approach could lead to the formation of small CQDs (17.5 nm) with unique physicochemical characteristics including steady-state and life-time fluorescence (□= 0.57 ns) and tunable emissions dependent on excitation wavelengths. Such unprecedented study may pave the way to further valorization of waste feedstocks to CQDs and similar photoactive nanomaterials with promising fluorescence behavior.

Associate content

Supporting Information

^{13}C-NMR spectrum of the residue, HR-TEM images of the residue treated in the absence of the solid acid catalyst, DRIFT spectrum of the obtained acid catalyst, TEM from obtained acid catalyst. Spectra of Fluorescence for CQDs at different reaction times: 30, 60 and 120 min. Conditions for the Quantum Yield measurements. XPS survey of CQDs. FT-IR spectrum of CQDs. Zeta potential of CQDs

Author information

Corresponding authors: Rafael Luque (q62alsor@uco.es) and M. Algarra (malgarra67@gmail.com).

Acknowledgments

Authors gratefully acknowledge funding from MINECO under CTQ2014-56422-P, CTQ2015-68951-C3-3R and CTQ2016-78289-P projects. R. Luque is also grateful for funding (project P10-FQM-6711) by Consejería

de Ciencia e Innovación, Junta de Andalucía. G. de Miguel also thanks the MINECO for a ‘‘RyC’’ contract (RYC-2013-12772). Funding from CESAM-Centre for Environmental and Marien studies, project POCI-01-0145-FEDER-007638 (FCT UID/AMB/50017/2013) from FCT/MEC using financial funds as well as FEDER co-financed (when appropriate) under PT2020 Partnership Agreement. M. Algarra is also grateful to ARDITI for financial support under M1420-01-0145-FEDER-000005-CQM+ project (Madeira 14-20).The publication has been prepared with support from RUDN University Program 5-100.

References

(1) Pokhrel, D.; Viraraghavan, T. Treatment of pulp and paper mill wastewater-a review. *Sci Total Environ*. **2004**, *333*(1), 37-58, DOI 10.1016/j.scitotenv.2004.05.017

(2) Kamali, M.; Khodaparast, K. Review on recent developments on pulp and paper mill wastewater treatment. *Ecotox. Environm. Safety*. **2015**, *114*, 326-342, DOI 10.1016/j.ecoenv.2014.05.005.

(3) Kamali, M.; Gameiro, T.; Costa, M. E. V.; Capela. I.; Anaerobic digestion of pulp and paper mill wastes. An overview of the developments and improvement opportunities. *Chem. Eng. J*. **2016**. *298*, 162-182, DOI 10.1016/j.cej.2016.03.119.

(4) CEPI-Confederation of European Paper Industries, www.cepi.org/, accessed on February 2017.

(5) ICFPA - International Council of Forest and Paper Associations (www.icfpa.org) accessed on February 2017

(6) CELPA-Portuguese Paper Industry Association (www.celpa.pt/en/factory-and-products) accessed on February 2017.

(7) Ashrafi, O.; Yerushalmi, L.; Haghighat, F. Wastewater treatment in the pulp-and-paper industry: A review of treatment processes and the associated

greenhouse gas emission. *J. Environ. Manage*. **2015**. *158*, 146-157, DOI 10.1016/j.jenvman.2015.05.010.

(8) R. C. E. Modolo, Valorization of solid wastes from cellulose and paper industry, PhD Thesis, University of Aveiro, Portugal. 2014.

(9) Monte, M.C.; Fuente, E.; Blanco, A.; Negro, C. Waste management from pulp and paper production in the European Union. *Waste Manage*. **2009**. *29*(1), 293-308, DOI 10.1016/j.wasman.2008.02.002.
(10) European List of Wastes, Commission Decision 2000/532/EC
(11) Council Directive 86/278/EEC of 12 June 1986 on the protection of the environment, and in particular of the soil, when sewage sludge is used in agriculture.
(12) Meyer, T.; Edwards, E.A. Anaerobic Digestion of Pulp and Paper Mill Wastewater and Sludge. *Water Res*. **2014**. *65*, 321-349, DOI 10.1016/j.watres.2014.07.022.
(13) Wang, T.L.; Wang, J.G.; Littlewood, J; Cheng, H.B. Co-production of biorefinery products from kraft paper sludge and agricultural residues: opportunities and challenges. *Green Chem*. **2014**, *16*(3), 1527-1533, DOI 10.1039/C3GC41984C.
(14) Calvo, A.I.; Tarelho, L.A.C.; Teixeira, E.R.; Alves, C.; Nunes, T.; Duarte, M.; Coz, E.; Custodio, D.; Castro, A.; Artiñano, B.; Fraile, R. Particulate emissions from the co-combustion of forest biomass and sewage sludge in a bubbling fluidised bed reactor. *Fuel Process. Technol*. **2013**, *114*, 58-68, DOI 10.1016/j.fuproc.2013.03.021.
(15) Ferreira, C.I.A.; Calisto, V.; Cuerda-Correa, E.M.; Otero, M.; Nadais, H.; Esteves, V.I. Comparative valorisation of agricultural and industrial biowastes by combustion and pyrolysis. *Bioresource Technol*. **2016**, *218*, 918-925, DOI 10.1016/j.biortech.2016.07.047.
(16) Jaria, G.; Silva, C.P.; Ferreira, C.I.A.; Otero, M.; Calisto, V. Sludge from paper mill effluent treatment as raw material to produce carbon adsorbents: An alternative waste management strategy. *J. Environ. Manag*. **2017**. *188*, 203-211, DOI 10.1016/j.jenvman.2016.12.004.
(17) Modolo, R.; Ferreira, V.M.; Machado, L.M.; Rodrigues, M.; Coelho, I. Construction materials as a waste management solution for cellulose sludge. *Waste Manage*. **2011**. *31*(2), 370-377, DOI 10.1016/j.wasman.2010.09.017.
(18) Lim, S.L.; Shen, W.; Gao, Z. Carbon quantum dots and their applications. *Chem. Soc. Rev*. **2015**, *44*(1), 362 381, DOI 10.1039/C4CS00269E.

(19) Alivisatos, A.P. Semiconductor Clusters, Nanocrystals, and Quantum Dots. *Science*. **1996**. *271*, 933-937, DOI 10.1126/science.271.5251.933.
(20) Lu, Q.; Wu, C.; Liu, D.; Wang, H.; Su, W.; Li, H.; Zhang, Y.; Yao, S. A facile and simple method for synthesis of graphene oxide quantum dots from black carbon. *Green Chem*. **2017**, *19*(4), 900-904, DOI 10.1039/C6GC03092K.
(21) Jiang, K.; Sun, S.; Zhang, L.; Lu, Y.; Wu, A.; Cai, C.; Lin, H. Red, Green, and Blue Luminescence by Carbon Dots: Full-Color Emission Tuning and Multicolor Cellular Imaging. *Angew. Chem. Int. Ed*. **2015**. *54*(18), 5360-5363, DOI 10.1002/anie.201501193.
(22) Campos, B.B.; Contreras-Cáceres, R.; Bandosz, T.J.; Jiménez-Jiménez, J.; Rodríguez-Castellón, E.; Esteves da Silva, J.C.G.; Algarra, M. Carbon dots as fluorescent sensor for detection of explosive nitrocompounds. *Carbon.* **2016**, *106*, 171-178, DOI, 10.1016/j.carbon.2016.05.030.
(23) Campos, B.B.; Moreno Oliva, M.; Contreras-Cáceres, R.; Rodriguez-Castellón, E.; Jiménez-Jiménez, J.; Esteves da Silva, J.C.G.; Algarra, M.. Carbon dots on based folic acid coated with PAMAM dendrimer as platform for Pt(IV) detection. *J. Colloid Interface Sci*. **2016**, *465*,165-173, DOI 10.1016/j.jcis.2015.11.059.
(24) Zhang, X.; Zhang, Y.; Wang, Y.; Kalytchuk, S.; Kershaw, S.V.; Wang, Y.; Wang, P.; Zhang, T.; Zhao, T.; Zhang, H.; Cui, T.; Wang, Y.; Zhao, J.; Yu, W.W.; Rogach, A.L. Color-Switchable Electroluminescence of Carbon Dot Light-Emitting Diodes. *ACS Nano.* **2013**, *18*, 11234-11241, DOI 10.1021/nn405017q.
(25) Alam, A.M.; Park, B.Y.; Ghouri, Z.K.; Park, M.; Kim, H.Y. Synthesis of carbon quantum dots from cabbage with down- and up-conversion photoluminescence properties: excellent imaging agent for biomedical applications. *Green Chem*. **2015**. *17*(7), 3791-3797, DOI 10.1039/C5GC00686D.
(26) Fernando, K.A.S.; Sahu, S.; Liu, Y.; Lewis, W.K.; Guliants, E.A.; Jafariyan, A.; Wang, P.; Bunker, C.E.; Sun, Y.P. Carbon quantum dots and applications in photocatalytic energy conversion. *ACS Appl. Mater. Interfaces.* **2015**. *7*, 8363-8376, DOI 10.1021/acsami.5b00448.

(27) Barman, M.K.; Jana, B.; Bhattacharyya, S.; Patra, A. Photophysical Properties of Doped Carbon Dots (N, P, and B) and Their Influence on Electron/Hole Transfer in Carbon Dots–Nickel (II) Phthalocyanine Conjugates. *J. Phys. Chem. C*. **2014**. *118*(34), 20034-20041, DOI 10.1021/jp507080c.

(28) Shi, Y.; Na, Y.; Su, T.; Li, L.; Yu, J.; Fan, R.; Yang, Y. Fluorescent Carbon Quantum Dots Incorporated into Dye-Sensitized TiO_2 Photoanodes with Dual Contributions. *Chem. Sus. Chem*. **2016**. *9*(12), 1498-1503, DOI 10.1002/cssc.201600067.

(29) Marinovic, A.; Kiat, L.S.; Dunn, S.; Titirici, M.M.; Briscone, J. Carbon-Nanodot Solar Cells from Renewable Precursors. *Chem. Sus. Chem*. **2017,** *10*(5), 1004-1013, DOI 10.1002/cssc.201601741.

(30) Hojaghan, H.S.; Niasari M.S. Degradation of methylene blue as a pollutant with N-doped graphene quantum dot/titanium dioxide nanocomposite. *J. Cleaner Prod*. **2017,** *148*, 31-36, DOI 10.1016/j.jclepro.2017.01.169.

(31) Ojeda, M.; Balu, A.M.; Barron, V.; Pineda, A.; Garcia, A.; Romero, A.; Luque, R. Solventless mechanochemical synthesis of magnetic functionalized catalytically active mesoporous SBA-15 nanocomposites. *J. Mater. Chem A,* **2014**. *2*(2), 387-393, DOI 10.1039/C3TA13564K.

(32) Pandey, S.; Mewada, A.; Oza, G.; Thakur, M.; Mishra, N.; Sharon, M. Synthesis and centrifugal separation of fluorescent carbon dots at room temperature. *Nanosci. Nanotech*. **2013**, *5*(7), 775-779, DOI 10.1166/nnl.2013.1617.

(33) Zhu, S.; Song, Y.; Zhao, X.; Shao, J.; Zhang, J.; Yang, B. The photoluminescence mechanism in carbon dots (graphene quantum dots, carbon nanodots, and polymer dots): current state and future perspective. *Nano Res*. **2015,** *8*(2), 355-381, DOI 10.1007/s12274-014-0644-3.

(34) Dhenadhayalan, N.; Lin, K.C.; Suresh, R.; Ramamurthy, P. Unravelling the Multiple Emissive States in Citric-Acid-Derived Carbon Dots. *J. Phys. Chem. C*. **2016**, *120*, 1252-1261, DOI 10.1021/acs.jpcc.5b08516.

(35) Algarra, M.; Pérez-Martín, M.; Cifuentes-Rueda, M.; Jiménez-Jiménez, J.; Esteves da Silva, J.C.G.; Bandosz, T.J.; Rodríguez-Castellón,

E.; López-Navarrete, J.T.; Casado, J. Carbon dots obtained using hydrothermal treatment of formaldehyde. Cell imaging in vitro. *Nanoscale*, **2014**, *6*(15), 9071-9077, DOI 10.1039/C4NR01585A.
(36) Kusová, K.; Pelant, I.; Valenta. Bright trions in direct-bandgap silico n nanocrystalsrevealed by low-temperature single-nanocrystalspectroscopy. *J. Light Sci. & Appl.* **2015**, *4*(10), e336 (1-8), DOI 10.1038/lsa.2015.109.
(37) Sun, Y. P.; Zhou, B.; Lin, Y.; Wang, W.; Fernando, K. S.; Pathak, P.; Luo, P. G. Quantum-sized carbon dots for bright and colorful photoluminescence. *JACS.* **2006**, *128*(24), 7756-7757, DOI 10.1021/ja062677d.
(38) Moulder, J.F.; Stickle, W.F.; Sobol, P.E.; Bomben, K.D. Handbook of X-ray photoelectron spectroscopy: a reference book of standard spectra for identification and interpretation of XPS data. Eds. Jill Chastain, and Roger C. King. Eden Prairie, Minnesota: Physical Electronics Division, Perkin-Elmer Corporation, **1992**.
(39) Zorn, G.; Liu L.H.; Arnadottir, L.; Wang, H.; Gamble, L.J.; Castner, D.G.; Yan, M. X-ray photoelectron spectroscopy investigation of the nitrogen species in photoactive perfluorophenylazide-modified. *J. Phys. Chem. C*. **2014**, *118*(1), 376-383, DOI 10.1021/jp409338y.
(40) Beamson, G.; Briggs, D. High Resolution XPS of Organic Polymers. Chichester: The Scienta ESCA300 Database, John Wiley and Son. **1992**.
(41) Di, J.; Xia, J.; Ge, Y.; Li, H.; Ji, H.; Xu, H.; Li, M. Novel visible-light-driven CQDs/Bi_2WO_6 hybrid materials with enhanced photocatalytic activity toward organic pollutants degradation and mechanism insight. *Appl. Catal. B Environ.* **2015**, *168*, 51-61, DOI 10.1016/j.apcatb.2014.11.057.
(42) Zhang, X.; Wang, F.; Huang, H.; Li, H.; Han, X.; Liu, Y.; Kang, Z. Carbon quantum dot sensitized TiO_2 nanotube arrays for photoelectrochemical hydrogen generation under visible light. *Nanoscale*, **2013**, *5*(6), 2274-2278, DOI 10.1039/C3NR34142A.

Supporting Information

Catalyzed microwave-assisted preparation of carbon quantum dots from lignocellulosic residues

Daily Rodríguez-Padrón,[a] Manuel Algarra,[b]*, Luis A.C. Tarelho[c], Jorge Frade,[d] Ana Franco,[a] Gustavo de Miguel,[e] José Jiménez-Jiménez,[b] Enrique Rodríguez-Castellón,[b] Rafael Luque[b]*

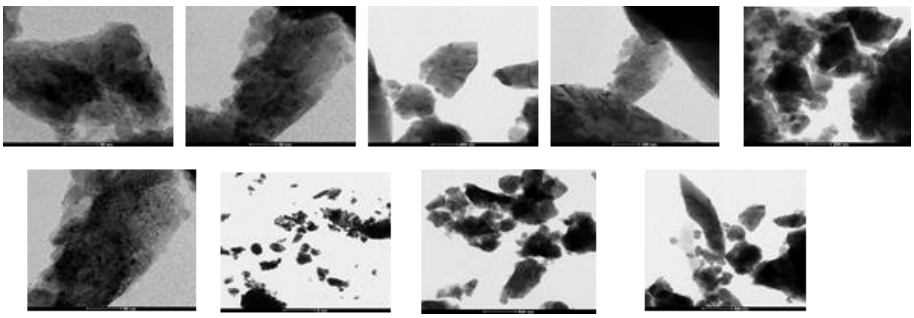

Figure S1. HR-TEM images of the residue treated in the absence of the solid acid catalyst.

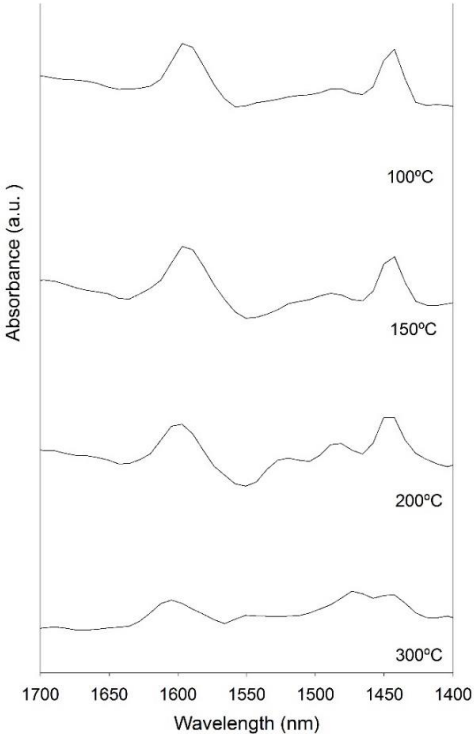

Figure S2. Drift-Py of the obtained acid catalyst.

The acidic properties of the obtained acid catalyst were studied by DRIFT experiments. In the spectrum the bands at 1440 and 1592 cm^{-1} appear, which indicate the peculiar Lewis acidity of this material. This material maintained a remarkable acidity, even at high temperatures (200 and 300 ºC), with visible acid centers distinguishable from noise. This behavior has a high value for acid catalyzed processes.

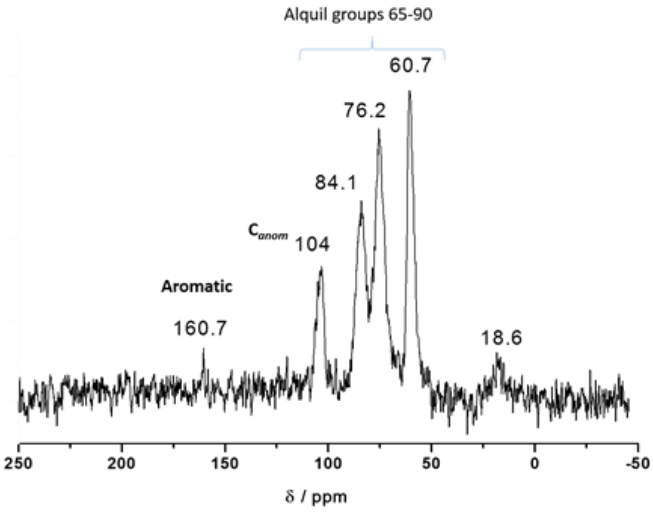

Figure S3. C^{13}-NMR spectrum of the residue.

Cápitulo 4

4. Mechanochemical synthesis of biomass-templated nanomaterials for energy storage and catalytic applications

4.1. Hypothesis

A wide range of materials have been reported to date, by using mechanochemical protocols and employing biomass residues as templates to control the resulting structure and morphology. The template method is an effective and simple strategy to obtain nanostructures with controlled textural and morphological characteristics. Most of the reported approaches in this sense consist of two steps, firstly, the desired materials or precursors assemble around the surface of a template via chemical or physical adherence to form transitional composites, and subsequently, the templates are selectively removed from the composite structures. If the template is fully converted to the desired materials, the method is called sacrificial template. Biomass waste can represent an alternative to the typical carbonaceous materials, resulting not just cheaper, but more effective catalytic systems with tunable properties.

4.2. Objectives

The preparation of several metal oxides, namely iron and titanium oxide, will be carried out following a mechanochemical strategy. Different biomass residues will be employed as sacrificial templates, including spent coffee grounds, egg-white from expired eggs and orange peel. Full characterization of the chemical, structural, textural and morphological features of the samples will be performed. The prepared materials will be employed for catalytic and energy storage applications. In particular, three catalytic reactions will be tested, namely 1) production of vanillin from isoeugenol, 2) synthesis of *N*-heterocycles from levulinic acid and 3) oxidation of diphenyl sulfide. Additional research related to the use of

biomass as sacrificial template and to the formation of N-heterocycles from levulinic acid have been included in Appendice 8.5-8.7.

4.3. Spent coffee grounds-templated magnetic nanocatalysts for mild oxidations

Mechanochemical protocols were employed for the preparation of a serie of iron oxide magnetic nanomaterials. Spent coffee grounds were used as sacrificial template, giving rise to controlled morphology and textural properties. It is worth to highlight that spent coffee grounds also confer magnetic characteristics to the synthesized materials, without using additional reagents in the synthetic process. The prepared materials were tested in the catalytic oxidation of isoeugenol to vanillin, under both conventional heating and microwave-assisted conditions. Remarkably, this work gave rise to a patent for the preparation of magnetic nanoparticles from spent coffee grounds, as can be observed in Appendix 8.8.

ACS Sustainable Chemistry & Engineering
Research Article
pubs.acs.org/journal/ascecg

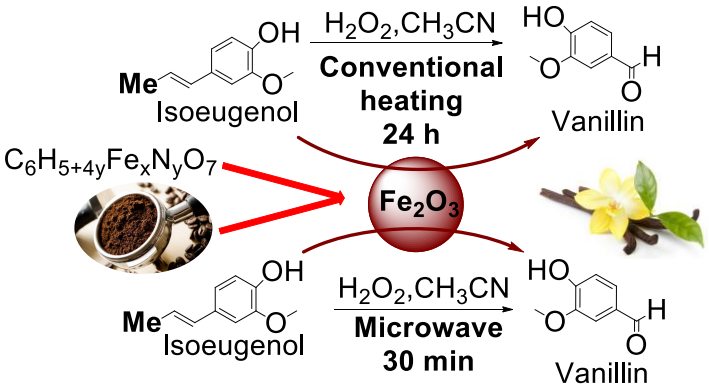

Daily Rodríguez-Padrón, Mario J. Muñoz-Batista, Hangkong Li, Kaimin Shih, Alina M. Balu, Antonio Pineda, Rafael Luque. **2019**. Spent coffee grounds-templated magnetic nanocatalysts for mild oxidations. *ACS Sustainable Chemistry & Engineering*. 10.1021/acssuschemeng.9b02919. IF: 6.14.

Spent coffee grounds-templated magnetic nanocatalysts for mild oxidations

Daily Rodríguez-Padrón,[a+] Mario J. Muñoz-Batista,[a+] Hangkong Li[b], Kaimin Shih[b], Alina M. Balu,[a*] Antonio Pineda,[a] and Rafael Luque[a,c*]

[a]*Departamento de Química Orgánica, Universidad de Córdoba, Campus de Rabanales, Edificio Marie Curie (C-3), Ctra Nnal IV-A, Km 396, E14014, Cordoba, Spain.* [*] *A.M.B. qo2balua@uco.es , R.L. rafael.luque@uco.es*

[b]*Department of Civil Engineering, Room 6-18A, Haking Wong Building, The University of Hong Kong, Pokfulam Road, Hong Kong,*

[c]*Peoples Friendship University of Russia (RUDN University), 6 Miklukho-Maklaya Str., 117198, Moscow, Russia*

[+]These authors contribute equally to this work

Environmental harmful effects of spent coffee in stream waters pushed our research group to find new applications for this waste material. A new family of magnetic nanocatalysts was synthesized, based on spent coffee grounds and ammonium iron (III) citrate as iron precursor via solvent-free mechanochemical milling followed by calcination at different temperatures. XRD data together with magnetic susceptibility measurements showed the unique properties of these materials, including the unprecedented presence of a maghemite phase at calcination temperatures as high as 800ºC. The work is completed with the help of a multiethnic characterization approach based on data obtained by N_2 physisorption, TEM-HRTEM, XPS and TGA thermogravimetric analysis. Considering the advantages related to magnetic features, mostly associated with the simple recovery and reuse, materials were tested in the catalytic oxidation of isoeugenol towards vanillin under both, conventional heating and microwave assisted conditions. Remarkably, a clear enhancement of the catalytic behaviour was observed by using microwave irradiation. The results evidenced that

hematite content could be a decisive factor to control the activity and selectivity of the reaction.

Keywords: Spent coffee grounds, biomass valorization, iron oxide, magnetic materials, heterogeneous catalysis, vanillin, isoeugenol oxidation.

Introduction

Caffeine is the constituent of many common household drinks including coffee, tea, and non-alcoholic beverages, suggested to be the most widely consumed drug in the world.[1] Coffee is one of the most famous caffeinated beverages to date, and its commercial importance has been growing steadily.[2,3] However, this popular drink generates a lot of waste that can result in deleterious effects to the environment.

Numerous studies have reported the presence of caffeine in wastewater treatment plant effluents,[4,5] surface water,[6] groundwater[7] and even in marine environments.[8–10] Moreover, the toxic effects of this drug in various bioorganisms have been broadly investigated. These studies show that many species appear to be quite tolerant to environmental levels of caffeine, however, current caffeine levels are approaching toxicity threshold for a few aquatic organisms.[11] Furthermore, previous studies on sea anemones showed that caffeine contributes to the problem of coral bleaching by causing the detachment of host cells from corals.[12] Thus, there is a vital need to find a proper utilization and industrial application for the caffeinated by-products (e.g. coffee).[13–17]

In this sense, waste valorization is an attractive alternative, which can offer several opportunities to harvest value from different types of residues.[18–20] In fact, food waste components could lead to numerous possibilities for the production of added value chemicals, fuels and materials with a wide range of applications.[17,20,21]

Two routes for biomass valorization have been explored, namely, 1) the valorization of spent coffee to obtain magnetic nanomaterials with catalytic applications and 2) the valorization of isoeugenol, a biomass-

derived platform molecule, by means of its oxidation to vanillin, catalyzed by biomass-templated (spent coffee ground-templated) magnetic nanocatalysts.

Particularly, magnetic nanoparticles have been greatly studied due to their textural and morphological properties as well as their simple recovery and manipulation.[22–26] The unique functional surface of magnetic nanoentities also could allow the immobilization of homogeneous species including metals, organoligands/organocatalysts, N-heterocyclic carbenes and biomolecules. This behavior has opened exciting opportunities in many areas such as catalysis, biotechnology,[27,28] biosensing[29–31] and biomedicine.[32,33] Advanced magnetic systems have been developed by using several synthetic approaches. In this sense, mechanochemistry is a highly promising and simple methodology, since it does not require the use of solvents, avoiding environmental problems related to their toxicity and use thereof.[25,34–39]

Although the use of mechanochemistry itself already represents a sustainable option to the conventional methods in solution, most of the mechanochemicals methods reported in the literature for the preparation of magnetic iron oxide employ propionic acid and/or related templating/reducing agents to generate the magnetic phase (magnetite/maghemite).[35,40–46] Such reagents together with the iron salt results in the formation of an iron carboxylate compound, followed by calcination to generate the magnetic iron oxide crystalline phase. Nonetheless, propionic acid is an expensive reagent and not particularly environmentally friendly (reported to affect plants by decreasing their resistance and vigour and even by possibly inducing their die-back).[47] Herein, our research group proposes the use of spent coffee grounds as both sacrificial template and replacement of propionic acid for the preparation of iron oxide nanoparticles with magnetic properties.

Iron oxide-based nanomaterials possess great applications in catalysis and, specially, have been broadly employed in the oxidation of isoeugenol to vanillin. Valorization of isoeugenol has greatly attracted the interest of the scientific community in the past years, since it can replace traditional feedstocks for the production of vanillin such as guaiacol and glyoxylic

acid, which are petrol-based intermediates. Hence, in this work spent coffee ground-templated magnetic nanocatalysts have been successfully employed in the catalytic oxidation of isoeugenol to vanillin with promising results.

Experimental part

Synthesis of magnetic nanomaterials based on iron oxide and spent coffee

A mechanochemical methodology was employed for the preparation of the nanonocomposites, due to its advantages in terms of simplicity, cleaning and environmental benignity (Scheme 1). Six materials, based on iron oxide and spent coffee, were synthesized using a ratio 2:1 spent coffee/metal precursor (ammonium iron (III) citrate: $C_6H_8O_7xFe_3{}^{+}yNH_3$), in a ball mill (Retsch PM100 ball mill model), at 350 rpm for 10 min. Subsequently, the materials were oven dried at 100 °C for 24 h, and finally calcined in N_2 atmosphere at temperatures between 300 and 800 ºC.[48]

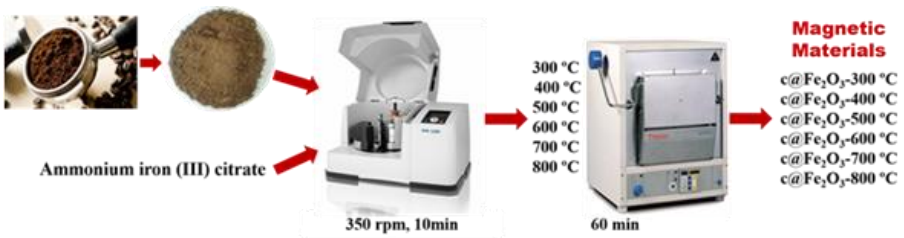

Scheme 1. Overview of the synthetic strategy of $c@Fe_2O_3$ nanocatalysts.

Material Characterization

The synthesized materials were characterized by several techniques, including Thermogravimetric Analysis (TGA), X-ray Diffraction (XRD), N_2 physisorption, X-ray Photoelectronic Spectroscopy (XPS) and Transmission Electronic Microscopy (TEM). Moreover, magnetic susceptibility of the six prepared materials was measured.

Thermogravimetric analysis was accomplished by simultaneous TG-DTA measurement using the System Setaram Setsys 12 TGA instrument.

Samples were heated at a rate of 10 °C min^{-1}, in nitrogen atmosphere (40 mL min^{-1}) at the temperature range 50–1000 °C.
The X-ray powder diffraction data were collected using the D8 Advanced Diffractometer (Bruker AXS) with the Lynxeye detector, which operated at 40 kV and 40 mA with Cu Kα radiation at room temperature. The 2θ scan range was from 10° to 80°, with a step size of 0.02°, a counting time of 0.2 seconds for phase identification and 1 second for phase quantification. Phase identifications were conducted using the Bruker Diffrac-plus EVA software, supported by the Powder Diffraction File (PDF) database of the International Centre for Diffraction Data (ICDD). The QXRD analysis was carried out with TOPAS 4.2 software (Bruker AXS GmbH, Germany).
Nitrogen adsorption measurements were carried out at the temperature of liquid nitrogen (77 K) in the Micromeritics ASAP 2000 instrument. The samples were degassed for 24 h at 140 ºC under vacuum ($p<10^{-2}$ Pa) and subsequently analyzed. The linear part of the BET equation ($0.05<P_0<0.22$) was used to calculate the specific surface area. The pore size distribution was obtained from the desorption branch of the N_2 physisorption isotherms and the Barret–Joyner–Halenda (BJH) formula.
XPS experiments were accomplished in an ultrahigh vacuum multipurpose surface analysis instrument SpecsTM. The samples were evacuated overnight under vacuum (10^{-6} Torr) and subsequently, measurements were performed at room temperature using a conventional X-ray source with a Phoibos 150-MCD energy detector. XPS spectra were analyzed employing the XPS CASA software.
The morphology of the samples was examined by Transmission Electron Microscopy (TEM) and high-resolution TEM (HRTEM) using a Field Emission Electron Microscope STEM (JEOL Model JEM-2100F). The magnetic susceptibility of the six nanomaterials was determined at room temperature and at low frequency (470 Hz), using the Bartington MS-2 instrument.

The surface acidity of the materials was determined by pyridine (PY) and 2,6-dimethylpyridine (DMPY) titration experiments. The analysis was carried out using 25 mg of the catalysts, at 300 °C, via gas phase

adsorption. Cyclohexane solutions of probe molecules (0.989 M of PY and 0.686 M of DMPY) were, respectively, injected into a gas chromatograph through a microreactor in which the catalyst was previously placed. Results were analyzed by gas chromatography with a flame ionization detector (FID) and using an analytical column of 0.5 m length, containing 5 wt % of polyphenylether in the Chromosorb AW-DMCS in 80/100. Particularly, pyridine adsorbs nonspecifically in both types of centers, namely Lewis and Brønsted acid centers, as expected due to its low steric hindrance. In turn, dimethyl-pyridine, which possess a high steric hindrance associated with the methyl groups, adsorbs only on Brønsted acid centers. Thus, the difference between the amounts of PY (total acidity) and DMPY (Brønsted acidity) adsorbed should correspond to Lewis acidity in the materials.

Catalytic experiments

The catalytic oxidation of isoeugenol to vanillin was performed in a multiple parallel synthesis system (Carrusel Reaction Station), using 0.8 mL of isoeugenol, 1.2 mL of H_2O_2, 8 mL of acetonitrile and 0.1 g of the previously synthesized magnetic nanocatalysts.[49] The reaction mixture was stirred at 90 °C for 24 h. Oxidation of isoeugenol was additionally tested using 0.2 mL of isoeugenol, 0.3 mL of H_2O_2, 2 mL of acetonitrile and 0.025 g of catalyst in the CEM-Discover microwave reactor, equipped with a PC-controlled interface. The reaction mixture was stirred for 10 and 30 min, respectively, employing a Power of 300 W.

Reusability studies were carried out by recovering the catalysts and repeating the reaction using the same operating conditions, previously described for conventional heating oxidation of isoeugenol.[50]

Samples from the reactions were characterized by Gas Chromatography in an Agilent 6890N gas chromatograph (60 mL min^{-1} N_2 carrier flow, 20 psi column top head pressure) using a flame ionization detector (FID) and a capillary column Petrocol 100 m x 0.25 nm x 0.5 μm.

Results and discussion

Valorization of spent coffee grounds towards magnetic nanomaterials through a solvent-free mechanochemical strategy was successfully achieved. Coffee residues were employed as sacrificial template, allowing the formation of nanostructured iron oxide by chemical and/or physical adherence of the iron precursor around the surface of the aforementioned waste. The iron salt, in this case ammonium iron (III) citrate is hydrolyzed during the milling process to give rise to iron hydroxide, which is subsequently transformed into the corresponding oxide by a thermal treatment.

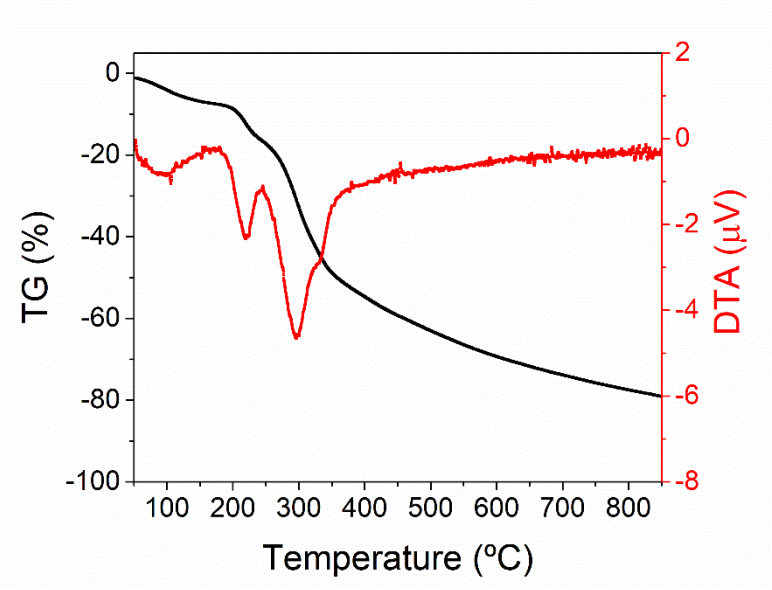

Figure 1. TG and DTA analysis of spent coffee and ammonium iron (III) citrate, after the milling process.

Thermogravimetric analysis of the mixture (spent coffee grounds and ammonium iron (III) citrate), obtained from the mechanochemical step, was performed in order to investigate the desorption-calcination of the parent materials (Figure 1). The first progressive weight loss of ca. 10 wt % from 100 to 200 ºC (endothermic-DTA signal) was observed, most

likely related to the presence of water in the material. From ca. 250 ºC, a progressive but more pronounced weight loss was noticed, which can be assigned to the combustion-desorption of carbonaceous species. Accordingly, DTA experiments exhibited two exothermic signals at 166 and 242 ºC. After heating up to 800 ºC, a weight loss of ca. 77% was displayed, being in good agreement with the expected result considering the ratio 2:1 spent coffee/metal precursor. Such data suggested that after calcination at 800 ºC almost not remaining carbonaceous species were present in the material.

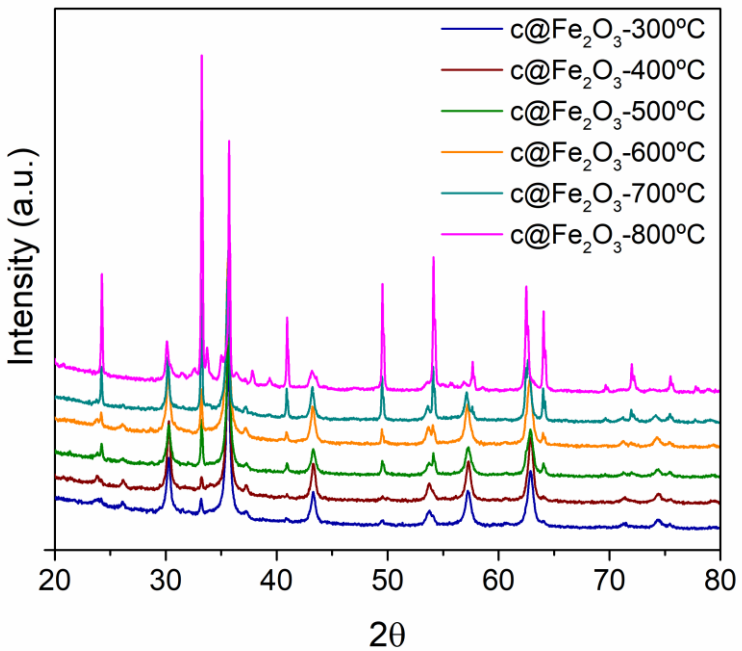

Figure 2. X-ray diffraction patterns of c@Fe_2O_3 nanocatalysts.

The structure and arrangement of the six magnetic nanocomposites have been investigated by X-ray Diffraction analysis. All the samples can be indexed to two phases, namely: maghemite and hematite (Fe_2O_3), with a clear increase of the hematite phase by increasing the calcination temperature, as well as a slight increment of the crystallinity (Figure 2).

Particularly, the diffraction peaks at 2θ = 33.2º, 40.9º, 49.5°, 54.1° and 64.1º correspond to (104), (113), (024), (116) and (300) crystallographic planes of hematite phase, respectively.[18,51] The clear increment of the aforementioned peaks confirmed the increase of hematite phase with the calcination temperature (from 300 ºC to 800 ºC). Nonetheless and interestingly, after increasing the temperature even to 800 ºC, certain maghemite phase was still present in the sample, resulting in materials that combine both, remarkable magnetic properties and good catalytic potentiality (since the hematite phase has been reported as most active phase of iron oxide for oxidation reactions).[18,38,51]

Phase quantification was applied to investigate the content of these two phases in each sample (Table 1). As expected, hematite phase content increased from 4.9% to 38.3% by increasing the temperature from 300 ºC to 800 ºC, with the consequent decrease of the maghemite content. Crystal size of both phases was, as well, determined. It was observed an increment of the crystal size for the hematite phase at higher calcination temperatures. In turn, maghemite particle size remains stable, with values variating between 15 and 20 nm.

Table 1. Phase quantification, crystal size and magnetic susceptibility of c@Fe_2O_3 nanocatalysts.

Sample	%wt. Hematite	Size Hematite (nm)	%wt. Maghemite	Size Maghemite (nm)	Magnetic susceptibility (10^{-6} m^3Kg^{-1})
c@Fe_2O_3-300 ºC	4.9	69.3	95.1	15.2	254
c@Fe_2O_3-400 ºC	4.5	57.2	95.5	18.6	203
c@Fe_2O_3-500 ºC	5.2	78.5	94.8	14.7	219
c@Fe_2O_3-600 ºC	10.1	78.0	89.9	15.6	182
c@Fe_2O_3-700 ºC	33.0	114.5	67.0	20.0	166
c@Fe_2O_3-800 ºC	38.3	115.5	62.7	18.9	125

The data of magnetic susceptibility are in strong agreement with the aforementioned XRD results for the synthesized materials and assert their magnetic characteristics. Such values give to these materials attractive features for magnetic separation. As expected, the magnetic susceptibility decreased with the increment of the calcination temperature, but nevertheless it is noticeable that even after calcination at 800 ºC, the material preserved its magnetic characteristics.

Textural properties of synthesized nanomaterials have been investigated with N_2 physi-sorption analysis and the results are included in Table 2. The analyzed materials displayed certain mesoporosity, with pore sizes ranging from 15 to 22 nm and pore volumes around 0.10 $cm^3\ g^{-1}$. Accordingly, adsorption-desorption isotherms of the six samples resulted to be type IV, as can be observed in Figure S1, corresponding with mesoporous-type materials. As expected, c@Fe_2O_3-300 ^oC nanomaterial exhibited the highest surface area value (22 $m^2\ g^{-1}$), with a gradual decrease of this observable for the materials prepared at higher calcination temperatures, also associated with the increment of crystallinity.

Table 2 Textural properties of c@Fe_2O_3 nanomaterials.

Sample	S_{BET} ($m^2\ g^{-1}$)[a]	V_{BJH} ($cm^3\ g^{-1}$)[b]	d_{BJH} (nm)[c]
c@Fe_2O_3-300 ^oC	22	0.09	15
c@Fe_2O_3-400 ^oC	16	0.11	22
c@Fe_2O_3-500 ^oC	15	0.11	21
c@Fe_2O_3-600 ^oC	14	0.08	18
c@Fe_2O_3-700 ^oC	10	0.14	29
c@Fe_2O_3-800 ^oC	<10	0.12	25

[a]S_{BET}: specific surface area was calculated by the Brunauer-Emmett-Teller (BET) equation. [b] V_{BJH}: pore volumes were calculated by the Barret-Joyner-Halenda (BJH) equation using the adsorption branch of the isotherm. [c] d_{BJH}: mean pore size diameter was calculated by the Barret-Joyner-Halenda (BJH) equation, using the desorption branch of the isotherm.

The morphology of the synthesized materials was studied using both, TEM and HRTEM analysis. TEM (A) and HRTEM (B) images of a representative sample, namely c@Fe_2O_3-700 ºC, are shown in Figure 3. TEM micrographs of the samples displayed the presence of homogeneous quasi-spherical nanoparticles (Figure 3A). HRTEM technique allows the determination of the periodic fringe spacing of crystallographic planes of iron oxide (Figure 3B). Although, periodic fringe spacing of 0.2559 nm is similar for both, {311} plane of γ-Fe_2O_3 and {110} plane of α-Fe_2O_3,[52,53] the periodic fringe spacing of 0.4865 nm agrees well with the d-spacing related to {111} plane of γ-Fe_2O_3.[53] Such result is in accordance with XRD data, confirming the presence of maghemite phase in the materials, even at high calcination temperatures.

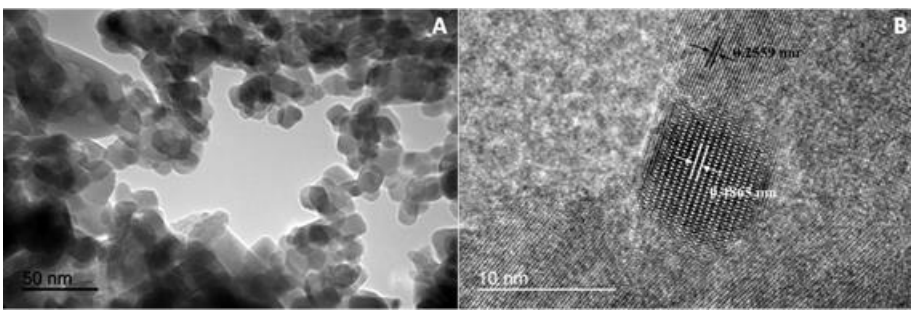

Figure 3. Representative (A) TEM and (B) HRTEM images of c@Fe_2O_3 nanocatalysts (c@Fe_2O_3-700 ºC).

The chemical environment of the samples, as well as superficial elemental quantification, were obtained with the help of the X-ray photoelectron spectroscopy. Figure 4 displays the spectra and fitting analysis of Fe2p XPS region of c@Fe_2O_3 series. No significant differences were observed

between the samples, which describe the typical spectra of Fe_2O_3 with a reference peak Fe2p $_{3/2}$ located at ca. 710.5 eV (Table 3).[54,55] These results also confirm that the magnetic properties are generated by the presence of a maghemite phase. In Table 3 we also included information concerning the reference position of O1s and C1s XPS region. O1s showed a slight sift associated with the content of maghemite and hematite in the structure. Higher binding energy can be related to higher maghemite/hematite concentration ratio. Such results can be explained considering that maghemite has lower electron density of the oxygen atoms of the surface hydroxyl groups in comparison with hematite.[56] Also interesting are the measured difference in the Fe/C ratio. As described in Table 3, the ratio Fe/C increase with the calcination temperature employed during the synthesis. This marked difference is associated with the synthetic protocol, which allows obtaining cleaner surfaces of residual carbon by elimination of the sacrificial template.

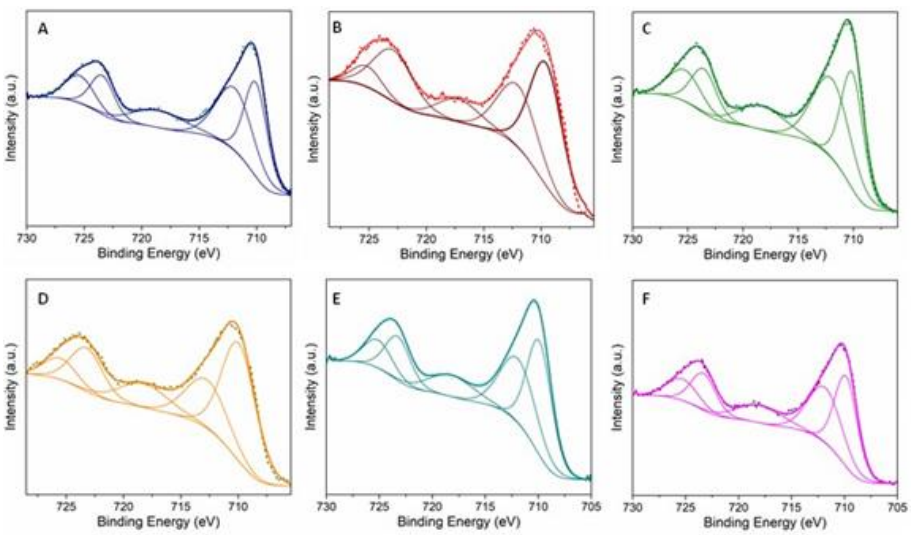

Figure 4. Deconvoluted XPS spectra in Fe2p region of c@Fe_2O_3 nanocatalysts. (A) c@Fe_2O_3-300 ^{o}C, (B) c@Fe_2O_3-400 ^{o}C, (C) c@Fe_2O_3-500 ^{o}C, (D) c@Fe_2O_3-600 ^{o}C, (E) c@Fe_2O_3-700 ^{o}C, (F) c@Fe_2O_3-800 ^{o}C.

Table 3. XPS binding energies and Fe/C atomic ratio.

Sample	Fe $2p_{3/2}$ (eV)	C 1s (eV)	O 1s (eV)	Fe/C
c@Fe_2O_3-300 ºC	710.5	284.6	530.8	0.13
c@Fe_2O_3-400 ºC	710.3	284.6	530.9	0.50
c@Fe_2O_3-500 ºC	710.6	284.6	530.7	0.78
c@Fe_2O_3-600 ºC	710.4	284.6	529.9	0.89
c@Fe_2O_3-700 ºC	710.5	284.6	530.1	1.11
c@Fe_2O_3-800 ºC	710.3	284.6	529.8	1.20

Catalytic measurements: conventional heating and microwave-assisted reactions

As aforementioned, applicability of the samples was analysed during selective production of vanillin from isoeugenol (Scheme 2).

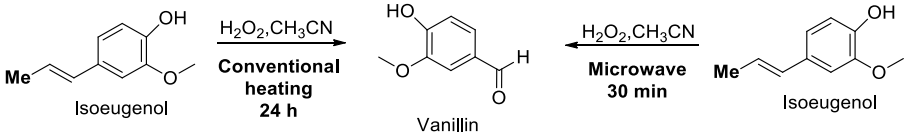

Scheme 2. Reaction scheme under conventional heating and microwave irradiation condition.

Evaluation of the catalytic properties was thus evaluated using conversion (X) and vanillin selectivity (S) as is described in Figure 5A. In this case, the first thing that must be highlighted is that all samples show activity under experimental conditions used. Obtained data describe a mild decrease of the conversion up to sample c-Fe_2O_3-500 ºC, with a subsequent strong enhancement of this observable which shows maximum values (ca. 51 %) for the samples calcinated at 700-800 ºC.

Importantly, the enhancement factors (2.6 and 3.5 for c-Fe_2O_3-300 ºC and c-Fe_2O_3-700 ºC, respectively) are clearly competitive with the commercial iron oxide (Fe_2O_3-comm) (29 %), as well as with the commercial magnetite (Fe_3O_4-comm) (26%), here used as references. On the other hand, the carbonaceous structure obtained by calcination at 300 ºC of spent coffee showed null activity. As described in XRD analysis, the enhancement of calcination temperature drives as expected to higher crystallinity and hematite concentration, which can be strongly correlated (assuming a constant structural interaction situation between hematite and maghemite) with the enhancement of the activity (Figure 5B). In fact, two groups can be easily separated. Figure 5B shows that materials synthesized at 300-600 ºC (grey line) produce relatively small quantities of Hematite (below 12 wt.%), which generates relative low conversions (below 37 %), while larger amounts of Hematite (black line) can be correlated with higher value of conversion (above 50 %). Such effect has been previously reported, confirming hematite as the main catalytically active phase of iron oxide for this reaction.[18]

Even though, the data of Figure 5A agree with all previous works in the fact that the most active composite sample contains higher hematite amount in the structure,[18,38,51] the c@Fe_2O_3 series behaviour is in relative opposition to previously electron-rich effects or enhancement of a positive charge handling associated with carbon-related entities.[18,37,57–59] Our carbonaceous coffee waste-derived material would not be presenting the electrons at defective sites, which are usually related with active sites for oxidation reactions, taking into account that maximum activity was obtained when residual carbon of the template is almost removed (See TGA presented in Figure 1). In addition, vanillin selectivity showed a similar behaviour (Figure 5A), with a sharp maximum, according to standard errors, for samples c-Fe_2O_3-700 ºC and c-Fe_2O_3-800 ºC as well. Interpretation of selectivity is a relative complex task during isoeugenol oxidation reaction. Besides vanillin, production of eugenol, diphenyl ether as well as others products such as dihydrodiisoeugenol can be formed.[18,37,38] In our case, the other major product can be associated with the production of diphenyl ether. Increasing production of vanillin is

typically associated with an enhancement of the acidity,[51] however, according to data presented in Table S1 of the supporting information, this observable would not be defining the catalytic properties of the samples. The acidity properties describe in Table S1 are in accordance with previous reports in which is discussed the reason of the higher acidity of maghemite in comparison with hematite. Such results are also related to the shift of O1s detected by XPS (Table 2). The partial charge of the oxygen atoms of maghemite should be less than hematite, provoking the higher acidity of samples with higher content of maghemite.[60] Such results reinforce the idea that optimization of the reaction may be directly related to the effect of an active hematite phase and contribution of maghemite is not decisive for the catalytic response while mainly provide the desired magnetic properties.

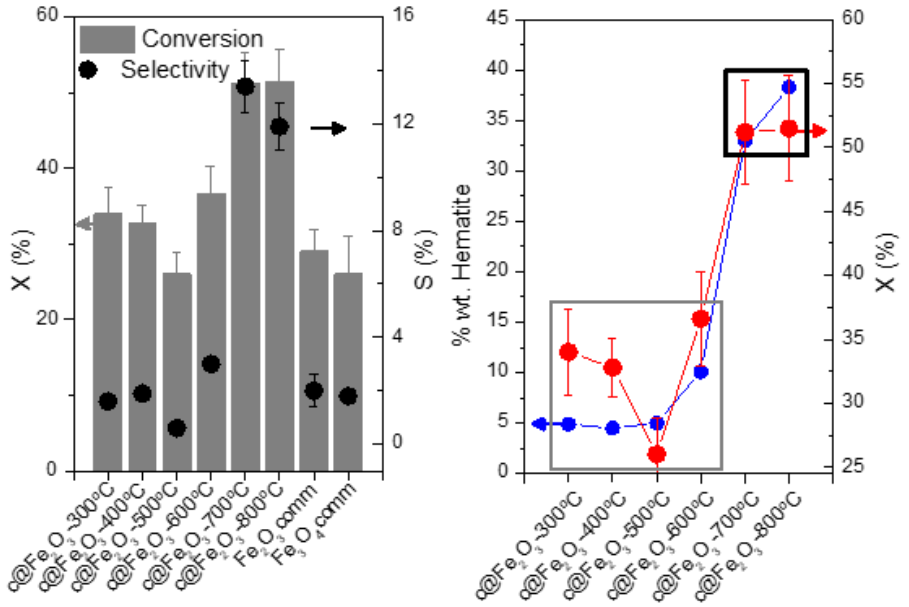

Figure 5. (A) Conversion (X) and vanillin selectivity (S) under conventional heating condition and (B) Plot showing the correlation between activity and hematite concentration.

The enhancement of hematite particle size from ca. 70 nm for samples calcinated below 600 ºC, to ca. 115 nm for samples c@Fe_2O_3-(700-800) ºC has been shown detrimental of activity,[61,62] usually discussed in terms of a gradually decreasing of surface area associated to the thermal recrystallization of primarily formed hematite nanoparticles.[63] However, in our case, the growth of hematite crystal size seems to be beneficial, since the active phase is more accessible for the adsorption of isoeugenol (Table 1). On the other hand, as higher activity was obtained for highly crystallised samples, the beneficial effect of electron transfer could be also mentioned as a secondary positive factor.

With the aim to improve the efficiency of vanillin production, a microwave-assisted oxidation reaction was carried out (Figure 6).[50] As has been described in previous contributions, microwave-assisted approach has several advantages over conventional heating, since microwave allows the enhancement of reaction rate, providing a more uniform temperature, different reactions pathways and improvement of the efficiency of active sites in the catalytic material.[64–66]

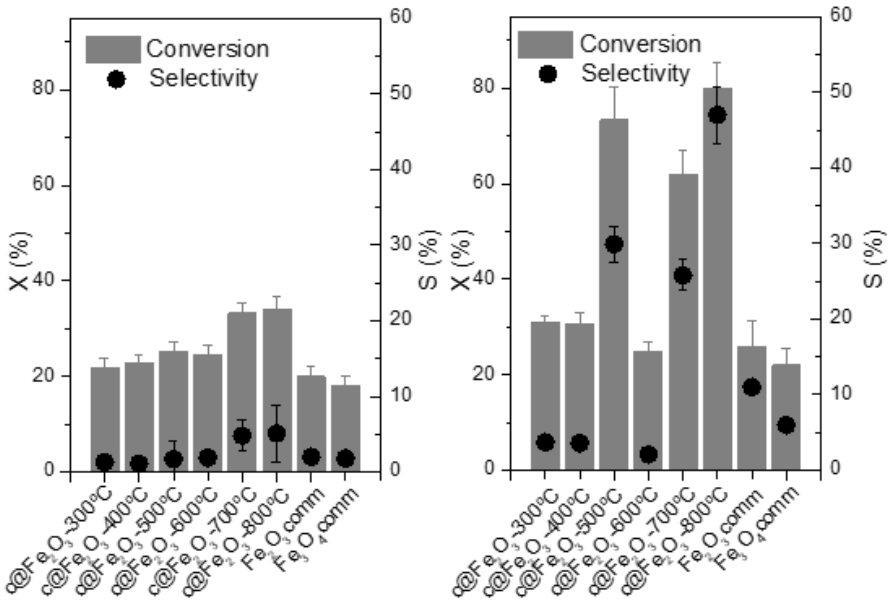

Figure 6. Conversion and vanillin selectivity under microwave

irradiation conditions. (A) After 10 min of reaction and (B) after 30 min of reaction.

Figure 6A and 6B show the obtained conversion and selectivity after 10 and 30 min of reaction, respectively. The experimental results describe a similar train behaviour to those obtained under conventional heating, where optimum conversion value was obtained for the sample with the highest hematite content (Table 1 and Figure 5B). After 10 min of reaction, it is already possible to measure conversions of ca. 26% for samples c-Fe_2O_3-700 ^oC and c-Fe_2O_3-800 ^oC, while outstanding activity values, above 80% of conversion was obtained using the sample calcinated at 800 ^oC. As well, commercial references, Fe_2O_3-comm and Fe_3O_4-comm displayed lower conversion and selectivity values. Such situation can be extended to the interpretation of the selectivity data of Figure 6B (higher vanillin selectivity for samples synthesized at higher calcination temperatures).

Recycling stability of the samples under experimental conditions is a key criterion for assessing its applicability. Thus, the re-utilization of two representative samples (c-Fe_2O_3-300 ^oC and c-Fe_2O_3-700 ^oC) was examined by three consecutive runs under the same conditions, as is described in the experimental section.

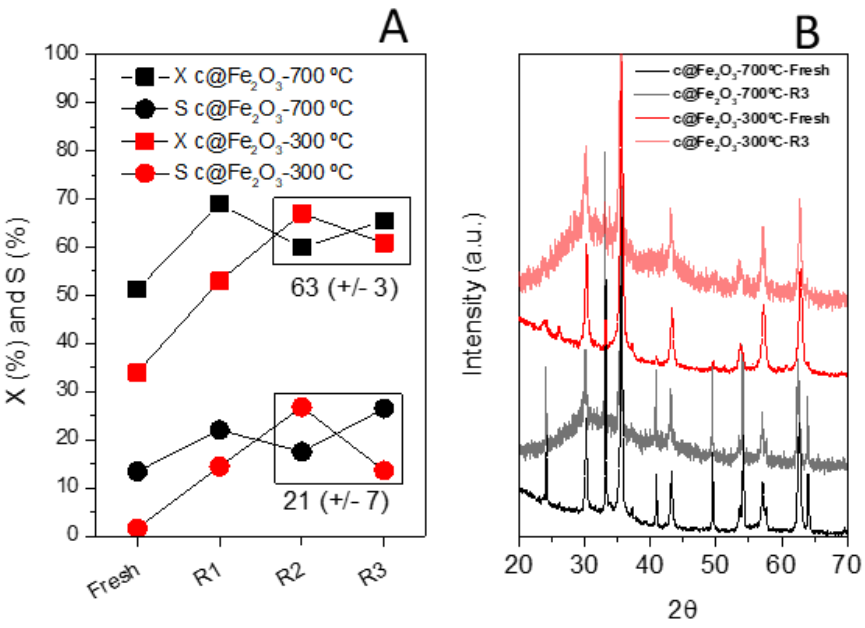

Figure 7. (A) Recycling experiments of c@Fe_2O_3-700 ºC (black) and c@Fe_2O_3-300 ºC (red) samples. (B) XRD spectra of fresh and spent (after cycle 3: R3) materials.

As can be seen in Figure 7A, after the first cycle (R1), both samples showed an enhancement of the activity and selectivity, which is maintained during cycles 2 and 3 (R2 and R3). In fact, advantageously, the strong increase of the activity of sample synthesized at 300 ºC (c-Fe_2O_3-300 ºC), by at least a factor of ca. 1.3, make it competitive respect to the samples calcinated at 700 ºC. These results can be understood in term of an in-situ amorphization of the samples during the reaction (Figure 7B). In several instances, the catalytic performance of amorphous phases was demonstrably superior in comparison with their crystalline counterparts, due in part to their greater flexibility,[67] which, as demonstrated using Fe_2O_3-containing nanomaterials, could possibly reduce the high binding energy of the Fe–O bond in the Fe_2O_3 structure, therefore making them more reactive in the oxidation process.[68] In addition, the results

suggested that no considerable iron leaching was occurring during the reaction processes.

Conclusions

The contribution presents a series of new magnetic iron oxide nanocatalysts obtained using coffee waste as a sacrificial template by a solvent-free mechanochemistry protocol. Samples maintained its magnetic properties thought all calcination range, which allows obtaining a highly active catalyst for the selective production of vanillin from isoeugenol under conventional heating and microwave-assisted reactions. Optimum activity and vanillin selectivity were defined, according to a complete characterization approach, by a well-defined hematite structure, free of carbonaceous superficial entities. Interestingly, the magnetic effects are maintained at very high calcination temperature driving a remarkable crystalized iron oxide structure. Samples with higher content of hematite outperform pure Fe_2O_3 commercial reference under both experimental conditions. The study was also able to demonstrate that an *in-situ* amorphization occurs during the oxidation reaction, which could make the iron oxide crystal more flexible and therefore more catalytically active in the selective generation of vanillin.

Conflicts of interest

There are no conflicts to declare.

Acknowledgements

Rafael Luque gratefully acknowledges MINECO for funding project CTQ2016-78289-P, co-financed with FEDER funds. Daily Rodriguez-Padron also gratefully acknowledges MINECO for providing a research contract under the same project. M. J. Muñoz-Batista acknowledges MINECO for a Juan de la Cierva postdoctoral contract (ref. FJCI-2016-

29014). The publication has been prepared with support from RUDN University, Program 5-100.

References

(1) Loomis, D.; Guyton, K. Z.; Grosse, Y.; Lauby-Secretan, B.; El Ghissassi, F.; Bouvard, V.; Benbrahim-Tallaa, L.; Guha, N.; Mattock, H.; Straif, K.; et al. Carcinogenicity of Drinking Coffee, Mate, and Very Hot Beverages. *Lancet. Oncol.* **2016**, *17* (7), 877–878. https://doi.org/10.1016/S1470-2045(16)30239-X.

(2) Murthy, P. S.; Madhava Naidu, M. Sustainable Management of Coffee Industry By-Products and Value Addition—A Review. *Resour. Conserv. Recycl.* **2012**, *66*, 45–58. https://doi.org/10.1016/J.RESCONREC.2012.06.005.

(3) Reissig, C. J.; Strain, E. C.; Griffiths, R. R. Caffeinated Energy Drinks—A Growing Problem. *Drug Alcohol Depend.* **2009**, *99* (1–3), 1–10. https://doi.org/10.1016/J.DRUGALCDEP.2008.08.001.

(4) Comeau, F.; Surette, C.; Brun, G. L.; Losier, R. The Occurrence of Acidic Drugs and Caffeine in Sewage Effluents and Receiving Waters from Three Coastal Watersheds in Atlantic Canada. *Sci. Total Environ.* **2008**, *396* (2–3), 132–146. https://doi.org/10.1016/j.scitotenv.2008.02.031.

(5) Spongberg, A.; Witter, J. Pharmaceutical Compounds in the Wastewater Process Stream in Northwest Ohio. *Sci. Total Environ.* **2008**, *397* (1–3), 148–157. https://doi.org/10.1016/J.SCITOTENV.2008.02.042.

(6) Buerge, I. J.; Thomas Poiger; Müller, M. D.; Buser, H.-R. Caffeine, an Anthropogenic Marker for Wastewater Contamination of Surface Waters. *Environ. Sci. Technol.* **2003**, *37*, 691–700. https://doi.org/10.1021/ES020125Z.

(7) Buszka, P. M.; Yeskis, D. J.; Kolpin, D. W.; Furlong, E. T.; Zaugg, S. D.; Meyer, M. T. Waste-Indicator and Pharmaceutical Compounds in Landfill-Leachate-Affected Ground Water near Elkhart, Indiana, 2000–2002. *Bull. Environ. Contam. Toxicol.* **2009**, *82* (6), 653–659. https://doi.org/10.1007/s00128-009-9702-z.

(8) Siegener, R.; Chen, R. F. Caffeine in Boston Harbor Seawater. *Mar. Pollut. Bull.* **2002**, *44* (5), 383–387. https://doi.org/10.1016/S0025-326X(00)00176-4.

(9) Weigel, S.; Kuhlmann, J.; Hühnerfuss, H. Drugs and Personal Care Products as Ubiquitous Pollutants: Occurrence and Distribution of Clofibric Acid, Caffeine and DEET in the North Sea. *Sci. Total Environ.* **2002**, *295* (1–3), 131–141. https://doi.org/10.1016/S0048-9697(02)00064-5.

(10) Weigel, S.; Berger, U.; Jensen, E.; Kallenborn, R.; Thoresen, H.; Hühnerfuss, H. Determination of Selected Pharmaceuticals and Caffeine in Sewage and Seawater from Tromsø/Norway with Emphasis on Ibuprofen and Its Metabolites. *Chemosphere* **2004**, *56* (6), 583–592. https://doi.org/10.1016/J.CHEMOSPHERE.2004.04.015.

(11) Katz, D., M.; Cantwell; Sullivan., J. Caffeine in an Urbanized Estuary: Past and Present Influence of Wastewater Effluents in Boston Harbor. In *Society of Environmental Toxicology and Chemistry (SETAC)*; 2016.

(12) Pollack, K.; Balazs, K.; Ogunseitan, O. Proteomic Assessment of Caffeine Effects on Coral Symbionts. *Environ. Sci. Technol.* **2009**, *43* (6), 2085–2091. https://doi.org/10.1021/es802617f.

(13) Campos-Vega, R.; Loarca-Piña, G.; Vergara-Castañeda, H. A.; Oomah, B. D. Spent Coffee Grounds: A Review on Current Research and Future Prospects. *Trends Food Sci. Technol.* **2015**, *45* (1), 24–36. https://doi.org/10.1016/J.TIFS.2015.04.012.

(14) Ballesteros, L. F.; Cerqueira, M. A.; Teixeira, J. A.; Mussatto, S. I. Characterization of Polysaccharides Extracted from Spent Coffee Grounds by Alkali Pretreatment. *Carbohydr. Polym.* **2015**, *127*, 347–354. https://doi.org/10.1016/J.CARBPOL.2015.03.047.

(15) Mata, T. M.; Martins, A. A.; Caetano, N. S. Bio-Refinery Approach for Spent Coffee Grounds Valorization. *Bioresour. Technol.* **2018**, *247*, 1077–1084. https://doi.org/10.1016/J.BIORTECH.2017.09.106.

(16) Park, J.; Kim, B.; Lee, J. W. In-Situ Transesterification of Wet Spent Coffee Grounds for Sustainable Biodiesel Production. *Bioresour. Technol.* **2016**, *221*, 55–60.

https://doi.org/10.1016/J.BIORTECH.2016.09.001.

(17) Luna-Lama, F.; Rodríguez-Padrón, D.; Puente-Santiago, A. R.; Muñoz-Batista, M. J.; Caballero, A.; Balu, A. M.; Romero, A. A.; Luque, R. Non-Porous Carbonaceous Materials Derived from Coffee Waste Grounds as Highly Sustainable Anodes for Lithium-Ion Batteries. *J. Clean. Prod.* **2019**, *207*, 411–417. https://doi.org/10.1016/j.jclepro.2018.10.024.

(18) Filiciotto, L.; Balu, A. M.; Romero, A. A.; Rodríguez-Castellón, E.; Van Der Waal, J. C.; Luque, R. Benign-by-Design Preparation of Humin-Based Iron Oxide Catalytic Nanocomposites. *Green Chem.* **2017**, *19* (18), 4423–4434. https://doi.org/10.1039/c7gc01405h.

(19) Schutyser, W.; Renders, T.; Van den Bosch, S.; Koelewijn, S.-F.; Beckham, G. T.; Sels, B. F. Chemicals from Lignin: An Interplay of Lignocellulose Fractionation, Depolymerisation, and Upgrading. *Chem. Soc. Rev.* **2018**, *47* (3), 852–908. https://doi.org/10.1039/C7CS00566K.

(20) Lin, C. S. K.; Pfaltzgraff, L. A.; Herrero-Davila, L.; Mubofu, E. B.; Abderrahim, S.; Clark, J. H.; Koutinas, A. A.; Kopsahelis, N.; Stamatelatou, K.; Dickson, F.; et al. Food Waste as a Valuable Resource for the Production of Chemicals, Materials and Fuels. Current Situation and Global Perspective. *Energy Environ. Sci.* **2013**, *6* (2), 426. https://doi.org/10.1039/c2ee23440h.

(21) Rodríguez-Padrón, D.; Puente-Santiago, A. R.; Balu, A. M.; Muñoz-Batista, M. J.; Luque, R. Environmental Catalysis: Present and Future. *ChemCatChem* **2019**, *11* (1), 18–38. https://doi.org/10.1002/cctc.201801248.

(22) Ojeda, M.; Balu, A. M.; Barrón, V.; Pineda, A.; Coleto, Á. G.; Romero, A. Á.; Luque, R. Solventless Mechanochemical Synthesis of Magnetic Functionalized Catalytically Active Mesoporous SBA-15 Nanocomposites. *J. Mater. Chem. A* **2014**, *2* (2), 387–393. https://doi.org/10.1039/C3TA13564K.

(23) Polshettiwar, V.; Luque, R.; Fihri, A.; Zhu, H.; Bouhrara, M.; Basset, J.-M. Magnetically Recoverable Nanocatalysts. *Chem. Rev.* **2011**, *111* (5), 3036–3075. https://doi.org/10.1021/cr100230z.

(24) Laurent, S.; Forge, D.; Port, M.; Roch, A.; Robic, C.; Vander Elst, L.;

Muller, R. N. Magnetic Iron Oxide Nanoparticles: Synthesis, Stabilization, Vectorization, Physicochemical Characterizations, and Biological Applications. *Chem. Rev.* **2008**, *108* (6), 2064–2110. https://doi.org/10.1021/cr068445e.

(25) Rodriguez-Padrón, D.; Puente-Santiago, A. R.; Balu, A. M.; Romero, A. A.; Luque, R. Solventless Mechanochemical Preparation of Novel Magnetic Bioconjugates. *Chem. Commun.* **2017**, *53* (54), 7635–7637. https://doi.org/10.1039/c7cc03975a.

(26) Gawande, M. B.; Branco, P. S.; Varma, R. S. Nano-Magnetite (Fe3O4) as a Support for Recyclable Catalysts in the Development of Sustainable Methodologies. *Chem. Soc. Rev.* **2013**, *42* (8), 3371. https://doi.org/10.1039/c3cs35480f.

(27) Liu, G.; Lin, Y.; Ostatná, V.; Wang, J. Enzyme Nanoparticles-Based Electronic Biosensor. *Chem. Commun.* **2005**, *0* (27), 3481. https://doi.org/10.1039/b504943a.

(28) Sarauli, D.; Wettstein, C.; Peters, K.; Schulz, B.; Fattakhova-Rohlfing, D.; Lisdat, F. Interaction of Fructose Dehydrogenase with a Sulfonated Polyaniline: Application for Enhanced Bioelectrocatalysis. *ACS Catal.* **2015**, *5* (4), 2081–2087. https://doi.org/10.1021/acscatal.5b00136.

(29) Uhlen, M. Magnetic Separation of DNA. *Nature* **1989**, *340* (6236), 733–734. https://doi.org/10.1038/340733a0.

(30) Jia, X.; Xu, M.; Wang, Y.; Ran, D.; Yang, S.; Zhang, M. Polydopamine-Based Molecular Imprinting on Silica-Modified Magnetic Nanoparticles for Recognition and Separation of Bovine Hemoglobin. *Analyst* **2013**, *138* (2), 651–658. https://doi.org/10.1039/C2AN36313E.

(31) Chen, Q.; Zhu, L.; Chen, J.; Jiang, T.; Ye, H.; Ji, H.; Tsang, S.; Zhao, Z.; Yi, T.; Chen, H. Recent Progress in Nanomaterial-Based Assay for the Detection of Phytotoxins in Foods. *Food Chem.* **2019**, *277*, 162–178. https://doi.org/10.1016/J.FOODCHEM.2018.10.075.

(32) Di Corato, R.; Bigall, N. C.; Ragusa, A.; Dorfs, D.; Genovese, A.; Marotta, R.; Manna, L.; Pellegrino, T. Multifunctional Nanobeads Based on Quantum Dots and Magnetic Nanoparticles: Synthesis and Cancer Cell Targeting and Sorting. *ACS Nano* **2011**, *5* (2),

1109–1121. https://doi.org/10.1021/nn102761t.

(33) Yoon, T.-J.; Yu, K. N.; Kim, E.; Kim, J. S.; Kim, B. G.; Yun, S.-H.; Sohn, B.-H.; Cho, M.-H.; Lee, J.-K.; Park, S. B. Specific Targeting, Cell Sorting, and Bioimaging with Smart Magnetic Silica Core-Shell Nanomaterials. *Small* **2006**, *2* (2), 209–215. https://doi.org/10.1002/smll.200500360.

(34) Tsuzuki, T.; McCormick, P. G. Mechanochemical Synthesis of Nanoparticles. *J. Mater. Sci.* **2004**, *39* (16/17), 5143–5146. https://doi.org/10.1023/B:JMSC.0000039199.56155.f9.

(35) Muñoz-Batista, M. J.; Rodriguez-Padron, D.; Puente-Santiago, A. R.; Luque, R. Mechanochemistry: Towards Sustainable Design of Advanced Nanomaterials for Electrochemical Energy Storage and Catalytic Applications. *ACS Sustain. Chem. Eng.* **2018**, *6* (8), 9530–9544. https://doi.org/10.1021/acssuschemeng.8b01716.

(36) Ralphs, K.; Hardacre, C.; James, S. L. Application of Heterogeneous Catalysts Prepared by Mechanochemical Synthesis. *Chem. Soc. Rev.* **2013**, *42* (18), 7701. https://doi.org/10.1039/c3cs60066a.

(37) Franco, A.; De, S.; Balu, A. M.; Garcia, A.; Luque, R. Mechanochemical Synthesis of Graphene Oxide-Supported Transition Metal Catalysts for the Oxidation of Isoeugenol to Vanillin. *Beilstein J. Org. Chem.* **2017**, *13*, 1439–1445. https://doi.org/10.3762/bjoc.13.141.

(38) Franco, A.; De, S.; Balu, A. M.; Romero, A. A.; Luque, R. Selective Oxidation of Isoeugenol to Vanillin over Mechanochemically Synthesized Aluminosilicate Supported Transition Metal Catalysts. *ChemistrySelect* **2017**, *2* (29), 9546–9551. https://doi.org/10.1002/slct.201701273.

(39) Baig, R. B. N.; Varma, R. S. Alternative Energy Input: Mechanochemical, Microwave and Ultrasound-Assisted Organic Synthesis. *Chem. Soc. Rev.* **2012**, *41* (4), 1559–1584. https://doi.org/10.1039/C1CS15204A.

(40) Ostovar, S.; Franco, A.; Puente-Santiago, A. R.; Pinilla-de Dios, M.; Rodríguez-Padrón, D.; Shaterian, H. R.; Luque, R. Efficient Mechanochemical Bifunctional Nanocatalysts for the Conversion of Isoeugenol to Vanillin. *Front. Chem.* **2018**, *6*, 77.

https://doi.org/10.3389/fchem.2018.00077.

(41) Ojeda, M.; Pineda, A.; Romero, A. A.; Barrón, V.; Luque, R. Mechanochemical Synthesis of Maghemite/Silica Nanocomposites: Advanced Materials for Aqueous Room-Temperature Catalysis. *ChemSusChem* **2014**, *7* (7), 1876–1880. https://doi.org/10.1002/cssc.201400055.

(42) Ouyang, W.; Kuna, E.; Yepez, A.; Balu, A.; Romero, A.; Colmenares, J.; Luque, R. Mechanochemical Synthesis of TiO2 Nanocomposites as Photocatalysts for Benzyl Alcohol Photo-Oxidation. *Nanomaterials* **2016**, *6* (5), 93. https://doi.org/10.3390/nano6050093.

(43) Xu, C.; De, S.; Balu, A. M.; Ojeda, M.; Luque, R. Mechanochemical Synthesis of Advanced Nanomaterials for Catalytic Applications. *Chem. Commun.* **2015**, *51* (31), 6698–6713. https://doi.org/10.1039/C4CC09876E.

(44) Ojeda, M.; Balu, A. M.; Barrón, V.; Pineda, A.; Coleto, Á. G.; Romero, A. Á.; Luque, R. Solventless Mechanochemical Synthesis of Magnetic Functionalized Catalytically Active Mesoporous SBA-15 Nanocomposites. *J. Mater. Chem. A* **2014**, *2* (2), 387–393. https://doi.org/10.1039/C3TA13564K.

(45) Cerdan, K.; Ouyang, W.; Colmenares, J. C.; Muñoz-Batista, M. J.; Luque, R.; Balu, A. M. Facile Mechanochemical Modification of G-C3N4 for Selective Photo-Oxidation of Benzyl Alcohol. *Chem. Eng. Sci.* **2018**, *194*, 78–84. https://doi.org/10.1016/j.ces.2018.04.001.

(46) Gawande, M. B.; Luque, R.; Zboril, R. The Rise of Magnetically Recyclable Nanocatalysts. *ChemCatChem* **2014**, *6* (12), 3312–3313. https://doi.org/10.1002/cctc.201402663.

(47) Armstrong, J.; Armstrong, W. Phragmites Die-Back: Toxic Effects of Propionic, Butyric and Caproic Acids in Relation to PH. *New Phytol.* **1902**, *142* (2), 201–217.

(48) Padrón, D. R.; Balu, A. M.; Reyes, A. Á. R.; Luque, R. Procedimiento Para La Preparación de Nanoparticulas Magneticas de Oxido de Hierro a Partir de Residuos de Café Expendido, 2019.

(49) Datta, K. J.; Gawande, M. B.; Datta, K. K. R.; Ranc, V.; Pechousek, J.; Krizek, M.; Tucek, J.; Kale, R.; Pospisil, P.; Varma, R. S.; et al. Micro–

Mesoporous Iron Oxides with Record Efficiency for the Decomposition of Hydrogen Peroxide: Morphology Driven Catalysis for the Degradation of Organic Contaminants. *J. Mater. Chem. A* **2016**, *4* (2), 596–604. https://doi.org/10.1039/C5TA08386A.

(50) Gawande, M. B.; Shelke, S. N.; Zboril, R.; Varma, R. S. Microwave-Assisted Chemistry: Synthetic Applications for Rapid Assembly of Nanomaterials and Organics. *Acc. Chem. Res.* **2014**, *47* (4), 1338–1348. https://doi.org/10.1021/ar400309b.

(51) Márquez-Medina, M. D.; Rodríguez-Padrón, D.; Balu, A. M.; Romero, A. A.; Muñoz-Batista, M. J.; Luque, R. Mechanochemically Synthesized Supported Magnetic Fe-Nanoparticles as Catalysts for Efficient Vanillin Production. *Catalysts* **2019**, *9* (3), 290. https://doi.org/10.3390/catal9030290.

(52) Gao, Q. X.; Wang, X. F.; Di, J. L.; Wu, X. C.; Tao, Y. R. Enhanced Catalytic Activity of α-Fe2O3 Nanorods Enclosed with {110} and {001} Planes for Methane Combustion and CO Oxidation. *Catal. Sci. Technol.* **2011**, *1* (4), 574–577. https://doi.org/10.1039/c1cy00080b.

(53) Dar, M. I.; Shivashankar, S. A. Single Crystalline Magnetite, Maghemite, and Hematite Nanoparticles with Rich Coercivity. *RSC Adv.* **2014**, *4* (8), 4105–4113. https://doi.org/10.1039/C3RA45457F.

(54) Cuenca, J. A.; Bugler, K.; Taylor, S.; Morgan, D.; Williams, P.; Bauer, J.; Porch, A. Study of the Magnetite to Maghemite Transition Using Microwave Permittivity and Permeability Measurements. *J. Phys. Condens. Matter* **2016**, *28* (10), 106002. https://doi.org/10.1088/0953-8984/28/10/106002.

(55) Moulder, J. F.; Sticlke, W. F.; Sobol, P. E.; Bomben, K. D. *Handbook of X-Ray Photoelectron Spectroscopy*; PerkinElmer Corporation: Eden Prairie: MN, 1992.

(56) Watanabe, H.; Seto, J. The Intrinsic Equilibrium Constants of the Surface Hydroxyl Groups of Maghemite and Hematite. *Bull. Chem. Soc. Jpn.* **1990**, *63* (10), 2916–2921. https://doi.org/10.1246/bcsj.63.2916.

(57) Bohre, A.; Gupta, D.; Alam, M. I.; Sharma, R. K.; Saha, B. Aerobic Oxidation of Isoeugenol to Vanillin with Copper Oxide Doped Reduced Graphene Oxide. *ChemistrySelect* **2017**, *2* (10), 3129–3136. https://doi.org/10.1002/SLCT.201700415.

(58) Xu, C.; Puente-Santiago, A. R.; Rodríguez-Padrón, D.; Caballero, A.; Balu, A. M.; Romero, A. A.; Muñoz-Batista, M. J.; Luque, R. Controllable Design of Polypyrrole-Iron Oxide Nanocoral Architectures for Supercapacitors with Ultrahigh Cycling Stability. *ACS Appl. Energy Mater.* **2019**. https://doi.org/10.1021/acsaem.8b02167.

(59) Zhu, X.; Zhu, Y.; Murali, S.; Stoller, M. D.; Ruoff, R. S. Nanostructured Reduced Graphene Oxide/Fe2O3 Composite as a High-Performance Anode Material for Lithium Ion Batteries. *ACS Nano* **2011**, *5* (4), 3333–3338. https://doi.org/10.1021/nn200493r.

(60) Watanabe, H.; Seto, J. etsu. The Catalysis of Maghemite and Hematite on the Aldol and the Retro-Aldol Condensation of Acetone. *Bull. Chem. Soc. Jpn* **1991**, *64*, 2411–2415. https://doi.org/https://doi.org/10.1246/bcsj.64.2411.

(61) Shi, F.; Tse, M. K.; Pohl, M. M.; Brückner, A.; Zhang, S.; Beller, M. Tuning Catalytic Activity between Homogeneous and Heterogeneous Catalysis: Improved Activity and Selectivity of Free Nano-Fe2O3 in Selective Oxidations. *Angew. Chemie - Int. Ed.* **2007**, *46* (46), 8866–8868. https://doi.org/10.1002/anie.200703418.

(62) Carrillo, A. I.; Serrano, E.; Luque, R.; García-Martínez, J. Microwave-Assisted Catalysis by Iron Oxide Nanoparticles on MCM-41: Effect of the Support Morphology. *Appl. Catal. A Gen.* **2013**, *453*, 383–390. https://doi.org/10.1016/J.APCATA.2012.12.041.

(63) Hermanek, M.; Zboril, R.; Medrik, I.; Pechousek, J.; Gregor, C. Catalytic Efficiency of Iron(III) Oxides in Decomposition of Hydrogen Peroxide: Competition between the Surface Area and Crystallinity of Nanoparticles. *J. Am. Chem. Soc.* **2007**, *129* (35), 10929–10936. https://doi.org/10.1021/ja072918x.

(64) Yepez, A.; De, S.; Climent, M.; Romero, A.; Luque, R.; Yepez, A.; De, S.; Climent, M. S.; Romero, A. A.; Luque, R. Microwave-Assisted Conversion of Levulinic Acid to γ-Valerolactone Using Low-Loaded

Supported Iron Oxide Nanoparticles on Porous Silicates. *Appl. Sci.* **2015**, *5* (3), 532–543. https://doi.org/10.3390/app5030532.

(65) Rathi, A. K.; Gawande, M. B.; Zboril, R.; Varma, R. S. Microwave-Assisted Synthesis – Catalytic Applications in Aqueous Media. *Coord. Chem. Rev.* **2015**, *291*, 68–94. https://doi.org/10.1016/J.CCR.2015.01.011.

(66) Sun, J.; Wang, W.; Yue, Q.; Sun, J.; Wang, W.; Yue, Q. Review on Microwave-Matter Interaction Fundamentals and Efficient Microwave-Associated Heating Strategies. *Materials (Basel).* **2016**, *9* (4), 231. https://doi.org/10.3390/ma9040231.

(67) Goldsmith, B. R.; Peters, B.; Johnson, J. K.; Gates, B. C.; Scott, S. L. Beyond Ordered Materials: Understanding Catalytic Sites on Amorphous Solids. *ACS Catal.* **2017**, *7* (11), 7543–7557. https://doi.org/10.1021/acscatal.7b01767.

(68) Mariana Balu, A.; Pineda, A.; Yoshida, K.; Manuel Campelo, J.; Gai, P. L.; Luque, R.; Angel Romero, A. Fe/Al Synergy in Fe2O3 Nanoparticles Supported on Porous Aluminosilicate Materials: Excelling Activities in Oxidation Reactions. *Chem. Commun.* **2010**, *46* (41), 7825–7827. https://doi.org/10.1039/c0cc02015j.

Supporting Information

Spent coffee grounds-templated magnetic nanocatalysts for mild oxidations

Daily Rodríguez-Padrón,[a+] Mario J. Muñoz-Batista,[a+] Hangkong Li[b], Kaimin Shih[b], Alina M. Balu,[a]* Antonio Pineda,[a] and Rafael Luque[a,c]*

Table S1: Surface acidity of c@Fe_2O_3 nanomaterials.

Sample	Lewis acidity (μmoles/g)[a]
c@Fe_2O_3-300 °C	20
c@Fe_2O_3-400 °C	20
c@Fe_2O_3-500 °C	19
c@Fe_2O_3-600 °C	16
c@Fe_2O_3-700 °C	11
c@Fe_2O_3-800 °C	9

[a]Total surface acidity is due to the presence of Lewis acid sites. No Brönsted acidity was appreciable to be quantized.

The acidic properties of the prepared nanomaterials were determined by the chromatographic method of pulses, using pyridine and dimethyl-pyridine as probe molecules. Particularly, pyridine adsorbs nonspecifically in both types of centers, namely Lewis and Brønsted acid centers, as expected due to its low steric hindrance. In turn, dimethyl-pyridine, which possess a high steric hindrance associated with the methyl groups, adsorbs only on Brønsted acid centers.

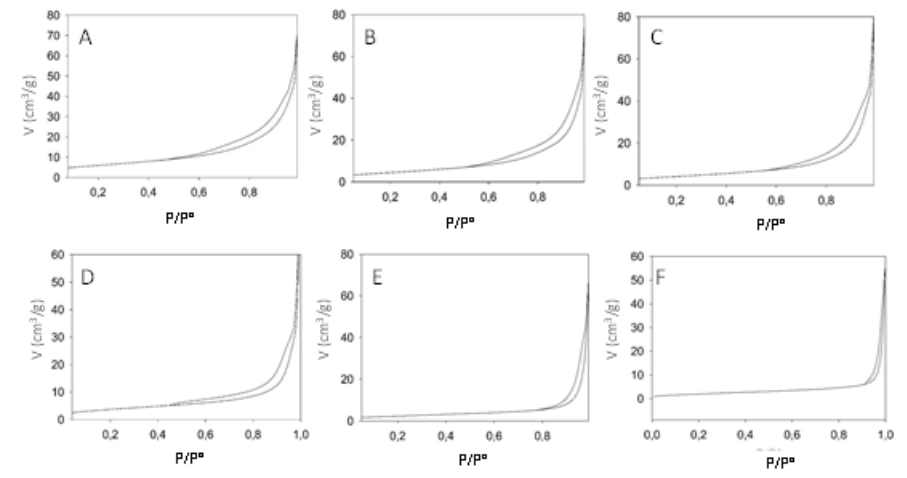

Figure S1. N_2 adsorption–desorption isotherms. (A) c@Fe_2O_3-300 °C, B) c@Fe_2O_3-400 °C, (C) c@Fe_2O_3-500 °C, (D) c@Fe_2O_3-600 °C, (E) c@Fe_2O_3-700 °C, (F) c@Fe_2O_3-800 °C.

4.4. Versatile protein-templated TiO_2 nanocomposite for energy storage and catalytic applications

A simple and solvent-free mechanochemical protocol was employed for the preparation of a titania-based nanocomposite, employing, in this case egg-white from expired eggs as biomass residue and sacrificial template to control the morphology and textural properties. A full characterization analysis was performed, using a multi-technique approach. Enhanced surface area was observed by employing egg-white, in comparison with the material prepared in absence of sacrificial template. The synthesized sample resulted to be a good and versatile candidate for its use as catalyst in the oxidation of diphenylsulfide and as anodic material for lithium-ion batteries.

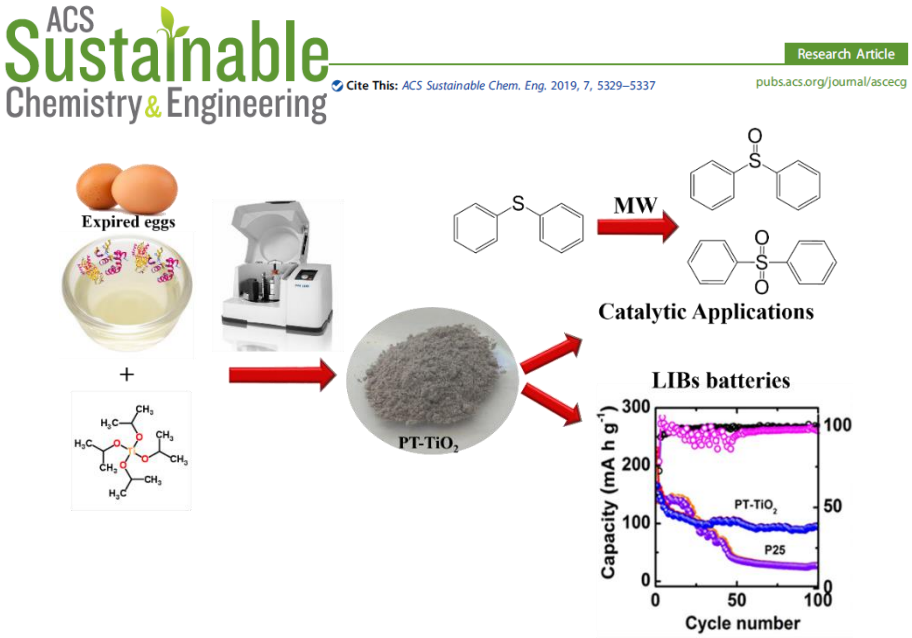

Daily Rodríguez-Padrón, Alain R. Puente-Santiago, Fernando Luna-Lama, Álvaro Caballero, A., Mario J. Muñoz Batista, Rafael Luque. **2019**. Versatile protein-templated TiO_2 nanocomposite for energy storage and catalytic applications. **ACS Sustainable Chemistry & Engineering**. 10.1021/acssuschemeng.8b06349. IF: 6.14.

Versatile protein-templated TiO_2 nanocomposite for energy storage and catalytic applications

Daily Rodríguez-Padrón,[a]‡ Alain R. Puente-Santiago,[a]‡ Fernando Luna-Lama,[b]Álvaro Caballero,[b] Mario J. Muñoz-Batista,[a] *and Rafael Luque[a,c]*

*[a] Departamento de Química Orgánica, Instituto de Química Fina y Nanoquímica, Universidad de Córdoba, Campus de Rabanales, Edificio Marie Curie (C-3), Ctra Nnal IV-A, Km 396, E14014, Cordoba, España. * M.J.M-B jmunoz385x@gmail.com, qo2mubam@uco.es, R.L. rafael.luque@uco.es*

[b] Departamento de Química Inorgánica e Ingeniería Química, Instituto de Química Fina y Nanoquímica, Universidad de Córdoba, Campus de Rabanales, Edificio Marie Curie (C-3), Ctra Nnal IV-A, Km 396, E14014, Cordoba, España.

[c]Peoples Friendship University of Russia (RUDN University), 6 Miklukho-Maklaya str., 117198, Moscow, Russia.

‡These authors contributed equally to the work.

A protein-templated titania nanocomposite (PT-TiO_2) was successfully synthesized by a water-free mechanochemical approach. A biomass valorization strategy was developed by employing egg white from expired eggs to control the morphology and textural features of the prepared titania. A remarkable enhancement of the surface area was achieved, in comparison with the synthesis of the material in absence of the biomass-derived template. Several techniques, such as SEM-mapping and CNHS analysis, supported the presence of carbon, nitrogen and sulfur residues in the obtained composite. Catalytic performance of PT-TiO_2 was explored in the oxidation of diphenyl sulfide, displaying promising results

in terms of conversion, selectivity and stability. The effect of the oxidant agent was additionally investigated by using hydrogen peroxide, urea hydrogen peroxide, oxygen and t-butyl- hydroperoxide. On the other hand, PT-TiO_2 nanocomposite was successfully proved as anodic material for LIBs delivering a reversible capacity of 107 mAh g^{-1} at 0.1 C with an excellent coulombic efficiency of 100% from the second cycle. In addition, the as-synthesized material showed significant capacity retention values of 76% among the second cycle and 100th cycle. PT-TiO_2 sample resulted to be a versatile material with potential catalytic and energy storage applications.

Keywords: White egg, titania, biomass valorization, LIBs, microwave assisted reaction, diphenyl sulfide oxidation.

Introduction

Development of new systems to produce sustainable energy and its efficient use are two of the main problems of modern-day society. It is well-known that energy vectors generated from traditional fuel-fossil sources and processes are basically responsible for problems of climate change and, as a response, the development of greener and highly efficient technologies, such as solar cells, lithium-ion batteries (LIBs) or production of new energy vectors (e.i. H_2) are presented as a potential alternative.[1,2] How we use the energy in the wide range of application available has equal relevance in the complicated current energy context. In particular, chemical industry is being one of the higher energy consumers around the world which makes the development of increasingly energy processes a key challenge of modern society. To solve the mentioned drawbacks, non-traditional energy sources for chemical applications have been gaining more interest in both laboratories and industrial scales. In this regard, the use of sustainable materials as 1) anode component for lithium-ion batteries (LIBs) with high and stable capacities and as 2) catalyst for microwave-assisted reactions has received considerable attention.[3–5]

Field of catalysis is very dependent on energy, requiring in many cases high energy consumption operating conditions such as high temperatures and pressures. For instance, natural or artificial light-assisted as well as sonication and microwave reactors have boosted energy efficiency in several catalytic processes, from new synthetic protocols to reactions.[6–10] Among a large variety of materials studied for catalytic applications, TiO_2-based compounds are presented as a promising alternative. Additionally, they have even been used as effective anode materials towards the generation of high-performance LIBs.[11,12] In fact, some reviews highlight TiO_2 as the most studied transition-metal oxide and one of the most investigated compounds in materials science.[13,14] Such versatility has produced an increase in scientific activity in this direction. From a structural point of view, relatively high surface areas in addition to small crystal sizes can be beneficial to many TiO_2-based materials and its application, as it improves the interaction between the samples and media.[7,13–16] There are several contributions in which structure and morphology properties of TiO_2 have been analyzed as a function of the synthetic protocol.[7,17] In this regard, although methods such as sol-gel, microemulsion, hydrothermal and microwave-assisted have shown several advantages and have produced an extended number of applicable materials,[18–21] also possess inherent disadvantages. Some of them with negative environmental effects regarding to high temperatures and the use of high levels of solvents and reagents. In this sense, biomass-derived templates have emerged as a simple and outstanding approach to produce TiO_2 materials minimizing time, chemicals, external water and waste.[22] Food residues constitute a significant part of non-used biomass materials. In fact, it is a problem extensively addressed by U.S. Environmental Protection Agency.[23] The aforementioned template methods could be a profitable outlet for both food residues and out of date food. Banana and orange peel, chicken egg and coffee waste grounds can be mentioned as representative examples, which have provided outstanding results as bio-template.[24–27] In addition, with a proper control of the calcination process, it is possible to maintain in the structure beneficial entities from the bio-template as is the case of biomass-derived nitrogen-doped carbon-oxides materials. Besides,

biomass residues confers high oxygen functionalities to the resulted carbons, which can act as anchoring sites for further metal deposition.[4]

In this contribution, we addressed an easy and environmental friendly synthesis of a TiO_2-based composite using white egg by a template methodology for catalytic and energy storage applications. The suitable balances of all properties allow obtaining a good reversible capacity (similar to other TiO_2 based electrode materials) as well as highly selective catalyst for the oxidation of diphenil sulfide to the corresponding sulfoxide. P25 TiO_2 is also reported as a commercial reference for both applications. Finally, a complete physico-chemical characterization of the as synthesized material attempts to correlate the results with a multitechnique characterization approach based on data obtained from XRD, XPS, SEM-EDX as well as N_2 physisorption measurements.

Experimental

Synthesis of protein-templated-TiO_2 (PT-TiO_2)

A water-free mechanochemical assisted protocol was employed for the synthesis of PT-TiO_2 sample (Scheme 1). Firstly, a 1:2 (wt.) metal precursor (titanium isopropoxide)/template (egg white from expired eggs: 40 days) ratio was mixed in a 125 mL reaction chamber and mechanochemically treated in a Retsch PM100 ball mill at 350 rpm for 10 min, employing eighteen 10 mm stainless steel balls. In a second step, the obtained composite material was oven-dried at 100 °C for 24 h, and finally calcined at 500 °C for 2h.

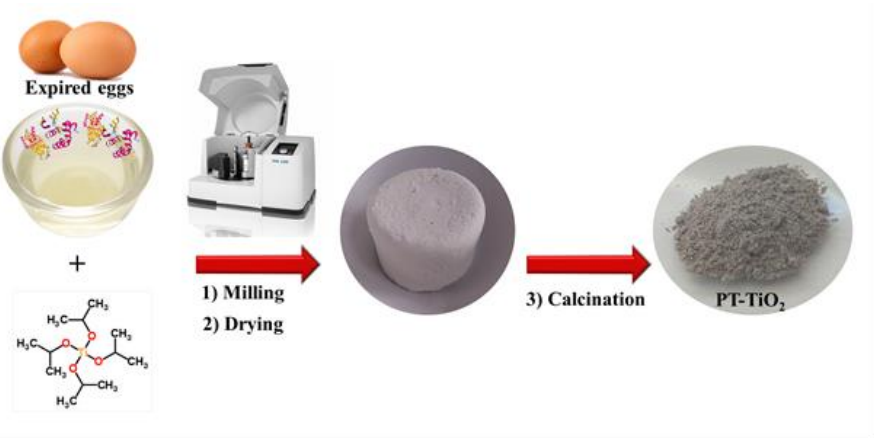

Scheme 1. Schematic representation of the synthetic protocol of PT-TiO_2 material.

Chemical analysis and textural characterization

The prepared PT-TiO_2 material was characterized by several techniques, including X-ray diffraction (XRD), X-Ray Photoelectron Spectroscopy (XPS), Thermogravimetric analysis (TGA), N_2 physisorption, Scanning Electronic Microscopy, Transmission Electronic Microscopy and CNHS measurements.

XRD analysis of PT-TiO_2 sample was accomplished in a Diffractometer (D8 Advanced Bruker AXS), employing a Lynxeye detector in a 10°-70° 2θ scan range. Results interpretation was performed helped by the Bruker Diffrac-plus EVA software and supported by the Powder Diffraction File (PDF) database of the International Centre for Diffraction Data (ICDD).

N_2 physisorption analysis was accomplished at the temperature of liquid nitrogen (77 K) in a Micromeritics ASAP 2000 instrument. Prior to analysis, TiO_2 reference and PT-TiO_2 sample were degassed for 24 h under vacuum ($p<10^{-2}$ Pa). The weight of both materials ranged between 0.15-0.20 g. BET analysis, in a $0.05<P_0<0.30$ range, was employed for determining the surface areas of the prepared materials. TGA measurements were accomplished on a Setaram Setsys 12 TGA

thermobalance. The sample was heated from 30 to 800 C, under air atmosphere (50 mL min^{-1}) at a rate of 10 °C min^{-1}.

The FEI Tecnai G2 system equipped with a CCD ("charge coupling device") camera was used in order to record TEM images of the synthesized materials. PT-TiO_2 sample was previously suspended in ethanol and subsequently deposited on a copper grid. SEM-mapping measurements were performed in a JEOL JSM-6490 LV microscope.

XPS experiments were carried out in an ultrahigh vacuum (UHV) multipurpose surface analysis system SpecsTM, equipped with the Phoibos 150-MCD energy detector. The measurements were carried out at pressures $<10^{-10}$ mbar, employing a X-ray source in a "stop and go" mode. XPS CASA program was used for analysis the obtained data.

Preparation of the electrodes and cells

The as-synthesized PT-TiO_2 material was mechanically mixed with PVDF polymer and a super conductive carbon black in a 1-methyl-2-pyrrolidinone solution (NMP) to (80:10:10) to obtain the anode material. Firstly, the resulting solution was deposited through the “doctor-blade” approach onto a Cu thin foil and secondly tiny disks of 13 mm were cut and were dried at 50 °C in vacuum conditions to fabricate anode electrodes, following previous work.[27]

Electrochemical characterization

Electrochemical characterization was performed using a reported setup.[27] Cyclic voltammetry (CV) measurements were acquired in a potential range of 0–3 V. Charge-discharge curves were carried out at 0.1A at a current rate of 0.1 A g^{-1} (approximate to 0.3C) and rate capability behaviour was tested varying current density from 33.5 to 670 mA g^{-1}.

Results and discussion

The preparation of the protein-templated TiO_2 nanocomposite (PT-TiO_2) was performed using egg white from expired eggs and titanium

isopropoxide as metal precursor, by a solvent-free mechanochemical strategy. Apart from its noticeable versatility, reproducibility and simplicity, the application of mechanochemistry as a synthetic procedure possess a marked sustainable character, since it avoids the employment of solvents and additional reagents. In this work, egg white was employed as a template in order to tune the morphological properties of the obtained TiO_2. Titanium isopropoxide together with the aforementioned template gave rise to a composite material by physical and/or chemical adherence. Besides the effect in the morphological properties, the presence of water from egg white also allows the hydrolysis of the titanium precursor, resulting in the formation of titanium hydroxide. The latest compound was calcined at 500 ºC, with the consequent formation of a nanostructured titanium oxide composite.

Structural characterization of the TiO_2-based nanocomposite.

The synthesized protein-templated TiO_2 nanocomposite was fully characterized by a multi-technique approach, including X-ray Diffraction (XRD), N_2-physisorption, Thermogravimetric analysis (TGA), Transmission Electronic Microscopy, Scanning Electronic Microscopy, CHNS measurements and X-ray Photoelectronic Spectroscopy (XPS). For comparison, a TiO_2 material was additionally prepared by a similar protocol in absence of the template. Basic characterization of such TiO_2 reference was performed by XRD and N_2-physisorption.

Crystal structure and arrangement of PT-TiO_2 and TiO_2 reference were evaluated by XRD analysis. XRD pattern of TiO_2 reference displayed a highly crystalline structure with the presence of several peaks at 25.4º, 37.0º, 37.9º, 38.5º, 48.1º, 54.0º, 55.1º and 62.8º, which can be attributed to (101), (103), (004), (112), (200), (105), (201) and (204) diffraction planes, respectivelly.[28] Although the peaks in the XRD pattern of PT-TiO_2 sample exhibited a reduced intensity, (Figure 1A) associated with a lower crystallinity, in comparison with the TiO_2 reference, both samples presented the same crystalline phase, namely anatase. This result could be attributed most likely to the mediation of the template in the synthetic process.

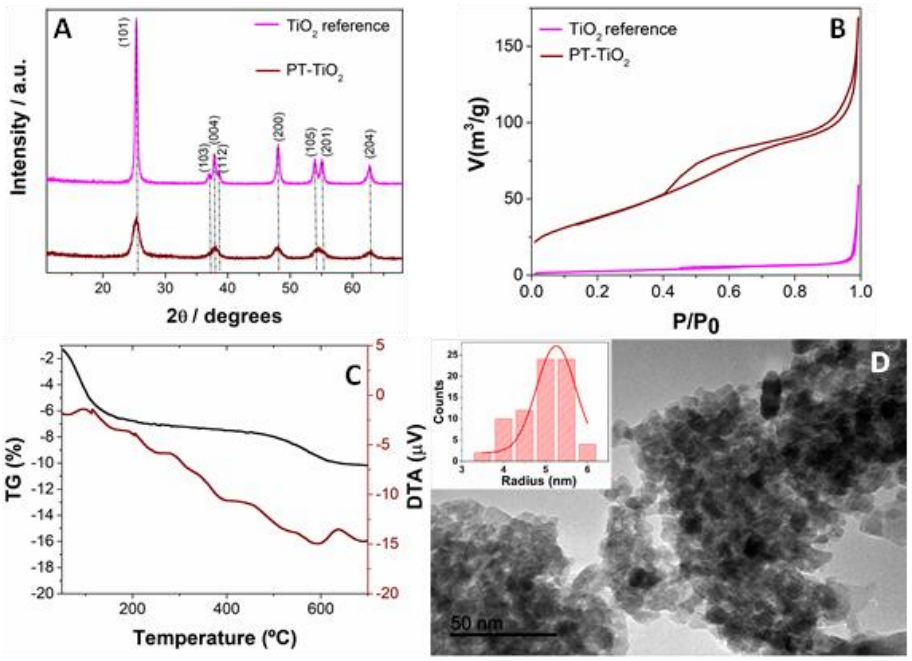

Figure 1. (A) XRD patterns and (B) N_2 absorption-desorption isotherms of PT-TiO_2 and TiO_2 reference, (C) TG and DTA analyses of PT-TiO_2, (D) TEM image of PT-TiO_2 (Inset: Particle size distribution).

Textural properties of both samples, PT-TiO_2 and TiO_2 reference, were investigated by N_2 adsorption-desorption measurements. A remarkable enhancement of the morphological features was observed by using egg white as template, as shown in Figure 1B. N_2 adsorption-desorption isotherms resulted to be type III and IV for TiO_2 reference and PT-TiO_2, respectively. Such result confirmed the mesoporous structure and the improved textural properties of the PT-TiO_2 in comparison with the material prepared in absence of the template. An outstanding surface area of 139 m^2g^{-1} was found for the PT-TiO_2 material, while TiO_2 reference displayed just a surface area of 10 m^2g^{-1} (Table 1). The superficial area of the composite, which is an important property for the studied application, is competitive in comparison with other synthetic methods such as sol-gel, micro-emulsion or hydrothermal in which the presence of external water and other solvents are required.[18–21] These results clearly confirmed the crucial role of the template in the controllable tuning of the

material textural characteristics. Thermal stability of the prepared PT-TiO_2 was studied by TGA measurements (Figure 1C). A first weight loss was found at 100 °C, related to the presence of water (unbounded/physisorbed). Afterwards, a progressive and slow weight loss of 10 % was observed from 200 to 700 °C (broad endothermic–DTA signal). This result can be attributed to the non-oxidative decomposition of organic residues in the PT-TiO_2.[27]

Table 1. Textural properties of the PT-TiO_2 and TiO_2 reference.

MATERIAL	S_{BET} (M^2 G^{-1})	V_{BJH} (CM^3 G^{-1})	D_{BJH} (NM)
PT-TIO_2	139	0.07	20.2
TIO_2 REF.	10	0.25	5.7

Figure 1D exhibit TEM micrograph of the PT-TiO_2 sample, which revealed a homogenous distribution of quasi-spherical nanoparticles with a mean radius of 5.2 nm. In addition, the morphology of the prepared material was evaluated by SEM analysis, which was in accordance with the nanostructured architecture observed by TEM. SEM-mapping results suggested the presence of Ti and O, as well as C, N and S, most likely due to the presence of protein residues in the obtained nanocomposite (Figure 2). Such results were corroborated by CNHS measurements, which showed 1.0 %, 1.3% and 0.4% of N, C and S, respectively.

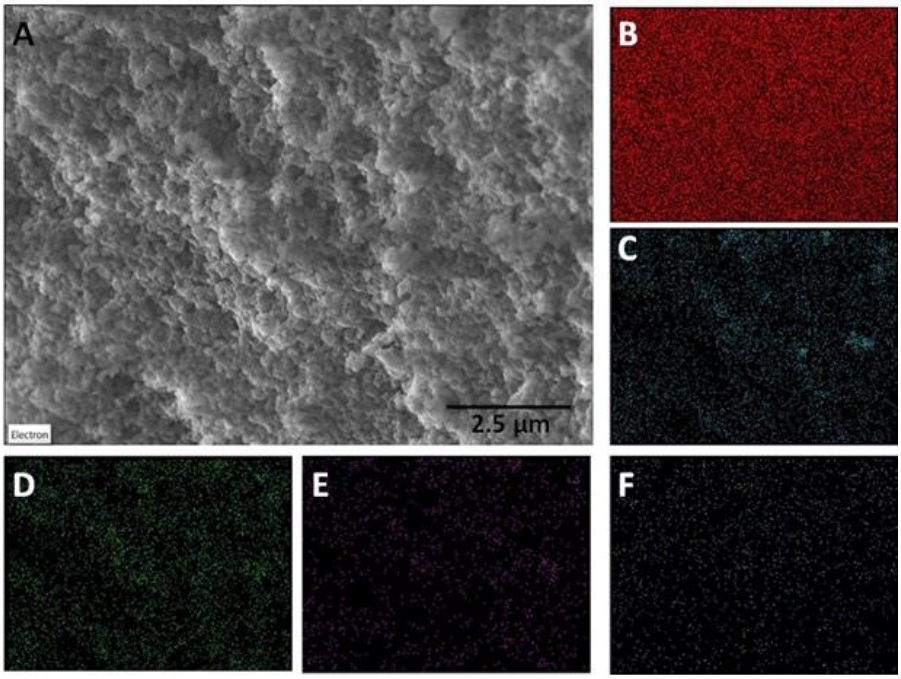

Figure 2. (A) SEM micrograph of PT-TiO_2 sample. SEM-mapping images of PT-TiO_2 sample for (B) Ti, (C) O, (D) C, (E) N and (F) S.

XPS analysis of the nano-composite was carried out to provide information related to the minor carbon, nitrogen, and sulphur species, as well as titanium and oxygen components. Figure 3A displays the C1s region. The main contribution can be related to spurious entities generated during the calcination process, although can also be associated to residual aliphatic C–H bonds of the albumin (284.6 eV).[29] The other two contributions can exclusively ascribable to different C-N structural moieties (286.2 and 287.9 eV), generated during heating treatment due to the denaturalization process of the protein.[30] These two chemical moieties (399.5 and 397.3 eV) also contribute to the N1s XPS region (Figure 3B). For S2p the fitting takes into two contributions, S2p3/2 and S2p1/2 (153.8 and 152.2 eV, respectively), resulting from the sulphur atoms coming from the protein molecules.[25] Ti2p core level spectra shows typical contribution of titania. The corresponding Ti 2p3/2 and Ti 2p1/2 peaks are located at 458.6 eV and 463.8 eV, respectively and correspond to Ti(IV).[31] Finally, the analysis of O1s XPS was fitted into two

components indicating the presence of the two types of oxygen expected in the sample. The main peak at 529.3 eV can be assigned to the oxygen lattice ions of the anatase network (Ti-O-Ti) and the contribution situated at 531.5 eV to the C-O. [31,32]

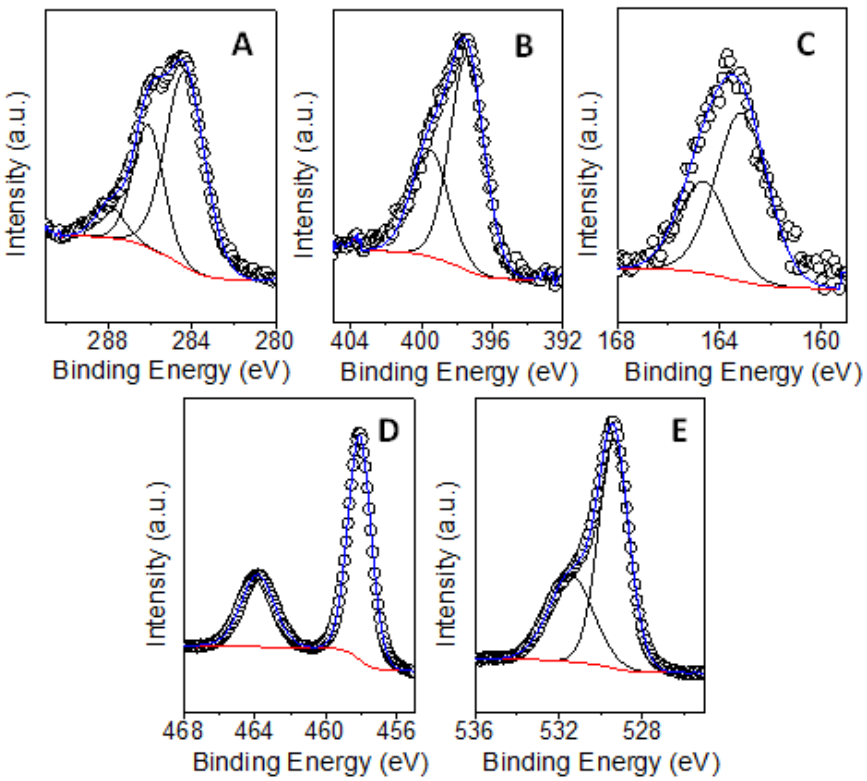

Figure 3. XPS deconvoluted spectra of PT-TiO_2 sample for (A) C1s, (B) N1s, (C) S2p, (D) Ti2p and (E) O1s.

Catalytic performance of PC-TiO_2 nanocomposite

The catalytic performance of PT-TiO_2 sample was evaluated in the microwave-assisted oxidation of diphenyl sulfide to the corresponding sulfoxide and sulfone (Scheme 2). The microwave irradiation was employed in order to decrease the reaction times, favoring as well the efficiency of the catalytic process, in terms of conversion. Sulfoxidation

has been usually hindered by problems related to the selectivity of the reaction, being particularly interesting the selective production of sulfoxide molecules (alkyl, aryl and benzyl derivatives) with potential applicability in the pharmaceutical industry. The selectivity of such kind of reactions will partially depend on the employed catalytic system. Specially, the use of heterogeneous catalysts possesses intrinsic advantages related to their easy recovery and reuse. Several contributions have reported sulfoxidation reactions in the presence of heterogeneous catalyst such as transition metal functionalized graphene oxide, ionic liquid complexes, transition-metal oxide clusters, tungsten (VI) organic complexes and carbon supported polyoxometalates. Remarkably, the prepared PT-TiO_2 material is advantageous, with respect to the aforementioned systems, due to its simple structure and facile preparation methodology.

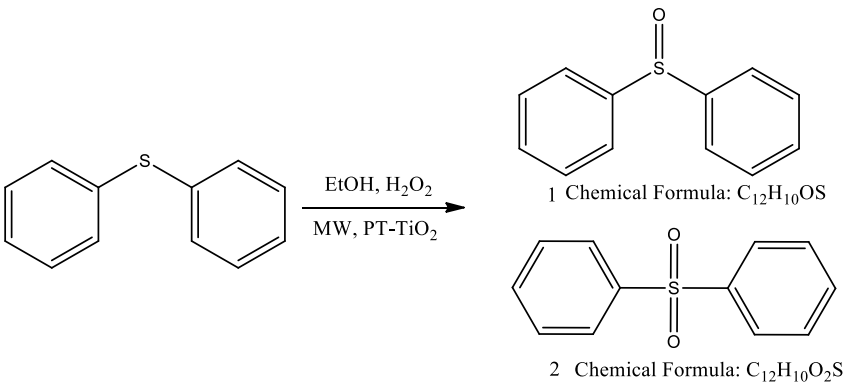

Scheme 2. Schematic representation of the diphenyl sulfide microwave-assisted oxidation.

Blank measurements were performed in order to confirm the essential role of the catalytic system in the reaction progress. Such analysis revealed that in absence of catalyst the reaction just displayed a 10% of conversion. In turn, by using the prepared PT-TiO_2 catalytic material, the reaction achieved a 90% of conversion (Figure 4A). P25 titania was, as well, employed in the oxidation of diphenyl sulfide, in order to compare the prepared material with a commercial reference. Both materials

displayed comparable results in terms of conversion, however a critical change in selectivity was observed (Figure 4B). The employment of P25 material, give rise to the complete oxidation of diphenyl sulfide to sulfone, with a selectivity to this product higher that 95%. On the other hand, the use of PT-TiO_2 allows the controllable oxidation of sulfide group to the corresponding sulfoxide, with a selectivity to this product of 90%. Such result could be understood attending the different crystallinity of both samples and to the presence of carbon species on the PT-TiO_2 surface. A decrease in crystallinity could be associated with a decrease in selectivity to the full oxidation product, most likely due to the reduction of active sites that promote, in this case, the complete oxidation of sulfide to form the sulfone product. As aforementioned, reported conversion were obtained after 1 h of reaction, faster than similar experiments carried out under typical operating conditions (temperature and oxidant agent).[33,34] Note that carbon balance was achieved above 97% in all catalytic tests, and thus only rather minor products are not shown.

Figure 4. Catalytic performance of PT-TiO_2 and TiO_2 P25, in terms of (A) conversion and (B) selectivity.

As shown in Figure 5, the influence of the oxidant agent was investigated by comparing the catalytic performance employing hydrogen peroxide, urea hydrogen peroxide (U-H_2O_2), oxygen and *t*-butyl- hydroperoxide (*t*-B-H_2O_2). The use of hydrogen peroxide presented the best catalytic performance in terms of balance between conversion (90 %) and selectivity (90 %). Although, selectivity to diphenyl sulfide increase by using U-H_2O_2 (S=94 %), O_2 (S=94 %) and *t*-B-H_2O_2 (S=96 %), the conversion decrease to 53 %, 5 % and 15 % conversion, respectively, support the use of hydrogen peroxide as the optimum oxidant agent.

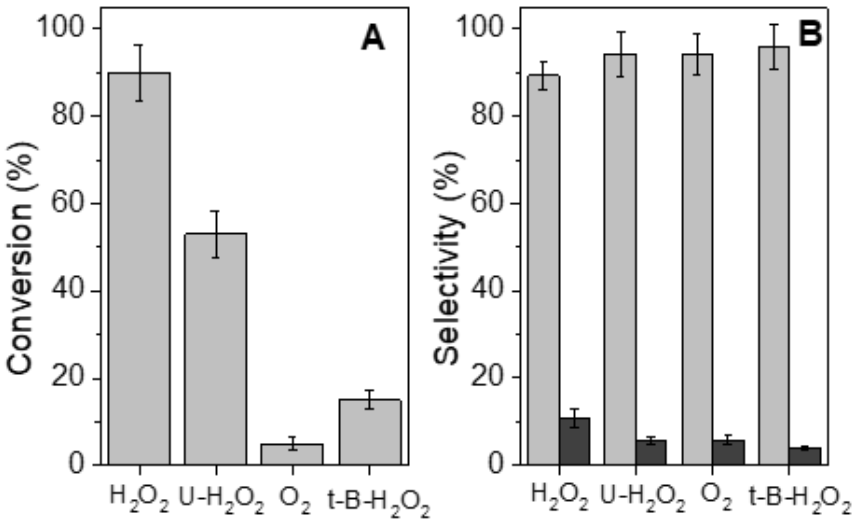

Figure 5. Catalytic performance of PT-TiO_2 employing different oxidant agents, in terms of (A) conversion and (B) selectivity.

Reusability studies were carried out in order to determine the stability of the material (Figure 6). After the first use, the catalyst was recovered, washed and reused in the reaction under identical operating conditions. Such process was repeated five times, revealing that the catalytic system remained stable, showing an 86 % conversion after the fifth use, with no considerable change in selectivity.

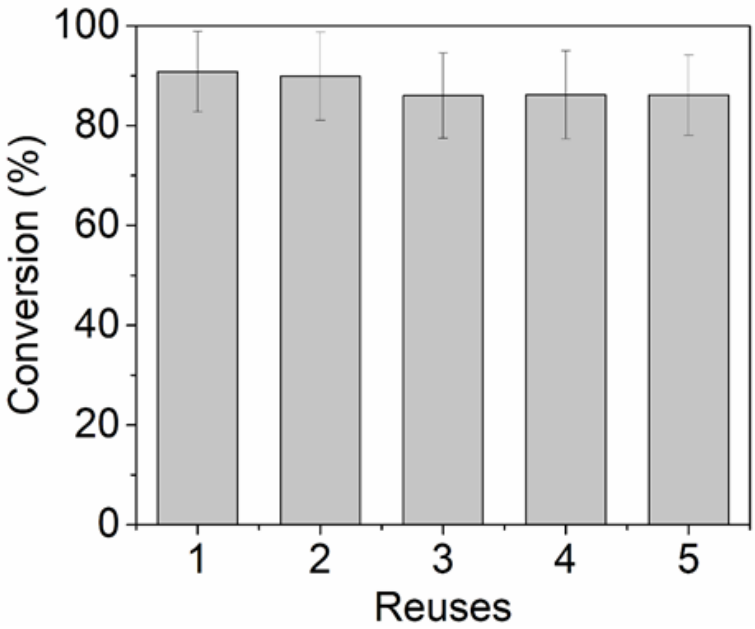

Figure 6. Reusability study of PT-TiO_2 nanocomposite.

Electrochemical characterization of PC-TiO_2 nanocomposite

The electrochemical performance of the PT-TiO_2 nanocomposite was explored as anode for lithium ion batteries and compared with the commercial TiO_2 material (P25). Figure 7A and 7B show the typical cyclic voltammogram (CV) curves of the PT-TiO_2 and P25 anode materials measured in the potential window of 1-3V at a sweep rate of 0.1 mV/s. The voltammograms of the mentioned anode materials display two pair of well-defined and stable peaks at 1.72 and 2.01V (vs Li^+/Li) indicating the lithium insertion/extraction processes in the crystalline anatase structure. Importantly, the higher intensities of the cathodic and anodic redox peaks of the PT-TiO_2 hybrid nanostructures regarding to the commercial TiO_2 structures represent a clear evidence of its enhanced electrochemical activity. The evolution of the cathodic potential peak (E_c) and anodic potential peak (E_a) for both anode materials are shown in Figure 7C and 7D. It can be observed that at faster scan rates, in

comparison with P25 anode electrodes, the potential peak separation as well as the peak shape of the PT-TiO_2 nanocomposite is closer to the initial voltammogram measured at a scan rate of 0.1 mV/s. Additionally, the PT-TiO_2 peak intensities surpassed around ten times the signal intensities of the commercial sample. The aforementioned behaviour revealed the higher reversibility of the TiO_2 nanocomposite material and supported its better electrochemical efficiency as an anode material in lithium half-cells.[32]

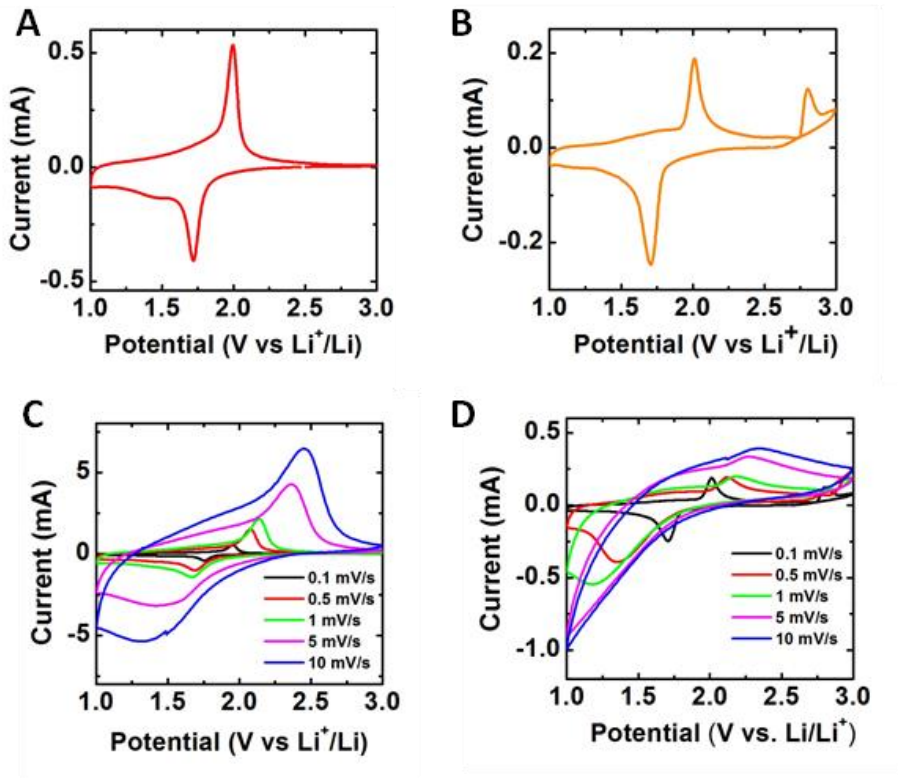

Figure 7. Electrochemical performance of the PT-TiO_2 and P25 TiO_2 in a half-cell LIB. Cyclic voltammogram of (A) PT-TiO_2 and (B) P25 TiO_2 at 0.1 mV s^{-1}. Cyclic voltammograms of (C) PT-TiO_2 and (D) P25 TiO_2 at 0.1, 0.5, 1, 5 and 10 mV s^{-1}.

The 1st, 2sd, 10th and 50th charged/discharged curves at 0.1 C of the P25 and synthesized nanocomposite are shown in the Figure 8A and 8B, respectively. Significantly, three characteristic regions can be observed in the discharged branches: the monotonous voltage drop region to 1.78V in which the insertion of lithium ion is very poor, the plateau voltage region of approximately 1.75-1.80V which can be linked to the equilibrium between tetragonal and orthorhombic phase with reversible lithium insertion/extraction reaction and the larger potential slope from 1.73V to 1V where the lithium insertion processes are favoured by the electric field forces.[32] The specific capacities and coulombic efficiencies of both anode materials were investigated at 0.1 C over 100 cycles to get insights on the charge/discharge electrochemical properties of both TiO_2-based anode materials (Figure 8C). The initial charge/discharge capacities for the PT-TiO_2 and P25 are 228 mA h g^{-1} and 163 m A g^{-1}, and 215 mA h g^{-1} and 168 m A g^{-1}, respectively, giving rise to coulombic efficiencies around 79% and 74%, respectively. The low coulombic efficiency values could be interpreted by the irreversible accumulation of lithium anions inside TiO_2 crystalline network and the subsequent formation of a partial solid electrolyte interphase (SEI) layer. Afterwards, in the second cycle, the charge/discharge capacities decrease to 161 mA h g^{-1} and 151 m A g^{-1} for the nanocomposite and to 142 mA g h^{-1} and 137 mA h g^{-1} for the commercial TiO_2, while the coulombic efficiencies rise up to 100% and 93%, respectively. However, after 100 cycles, the discharges capacities drop off to 109 mA g h^{-1} (76% of capacity retention of the second cycle) for the nanocomposite and 28 mA g h^{-1} (20% of capacity retention regarding to the second cycle) for the commercial TiO_2 LIBs, indicating the superior performance of the nanohybrid anode materials. We have to highlight that the PT-TiO_2 anode nanomaterials delivered a reversible capacity of 107 mA h g^{-1} at 0.1C, which is in the order of other TiO_2 based electrode materials.[35,36]

The rate capabilities at 0.1 C, 0.2 C, 0.5 C, 1 C and 2C were performed to compare the electrochemical performance of both batteries at different current densities (Figure 8D). As it is expected, the capacity of the commercial TiO_2 decrease rapidly at higher rate cycling values. P25

anodes deliver capacities of 145 mA g h^{-1}, 97 mA g h^{-1}, 25 mA g h^{-1}, 11 mA g h^{-1} and 5 mA g h^{-1} at 0.1 C, 0.2 C, 0.5C, 1C and 2C, respectively. On the other hand, PT-TiO_2 nanocomposites exhibit higher capacities of 167 mA g h^{-1}, 140 mA g h^{-1}, 116 mA g h^{-1}, 98 mA h g^{-1} and 84 mA g h^{-1}, respectively, demonstrating the remarkable effect of structural TiO_2 changes produced by the biotemplated approach on the electrochemical performances of the PT-TiO_2 nanocomposite anode electrodes. Notably, lower crystallinity features of the nanocomposite materials could create a number of structural defects in the crystalline TiO_2 networks which allow the transport of Li ions across the defects and in turn the improvements of their performances as anode electrodes. In brief, the obtained capacities values of the PT-TiO_2 nanomaterial are very close to the values reported for high-performance LIBs based on carbon coated hollow TiO_2 microspheres, which represent, up to now, in terms of specific capacity, retention and coulombic efficiency, one of the more successful TiO_2 based lithium ion batteries.[37,38]

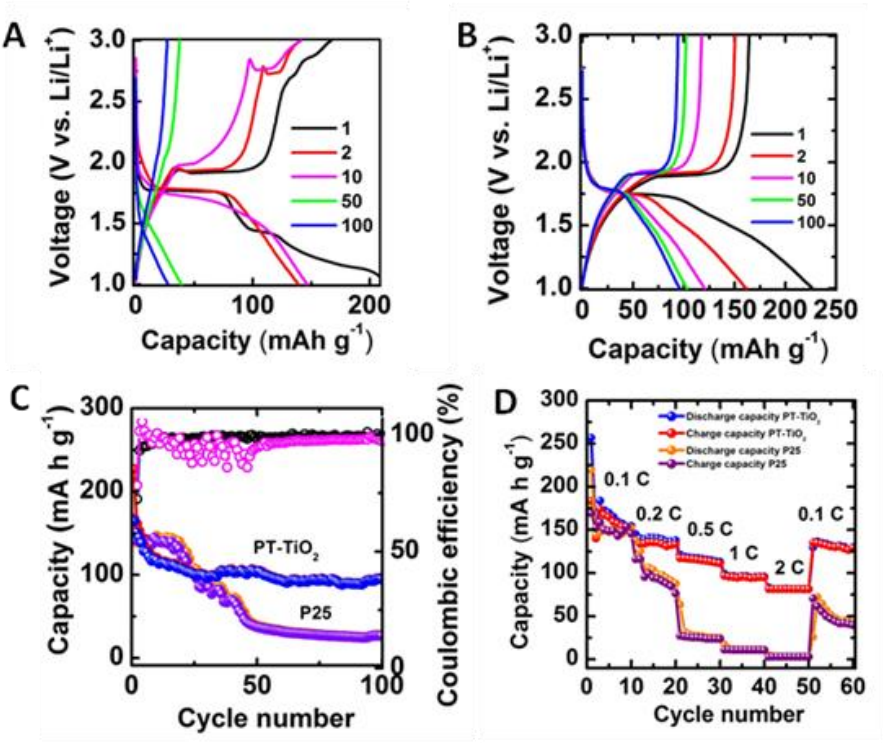

Figure 8. Charge-discharge profiles for (A) P25 TiO_2 and (B) PT-TiO_2 at a current rate of 0.1 A g^{-1} (approximate to 0.3C). (C) Specific capacity and coulombic efficiency versus cycle number for PT-TiO_2 and P25 TiO_2 materials, respectively, at 0.1 A g^{-1} and (D) Rate capability performances of both anode materials at different current densities from 0.1 C to 2C, returning to 0.1 C for PT-TiO_2 and P25, respectively. (1C = 335 $mAhg^{-1}$)

Conclusions

Valorisation of egg white from expired eggs was accomplished through their use as template in the synthesis of titania with upgraded morphological properties. Surface area increased from 10 to 139 m^2 g^{-1} by employing egg white as template. Remarkably the synthetic process was carried out by a water-free (or any solvent) mechanochemical strategy. The obtained composite material presented a homogenous particles size distribution, with a mean radius of 5.2 nm. PT-TiO_2 demonstrated to be a good candidate for their use in catalytic and energy

storage applications. Controllable and selective oxidation of diphenyl sulfide was achieved employing PT-TiO_2 as catalytic material. In addition, the synthesized nanocomposite has demonstrated to be a successful candidate for the design of highly sustainable LIBs batteries. The template approach enables a notable improvement on the TiO_2 surfaces properties which in turn boost the Li ion transport across the crystalline semiconductor network and the electrochemical performances of the resulting LIBs.

Acknowledgements

Rafael Luque gratefully acknowledges MINECO for funding project CTQ2016-78289-P, co-financed with FEDER funds. Daily Rodriguez-Padron also gratefully acknowledges MINECO for providing a research contract under the same project. Alain R. Puente-Santiago acknowledges the Research Program of the University of Cordoba for its financial support through a postdoctoral contract (Modality 5.1). M.J. Muñoz-Batista acknowledges MINECO for a Juan de la Cierva postdoctoral contract (Ref. FJCI-2016-29014). RUDN University Program 5-100 has contribute to the preparation of this work.

References

(1) Palo, D. R.; Dagle, R. A.; Holladay, J. D. Methanol Steam Reforming for Hydrogen Production. *Chem. Rev.* **2007**, *107*, 3992–4021. https://doi.org/10.1021/CR050198B.

(2) Chu, S.; Cui, Y.; Liu, N. The Path towards Sustainable Energy. *Nat. Mater.* **2017**, *16* (1), 16–22. https://doi.org/10.1038/nmat4834.

(3) Grey, C. P.; Tarascon, J. M. Sustainability and in Situ Monitoring in Battery Development. *Nat. Mater.* **2017**, *16* (1), 45–56. https://doi.org/10.1038/nmat4777.

(4) Rodriguez-Padron, D.; Puente-Santiago, A.; Balu, A. M.; Munoz-Batista, M. J.; Luque, R. Environmental Catalysis: Present and Future. *ChemCatChem* **2018**, *10*. https://doi.org/10.1002/cctc.201801248.

(5) Muñoz Batista, M. J.; Rodríguez-Padrón, D.; Puente Santiago, A. R.;

Luque, R. Mechanochemistry: Towards Sustainable Design of Advanced Nanomaterials for Electrochemical Energy Storage and Catalytic Applications. *ACS Sustain. Chem. Eng.* **2018**, *6* (8), 9530–9544. https://doi.org/10.1021/acssuschemeng.8b01716.

(6) Colmenares, J. C.; Luque, R. Heterogeneous Photocatalytic Nanomaterials: Prospects and Challenges in Selective Transformations of Biomass-Derived Compounds. *Chem. Soc. Rev.* **2014**, *43* (3), 765–778. https://doi.org/10.1039/C3CS60262A.

(7) Kubacka, A.; Fernández-García, M.; Colón, G. Advanced Nanoarchitectures for Solar Photocatalytic Applications. *Chem. Rev.* **2012**, *112* (3), 1555–1614. https://doi.org/10.1021/cr100454n.

(8) Varma, R. S. Journey on Greener Pathways: From the Use of Alternate Energy Inputs and Benign Reaction Media to Sustainable Applications of Nano-Catalysts in Synthesis and Environmental Remediation. *Green Chem.* **2014**, *16* (4), 2027. https://doi.org/10.1039/c3gc42640h.

(9) Lops, C.; Ancona, A.; Di Cesare, K.; Dumontel, B.; Garino, N.; Canavese, G.; Hérnandez, S.; Cauda, V. Sonophotocatalytic Degradation Mechanisms of Rhodamine B Dye via Radicals Generation by Micro- and Nano-Particles of ZnO. *Appl. Catal. B Environ.* **2019**, *243*, 629–640. https://doi.org/10.1016/J.APCATB.2018.10.078.

(10) Zuliani, A.; Munoz-Batista, M. J.; Luque, R. Microwave-Assisted Valorization of Pig Bristles: Towards Visible Light Photocatalytic Chalcocite Composites. *Green Chem.* **2018**, *20*, 3001–3007. https://doi.org/10.1039/C8GC00669E.

(11) Li, W.; Wang, F.; Liu, Y.; Wang, J.; Yang, J.; Zhang, L.; Elzatahry, A. A.; Al-Dahyan, D.; Xia, Y.; Zhao, D. General Strategy to Synthesize Uniform Mesoporous TiO2/Graphene/Mesoporous TiO2 Sandwich-Like Nanosheets for Highly Reversible Lithium Storage. *Nano Lett.* **2015**, *15* (3), 2186–2193. https://doi.org/10.1021/acs.nanolett.5b00291.

(12) Lee, D.-H.; Lee, B.-H.; Sinha, A. K.; Park, J.-H.; Kim, M.-S.; Park, J.; Shin, H.; Lee, K.-S.; Sung, Y.-E.; Hyeon, T. Engineering Titanium

Dioxide Nanostructures for Enhanced Lithium-Ion Storage. *J. Am. Chem. Soc.* **2018**, jacs.8b09487. https://doi.org/10.1021/jacs.8b09487.

(13) Linsebigler, A. L.; Lu, G.; Yates, J. T. Photocatalysis on TiO2 Surfaces: Principles, Mechanisms, and Selected Results. *Chem. Rev.* **1995**, *95* (3), 735–758. https://doi.org/10.1021/cr00035a013.

(14) Henderson, M. A. A Surface Science Perspective on TiO2 Photocatalysis. *Surf. Sci. Rep.* **2011**, *66* (6–7), 185–297. https://doi.org/10.1016/J.SURFREP.2011.01.001.

(15) Roy, P.; Berger, S.; Schmuki, P. TiO2 Nanotubes: Synthesis and Applications. *Angew. Chem. Int. Ed. Engl.* **2011**, *50* (13), 2904–2939. https://doi.org/10.1002/anie.201001374.

(16) Dahl, M.; Liu, Y.; Yin, Y. Composite Titanium Dioxide Nanomaterials. *Chem. Rev.* **2014**, *114* (19), 9853–9889. https://doi.org/10.1021/cr400634p.

(17) Chen, X.; Mao, S. S. Titanium Dioxide Nanomaterials: Synthesis, Properties, Modifications, and Applications. *Chem. Rev.* **2007**, *107* (7), 2891–2959. https://doi.org/10.1021/cr0500535.

(18) Mattsson, A.; Leideborg, M.; Larsson, K.; Westing, G.; Österlund, L. Adsorption and Solar Light Decomposition of Acetone on Anatase TiO 2 and Niobium Doped TiO2 Thin Films. *J. Phys. Chem. B* **2006**, *110* (3), 1210–1220. https://doi.org/10.1021/jp055656z.

(19) Soria, J.; Sanz, J.; Sobrados, I.; Coronado, J. M.; Herna, M. D.; Fresno, F. Water-Hydroxyl Interactions on Small Anatase Nanoparticles Prepared by the Hydrothermal Route. *J. Phys. Chem. C* **2010**, *114*, 16534–16540.

(20) Muñoz-Batista, M. J.; Nasalevich, M. A.; Savenije, T. J.; Kapteijn, F.; Gascon, J.; Kubacka, A.; Fernández-García, M. Enhancing Promoting Effects in G-C3N4-Mn+/CeO2-TiO2 Ternary Composites: Photo-Handling of Charge Carriers. *Appl. Catal. B Environ.* **2015**, *176–177*, 687–698. https://doi.org/10.1016/j.apcatb.2015.04.051.

(21) Caudillo-Flores, U.; Muñoz-Batista, M. J.; Kubacka, A.; Zárate-Medina, J.; Cortés, J. A.; Fernández-García, M. Measuring and Interpreting Quantum Efficiency of Acid Blue 9 Photodegradation

Using TiO2-Based Catalysts. *Appl. Catal. A Gen.* **2018**, *550* (July 2017), 38–47. https://doi.org/10.1016/j.apcata.2017.10.016.

(22) Muñoz-Batista, M. J.; Caudillo-Flores, U.; Ung-Medina, F.; del Carmen Chávez-Parga, M.; Cortés, J. A.; Kubacka, A.; Fernández-García, M. Gas Phase 2-Propanol Degradation Using Titania Photocatalysts: Study of the Quantum Efficiency. *Appl. Catal. B Environ.* **2017**, *201*, 400–410. https://doi.org/10.1016/j.apcatb.2016.08.014.

(23) Agency, U. S. E. P. Sustainable Management of Food https://www.epa.gov/sustainable-management-food (accessed Nov 30, 2018).

(24) Gao, S.; Yan, Y.; Chen, G. External Water-Free Approach toward TiO2Nanoparticles Embedded in Biomass-Derived Nitrogen-Doped Carbon. *ACS Sustain. Chem. Eng.* **2016**, *4* (3), 844–850. https://doi.org/10.1021/acssuschemeng.5b00904.

(25) Yan, J.; Wu, G.; Li, L.; Yu, A.; Sun, X.; Guan, N. Synthesis of Uniform TiO2 Nanoparticles with Egg Albumen Proteins as Novel Biotemplate. *J. Nanosci. Nanotechnol.* **2010**, *10* (9), 5767–5775. https://doi.org/10.1166/jnn.2010.2501.

(26) Liu, R.-L.; Ji, W.-J.; He, T.; Zhang, Z.-Q.; Zhang, J.; Dang, F.-Q. Fabrication of Nitrogen-Doped Hierarchically Porous Carbons through a Hybrid Dual-Template Route for CO2 Capture and Haemoperfusion. *Carbon N. Y.* **2014**, *76*, 84–95. https://doi.org/10.1016/J.CARBON.2014.04.052.

(27) Luna-Lama, F.; Rodríguez-Padrón, D.; Puente-Santiago, A. R.; Muñoz-Batista, M. J.; Caballero, A.; Balu, A. M.; Romero, A. A.; Luque, R. Non-Porous Carbonaceous Materials Derived from Coffee Waste Grounds as Highly Sustainable Anodes for Lithium-Ion Batteries. *J. Clean. Prod.* **2019**, *207*, 411–417. https://doi.org/10.1016/J.JCLEPRO.2018.10.024.

(28) Muñoz-Batista, M. J.; Ballari, M. M.; Cassano, A. E.; Alfano, O. M.; Kubacka, A.; Fernández-García, M. Ceria Promotion of Acetaldehyde Photo-Oxidation in a TiO2-Based Catalyst: A Spectroscopic and Kinetic Study. *Catal. Sci. Technol.* **2014**, *5* (3), 1521–1531. https://doi.org/10.1039/C4CY01293C.

(29) Verma, S.; Baig, R. B. N.; Nadagouda, M. N.; Varma, R. S. Sustainable Strategy Utilizing Biomass: Visible-Light-Mediated Synthesis of γ-Valerolactone. *ChemCatChem* **2016**, *8* (4), 690–693. https://doi.org/10.1002/cctc.201501352.

(30) Rodríguez-Padrón, D.; Puente-Santiago, A. R.; Caballero, A.; Balu, A. M.; Romero, A. A.; Luque, R. Highly Efficient Direct Oxygen Electro-Reduction by Partially Unfolded Laccases Immobilized on Waste-Derived Magnetically Separable Nanoparticles. *Nanoscale* **2018**, *10* (8), 3961–3968. https://doi.org/10.1039/C8NR00512E.

(31) Ouyang, W.; Muñoz-Batista, M. J.; Kubacka, A.; Luque, R.; Fernández-García, M. Enhancing Photocatalytic Performance of TiO2 in H 2 Evolution via Ru Co-Catalyst Deposition. *Appl. Catal. B Environ.* **2018**, *238* (July), 434–443. https://doi.org/10.1016/j.apcatb.2018.07.046.

(32) Gao, S.; Yan, Y.; Chen, G. External Water-Free Approach toward TiO2 Nanoparticles Embedded in Biomass-Derived Nitrogen-Doped Carbon. *ACS Sustain. Chem. Eng.* **2016**, *4* (3), 844–850. https://doi.org/10.1021/acssuschemeng.5b00904.

(33) Radko, M.; Kowalczyk, A.; Bidzińska, E.; Witkowski, S.; Górecka, S.; Wierzbicki, D.; Pamin, K.; Chmielarz, L. Titanium Dioxide Doped with Vanadium as Effective Catalyst for Selective Oxidation of Diphenyl Sulfide to Diphenyl Sulfonate. *J. Therm. Anal. Calorim.* **2018**, *132* (3), 1471–1480. https://doi.org/10.1007/s10973-018-7119-9.

(34) Al-Maksoud, W.; Daniele, S.; Sorokin, A. B. Practical Oxidation of Sulfides to Sulfones by H2O2catalysed by Titanium Catalyst. *Green Chem.* **2008**, *10* (4), 447–451. https://doi.org/10.1039/b717696a.

(35) Ren, M.; Xu, H.; Li, F.; Liu, W.; Gao, C.; Su, L.; Li, G.; Hei, J. Sugarapple-like N-Doped TiO2@carbon Core-Shell Spheres as High-Rate and Long-Life Anode Materials for Lithium-Ion Batteries. *J. Power Sources* **2017**, *353*, 237–244. https://doi.org/10.1016/J.JPOWSOUR.2017.04.015.

(36) Senthil, C.; Kesavan, T.; Bhaumik, A.; Yoshio, M.; Sasidharan, M. Nitrogen Rich Carbon Coated TiO2 Nanoparticles as Anode for

High Performance Lithium-Ion Battery. *Electrochim. Acta* **2017**, *255*, 417–427. https://doi.org/10.1016/J.ELECTACTA.2017.10.001.

(37) Jin, Z.; Yang, M.; Wang, J.; Gao, H.; Lu, Y.; Wang, G. One-Pot Fabrication of Hierarchical Nanosheet-Based TiO2-Carbon Hollow Microspheres for Anode Materials of High-Rate Lithium-Ion Batteries. *Chem. - A Eur. J.* **2016**, *22* (17), 6031–6036. https://doi.org/10.1002/chem.201505099.

(38) Liu, H.; Li, W.; Shen, D.; Zhao, D.; Wang, G. Graphitic Carbon Conformal Coating of Mesoporous TiO2 Hollow Spheres for High-Performance Lithium Ion Battery Anodes. *J. Am. Chem. Soc.* **2015**, *137* (40), 13161–13166. https://doi.org/10.1021/jacs.5b08743.

4.5. Benign-by-design orange peel-templated nanocatalyst for continuous flow conversion of levulinic acid to N-heterocycles

Finally, another biomass derived residue, in this case orange peel, was used for the preparation of titania based materials through a mechanochemical protocol. Such methodology has demonstrated, along this doctoral thesis, to be highly suitable for the preparation of biomass-templated materials with good textural and morphological features. The synthesized samples were post-modified with ruthenium nanoparticles, at different concentrations. The catalytic performance of such materials was investigated in the reductive amination of levulinic acid towards *N*-heterocycles under flow conditions.

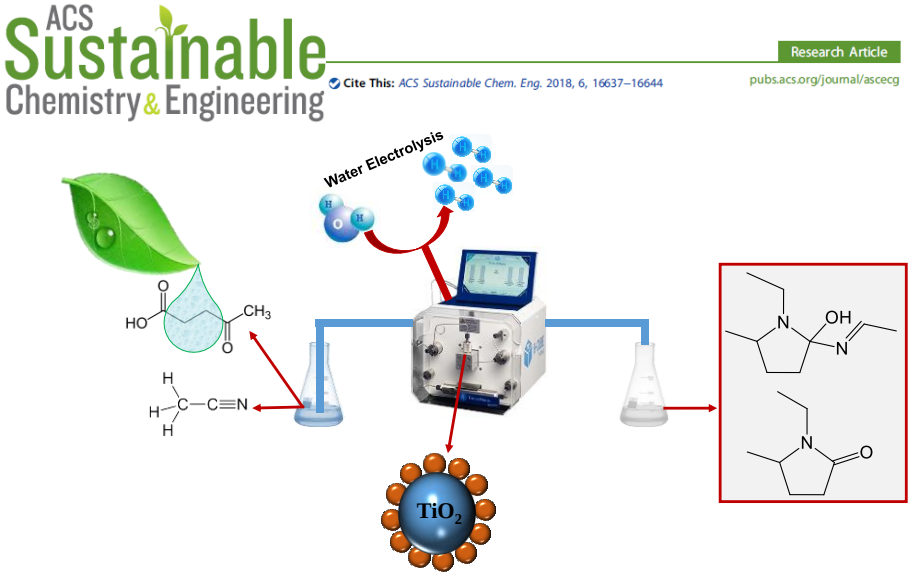

Daily Rodríguez-Padrón, Alain R. Puente-Santiago, Alina M. Balu, Antonio A. Romero, Mario J. Muñoz-Batista, Rafael Luque. **2018**. Benign-by-design Orange peel-templated nanocatalysts for continuous flow conversion of levulinic acid to N-heterocycles. **ACS Sustainable Chemistry & Engineering.** 6(12), 16637-16644. 10.1021/acssuschemeng.8b03896. . IF: 6.14.

Benign-by-design Orange peel-templated nanocatalysts for continuous flow conversion of levulinic acid to N-heterocycles

Daily Rodríguez-Padrón,[a] Alain R. Puente-Santiago.[a] Alina M. Balu,[a] Antonio A. Romero,[a] Mario J. Muñoz-Batista,[a]* and Rafael Luque[a,b]*

[a]*Departamento de Química Orgánica, Universidad de Córdoba, Campus de Rabanales, Edificio Marie Curie (C-3), Ctra Nnal IV-A, Km 396, E14014, Cordoba, Spain.* * *M.j.M-B jmunoz385x@gmail.com, R.L. rafael.luque@uco.es*

[b]*Peoples Friendship University of Russia (RUDN University), 6 Miklukho-Maklaya Str., 117198, Moscow, Russia*

In this work, two different strategies have been employed to explore the potential valorization of biomass waste. A TiO_2 based sample was prepared by a dry-milling strategy, involving orange peel valorization towards nanostructured materials. Subsequently ruthenium deposition was accomplished by a chemical reduction method to obtain different ruthenium loadings on the titania support. The prepared catalysts were characterized using a multi-technique approach in terms of chemical, structural and morphological properties. Levulinic acid, a typical model molecule associated with lignocellulosic biomass, was subsequently converted into N-heterocycles in a continuous flow reactor. The prepared Ru-TiO_2 systems exhibited outstanding catalytic performance in terms of conversion and selectivity. Maximum activity (79%, 85 % selectivity to 1-ethyl-2-(ethylideneamino)-5-methylpyrrolidin-2-ol) was achieved for the sample containing 3 wt. % Ru, homogeneously deposited on the titania surface. The obtained results were interpreted with help of a complete post-reaction characterization analysis of the most active sample.

Introduction

Biomass valorization recently emerged as an alternative for the production of fuels, chemicals and materials.[1–5] Particularly, biomass-derived chemicals have been a green source to generate starting compounds towards sustainable Nitrogen heterocycles (N-heterocycles) production.[6] N-heterocycles represent an attractive family of organic compounds which are present in many of the most demanded chemicals in modern society.[7] Their unique ability to be used as biomimetics as well as active pharmacophores makes them valuable compounds towards the design of a myriad of chemicals such as photocatalysts, dyes, agrochemical compounds, polymers and pharmaceutical compounds.[8–11] In this remark various approaches have been developed for the preparation of N-heterocycles. Yan et al. have developed an easy one-pot synthetic protocol to generate pyrrole molecules from waste shrimp shells derived compounds with significant yields.[12] Furthermore, Xu et al. have reported an innovative method to directly transform different lignocellulose biomass in a number of heterocycles including pyrroles, pyridines and indoles using commercial zeolites as catalysts via thermocatalytic conversion and ammonization approach.[13] Recently, a one-step synthesis from glucose of N-heterocycles products via an efficient ammonium catalytic system was successfully achieved using tungsten-based catalysts.[14] Among the most promising platform molecules towards biomass valorization is levulinic acid (LA), accessible from lignocellulosic biomass via simple hydrolysis.[1,15–17] LA has been employed to produce valuable N-substituted pyrrolidones by a catalytic reductive amination process followed by subsequent cyclization.[18–20] However, the majority of the synthetic procedures to obtain N-heterocycles usually employs compounds derived from limited resources derived from crude oil using complex multistep-processes.[21,22] Additionally, the most employed catalysts for these reactions are those with excellent π-Lewis acidity like palladium, copper and transition-metal complexes, which lead to undesirable drawbacks such as poor recyclability of catalysts, long reaction times, harsh reaction conditions, toxic organic solvents, among others.[23–26] It is worth to point out that

approaches towards the synthetic studies of N-heterocyclic compounds have also been commonly carried out in batch conditions, keeping significant limitations for their direct application at large scale production. Consequently, finding new synthetic pathways for N-heterocycles through the development of sustainable heterogeneous catalysts, together with the application of flow chemistry desirably offers advantages such as facile scale-up, energy safety, well-defined flows, enhance heat and mass transfer.

Ultimately, a number of attempts have been directed to the design of heterogeneous catalysts employing a green strategy (benign-by-design). Significant breakthroughs have been achieved by our research group taking into account the advantages of mechanochemical processes including short reaction times and the possibility of avoiding circumventing solvent issues.[27,28] In this regard, our research group have developed various nanomaterials, employing biomass-derived residues as sacrificial templates.[27–30]

In this work, biomass valorization was applied towards both chemicals and materials preparation. Titania based catalytic systems were prepared employing orange peel as sacrificial template and utilized in the conversion of levulinic acid, a biomass derived molecule, resulting in attractive nitrogen-heterocycle compounds.

Experimental

Synthesis of TiO_2-based nanocatalysts

Prior to the preparation of the titania based catalyst, orange peel residues were firstly milled in a ball mill (Emax ball mill model, Retsch), at 900 rpm for 10 min (Figure S1). The preparation of TiO_2 was then carried out by a mechanochemical protocol, employing a 2:1 metal precursor (titanium isopropoxide)/sacrificial template (orange peel) ratio, in a Retsch PM100 ball mill (125 mL reaction chamber and eighteen 10 mm stainless steel balls). Subsequently, the material was oven-dried at 100 °C for 24 h, and finally calcined at 500 °C for 2h.

In a second step, Ru was deposited onto the TiO_2 nanomaterial by a chemical deposition method using $RuCl_3 \bullet xH_2O$. The titania was firstly

suspended in deionized water for 30 min, followed by adding the proper quantity of $RuCl_3 \bullet xH_2O$, in order to prepare three catalysts with 1, 2 and 3 wt. % of Ru, respectively. A hydrazine solution was then added with the consequent ruthenium deposition (Ru/hydrazine molar ratio 1/3). The obtained mixture was stirred for 30 min and the final solids were filtered, washed with deionized water and dried at 100 °C.

Material characterization

XRD analysis was performed in the Bruker D8 Advance Diffractometer with the LynxEye detector. The XRD patterns were recorded in a 2θ scan range from 10° to 70°. Bruker Diffrac-plus Eva software, supported by Power Diffraction File database, was used for phase identification. N_2 adsorption-desorption measurements were performed in the Micromeritics ASAP 2000 equipment. The samples were previously degassed for 24 h under vacuum ($p<10^{-2}$ Pa). In addition, SEM-EDX images were acquired in the JEOL-SEM JSM-7800 LV scanning microscope.

XPS experiments were accomplished in an ultrahigh vacuum multipurpose surface analysis instrument SpecsTM. The samples were evacuated overnight under vacuum (10^{-6} Torr) and subsequently, measurements were performed at room temperature using a conventional X-ray source with a Phoibos 150-MCD energy detector. XPS spectra were analyzed employing the XPS CASA software. In addition, ruthenium leaching in the reaction solutions, tacked every 10 min during 90 min, for the 3%Ru/TiO_2 catalyst was determined by ICP–MS in an Elan DRC-e (PerkinElmer SCIEX) spectrometer.

Catalytic experiments

Catalytic experiments were performed in the H-Cube Mini Plus™ flow hydrogenation reactor. The four catalysts (TiO_2, 1% Ru/TiO_2, 2% Ru/TiO_2 and 3% Ru/TiO_2) were packed (ca. 0.1 g of catalyst per cartridge) in 30 mm long ThalesNano CatCarts. Firstly, the system was washed with 1) methanol and 2) acetonitrile (0.3 mL/min, 20 min for each solvent). A 0.3 M solution of levulinic acid in acetonitrile was subsequently pumped through and the optimum reaction conditions were set (90 °C, 50 bar, 0.3 mL/min). During the reaction, hydrogen was *in situ* generated by water electrolysis in the H-Cube equipment. The continuous flow process was

followed for 90 min, collecting samples every 10 min for further analysis by GC-MS. Finally, the system was washed with acetonitrile in order to recover the employed catalysts and accomplish a post-reaction characterization.

The catalytic performance (in terms of conversion and selectivity) was investigated by gas chromatography (GC) in an Agilent 6890N gas chromatograph (60 mL min^{-1} N_2 carrier flow, 20 psi column top head pressure) using a flame ionization detector (FID). The capillary column HP-5 (30 m × 0.32 mm × 0.25 mm) was employed. In addition, the collected liquid fractions were analysed by GC-MS using the 5977B High Efficiency Source (HES) GC/MSD, in order to identify the obtained products.

Results and discussion

The preparation of Ru/TiO_2 nanocatalysts was performed using a two-steps strategy (Scheme 1). Firstly, the synthesis of TiO_2 was successfully achieved by a solvent-free mechanochemical approach using orange peel and titanium isopropoxide as metal precursor. Orange peel residues are employed as sacrificial template to obtain nanostructured TiO_2 with defined morphology. Orange peel residues have been characterized by SEM and EDX-mapping analyses in order to understand their morphology and chemical nature (Figure S2). Titanium isopropoxide assembles around the surface of the template via chemical and/or physical adherence to form transitional composites and then, the aforementioned template is selectively removed from such composite structure.[31] Titanium isopropoxide is hydrolysed by the presence of water from the orange peel residues. The obtained titanium hydroxide is thermally treated at 500 ºC with the consequent formation of the desired titania. In order to determine the influence of the sacrificial template on the morphology and crystalline structure of titania, a material was prepared by a similar protocol in absence of the orange peel residues. N_2-physisorption measurements of the obtained titania displayed low surface area (>5 m^2g^{-1}), which in turn prevent the efficient ruthenium deposition and therefore affect the catalytic performance. In addition,

XRD and SEM analyses of the aforementioned titania have been provided in Figure S3.

Specially, the employment of a mechanochemical protocol, which does not require the use of solvents and/or additional reagents, together with the valorization of an underutilized residue (e.g. orange peel), may pave the way to further design of sustainable alternatives for the preparation of nanomaterials.

In a second step, the deposition of different ruthenium loading on the TiO_2 surface was rendered by a simple chemical deposition procedure (Scheme 2). In order to characterize the obtained materials, several techniques were employed, including X-ray Diffraction (XRD), N_2-physisorption, Scanning Electronic Microscopy and X-ray Photoelectronic Spectroscopy (XPS).

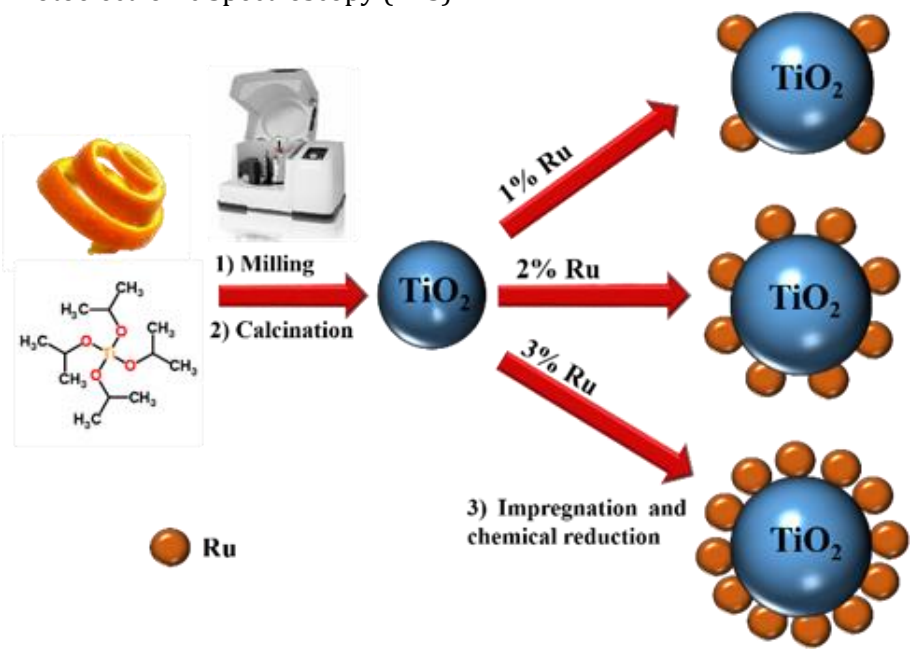

Scheme 1. Overview of the synthetic strategy of Ru/TiO_2 nanocatalysts.

Determination of surface areas, pore volumes and pore diameters of the designed catalysts was achieved by N_2 physisorption analysis. N_2 adsorption-desorption isotherms of the four samples exhibited a type IV profile, corresponding with mesoporous materials, with a low surface

area (ca. 20 $m^2 g^{-1}$). The deposition of ruthenium on the TiO_2 support gave rise to a slightly decrease of surface area and pore volume values (as expected). However, the aforementioned properties did not considerably change after ruthenium deposition and therefore their effect on the catalytic performance can be considered as negligible (Table 1). In general, textural properties were satisfying, taken into account the catalysts preparation method.

XRD measurements were performed in order to investigate the crystal structure and arrangement of the TiO_2 based catalysts. XRD patterns of the four samples exhibited several peaks at 25.3°, 37.0°, 37.9°, 38.7°, 48.1°, 53.9°, 55.2° and 62.7°, which can be associated to (101), (103), (004), (112), (200), (105), (201) and (204) diffraction of anatase phase, respectively (Figure 1).[32,33] Besides, as it is expected ruthenium deposition process did not affect considerably the crystallinity and arrangement of the TiO_2 nanomaterial. Additionally, size, microstrain and cell parameters were evaluated with XRD using the Williamson–Hall formalism (Table 2),[34] demonstrating that there are not considerable changes and therefore corroborating that anatase phase was not affected by the deposition method, with no doping of the TiO_2 structure. These results are also in good agreement with previous reports in which chemical deposition methods were employed to deposit noble metals onto anatase titania surfaces.[35,36] The effective deposition of Ru-entities on the TiO_2 surface was evidenced from SEM-mapping results. Figure 2 displayed the presence of titanium, oxygen and ruthenium, which are homogeneously distributed on the materials surface.

Table 1. Morphological properties of the samples.

Sample	S_{BET}[a] ($m^2 g^{-1}$)	V_{BJH}[b] ($cm^3 g^{-1}$)	D_{BJH}[c] (nm)
TiO_2	20	0.12	14.8
1%Ru/TiO_2	20	0.11	14.9
2%Ru/TiO_2	19	0.11	15.0
3%Ru/TiO_2	19	0.10	16.0

[a] S_{BET}: specific surface area was calculated by the Brunauer–Emmett Teller (BET) equation. [b] V_{BJH}: pore volumes were calculated by the Barret–Joyner–Halenda (BJH) equation using the adsorption branch of

the isotherm. [c] D_{BJH}: mean pore size diameter was calculated by the Barret–Joyner–Halenda (BJH) equation using the desorption branch of the isotherm.

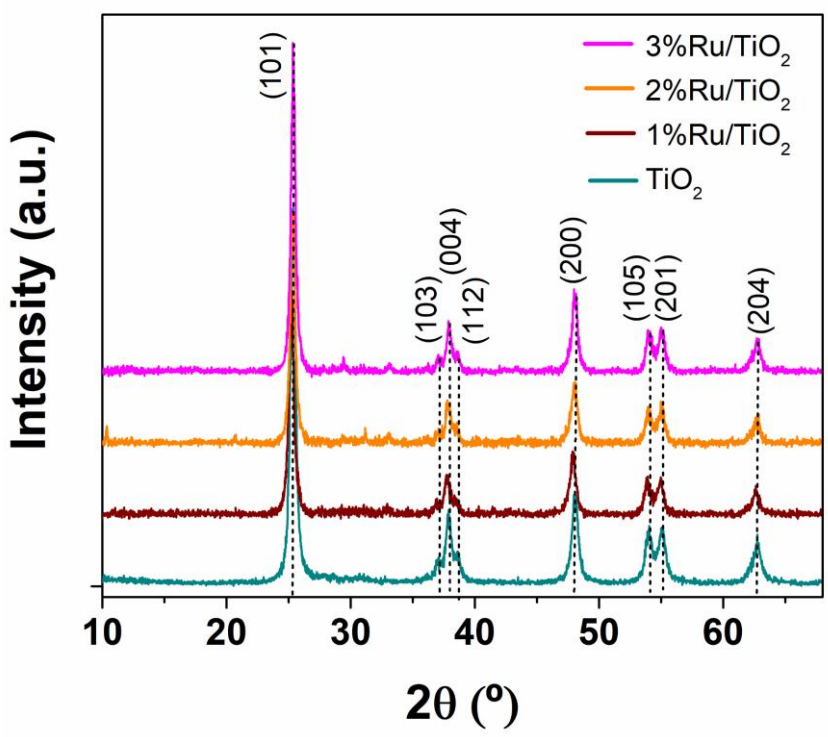

Figure 1. XRD patterns of TiO_2, 1%Ru/TiO_2, 2%Ru/TiO_2 and 3%Ru/TiO_2 materials.

Table 2. XRD-derived parameters for the anatase phase of the samples.

Sample	**Size (nm) TiO_2**	**Microstrain $\langle\xi^2\rangle^{1/2}$ (x 10^{-3}) TiO_2**	**TiO_2 Anatase Cell parameters (Å)**	
			a	**b**
TiO_2	20	2.2	3.79	9.49
1%Ru/TiO_2	20	2.3	3.79	9.50
2%Ru/TiO_2	20	2.1	3.79	9.49
3%Ru/TiO_2	20	2.1	3.79	9.49

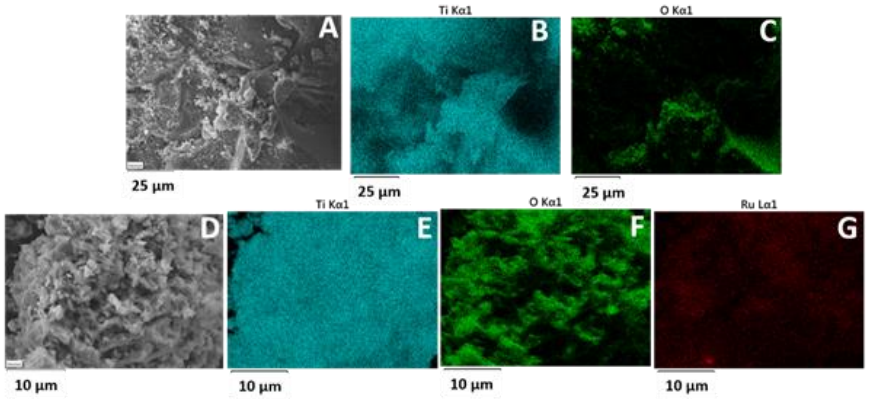

Figure 2. SEM-mapping images of (A-C) TiO_2 and (D-G) 3%Ru/TiO_2 nanomaterials.

XPS analysis of Ru/TiO_2 samples and titania reference were carried out in order to provide information related to the carbon, oxygen, titanium and ruthenium components. In particular, C1s, O1s, Ti2p, Ru3p and Ru3d XPS regions were analysed. As discussed in previous contributions, analysis of ruthenium-titania containing materials shows a very strong overlap between Ru3d and C1s as well as Ti2p and Ru3p regions.[15,37,38] Figure 3A displays the spectra obtained for C1s and Ru3d XPS regions. Spectra show a clear contribution at ca. 281.9 eV (only for Ru/TiO_2 samples) which can be associated with Ru(IV) oxidation state.[28,39] The shape/width suggest that no significant contribution of metallic ruthenium is present on surface of the particles. This contribution was used as reference during the fitting methodology as is presented in Figure 3B for $3Ru/TiO_2$ sample.[15,28,39] XPS information concerning Ti2p and Ru3p XPS regions for the samples are graphically presented in Figure 3C. Absence of significant differences can be noticed for the Ti $2p_{3/2}$ XPS peak, which was observed at ca. 458.6 eV for all Ru/TiO_2 samples and titania reference.[39] This value is characteristic of Ti(IV) species of titania materials. In addition, an increase of the width in the $Ru3p_{3/2}/Ti2p_{1/2}$ region for samples containing Ru respect to the pure titania reference was detected. In fact, higher FWHM could be observed with an increase in Ru

amount. Deconvolution analysis (Figure 3D) confirmed a dominant Ru (IV) oxidation state with typical emission lines at ca. 462.6 ($Ru3p_{3/2}$) and ca. 485.6 eV ($Ru3p_{1/2}$).[15] A summary of representative contribution positions for Ru (3d and 3p), O1s and Ti2p as well as Ru/Ti surface atomic ratio is presented in Table 3. Table 3 also presents Ru/Ti ratio obtained by ICP-MS, denoted as e.a. As expected, Ru concentration changes through the series for both superficial and bulk species. Comparison of the ratios indicates that Ru component showed a good dispersion on the surface of the active support (Figure 4). In fact, the graphical representation of superficial Ru/Ti ratio vs bulk Ru/Ti ratio displayed a linear trend indicating similar dispersion values of the co-catalysts on the titania surface.

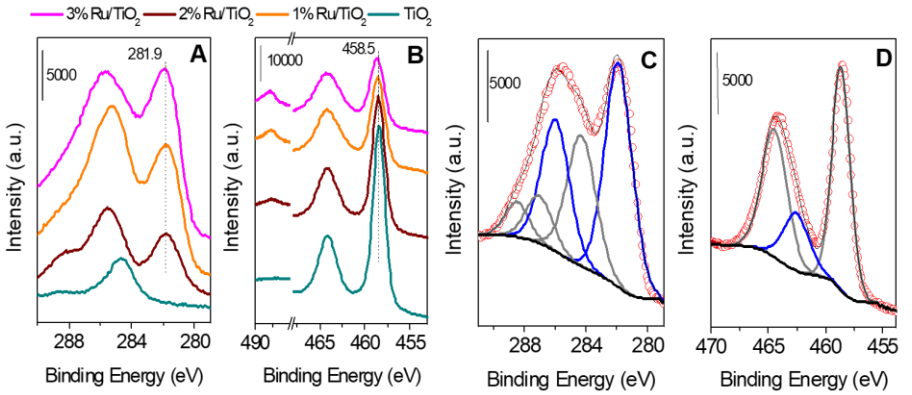

Figure 3. XPS spectra of TiO_2, 1%Ru/TiO_2, 2%Ru/TiO_2 and 3%Ru/TiO_2 nanomaterials for (A) C1s-Ru3d and (B) Ti2p-Ru3p regions. Deconvoluted XPS spectra of 3%Ru/TiO_2 for (C) C1s-Ru3d and (D) Ti2p-Ru3p regions.

Table 3. XPS binding energy and Ru/Ti atomic ratio.

Sample	**Ti 2p / eV**	**O 1s / eV**	**Ru 3d $_{5/2}$ / eV**	**Ru 3p $_{1/2}$ / eV**	**Ru 3p $_{3/2}$ / eV**	**Ru/Ti**	**Ru/Ti (e.a.) ICP-MS**
TiO_2	458.5	530.2	-		-	-	-
1%Ru/TiO_2	458.5	530.2	281.8	485.6	462.5	0.1	0.09
2%Ru/TiO_2	458.5	530.4	281.8	485.6	462.5	0.4	0.18
3%Ru/TiO_2	458.6	530.5	281.9	485.7	462.6	0.6	0.26

Figure 4. Ru/Ti atomic ratio. Bulk (e.a.) vs Superficial (XPS).

The catalytic performance of the prepared materials was evaluated in the conversion of levulinic acid to nitrogen-heterocycles under continuous flow conditions. The three ruthenium containing samples were tested, as well as the non-modified TiO_2 nanomaterial (Figure 5A). In addition, a blank measurement was performed without catalyst, revealing that the reaction does not proceed in absence of an effective catalytic system. After obtaining a pseudo-stationary state (typically obtained after 60 min of reaction for all the catalysts, ca. 2 mins residence time), conversions of 4%, 17% and 76% were obtained for 1%Ru/TiO_2, 2%Ru/TiO_2 and 3%Ru/TiO_2, respectively, while the non-modified TiO_2 did not display any catalytic activity (Figure 5A, red ball solid line), with a high selectivity towards N-heterocycle formation (Figure 5A).

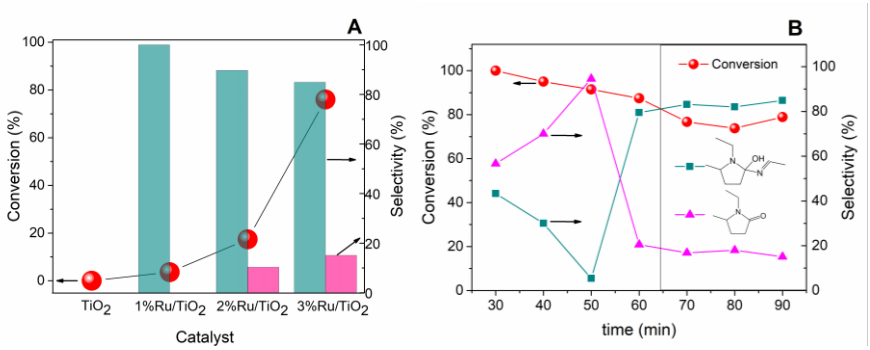

Figure 5. (A) Catalytic performance of TiO_2, 1%Ru/TiO_2, 2%Ru/TiO_2 and 3%Ru/TiO_2 nanocatalyst. Reaction conditions: 0.3 M levulinic acid solution in acetonitrile, 0.1 g of catalyst, T=90 °C, P=50 bar, Flow=0.3 mL/min. (B) Catalytic activity of 3%Ru/TiO_2 during 90 min of reaction. (Color code. Blue: selectivity to 1-ethyl-5-methylpyrrolidin-2-one, Pink: selectivity to 1-ethyl-2-(ethylideneamino)-5-methylpyrrolidin-2-ol).

Figure 5B shows details of the flow catalytic process for the most active sample. It is worth to mention that the formation of the heterocycles was achieved through the Paal-Knorr Pyrrole synthesis (Scheme 2) which involves the condensation of a 1,4-dicarbonyl compound such as levulinic acid, with an excess of amine (in this case, ethyl amine).[40] The latest molecule was generated *in-situ* by hydrogenation of acetonitrile, acting both as solvent and reactant. It has been reported that the cyclization step is rate-determining and involves a nucleophilic addition on a carbonyl group by the nitrogen of an intermediate. The 1,4-dicarbonyl molecule acts as an electrophile both in the initial step of the reaction with the amine and in the cyclization step.[41]

Additionally, upon formation of the cyclic compound, the reaction proceeded via alcohol dehydration to form the corresponding alkene. The hydroxyl (OH) group donates two electrons to H^+ generating an alkylloxonium ion, which can act as a good leaving group. The obtained product ($C_7H_{11}NO$, 125.08 g/mol) was detected and identified by GC-MS. However, the selectivity towards this molecule was almost negligible. In turn, under hydrogen pressure, the obtained alkene is effectively hydrogenated to give rise to 1-ethyl-5-methylpyrrolidin-2-one, $C_7H_{13}NO$

(127.10 g/mol), observed as major product in the first 50 min reaction (Figure 5B).

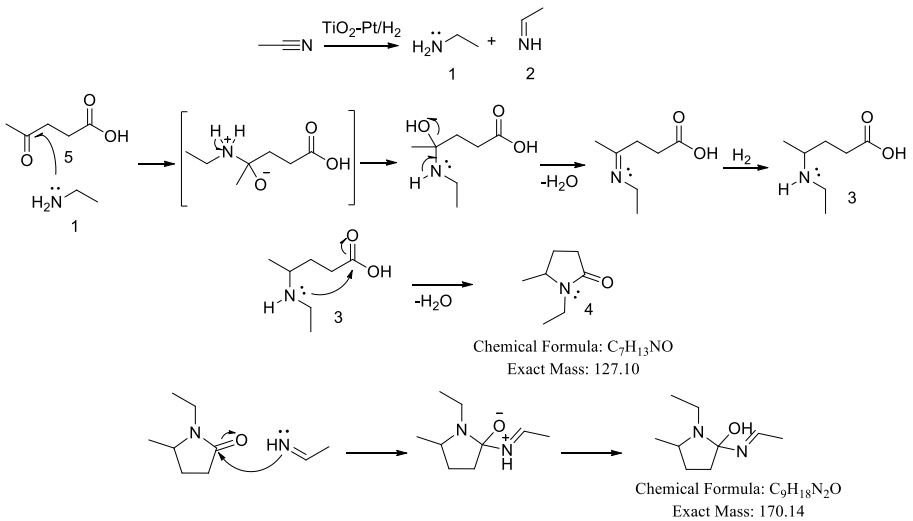

Scheme 2. Mechanism of the N-heterocycle formation.

After 60 min of reaction, the selectivity drastically changed, providing 1-ethyl-2-(ethylideneamino)-5-methylpyrrolidin-2-ol, $C_9H_{18}N_2O$ (170.14 g/mol), as major product. This result can be attributed to the partial loss of activity and stabilization of the catalyst (Figure 5B). Consequently, hydrogenation of acetonitrile did not just give rise to ethylamine but also to ethanimine, which can further attack the carbonyl group of 1-ethyl-5-methylpyrrolidin-2-one with the selective formation of 1-ethyl-2-(ethylideneamino)-5-methylpyrrolidin-2-ol. Afterwards, the conversion and selectivity values remained stable, achieving a pseudo-stationary state.

In addition, 3%Ru/TiO_2 was applied, for comparison, in the synthesis of N-heterocycles, from levulinic acid and ethylamine (Figure S4). Similar conversion values were obtained, with higher selectivity to 1-ethyl-5-methylpyrrolidin-2-one. This result can be understood, considering the absence of ethanimine in the reaction employing ethylamine instead of acetonitrile.

The structure of the obtained products was deduced from the observed fragmentation pattern in the MS spectra (Figure 6). Notably, both compounds possess a common fragmentation pattern, suggesting that $C_7H_{13}NO$ and $C_9H_{18}N_2O$ possess a common skeleton and therefore that 1-ethyl-2-(ethylideneamino)-5-methylpyrrolidin-2-ol may be obtained by a synthetic pathway which involves 1-ethyl-5-methylpyrrolidin-2-one. The molecular ions of $C_7H_{13}NO$ and $C_9H_{18}N_2O$ were found at m/z 127.1 and 169.1, respectively. The molecular ions easily fragment by α-cleavage preferably yielding an $[M\text{-}CH_3]^+$ ion, m/z 112.1 and 154.1 related to $C_7H_{13}NO$ and $C_9H_{18}N_2O$, respectively. Subsequently, $[M\text{-}CH_3]^+$ ion of 1-ethyl-2-(ethylideneamino)-5-methylpyrrolidin-2-ol further fragmented, explaining the base peak at m/z 112.1 corresponding to $[M\text{-}C_2H_4N]^+$.

In order to compare the catalytic performance of the catalyst obtained employing orange peel, with other commercial materials, the investigated reaction was performed using 3%Ru/P25 and commercial Ru/C. 3%Ru/P25 was synthesized employing commercial titania (P25) and applying the same ruthenium deposition method. The obtained results revealed that the orange peel templated nanocatalyst exhibited outstanding and competitive activity in terms of conversion and selectivity. Moreover, it is worth to mention that 3%Ru/TiO_2 was obtained by a sustainable solvent free methodology, which represents an outstanding alternative from an environmental point of view (Figure S5).

In order to further support the proposed deactivation and stabilization of the most active material, a complete post-reaction characterization analysis was carried out. XPS, XRD and SEM-mapping measurement of the spent 3%Ru/TiO_2 were conducted (Figure 6). Figure 6A shows C1s-Ru3d XPS region of both, fresh and used 3Ru%/TiO_2 sample. The spectra exhibited essentially the same electronic properties for fresh and spent catalyst (Ti(IV) and Ru(IV) oxidation state). Noticeable, no evidence of reduced Ru species were detected. Interestingly, XPS measurements revealed the increment of the C/Ru ratio which can be mainly associated with the adsorption of carbon species on the catalytic surface. This carbon species could be associated with coke and/or organic surface compounds which could block the active sites and lead to the proposed deactivation process. XRD analysis of the used catalyst gives rise to

similar XRD patterns, confirming that crystallinity and anatase arrangement did not suffer significant changes during the reaction (Figure 6B). However, it is worth to mention, the appearance of a broad and weak peak around 29° which is usually attributed to the presence of carbon-based compounds on the material surface.[42]

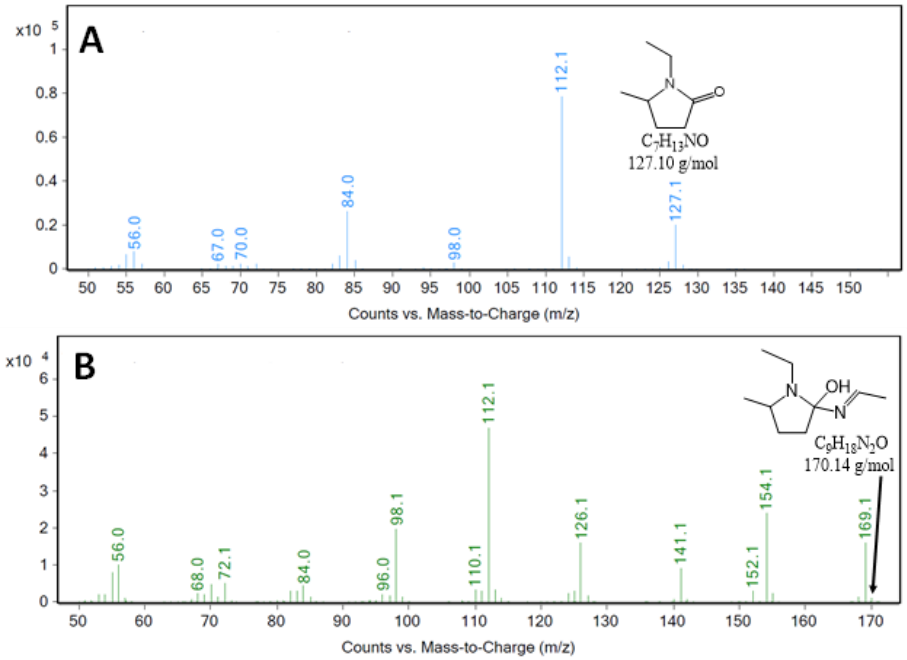

Figure 6. (A-B) GC-MS spectra of the products obtained from the continuous flow conversion of levulinic acid to Nitrogen-heterocycles.

Solid chemical composition analysis was tested by ICP-MS of the reaction solutions (Table 4). As described in the experimental section and presented in Figure 5B, liquid samples were collected every 10 min. Certain leaching was observed in the first 60 min, associated with Ru weakly linked to the TiO_2 support (Table 4). However, it represents such leaching represents ca. 1% of the initial concentration of ruthenium in 3%Ru/TiO_2. Remarkably, after 60 min of reaction, no leaching was further detected, coinciding with the proposed stabilization of the activity and selectivity of the system. Furthermore, SEM-mapping analysis corroborated the aforementioned ICP results as can be observed in Figure 5 (C-F). In summary, the stabilization of the catalytic properties

under the operating condition is complex involving the accumulation of carbon entities on the surfaces, a leaching process as well as stabilization of hydrodynamic conditions.

Table 4. Ruthenium concentration at the liquid phase of collected samples for the flow catalytic reaction using the 3%Ru/TiO_2 catalyst.

time	Ru concentration/ ug L^{-1}
30	95
50	15
60	ND
90	ND

ND: denotes not detected.

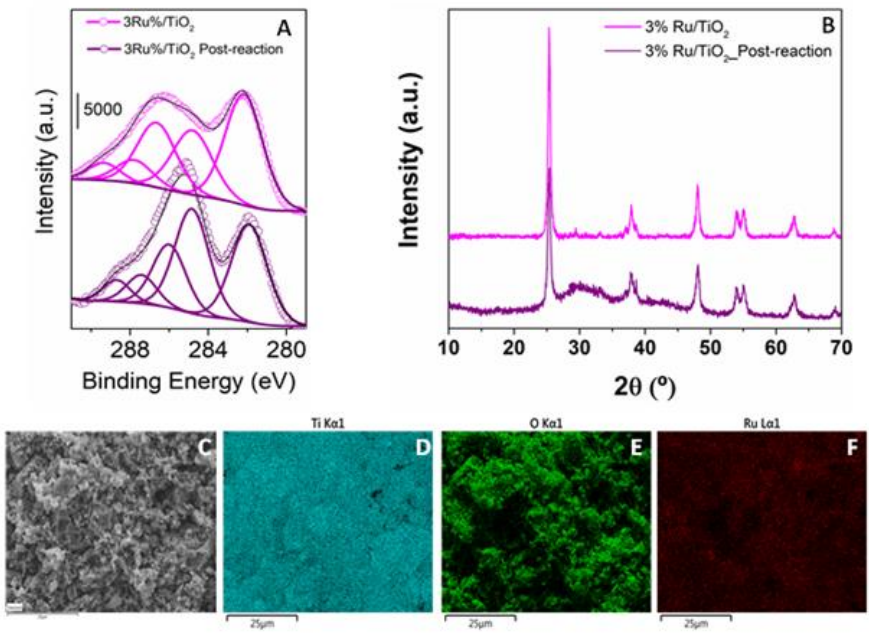

Figure 7. (A) XPS spectra in the C1s region and (B) XRD patterns of the fresh and used 3%Ru/TiO_2 catalyst. (C-F) SEM-mapping images of 3%Ru/TiO_2 material.

Conclusions

Two routes for biomass valorisation have been explored, for both materials and chemicals preparation. Regarding materials synthesis, a mechanochemical protocol was developed for the synthesis of TiO_2 based nanocatalysts employing orange peel, an underutilized residue, as sacrificial template. The obtained titania was successfully modified with different ruthenium concentrations by a chemical deposition method. The conversion of levulinic acid, a biomass-derived compound, was subsequently investigated in a continuous flow process employing the ruthenium-modified TiO_2 systems. Ethylamine, in-situ generated by hydrogenation of acetonitrile, reacted with levulinic acid to obtain N-heterocyclic compounds with a wide range of potential applications. The ruthenium concentration in the catalysts resulted to be a determining factor for the reaction conversion. Particularly, the sample with higher ruthenium percentage gives rise to the best catalytic performance, achieving a pseudo-stationary state after 60 min of reaction, with remarkable conversion and selectivity values. This contribution paves the way for the design of sustainable strategies for biomass valorisation towards chemicals and materials.

Conflicts of interest

There are no conflicts to declare.

Acknowledgements

Mario J. Munoz-Batista gratefully acknowledges MINECO for a JdC contract (Ref. FJCI-2016-29014). Rafael Luque gratefully acknowledges support from MINECO under project CTQ2016-78289-P, co-financed with FEDER funds. Daily Rodriguez-Padrón and Alain R. Puente-Santiago also gratefully acknowledge MINECO for providing research contracts under the same project. Alain R. Puente-Santiago also acknowledges University of Cordoba for a contract from “Plan Propio de Investigacion” Ref. PP2018-12-0672.

This publication has been prepared with support from RUDN University Program 5-100.

References

1 Alonso, D. M., Bond, J. Q., Dumesic, J. A. Catalytic conversion of biomass to biofuels. *Green Chem.*, **2010**, *12*(9), 1493–1513.

2 Colmenares, J. C., Luque, R. Heterogeneous photocatalytic nanomaterials: prospects and challenges in selective transformations of biomass-derived compounds. *Chem. Soc. Rev.*, **2014**, *43*(3), 765–778.

3 Binder, J. B., Raines, R. T. Simple chemical transformation of lignocellulosic biomass into furans for fuels and chemicals. *J. Am. Chem. Soc.* **2009**, *131*(5), 1979–1985.

4 Besson, M., Gallezot, P., Pinel, C. Conversion of biomass into chemicals over metal catalysts. *Chem. Rev.*, **2014**, *114*(3), 1827–1870.

5 Zhou, C. H., Xia, X., Lin, C. X., Tong, D. S., Beltramini, Catalytic conversion of lignocellulosic biomass to fine chemicals and fuels. J. *Chem. Soc. Rev.*, **2011**, *40*(11), 5588-5617.

6 Bhusal, R. P., Sperry, J., Flexible synthesis of diverse N-heterocycles from substrates attainable from biomass. *Green Chem.*, **2016**, *18*(8), 2453–2459.

7 Vitaku, E., Smith, D. T., Njardarson, J. T. Analysis of the structural diversity, substitution patterns, and frequency of nitrogen heterocycles among US FDA approved pharmaceuticals: miniperspective. *J. Med. Chem.*, **2014**, *57*(24), 10257–10274.

8 Kurpil, B., Savateev, A., Papaefthimiou, V., Zafeiratos, S., Heil, T., Özenler, S., Dontsova D., Antonietti, M. Hexaazatriphenylene doped carbon nitrides—Biomimetic photocatalyst with superior oxidation power. *Appl. Catal. B Environ.*, **2017**, *217*, 622–628.

9 Agalave, S. G., Maujan, S. R., Pore, V. S. Click chemistry: 1, 2, 3-triazoles as pharmacophores. *Chem. - An Asian J.*, **2011**, *6*(10), 2696–2718.

10 Hong, M., Tang, X., Falivene, L., Caporaso, L., Cavallo, L., Chen, E. Y. X. Proton-transfer polymerization by N-heterocyclic carbenes: monomer and catalyst scopes and mechanism for converting dimethacrylates into unsaturated polyesters. *J. Am. Chem. Soc.*, **2016**, *138*(6), 2021–2035.

11 Lu, L. Q., Chen, J. R., Xiao, W. J. Development of cascade reactions for the concise construction of diverse heterocyclic architectures. *Acc. Chem. Res.*, **2012**, *45*(8), 1278–1293.

12 Gao, X., Chen, X., Zhang, J., Guo, W., Jin, F., Yan, N. Transformation of chitin and waste shrimp shells into acetic acid and pyrrole. *ACS Sustain. Chem. Eng.*, **2016**, *4*(7), 3912–3920.

13 Xu, L., Yao, Q., Deng, J., Han, Z., Zhang, Y., Fu, Y., Huber G. W., Guo, Q. Renewable N-heterocycles production by thermocatalytic conversion and ammonization of biomass over ZSM-5. *ACS Sustain. Chem. Eng.*, **2015**, *3*(11), 2890–2899.

14 Chen, X., Yang, H., Hülsey, M. J., Yan, N. One-step synthesis of N-heterocyclic compounds from carbohydrates over tungsten-based catalysts. *ACS Sustain. Chem. Eng.*, **2017**, *5*(11), 11096–11104.

15 Xu, C., Ouyang, W., Munoz-Batista, M., Fernandez-Garcia, M., Luque, R. Highly active catalytic Ru/TiO2 nanomaterials for continuous flow production of γ-valerolactone. *ChemSusChem*, **2018**, DOI:10.1002/cssc.201800667.

16 Luque, R. Benign-by-design catalysts and processes for biomass conversion.*Curr. Opin. Green Sustain. Chem.*, **2016**, *2*, 6–9.

17 Kumar, P., Barrett, D. M., Delwiche, M. J., Stroeve, P. Methods for pretreatment of lignocellulosic biomass for efficient hydrolysis and biofuel production. *Ind. Eng. Chem. Res.*, **2009**, *48*(8), 3713–3729.

18 Huang, Y. B., Dai, J. J., Deng, X. J., Qu, Y. C., Guo, Q. X., Fu, Y. Ruthenium-Catalyzed Conversion of Levulinic Acid to Pyrrolidines by Reductive Amination. *ChemSusChem*, **2011**, *4*(11), 1578–1581.

19 Du, X. L., He, L., Zhao, S., Liu, Y. M., Cao, Y., He, H. Y., Fan, K. N. Hydrogen-Independent reductive transformation of carbohydrate biomass into γ-valerolactone and pyrrolidone derivatives with supported gold catalysts. *Angew. Chemie*, **2011**, *123*(34), 7961–

7965.

20 Touchy, A. S., Hakim Siddiki, S. M. A., Kon, K., Shimizu, K. I. Heterogeneous Pt catalysts for reductive amination of levulinic acid to pyrrolidones. *ACS Catal.*, **2014**, *4*(9), 3045–3050.

21 Rizk, T., Bilodeau, E. J. F., Beauchemin, A. M. Synthesis of Pyridines and Pyrazines Using an Intramolecular Hydroamination-Based Reaction Sequence. *Angew. Chemie*, **2009**, *121*(44), 8475–8477.

22 Venugopal, A., Sarkari, R., Anjaneyulu, C., Krishna, V., Kumar, M. K., Narender, N., Padmasri, A. H. Influence of acid-base sites on ZnO–$ZnCr_2O_4$ catalyst during dehydrocyclization of aqueous glycerol and ethylenediamine for the synthesis of 2-methylpyrazine: Kinetic and mechanism studies. *Appl. Catal. A Gen.*, **2014**, *469*, 398–409.

23 Chassaing, S., Bénéteau, V., Pale, P. Green Catalysts based on Zeolites for Heterocycle Synthesis. *Curr. Opin. Green Sustain. Chem.*, **2018**, *10*, 35–39.

24 Nakamura, I., Yamamoto, Y. Transition-metal-catalyzed reactions in heterocyclic synthesis. *Chem. Rev.*, **2004**, *104*(5), 2127–2198.

25 Guo, X. X., Gu, D. W., Wu, Z., Zhang, W. Copper-catalyzed C–H functionalization reactions: Efficient synthesis of heterocycles. *Chem. Rev.*, **2015**, *115*(3), 1622–1651.

26 Zeni, G., Larock, R. C. Synthesis of heterocycles via palladium π-olefin and π-alkyne chemistry *Chem. Rev.*, **2004**, *104*(5), 2285–2310.

27 Muñoz Batista, M. J., Rodríguez-Padrón, D., Puente Santiago, A. R., Luque, R. Mechanochemistry: towards sustainable design of advanced nanomaterials for electrochemical energy storage and catalytic applications. *ACS Sustain. Chem. Eng.*, **2018**, acssuschemeng.8b01716.

28 Xu, C., De, S., Balu, A. M., Ojeda, M., Luque, R. Mechanochemical synthesis of advanced nanomaterials for catalytic applications. *Chem. Commun.*, **2015**, *51*(31), 6698–6713.

29 Francavilla, M., Pineda, A., Romero, A. A., Colmenares, J. C., Vargas, C., Monteleone, M., Luque, R. Efficient and simple reactive milling preparation of photocatalytically active porous ZnO

nanostructures using biomass derived polysaccharides. *Green Chem.*, **2014**, *16*(5), 2876–2885.

30 Rodríguez-Padrón, D., Puente-Santiago, A. R., Caballero, A., Balu, A. M., Romero, A. A., Luque, R. Highly efficient direct oxygen electro-reduction by partially unfolded laccases immobilized on waste-derived magnetically separable nanoparticles. *Nanoscale*, **2018**, *10*(8), 3961–3968.

31 Rodríguez-Padrón, D., Balu, A. M., Romero, A. A., Luque, R. New bio-nanocomposites based on iron oxides and polysaccharides applied to oxidation and alkylation reactions. *Beilstein J. Org. Chem.*, **2017**, *13*, 1982–1993.

32 Muñoz-Batista, M. J., Gómez-Cerezo, M. N., Kubacka, A., Tudela, D., Fernández-García, M. Role of interface contact in CeO_2–TiO_2 photocatalytic composite materials. *ACS Catal.*, **2014**, *4*(1), 63–72.

33 Yang, H. G., Liu, G., Qiao, S. Z., Sun, C. H., Jin, Y. G., Smith, S. C., Zou, J., Cheng, H. M., Lu, G. Q. Solvothermal synthesis and photoreactivity of anatase TiO_2 nanosheets with dominant {001} facets. *J. Am. Chem. Soc.*, **2009**, *131*(11), 4078–4083.

34 Williamson, G. K., Hall, W. H. X-ray line broadening from filed aluminium and wolfram. *Acta Metall.*, **1953**, *1*(1), 22–31.

35 Fontelles-Carceller, O., Muñoz-Batista, M. J., Conesa, J. C., Fernández-García, M., Kubacka, UV and visible hydrogen photo-production using Pt promoted Nb-doped TiO2 photo-catalysts: Interpreting quantum efficiency. A. *Appl. Catal. B Environ.*, **2017**, *216*, 133–145.

36 Caudillo-Flores, U., Muñoz-Batista, M. J., Cortés, J. A., Fernández-García, M., Kubacka, A. UV and visible light driven H_2 photo-production using Nb-doped TiO_2: Comparing Pt and Pd co-catalysts. *Mol. Catal.*, **2017**, *437*, 1–10.

37 Paoli, E. A., Masini, F., Frydendal, R., Deiana, D., Schlaup, C., Malizia, M., Hansen, T. W., Horch, S., Stephens, I. E. L., Chorkendorff, I. Oxygen evolution on well-characterized mass-selected Ru and RuO_2 nanoparticles. *Chem. Sci.*, **2015**, *6*(1), 190–196.

38 Bock, C., Paquet, C., Couillard, M., Botton, G. A., MacDougall, B. R., Size-selected synthesis of PtRu nano-catalysts: reaction and size

control mechanism. *J. Am. Chem. Soc.*, 2004, *126*(25), 8028–8037.

39 Wanger, C. D., Riggs,W. M., Davis, L. E., Moulder, J. F., Muilenberg, G. E. Handbook of x-ray photoelectron spectroscopy: a reference book of standard data for use in x-ray photoelectron spectroscopy, Physical Electronics Division, Perkin-Elmer Corp. **1979**.

40 Li, J. J., Paal–Knorr pyrrole synthesis. In Name Reactions, Springer International Publishing, Cham, **2014**, pp. 454–455.

41 Amarnath, V., Anthony, D. C., Amarnath, K., Valentine, W. M., Wetterau, L. A., Graham, D. G. Intermediates in the Paal-Knorr synthesis of pyrroles. *J. Org. Chem.*, **199**1, *56*(24), 6924–6931.

42 Wen, T., Wang, J., Yu, S., Chen, Z., Hayat, T., Wang, X. Magnetic porous carbonaceous material produced from tea waste for efficient removal of As (V), Cr (VI), humic acid, and dyes. *ACS Sustain. Chem. Eng.*, **2017**, *5*(5), 4371–4380.

Supporting Information

Benign-by-design Orange peel-templated nanocatalysts for continuous flow conversion of levulinic acid to N-heterocycles

Daily Rodríguez-Padrón,[a] Alain R. Puente-Santiago.[a] Alina M. Balu,[a] Antonio A. Romero,[a] Mario J. Muñoz-Batista,[a]* and Rafael Luque[a,b]*

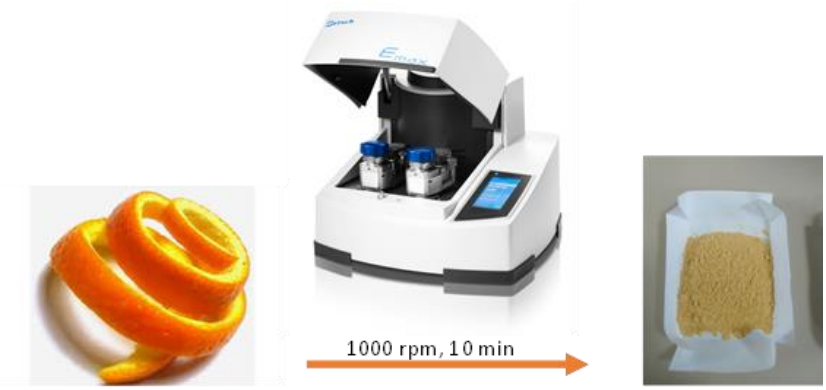

Figure S1. Schematic representation of orange peel pre-treatment.

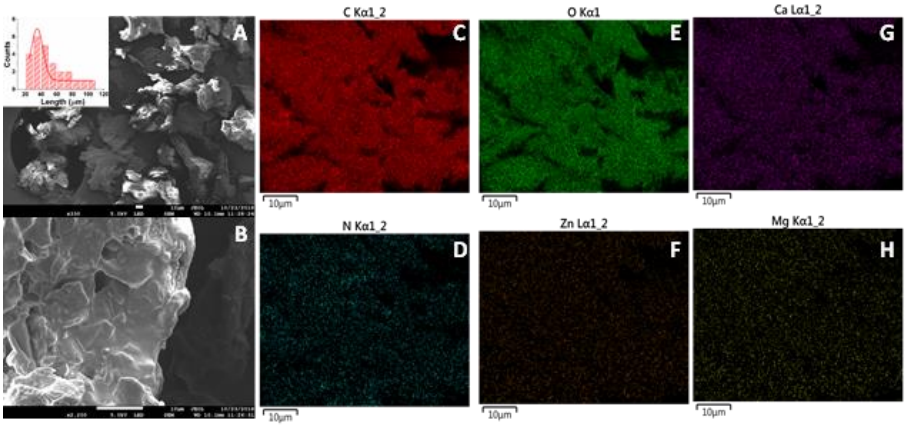

Figure S2. A-B SEM micrographs (Inset: Particle size distribution) and C-H SEM-mapping images of the orange peel dust employed as sacrificial template.

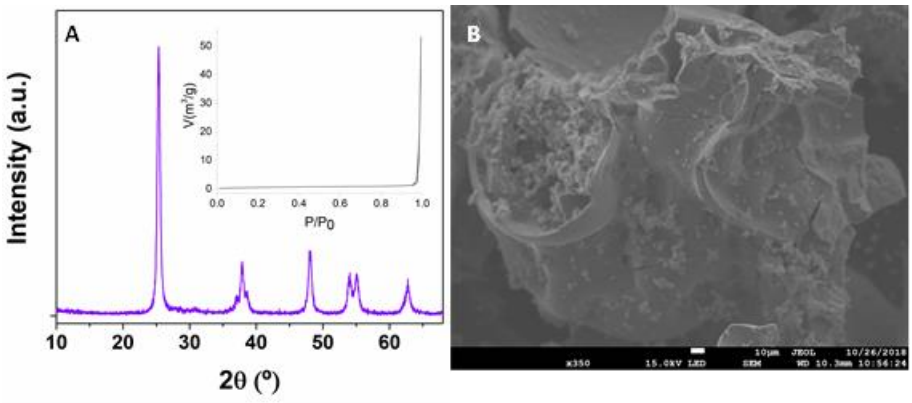

Figure S3. A. XRD pattern (Inset: N_2-physisorption isotherm) and B. SEM image of TiO_2 sample, prepared in absence of orange peel as sacrificial template.

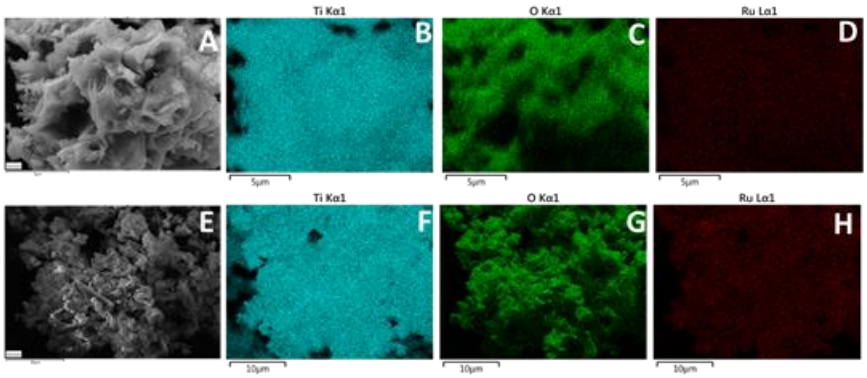

Figure S4. SEM-mapping images of (A-D) 1%Ru/TiO_2 and (E-H) 2%Ru/TiO_2 nanomaterials.

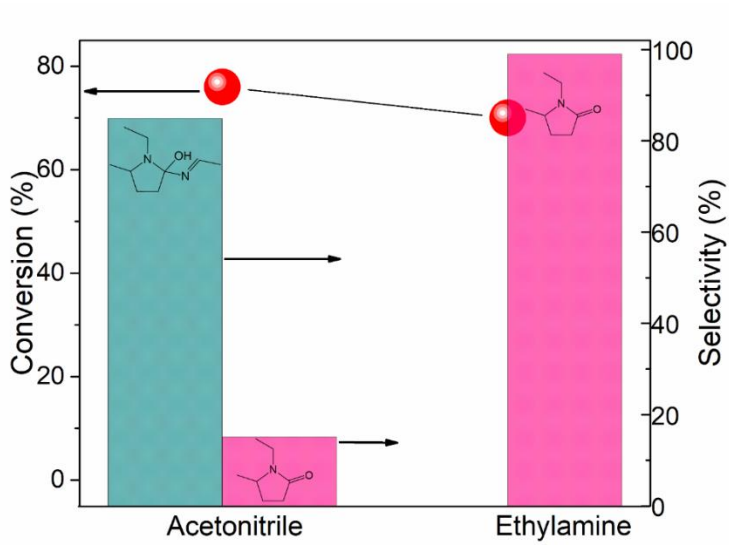

Figure S5. Catalytic performance of 3%Ru/TiO_2 in the synthesis of N-heterocycles, from levulinic acid and ethylamine.

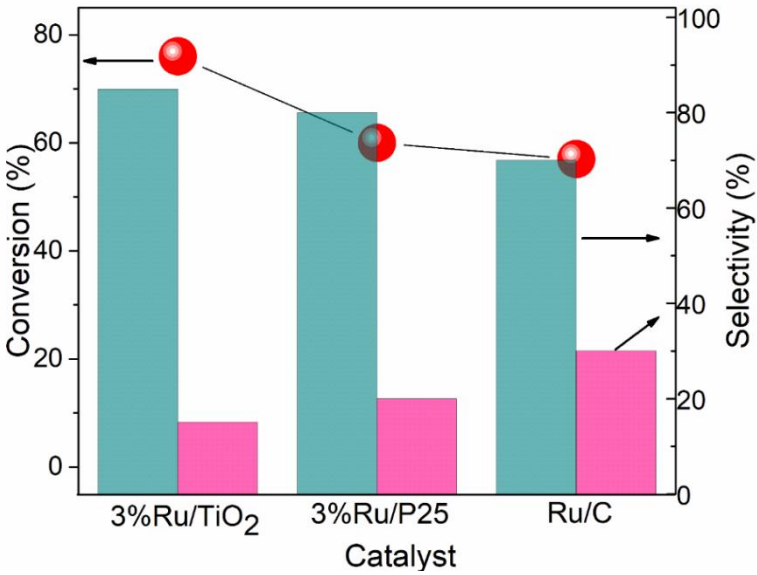

Figure S6. Catalytic performance of 3%Ru/TiO_2, 3%Ru/P25 and Ru/C nanocatalyst. Reaction conditions: 0.3 M levulinic acid solution in acetonitrile, 0.1 g of catalyst, T=90 °C, P=50 bar, Flow=0.3 mL/min

5. Conclusiones

5. Conclusiones

Como resultado de las investigaciones realizadas para la elaboración de la presente Memoria de Tesis Doctoral, pueden extraerse las siguientes conclusiones:

Se ha desarrollado exitosamente un protocolo mecanoquímico para la síntesis de nanobioconjugados, el cual fue evaluado para nanopartículas magnéticas de óxido de hierro y cobalto, así como empleando varias proteínas, específicamente albumina sérica bovina, hemoglobina y lacasa.

Se ha demostrado que el procedimiento desarrollado no daba lugar a cambios en la estructura nativa de las proteínas con alto contenido de α-hélice, como la Hb y la BSA.

Para proteínas como la lacasa, el procedimiento mecanoquímico diseñado puede dar lugar a cambios conformacionales en la estructura secundaria de dicha enzima. Sin embargo estas modificaciones pueden ser beneficiosas, si los centros activos de la enzima, en este caso los centros de cobre, quedan más expuestos, mejorando la respuesta bioelectrocatalítica del material.

Los bioconjugados preparados han sido utilizados exitosamente en el diseño de un supercapacitor con alta durabilidad, pudiendo allanar el camino hacia el desarrollo de dispositivos de almacenamientos de energía bioinspirados más sostenibles.

Los bioconjugados sintetizados también han demostrado ser activos en reacciones catalíticas como la electroreducción de oxígeno y la polimerización oxidativa de fenilendiaminas.

Varios materiales preparados mediante protocolos mecanoquímicos, incluyendo bioconjugados y óxidos metálicos soportados en materiales mesoporosos, demostraron ser catalizadores efectivos para la preparación de nanopartículas fluorescentes basadas en carbono, siguiendo tanto estrategias *top-down* como *botton-up*. El empleo de dichos materiales catalíticos permitió realizar las reacciones en condiciones moderadas, con menores temperaturas y tiempos de reacción.

Los protocolos mecanoquímicos también han sido empleados para la síntesis de nanopartículas de óxidos metálicos empleando residuos de biomasa como plantillas de sacrificio para la obtención de propiedades texturales y morfológicas controladas.

Los óxidos metálicos preparados, incluyendo óxidos de hierro y titanio, han sido empleados con éxito en varias reacciones, tales como la oxidación del difenilsulfuro, la oxidación del isoeugenol para la producción selectiva de vainillina y la aminación reductiva del ácido levulínico para la formación de compuestos heterocíclicos de nitrógeno.

En resumen se puede decir, que los métodos mecanoquímicos pueden ser empleados para la preparación de una amplia gama de materiales, desde bioconjugados, hasta nanopartículas soportadas y óxidos metálicos empleando residuos de la biomasa como plantillas de sacrificio. Los materiales preparados mediante metodologías mecanoquímicas, además del inherente carácter sostenible dado que no se utilizan disolventes ni reactivos adicionales en el proceso de síntesis, han mostrado resultados comparables e incluso mejorados con respecto a materiales similares obtenidos mediante métodos convencionales.

6. Indicios de calidad

Publicaciones totales: 30
Publicaciones totales en primer cuartil (Q1, datos del Journal Citation Reports): 23.
Revistas:

- Chemical Communications (1)
- Green Chemistry (2)
- Beilstein Journal of Organic Chemistry (1)
- Journal of Materials Chemistry A (1)
- Nanoscale (3)
- ACS Sustainable Energy and Engineering (8)
- ACS Applied Energy Materials (1)
- Advanced Energy Materials (1)
- Catalysts (4)
- Catalysis communicatons (1)
- Frontiers in Chemistry (2)
- ChemPhotoChem (1)
- Chemcatchem (1)
- Journal of Cleaner Production (1)
- Journal of Materials Chemistry C (1)
- Separation and Purification Technology (1)

Citas totales: 182

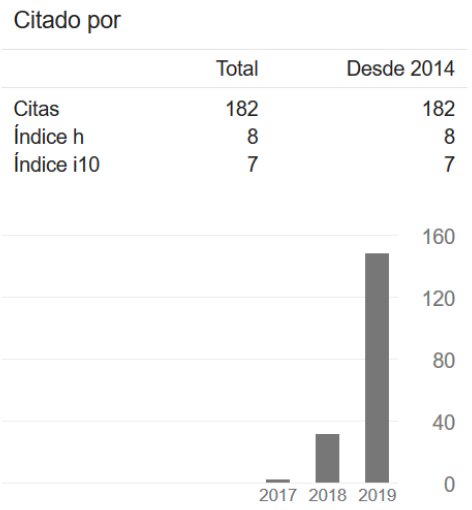

Otros indicadores científicos

7. Otros indicadores científicos

CURSOS DE POSTGRADO

2016

- "Separation and characterization of nanomaterials by AF^4 analysis (Asymmetric Flow Field Flow Fractionation)" University of Cordoba, Spain.

2017

- "EPR, basis and application in heterogeneous catalysis" University of Cordoba, Spain.
- "PerkinElmer Seminar INTOUR" University of Cordoba, Spain.

POSTERS Y PRESENTACIONES ORALES

- **2016 Daily Rodríguez-Padrón**, Alain Puente-Santiago, Almudena Benítez, Alina M. Balu, Antonio A. Romero, Rafael Luque, "Unprecedented Synthetic Approach To Obtain Bio-Modified Magnetic Materials", (Poster), V Congress of young researchers from the University of Cordoba, November 30th - December 2nd, Cordoba, Spain.
- **2017 Daily Rodríguez-Padrón**, Alain Puente-Santiago, Almudena Benítez, Alina M. Balu, Antonio A. Romero, Rafael Luque, "Bio-inspired functionalized magnetic nanomaterials as energy storage devices", (Oral), NANOUCO VI, January 25th-26th, Cordoba, Spain.
- **2017 Daily Rodríguez Padrón**, M. Dolores Márquez Medina, Mª Salud Climent Bellido, Alina M. Balu, Antonio A. Romero, Rafael Luque, " **From Organic Waste to Exceptional Magnetic Materials**", (Poster), Third Workshop & Fourth MC Meeting, March 27th-28th, Torremolinos (Malaga), Spain.
- **2017 Daily Rodríguez Padrón**, Araceli García, Borja Murube, Antonio A. Romero, Rafael Luque, Alina M. Balu, "**From walnut green shell to valuable products**", (Poster), Third Workshop & Fourth MC Meeting, March 27th-28th, Torremolinos (Malaga), Spain.

- **2017** M. Dolores Márquez, **Daily Rodríguez Padrón**, Alina M. Balu, Antonio A. Romero, Rafael Luque, "Isoeugenol conversion to vanilin using separable magnetic materials", (Poster), Third Workshop & Fourth MC Meeting, March 27th-28th, Torremolinos (Malaga), Spain.
- **2018 Daily Rodríguez-Padrón**, Alexander Jodlowski; Alain Puente-Santiago, Gustavo de Miguel, Alina M. Balu, Antonio A. Romero, Rafael Luque, "Síntesis de materiales fluorescentes empleando bioconjugados magnéticos activos catalíticamente", (Oral), VI Congreso de Jóvenes Investigadores de la Universidad de Córdoba, España
- **2018 Daily Rodríguez-Padrón**, Alain Puente-Santiago, Almudena Benítez, Alina M. Balu, Antonio A. Romero, Rafael Luque, "Synthesis of carbon-based fluorescent polymers driven by catalytically active magnetic bioconjugates", (Poster), mc2-Materials, Characterization and Catalysis Workshop, ETH, Suiza.
- **2018 Daily Rodríguez-Padrón**, Manuel Algarra, Luis A.C. Tarelho, Jorge Frade, Ana Franco Gustavo de Miguel, José Jiménez, Enrique Rodríguez-Castellón, Rafael Luque, "Catalyzed microwave-assisted synthesis of Carbon Quantum dots from **lignocellulosic residues**" (Oral), 4th Workshop & 5th MC meeting. Tesalonika, Grecia
- **2018 D. Rodríguez-Padrón**, A.R. Puente-Santiago, A. Caballero, A. Pineda, A.M. Balu, A.A. Romero, R. Luque, "Highly efficient direct oxygen electro-reduction by partially unfolded laccases immobilized on waste derived magnetically separable nanoparticles" (Poster), 4th Workshop & 5th MC meeting. Tesalonika, Grecia
- **2018** M. Dolores Marquez, **D. Rodríguez-Padrón**, F. Luna Lama, A. PuenteSantiago, A. Caballero, A. Balu, A. Romero, R. Luque, "N**-rich carbon material from coffee waste** and hemoglobin for high capacity battery electrodes" (Poster), 4th Workshop & 5th MC meeting. Tesalonika, Grecia
- **2018** A.R. Puente-Santiago, **D. Rodríguez-Padrón**, C. Silveira, L.O. Martins, S. Todorovic, F. Folgosa, M. Texeira, S. Verma, R.S. Varma, R. Luque, "High electrocatalytic oxidation currents of model lignin compounds driven by recombinat CotAlaccase modified sulfonate graphitic carbon nitride materials" (Poster), 4th Workshop & 5th MC meeting. Tesalonika, Grecia.
- **2018 Daily Rodríguez-Padrón**, Mario J. Muñoz-Batista, "Development of interdisciplinary skills through laboratory experiences" (Poster), II

Congreso Internacional Virtual de Investigación e Innovación Educativa CIVINEDU 2018.

- **2018** Mario J. Muñoz-Batista, **Daily Rodríguez-Padrón** "Development of a virtual laboratory for the study of photocatalytic phenomena"(Poster) II Congreso Internacional Virtual de Investigación e Innovación Educativa CIVINEDU 2018
- **2018** Ana Franco, Alina M.Balu, María Luisa Rodríguez Muñoz, Mª de la Salud Climent Bellido, **Daily Rodríguez-Padrón**, "Novel techonologies applied to education, interdisciplinarity between subjects" (Poster) VII Jornadas de Innovación Docente, Universidad San Jorge, Zaragoza, Spain.
- **2018** Ana Franco, Alina M.Balu, Rafael Luque, **Daily Rodríguez-Padrón**, "Introduction to nomenclature in Organic Chemistry through the use of a bilingual software/database program" (Poster) VII Jornadas de Innovación Docente, Universidad San Jorge, Zaragoza, Spain
- **2018 Daily Rodríguez-Padrón**, Alain R. Puente-Santiago, Mario J. Muñoz-Batista, Alvaro Caballero, Alina M. Balu, Antonio A. Romero, Rafael Luque, "**Carbonaceous material derived from spent coffee grounds** as higly sustainable anode material for lithium ion batteries" (Poster) I Jornadas Doctorales en Energías Renovables, Universidad de Jaén, Jaén, Spain.
- **2019 Daily Rodríguez-Padrón**, Alain R. Puente Santiago, Alina M. Balu, Antonio A. Romero, Mario J. Muñoz Batista, Rafael Luque. **Beningn-by-design orange peel-templated nanocatalysts** for continuous flow conversion of levulinic acid to N-heterocycles. (Poster), NANOUCO VI, January 21th-22th, Cordoba, Spain.
- **2019** Alain R. Puente Santiago, **Daily Rodríguez-Padrón**, Xuebo Quan, Mario J. Muñoz Batista, Ligia O. Martins, Sanny Verma, Rajender S. Varma, Jian Zhou, Rafael Luque. Superb electron transfer efficiency of immobilized recombinant CotA laccases for electrochemical biosensing. (Oral), NANOUCO VI, January 21th-22th, Cordoba, Spain.
- **2019** Cevher Altug, Mario J. Muñoz Batista, **Daily Rodríguez-Padrón**, Alina M. Balu, Antonio A. Romero, Rafael Luque. Continuous flow production of high value added chemicals promoted by Pt-P25 titania nano-catalysts. (Poster), NANOUCO VI, January 21th-22th, Cordoba, Spain.
- **2019** Gonzalo García Espejo, **Daily Rodríguez-Padrón**, Rafael Luque, Gustavo de Miguel, Luis Camacho. Perovskitas dobles: síntesis a través de

un procedimiento mecanoquímico. (Poster), NANOUCO VI, January 21th-22th, Cordoba, Spain.

PUBLICACIONES

1. **Autores:** Daily Rodríguez-Padrón; Alain R. Puente Santiago; Alvaro Caballero; Almudena Benítez; Alina M. Balu; Antonio A. Romero; Rafael Luque. **Año**: 2017. **Título del artículo:** Mechanochemical design of hemoglobin-functionalised magnetic nanomaterials for energy storage devices. **Revista:** Journal of Materials Chemistry A. **Volumen:** 5. **Páginas**: 16404-16411. 10.1039/C7TA04135G. **Índice de impacto:** 9.931 (Q1).
2. **Autores:** Daily Rodríguez-Padrón; Alain R. Puente Santiago; Alina M. Balu; Antonio A. Romero; Rafael Luque. **Año**: 2017. **Título del artículo:** Solventless mechanochemical preparation of novel magnetic bioconjugates. **Revista:** Chemical Communications. **Volumen:** 53. **Páginas**: 7635-7637. 10.1039/C7CC03975A. **Índice de impacto:** 6.319 (Q1).
3. **Autores:** Daily Rodríguez-Padrón; Alexander Jodlowski; Gustavo De Miguel; Alain Puente Santiago; Alina M. Balu; Rafael Luque. **Año**: 2018. **Título del artículo:** Synthesis of carbon-based fluorescent polymers driven by catalytically active magnetic bioconjugates. **Revista:** Green Chemistry. **Volumen:** 20. **Páginas**: 225-229. 10.1039/C7GC03295A. **Índice de impacto:** 9.125 (Q1).
4. **Autores:** Daily Rodríguez-Padrón; Alain R. Puente Santiago; Alvaro Caballero; Alina M. Balu; Antonio A. Romero; Rafael Luque. **Año**: 2018. **Título del artículo:** Highly efficient direct oxigen electro-reduction by partially unfolded laccases immobilized on waste-derived magnetically separable nanoparticles. **Revista:** Nanoscale. **Volumen:** 10. **Páginas**: 3961-3968. 10.1039/C8NR00512E. **Índice de impacto:** 7.367 (Q1).
5. **Autores:** Daily Rodríguez-Padrón; Alina Balu; Antonio A. Romero; Rafael Luque. **Año**: 2017. **Título del artículo:** New bio-nanocomposites based on iron oxides and polysaccharides applied to oxidation and alkylation reactions. **Revista:** Beilstein Journal of Organic Chemistry. **Volumen:** 13. **Páginas**: 1982-1993. 10.3762/bjoc.13.194, **Índice de impacto:** 2,762 (Q2).
6. **Autores:** Somayeh Ostovar, Ana Franco, Alain Puente Santiago, Daily Rodríguez-Padrón; Hamid R. Shaterian; Rafael Luque. **Año**: 2018. **Título**

del artículo: Efficient mechanochemical bifunctional nanocatalysts for the conversion of isoeugenol to vanillin. **Revista:** Frontiers in Chemistry. **Volumen:** 6, **Páginas**: 77. 10.3389/fchem.2018.00077. **Índice de impacto:** 4.155 (Q2).

7. **Autores:** Daily Rodríguez-Padrón; Manuel Algarra; Luis Tarelho; Jorge Frade; Ana Franco; Gustavo de Miguel; Jose Jimenez, Enrique Rodriguez-Castellon; Rafael Luque. **Año**: 2018. **Título del artículo:** Catalyzed microwave-assisted synthesis of Carbon Quantum dots from lignocellulosic residues. **Revista:** ACS Sustainable Chemistry & Engineering. **Volumen:** *6*(6), **Páginas**: 7200-7205. 10.1021/acssuschemeng.7b03848, **Índice de impacto:** 6.14 (Q1).
8. **Autores:** Daily Rodríguez-Padrón; Alexander Jodlowski; Gustavo de Miguel; Rafael Luque. **Año**: 2018. **Título del artículo:** Alternative perovskites for photovoltaics. **Revista:** Advanced Energy Materials. **Volumen:** *8*(21), **Páginas**: 1703120. 10.1002/aenm.201703120. **Índice de impacto:** 21.875 (Q1).
9. **Autores:** Mario J Munoz-Batista; Daily Rodríguez-Padrón; Alain R Puente-Santiago; Anna Kubacka; Rafael Luque; Marcos Fernandez-Garcia. **Año**: 2018. **Título del artículo:** Sunlight-driven production of H_2 using an annular flow photoreactor and g-C_3N_4-based catalysts. **Revista:** ChemPhotoChem. **Volumen:** *2*(10), **Páginas**: 870-877. 10.1002/cptc.201800064.
10. **Autores:** Ana Franco; Soledad Cebrian-Garcia; Daily Rodríguez-Padrón; Alain Puente-Santiago; Mario J Munoz-Batista; Alvaro Caballero; Alina M Balu; Antonio A Romero; Rafael Luque. **Año**: 2018. **Título del artículo:** Encapsulated laccases as effective electrocatalysts for oxygen reduction reactions. **Revista:** ACS Sustainable Chemistry & Engineering. **Volumen:** *6*(8), **Páginas**: 11058-11062. 10.1021/acssuschemeng.8b02529. **Índice de impacto:** 6.14 (Q1).
11. **Autores:** Daily Rodríguez-Padrón; Fernando Luna-Lama; Alain Puente-Santiago; Mario J Munoz-Batista; Alvaro Caballero; Alina M Balu; Antonio A Romero; Rafael Luque. **Año**: 2018. **Título del artículo:** Non-porous carbonaceous materials derived from coffee waste grounds as highly sustainable anodes for lithium-ion batteries. **Revista:** Journal of Cleaner

Production. **Volumen:** 207, **Páginas**: 411-417. 10.1016/j.jclepro.2018.10.024. I **Índice de impacto:** 5.651 (Q1)

12. **Autores:** Mario J Munoz-Batista; Daily Rodríguez-Padrón; Alain R Puente-Santiago; Rafael Luque. **Año**: 2018. **Título del artículo:** Mechanochemistry: Toward Sustainable Design of Advanced Nanomaterials for Electrochemical Energy Storage and Catalytic Applications. **Revista:** ACS Sustainable Chemistry & Engineering. **Páginas**: 9530-9544. 10.1021/acssuschemeng.8b01716. **Índice de impacto:** 6.14, (Q1).
13. **Autores:** Gonzalo Garcıa-Espejo, Daily Rodríguez-Padrón, Marta Perez-Morales, Rafael Luque, Gustavo de Miguel, Luis Camacho. **Año**: 2018. **Título del artículo:** Mechanochemical synthesis of one-dimensional (1D) hybrid perovskites incorporating polycyclic aromatic spacers: Highly fluorescent cation-based materials. **Revista:** Journal of Materials Chemistry C. **Volumen:** 6(28), **Páginas**: 7677-7682. 10.1039/C8TC02169D. **Índice de impacto:** 5.976, (Q1).
14. **Autores:** Daily Rodríguez-Padrón, Alain R. Puente-Santiago, Alina M. Balu, Mario J. Muñoz-Batista, Rafael Luque. **Año**: 2018. **Título del artículo:** Environmental catalysis: present and future**. Revista:** ChemCatChem. 10.1002/cctc.201801248. **Índice de impacto:** 4.674 (Q1).
15. **Autores:** Farveh Saberi, Daily Rodríguez-Padrón, Esmail Doustkhah, Somayeh Ostovar, Ana Franco, Hamid Reza shaterian, Rafael Luque. **Año**: 2018. **Título del artículo:** Mechanochemically modified aluminosilicates for efficient oxidation of vanillyl alcohol. **Revista:** Catalysis Communications. **Volumen:** 118, **Páginas**: 65-69. 10.1016/j.catcom.2018.09.017. **Índice de impacto:** 3.463 (Q2).
16. **Autores:** Farveh Saberi, Daily Rodríguez-Padrón, Araceli Garcia, Hamid Reza shaterian, Rafael Luque. **Año**: 2018. **Título del artículo:** Unprecedented Proline-Based Heterogeneous Organocatalyst for Selective Production of Vanillin. **Revista:** Catalysts. **Volumen:** 8(4), **Páginas**: 167. 10.3390/catal8040167. **Índice de impacto:** 3.082 (Q2).
17. **Autores:** Daily Rodríguez-Padrón, Alain R. Puente-Santiago, Alina M. Balu, Antonio A. Romero, Mario J. Muñoz-Batista, Rafael Luque. **Año**: 2018. **Título del artículo:** Benign-by-design Orange peel-templated nanocatalysts for continuous flow conversion of levulinic acid to N-heterocycles. **Revista:** ACS Sustainable Chemistry & Engineering**. Volumen:** 6(12), **Páginas**:

16637-16644. 10.1021/acssuschemeng.8b03896. **Índice de impacto:** 6.14 (Q1).

18. **Autores:** Alain R. Puente-Santiago, Daily Rodríguez-Padrón, Xuebo Quan, Mario J. Muñoz Batista, Lígia O. Martins, Sanny Verma, Rajender S.Varma, Jian Zhou, Rafael Luque. **Año**: 2018. **Título del artículo:** Unprecedented wiring efficiency of sulfonated carbon nitride materials: towards high-performance amperometric recombinant CotA laccases biosensors. **Revista:** ACS Sustainable Chemistry & Engineering. **Volumen:** 7(1), **Páginas**: 1474-1484. 10.1021/acssuschemeng.8b05107. **Índice de impacto:** 6.14 (Q1).
19. **Autores:** Cevher Altug, Mario J. Muñoz-Batista, Daily Rodríguez-Padrón,* Alina Mariana M Balu, Antonio Angel Romero and Rafael Luque. **Año**: 2018. **Título del artículo:** Continuous flow synthesis of amines from cascade reactions of nitriles and carbonyl-containing compounds promoted by Pt modified titania catalysts. **Revista:** Green Chemistry, **Volumen:** 21(2), **Páginas**: 300-306. 10.1039/C8GC03037E. (*corresponding author). **Índice de impacto:** 9.125 (Q1).
20. **Autores:** David Alba-Molina, Daily Rodríguez-Padrón, Alain R. Puente-Santiago, Juan J. Giner-Casares, María Teresa Martín-Romero, Luis Camacho, Rafael Luque. **Año**: 2019. **Título del artículo:** Mimicking the bioelectrocatalytic function of recombinant CotA laccase through electrostatically self-assembled bioconjugates. **Revista:** Nanoscale, **Volumen:** *11*(4), **Páginas**: 1549-1554. 10.1039/C8NR06001K. . **Índice de impacto:** 7.367 (Q1).
21. **Autores:** Daily Rodríguez-Padrón, Alain R. Puente-Santiago, Fernando Luna-Lama, Álvaro Caballero, A., Mario J. Muñoz Batista, Rafael Luque. **Año**: 2019. **Título del artículo:** Versatile protein-templated TiO_2 nanocomposite for energy storage and catalytic applications. **Revista:** ACS Sustainable Chemistry & Engineering. 10.1021/acssuschemeng.8b06349. **Índice de impacto:** 6.14 (Q1).
22. **Autores:** Chunping Xu, Alain R. Puente Santiago, Daily Rodríguez-Padrón,* Álvaro Caballero, Alina M. Balu, Antonio A. Romero, Mario J. Muñoz Batista, Rafael Luque. **Año**: 2019. **Título del artículo:** Controllable design of polypyrrole-iron oxide nanocoral architectures for supercapacitors with

ultrahigh cycling stability. **Revista:** ACS Applied Energy Materials**.** 10.1021/acsaem.8b02167. (*corresponding author)

23. **Autores:** Daily Rodríguez-Padrón, Alain R. Puente-Santiago, Alina M. Balu, Mario J. Muñoz-Batista, Rafael Luque. **Año**: 2019. **Título del artículo:** Continuous flow synthesis of high valuable N-heterocycles via catalytic conversion of levulinic acid. **Revista:** Frontiers in Chemistry, *7*, 103. 10.3389/fchem.2019.00103. **Índice de impacto:** 4.155 (Q2).
24. **Autores:** Maurizio Selva, Alvise Perosa, Daily Rodríguez-Padrón, Rafael Luque. **Año**: 2019. **Título del artículo:** Applications of Dimethyl Carbonate for the chemical upgrading of bio-sourced platform chemicals. **ACS Sustainable Chemistry & Engineering.** 10.1021/acssuschemeng.9b00464. **Índice de impacto:** 6.14 (Q1).
25. **Autores:** Yantao Wang, Deyang Zhao, Daily Rodríguez-Padrón, Christophe Len. **Año**: 2019. **Título del artículo:** Recent Advances in Catalytic Hydrogenation of Furfural **Revista:** Catalysts. **Volumen:** 9(10). **Páginas**: 796. **Índice de impacto**: 3.082 (Q2).
26. **Autores:** Daily Rodríguez-Padrón, Mario J. Muñoz-Batista, Hangkong Li, Kaimin Shih, Alina Mariana Balu, Antonio Pineda, and Rafael Luque. **Año**: 2019. **Título del artículo:** Spent coffee grounds-templated magnetic nanocatalysts for mild oxidations. **Revista:** ACS Sustainable Chemistry & Engineering. **Índice de impacto** 6.14 (Q1).
27. **Autores:** Gonzalo García-Espejo, Daily Rodríguez-Padrón, Rafael Luque, Luis Camacho and Gustavo de Miguel. **Año**: 2019. **Título del artículo:** Mechanochemical synthesis of three double perovskite: $Cs_2AgBiBr_6$, $(CH_3NH_3)_2TlBiBr_6$ and $Cs_2AgSbBr_6$. **Revista:** Nanoscale. **Volumen:** 11. **Páginas**: 16650-16657. **Índice de impacto:** 7.233 (Q1).
28. **Autores:** Amir Hossein Cheshme Khavar, Gholamreza Moussavi, Ali Reza Mahjou, Rafael Luque, Daily Rodríguez-Padrón, Mohammad Sattari. **Año**: 2019. **Título del artículo:** Enhanced visible light photocatalytic degradation of acetaminophen with Ag_2S-ZnO@rGO core-shell microsphere as a novel catalyst: Catalyst preparation and characterization and mechanistic catalytic experiments. **Revista:** Separation and Purification Technology. **Volumen:** 229. **Páginas**: 115803 **Índice de impacto**: 5.107 (Q1).
29. **Autores:** Somayeh Ostovar, Daily Rodríguez-Padrón, Farveh Saberi, Alina

M. Balu, Rafael Luque. **Año**: 2019. **Título del artículo:** Versatile Sulfathiazole-Functionalized Magnetic Nanoparticles as Catalyst in Oxidation and Alkylation Reactions. **Revista:** Catalysts. **Volumen:** 9(4), **Páginas**: 348-290. **Índice de impacto:** 3.082 (Q2).

30. **Autores:** Maria Dolores Márquez-Medina, Daily Rodríguez-Padrón, AlinaM. Balu, Antonio A. Romero, Mario J. Muñoz-Batista, Rafael Luque **Año**: 2019. **Título del artículo:** Mechanochemically Synthesized Supported Magnetic Fe-Nanoparticles as Catalysts for Efficient Vanillin Production. **Revista:** Catalysts. **Volumen:** 9(3), **Páginas:** 290 **Índice de impacto**: 3.082 (Q2).

PREMIOS

2019 Dan David Prize, Universidad de Tel-Aviv, Israel.

https://www.dandavidprize.org/scholars/2019/258-future-combatting-climate-change/1062-rodr%C3%ADguez-padr%C3%B3n-daily

2019 Accésits de la Segunda Edición del Premio Bienal de Fotografía científica dedicado a la nanoquímica.

PROYECTOS

- **COST Action Fp1306**, Valorisation Of Lignocellulosic Biomass Side Streams For Sustainable Production Of Chemicals, Materials & Fuels Using Low Enviromental Impact Technologies. Eu Fps Framework Program, Period 2014-2018. http://Www.Cost.Eu/Cost_Actions/Fps/Fp1306

- **CTQ2016-78289-P**. Desarrollo de Procesos Continuos Químico-Enzimáticos para valorización de Biomasa. **Ministerio de Ciencia e Innovación**. Rafael Luque Alvarez De Sotomayor. Universidad de Córdoba. 2016-2019.

- **12016073**. Valorization of lignocellulosic residues from the walnut shell through environmentally friendly procedures. **Almaco del Guadalquivir S.L**. Alina Balu. Universidad de Córdoba. 2016-2017.

- **Proyecto de innovación docente:** Novel techonologies applied to education, interdisciplinarity between subjects. Universidad de Córdoba. Spain. https://sites.google.com/view/innovacion-educativa/qu%C3%ADmica-pr%C3%A1ctica?authuser=0

- **COST Action CA18112,** Mechanochemistry for Sustainable Industry, Eu Fps Framework Program, Period 2019-2023. Participation as **MC member** representing Spain.
  https://www.cost.eu/actions/CA18112/#tabs|Name:management-committee

ESTANCIAS DE INVESTIGACIÓN

- **11/04/2018-30/04/2018**: DICEAM Department, School of Engineering, Facultad, instituto, centro: Università degli Studi "Mediterranea", Reggio Calabria, Extra-Regio, Italy
- **30/05/2019-01/09/2019**: PSL Research University, Chimie ParisTech – CNRS, Institut de Recherche de Chimie Paris, Paris, France

EXPERIENCIA COMO REVIEWER

- Desde Marzo de 2017 (3 reviews). **Molecular Catalysis.**
- Desde 2019 (3 reviews) **Green Chemistry**

GESTIÓN EN CARGOS UNIPERSONALES EN ESTRUCTURAS DE GESTIÓN ESTATUTARIAS

2017-2019: Representante de Estudiantes de Doctorado y Máster en el Consejo del Departamento de Química Orgánica

ACTIVIDAD DOCENTE: DOCENCIA EN TÍTULOS OFICIALES:

Título Oficial	Curso Académico	Horas impartidas
Grado de Ingeniería Electrónica	**2016/2017**	**30**
Grado en Biología	**2016/2017**	**27**
Grado de Ciencias Ambientales	**2016/2017**	**9**
Grado en Química	**2016/2017**	**12**
Grado de Ciencias Ambientales	**2017/2018**	**9**
Grado en Química	**2017/2018**	**6**
Grado en Biología	**2018/2019**	**54**
Grado de Ciencia y Tecnología de los Alimentos	**2018/2019**	**15**

8.Anexos

8.1. *Anexo 1.* Mechanochemistry: Toward Sustainable Design of Advanced Nanomaterials for Electrochemical Energy Storage and Catalytic Applications.

slw00 | ACSJCA | JCA11.1.4300/W Library-x64 | research.3f (R4.0.0 HF04:4882 | 2.1) 2018/05/11 22:44:00 | PROD-WS-120 | rq_69727 | 6/25/2018 07:42:43 | 15 | JCA-DEFAULT

ACS Sustainable Chemistry & Engineering

Feature

pubs.acs.org/journal/ascecg

Mechanochemistry: Toward Sustainable Design of Advanced Nanomaterials for Electrochemical Energy Storage and Catalytic Applications

Mario J. Muñoz-Batista,[†] Daily Rodriguez-Padron,[†] Alain R. Puente-Santiago,[†] and Rafael Luque*[,†,‡]

[†]Department of Organic Chemistry, University of Cordoba, Campus de Rabanales, Edificio Marie Curie (C-3), Ctra Nnal IV-A, Km 396, E14014 Cordoba, Spain

[‡]Peoples Friendship University of Russia (RUDN University), 6 Miklukho-Maklaya str., 117198, Moscow, Russia

ABSTRACT: Mechanochemistry has emerged as one of the most interesting synthetic protocols to produce new materials. Solvent-free methodologies lead to unique chemical processes during synthesis with the consequent formation of nanomaterials with new properties. The development of mechanochemistry as a synthetic method is supported by excellent results in a wide range of applications. This feature highlights some representative contributions focused on protocols that could be easily extended to the synthesis of other advanced nanomaterials. Materials for batteries, supercapacitors, and catalytic processes are discussed, indicating the potential future directions of each field. Theoretical aspects and a revision of recent real in situ analyses of the synthesis procedures are also featured. This contribution attempts to present, in a comprehensive way, mechanochemistry as an open research line and a consolidated methodology to synthesize advanced nanomaterials.

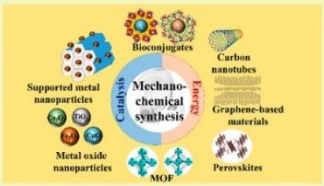

KEYWORDS: *Mechanochemistry, Nanomaterials, Catalysis, Electrochemical energy storage application, Green chemistry*

INTRODUCTION

Inspired by biological processes on liquid water, the indispensable presence of solvents for chemical reactions have been far too long a wrong assumption, which nowadays is still rarely questioned. Since solvents can disperse the heat, promote the interaction of reagents, and facilitate, especially on a large scale, efficient mixing, some reactions are not compatible with solvent-free approaches.[1−3] Nonetheless, solvent-free protocols possess energy and environmental advantages. Mechanical-assisted synthesis can significantly reduce the reaction times compared to similar conditions in conventional solvent-based synthetic methods which in turn facilitate a substantial savings on energy and cost.[4−7] An outstanding example is based in the synthesis of Cu-NHC complexes (NHC=N heterocyclic carbene).[8] Lamaty and co-workers have synthesized five Cu−NHC organometallic compounds using a planetary ball mill. The materials obtained showed improved yields compared with the analogous reactions in solution due to the highly efficient mixing of the precursors in the process. Additionally, Bolm and co-workers have developed a solvent-free approach of iridium-(III)-catalyzed C−H bond amidation of benzamides with sulfonyl azides.[9] The amidated products were obtained with higher yields and shorter reactions times (99 min) than those obtained by a conventional solvent-based chemistry (12 h).[10] In terms of environmental benefits, these protocols constitute a desirable alternative to carry out in safer ways reactions that require hazardous solvents by using solvent-free conditions. In this sense, the conventional methods for the synthesis of graphene usually involve toxic reagents which cause harmful effects on the environment.[11] To avoid the use of hazardous reagents, Ju et al. developed an ecofriendly green synthetic process in which edge-selectively carboxylated graphene nano-platelets (ECGnPs) were synthesized by the simple ball milling of graphite using dry ice (solid phase of carbon dioxide).[12] Moreover, these processes have potential applicability due to their extreme simplicity, cleanliness, reproducibility, and versatility.[13] Therefore, alternative solvent-free routes, based on the grinding or milling of the reactants, have sparked the interest of the scientific community.[14]

Despite the long history of mechanical-assisted reactions,[15,16] the term "mechanochemistry" has been only recently formalized by the IUPAC for the chemical literature as "a chemical reaction that is induced by the direct absorption of mechanical energy".[17] However, this terminology was introduced much earlier by Wilhelm Ostwald, who included mechanochemistry as part of physical chemistry and at the same level of thermochemistry, electrochemistry, or photochemistry.[18] Furthermore, Gerhard Heinicke in 1984 presented a widely accepted definition of

Received: April 16, 2018
Revised: May 18, 2018
Published: June 14, 2018

DOI: 10.1021/acssuschemeng.8b01716
ACS Sustainable Chem. Eng. XXXX, XXX, XXX−XXX

Step Closer To Achieving Sustainability? *Chem. Rev.* **2016**, *116*, 7159−7329.
(105) Cerdan, K.; Ouyang, W.; Colmenares, J. C.; Muñoz-Batista, M. J.; Luque, R.; Balu, A. M. Facile Mechanochemical Modification of g-C3N4 for Selective Photo-Oxidation of Benzyl Alcohol. *Chem. Eng. Sci.* **2018**, DOI: 10.1016/j.ces.2018.04.001.
(106) Filiciotto, L.; Balu, A. M.; Romero, A. A.; Rodríguez-Castellón, E.; van der Waal, J. C.; Luque, R. Benign-by-Design Preparation of Humin-Based Iron Oxide Catalytic Nanocomposites. *Green Chem.* **2017**, *19* (18), 4423−4434.
(107) Rodríguez-Padrón, D.; Jodlowski, A. D.; de Miguel, G.; Puente-Santiago, A. R.; Balu, A. M.; Luque, R. Synthesis of Carbon-Based Fluorescent Polymers Driven by Catalytically Active Magnetic Bioconjugates. *Green Chem.* **2018**, *20* (1), 225−229.
(108) Rodríguez-Padrón, D.; Puente-Santiago, A. R.; Caballero, A.; Balu, A. M.; Romero, A. A.; Luque, R. Highly Efficient Direct Oxygen Electro-Reduction by Partially Unfolded Laccases Immobilized on Waste-Derived Magnetically Separable Nanoparticles. *Nanoscale* **2018**, *10* (8), 3961−3968.
(109) Zhang, R.; Villanueva, A.; Alamdari, H.; Kaliaguine, S. Catalytic Reduction of NO by Propene over LaCo1−xCuxO3 Perovskites Synthesized by Reactive Grinding. *Appl. Catal., B* **2006**, *64* (3−4), 220−233.
(110) Zhang, R.; Villanueva, A.; Alamdari, H.; Kaliaguine, S. SCR of NO by Propene over Nanoscale LaMn1−xCuxO3 Perovskites. *Appl. Catal., A* **2006**, *307* (1), 85−97.
(111) Zhang, R.; Alamdari, H.; Kaliaguine, S. SO2 Poisoning of LaFe0.8Cu0.2O3 Perovskite Prepared by Reactive Grinding during NO Reduction by C3H6. *Appl. Catal., A* **2008**, *340* (1), 140−151.
(112) Kesić, Ž.; Lukić, I.; Zdujić, M.; Jovalekić, Č.; Veljković, V.; Skala, D. Assessment of CaTiO3, CaMnO3, CaZrO3 and Ca2Fe2O5 Perovskites as Heterogeneous Base Catalysts for Biodiesel Synthesis. *Fuel Process. Technol.* **2016**, *143*, 162−168.
(113) Pineda, A.; Balu, A. M.; Campelo, J. M.; Luque, R.; Romero, A. A.; Serrano-Ruiz, J. C. High Alkylation Activities of Ball-Milled Synthesized Low-Load Supported Iron Oxide Nanoparticles on Mesoporous Aluminosilicates. *Catal. Today* **2012**, *187* (1), 65−69.
(114) Hosseinpour, R.; Pineda, A.; Garcia, A.; Romero, A. A.; Luque, R. Efficient Aromatic C−H Bond Activation Using Aluminosilicate-Supported Metal Nanoparticles. *Catal. Commun.* **2014**, *48*, 73−77.
(115) Shen, D.; Cheng, C.; Liu, N.; Xiao, R. *Lignin Depolymerization (LDP) with Solvolysis for Selective Production of Renewable Aromatic Chemicals*; Springer, Singapore, 2016; pp 289−320.
(116) Toledano, A.; Serrano, L.; Pineda, A.; Romero, A. A.; Luque, R.; Labidi, J. Microwave-Assisted Depolymerisation of Organosolv Lignin via Mild Hydrogen-Free Hydrogenolysis: Catalyst Screening. *Appl. Catal., B* **2014**, *145*, 43−55.
(117) Toledano, A.; Serrano, L.; Balu, A. M.; Luque, R.; Pineda, A.; Labidi, J. Fractionation of Organosolv Lignin from Olive Tree Clippings and Its Valorization to Simple Phenolic Compounds. *ChemSusChem* **2013**, *6* (3), 529−536.
(118) Yepez, A.; Pineda, A.; Garcia, A.; Romero, A. A.; Luque, R. Chemical Transformations of Glucose to Value Added Products Using Cu-Based Catalytic Systems. *Phys. Chem. Chem. Phys.* **2013**, *15* (29), 12165−12172.
(119) Ojeda, M.; Pineda, A.; Romero, A. A.; Barrón, V.; Luque, R. Mechanochemical Synthesis of Maghemite/Silica Nanocomposites: Advanced Materials for Aqueous Room-Temperature Catalysis. *ChemSusChem* **2014**, *7* (7), 1876−1880.
(120) Grau-Atienza, A.; Campos, R.; Serrano, E.; Ojeda, M.; Romero, A. A.; Garcia-Martinez, J.; Luque, R. Insights into the Active Species of Nanoparticle-Functionalized Hierarchical Zeolites in Alkylation Reactions. *ChemCatChem* **2014**, *6* (12), 3530−3539.
(121) Masoomi, M. Y.; Beheshti, S.; Morsali, A. Mechanosynthesis of New Azine-Functionalized Zn(Ii) Metal−organic Frameworks for Improved Catalytic Performance. *J. Mater. Chem. A* **2014**, *2* (40), 16863−16866.
(122) Khosravi, A.; Mokhtari, J.; Naimi-Jamal, M. R.; Tahmasebi, S.; Panahi, L. Cu2 (BDC)2(BPY)−MOF: An Efficient and Reusable Heterogeneous Catalyst for the Aerobic Chan−Lam Coupling Prepared via Ball-Milling Strategy. *RSC Adv.* **2017**, *7* (73), 46022−46027.
(123) Li, R.; Ren, X.; Ma, H.; Feng, X.; Lin, Z.; Li, X.; Hu, C.; Wang, B. Nickel-Substituted Zeolitic Imidazolate Frameworks for Time-Resolved Alcohol Sensing and Photocatalysis under Visible Light. *J. Mater. Chem. A* **2014**, *2* (16), 5724−5729.
(124) Simon, P.; Gogotsi, Y. Materials for Electrochemical Capacitors. *Nat. Mater.* **2008**, *7* (11), 845−854.
(125) Herea, D. D.; Chiriac, H.; Lupu, N.; Grigoras, M.; Stoian, G.; Stoica, B. A.; Petreus, T. Study on Iron Oxide Nanoparticles Coated with Glucose-Derived Polymers for Biomedical Applications. *Appl. Surf. Sci.* **2015**, *352*, 117−125.
(126) Mio, H.; Kano, J.; Saito, F. Scale-up Method of Planetary Ball Mill. *Chem. Eng. Sci.* **2004**, *59* (24), 5909−5916.

DOI: 10.1021/acssuschemeng.8b01716
ACS Sustainable Chem. Eng. XXXX, XXX, XXX−XXX

8.2. *Anexo 2.* Environmental catalysis: present and future

ChemPubSoc Europe

DOI: 10.1002/cctc.201801248

CHEMCATCHEM Concepts

Environmental Catalysis: Present and Future

Daily Rodríguez-Padrón,[a] Alain R. Puente-Santiago,[a] Alina M. Balu,[a] Mario J. Muñoz-Batista,*[a] and Rafael Luque*[a, b]

Environmental catalysis plays a crucial role in sustainable development by the design of novel catalytic materials and technologies. Several environmental issues are addressed by catalytic processes such as decomposition of pollutants for air, water and soil remediation, hydrogen production, CO_2 reduction and biomass valorization, just to name a few. This contribution aims to provide a general overview of the main concepts and current advances in the environmental catalysis field. Special attention has been paid to photocatalysis and electrocatalysis, as sub-areas of catalysis with tremendous potential in sustainable applications, in particular with regard to the promotion of sustainable energies. In this contribution, the partnership between Catalysis and Green Chemistry is presented, in a comprehensive way, as an open research line which is imperative and decisive for a more sustainable future.

1. Introduction

The limited reserves of unrenewable crude oil, which may result in a crisis on the supplements of chemicals, materials, polymers, energy and fuels, as well as the emerging trend of global warming and the possible effects on human and environmental safety, have alerted the scientific community in order to move towards greener processes design. In this regard, Green Chemistry proposes the preferably use of renewable resources, decreasing waste amounts and avoiding additional reagents and solvents, which can have an unfavourable impact on the environment.[1] Taking into account such remarks and green chemistry principles,[2] catalysis has emerged as a key factor for the sustainable development of world economy,[3] where sustainable development can be defined as *development that meets the needs of the present generation without compromising the needs of future generations to meet their own needs.*[4] (Catalysis offers green chemistry advantages, avoiding the use of stoichiometric amounts of materials, increasing selectivity and decreasing energy requirements.[5–7] Specifically, catalytic biomass upgrading, water splitting, CO_2 reduction and light alkanes activation are key processes, which requires the urgent catalyst development.[8]

[a] D. Rodríguez-Padrón, Dr. A. R. Puente-Santiago, Dr. A. M. Balu, Dr. M. J. Muñoz-Batista, Prof. Dr. R. Luque
Departamento de Química Orgánica
Universidad de Córdoba
Campus de Rabanales
Edificio Marie Curie (C-3)
Ctra Nnal IV–A
Km 396
Córdoba E14014 (Spain)
E-mail: jmunoz385x@gmail.com
rafael.luque@uco.es

[b] Prof. Dr. R. Luque
Peoples Friendship University of Russia (RUDN University)
6 Miklukho-Maklaya str.
Moscow 117198 (Russia)

This manuscript is part of the Anniversary Issue in celebration of 10 years of ChemCatChem.

Defined by the IUPAC, catalysts are substances that increase the rate of a reaction without modifying the overall standard Gibbs energy change in the reaction.[9] Catalysis can be considered as a multi-disciplinary science, which involves chemical engineering, synthetic and physical chemistry, theoretical chemistry, solid state and surface science. Among the different alternatives in catalysis, biocatalysis, photocatalysis, electrocatalysis have emerged as the most promising possibilities. In addition, relative to others approaches such as photo-electro-catalysis or photo-thermo-catalysis appear as relevant alternatives to improve the efficiency of the catalytic process of several applications.[10,11]

Nowadays, most of the chemical processes (85–90%), which concern food, health, fuels and energy, involve at least one catalytic step. In this regard, efficiency is an essential factor, related to the maximization of the benefits with a minimum cost from different points of view, such as energy and materials consumption, environmental impact, among others.[12]

The aforementioned parameter can be separated as: a) *atom-efficiency,* related to the reduction of waste and by-products, b) *cost-efficiency,* associated to the reduction of capital investments and production time and c) *energy-efficiency,* linked to the reduction of the energy consumed during the process. In addition, the term E(nvironmental) factor, defined as the amount of waste produced per kg of product, has been employed as a convenient metric, particularly to determine the environmental impact of a manufacturing process. The E factor takes into account, not just the predicted amount of residue considering the stoichiometric equation, but the real waste formed in the process including solvents and other auxiliary materials.[13,14]

Through this contribution, a general overlook will be given related to the application of heterogeneous catalysis for the design of more sustainable process for today and for the future generations. Particular attention will receive photocatalysis and electrocatalysis, as sub-areas of catalytic science, due to their great potential for the development of a sustainable world with a potentially full utilization of renewables energies, such as

ChemPubSoc Europe

CHEMCATCHEM Concepts

sunlight energy. Environmental friendly (photo/electro) catalytic materials, catalyst preparation procedures, as well as relevant catalyzed reactions in the field of green chemistry have been recover in this work. (Figure 1)

2. Catalysis

Catalytic systems can be classified as homogeneous and heterogeneous. The inherent challenging and difficult separation and recovery of homogeneous catalysts have led to the development of heterogeneous systems. Particularly, heterogeneous catalysis is a process that requires the use of a catalyst that is in a different phase than the reactant and in which the reaction occurs at or near an interface between phases.[15–18]

Heterogeneous catalysts, as a priority of research activity in the green chemistry field, have gained increased attention for the development of the chemical industry.[19,20] Indeed, the high activity and selectivity of solid catalytic systems have resulted in more efficient processes from both, economic and environmental points of view.[21] Heterogeneous catalysts are still a crucial tool for the conversion of petroleum and natural gas towards more efficient fuels as well as more environmentally friendly energy sources, including hydrogen and biofuels.[22,23]

Environmental catalysis addresses problems related to the environment by developing innovative catalytic materials and technologies. This field promotes the quality of life and environment, a better use of resources and the development of sustainable processes and products.[24]

Sustainable Catalytic Materials

Myriad studies have been focused on the development of novel materials with potential catalytic applications.[25–29] Among the most prominent catalytic materials are noteworthy supported metal nanoparticles, composite materials, metal oxide nanoparticles, metal organic frameworks and more recently bioconjugates. From an environmental point of view, special attention has received the bening-by-design of biomass-derived catalyst, including materials with specific properties for application such as electro- and photo-catalysis.[30–32] Biomass is a wide concept, which includes lignocellulosic materials, starch/oilseed/sugar, aquatic cultures, and bio-derived wastes (agricultural/animal/anthropological residues). The pair biomass and

Daily Rodríguez-Padrón is a PhD student at the Universidad de Cordoba (Group FQM-383). She received her Degree in Chemistry at the University of Havana, Cuba in 2013, and her Master Degree at the University of Córdoba, Spain in 2016. After finishing her undergraduate studies, she worked at the Center of Genetic Engineering and Biotechnology, in Cuba, for one year, especially on synthesis of peptides. As part of her PhD investigations in the Group FQM-383 "Nanochemistry and biomass Valorization" she has worked on the design of nanomaterials through mechanochemical grinding processes, the functionalization of nanoparticles with proteins and their applications in catalysis, green chemistry, biomass valorization and electrochemistry.

Alain R. Puente Santiago received his degree in Nuclear Chemistry in 2007 from the Institute of Applied Science and Technologies (University of Havana, Cuba). After this, he started to work in the Institute of Materials Science, on the development of novel FETs microsensors. Then he moved to Spain in 2010 and he started his doctoral work in the University of Cordoba working in the design of functional nano-interfaces. In 2017 he obtained his PhD degree in Physical Chemistry with distinction. In the same year, he joined Prof. Luque's FQM-383 group as a postdoctoral fellow. His main project is focused on the development of new bio-inorganic functional nanomaterials for energy storage and catalytic applications.

Dr. M.J. Muñoz-Batista received his BA (Chemical Engineering) from CUJAE, Havana (Cuba) and his MS and PhD in Applied Chemistry (2015) from Universidad Autónoma de Madrid – Instituto de Catálisis y Petroleoquímica (CSIC). After two years as a postdoctoral researcher in the Instituto de Catálisis, he joined the group FQM-383 lead by Prof. Rafael Luque, with a Juan de la Cierva scholarship. His research interests focus on the development and characterization of new catalytic/photo-catalytic materials, gas phase batch/flow catalytic reactions, waste valorization and light-matter interactions, and reactor modelling.

Rafael Luque is Full Professor from Departamento de Quimica Organica at Universidad de Cordoba, where he graduated in 2005. Prof. Luque leads the group FQM-383 at UCO, published ca. 370 publications, filed 3 patent applications and edited 10 books as well as numerous contributions to book chapters and invited, guest, keynote and plenary lectures in scientific events worldwide (>100). Prof. Luque is Editor-in-chief of Molecular Catalysis and also member of the Editorial/Advisory Board of prestigious journals from most European and American publishing houses (>10) including ChemCatChem. Research interests from the group focus on the development of benign-by-design methodologies for nano/bio/photocatalyst preparation and their applications in catalysis, energy conversion and storage, flow chemistry and biomass/waste valorization. Prof. Luque was also recently appointed as Head of the Scientific Center for Molecular Design and Modern Organic Chemistry for the Medicinal Industry at RUDN University in Moscow (Russia).

ChemPubSoc Europe

CHEMCATCHEM Concepts

CONCEPTS

Putting the E in Catalysis: Environmental catalysis (bio-catalysis, electro-catalysis and photo-catalysis) are presented, in a comprehensive way, as future research avenues of high potential, imperative for a more sustainable future.

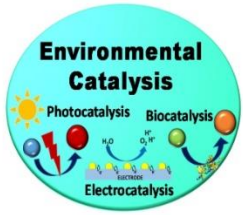

D. Rodríguez-Padrón, Dr. A. R. Puente-Santiago, Dr. A. M. Balu, Dr. M. J. Muñoz-Batista, Prof. Dr. R. Luque**

8.3. *Anexo 3.* Unprecedent wiring efficiency of sulfonated carbon nitride materials: towards high-performance amperometric recombinant CotA laccases biosensors

ACS Sustainable Chemistry & Engineering

Research Article

Cite This: *ACS Sustainable Chem. Eng.* 2019, 7, 1474−1484

pubs.acs.org/journal/ascecg

Unprecedented Wiring Efficiency of Sulfonated Graphitic Carbon Nitride Materials: Toward High-Performance Amperometric Recombinant CotA Laccase Biosensors

Alain R. Puente-Santiago,*[,†] Daily Rodríguez-Padrón,[†,▽] Xuebo Quan,[‡,▽] Mario J. Muñoz Batista,[†] Lígia O. Martins,[§] Sanny Verma,[∥] Rajender S. Varma,[⊥] Jian Zhou,*[,‡] and Rafael Luque*[,†,#]

[†]Departamento de Química Orgánica, Grupo FQM-383, Universidad de Cordoba, Campus de Rabanales, Edificio Marie Curie (C-3), Carretera Nacional IV-A, km 396, E14014 Cordoba, Spain

[‡]School of Chemistry and Chemical Engineering, Guangdong Provincial Key Lab for Green Chemical Product Technology, South China University of Technology, Guangzhou 510640, People's Republic of China

[§]Instituto de Tecnologia Química e Biológica António Xavier, Universidade Nova de Lisboa, Avenida da Republica, 2780-157 Oeiras, Portugal

[∥]Oak Ridge Institute for Science and Education, Post Office Box 117, Oak Ridge, Tennessee 37831, United States

[⊥]Regional Centre of Advanced Technologies and Materials, Department of Physical Chemistry, Faculty of Science, Palacky University, Šlechtitelů 27, 783 71 Olomouc, Czech Republic

[#]Peoples' Friendship University of Russia, 6 Miklukho-Maklaya Street, 117198 Moscow, Russia

ABSTRACT: Control of electron-transfer (ET) processes across electrochemically active biomaterials by tuning the surface properties of platform materials plays a key role in the design of highly efficient biosensors. In this work, ET rates of recombinant CotA laccases have been drastically improved by an immobilization process on sulfonic group-modified graphitic carbon nitride (Sg-CN) materials. Cyclic voltammetry (CV) and Fourier transform infrared (FTIR) spectroscopy revealed that the enzymes undergo striking conformational changes onto graphitic carbon nitride (g-CN), adopting an electrochemically inactive configuration while retain their nativelike structure with a superb ET efficiency on Sg-CN surfaces. In fact, the resulting CotA laccase/Sg-CN biomaterial displayed an ET rate constant of $(12 \pm 0.5)\ s^{-1}$, the highest value reported to date for a direct electron-transfer reaction of multicopper oxidases attached to carbon-based materials. Importantly, the combined parallel tempering Monte Carlo (PTMC) and all-atom molecular dynamics (AAMD) theoretical calculations proved CotA incorporation in a highly ordered array with an overall positive surface density composed of lysine and arginine domains in contact with net negatively charged Sg-CN surfaces, which promoted a 1200-fold improvement in the free enzyme ET rate constant. An ET pathway has been put forward that takes into account the orientation of CotA laccase on the Sg-CN surface. Additionally, CotA laccase/Sg-CN biomaterial was tested as an amperometric biosensor delivering outstanding bioelectrocatalytic activities in the oxidation of catechol and syringol, which are relevant emerging pollutants. In fact, the sensitivities of the CotA laccase/Sg-CN/ITO electrodes were 0.95 and 0.41 $A \cdot M^{-1} \cdot cm^{-2}$ for catechol and syringol, respectively, surpassing most of the laccase biosensors reported in the literature.

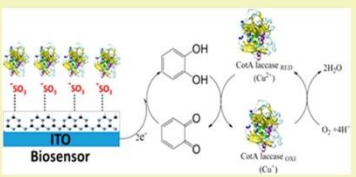

KEYWORDS: *Biosensors, Electrochemically active biomaterials, CotA laccase, Graphitic carbon nitride, Sulfonated graphitic carbon nitride, Priority pollutants*

INTRODUCTION

Electron-transfer (ET) processes from enzymes redox groups to electrodes have been widely investigated, owing to their significant impact for the design and development of enzyme-based sensors,[1,2] bioelectronic systems,[3,4] and biocatalytic cells.[5,6] Specifically, the design of hybrid electrically active biomaterials for the fabrication of highly efficient electrochemical biosensors with improved electronic properties is still a current challenge. In this regard, several strategies have been attempted to construct novel biosensors that exhibit efficient electronic wiring between redox proteins and electrodes.[7] Among them, the incorporation of carbon-based materials that promote good electronic wiring of redox proteins and the use of genetically engineered enzymes, which facilitate the most

Received: October 10, 2018
Revised: November 19, 2018
Published: November 23, 2018

DOI: 10.1021/acssuschemeng.8b05107
ACS Sustainable Chem. Eng. 2019, 7, 1474−1484

through Partially Exfoliated g-C3N4 Nanosheet Membranes with Self-Supporting Spacers. *Angew. Chem., Int. Ed.* **2017**, *56*, 8974−8980.
(31) Gu, Z. L.; Zhao, L.; Liu, S. T.; Duan, G. X.; Perez-Aguilar, J. M.; Luo, J. D.; Li, W. F.; Zhou, R. H. Orientational Binding of DNA Guided by the C2N Template. *ACS Nano* **2017**, *11*, 3198−3206.
(32) Li, B. Y.; Li, W. F.; Perez-Aguilar, J. M.; Zhou, R. H. Mild Binding of Protein to C2N Monolayer Reveals Its Suitable Biocompatibility. *Small* **2017**, *13*, 1603685.
(33) Xie, Y.; Zhou, J.; Jiang, S. Y. Parallel tempering Monte Carlo simulations of lysozyme orientation on charged surfaces. *J. Chem. Phys.* **2010**, *132*, 065101.
(34) Hess, B.; Kutzner, C.; van der Spoel, D.; Lindahl, E. GROMACS 4: algorithms for highly efficient, load-balanced, and scalable molecular simulation. *J. Chem. Theory Comput.* **2008**, *4*, 435−447.
(35) Humphrey, W.; Dalke, A.; Schulten, K. VMD: visual molecular dynamics. *J. Mol. Graphics* **1996**, *14*, 33−38.
(36) Wu, F.; Su, L.; Yu, P.; Mao, L. Q. Role of organic solvents in immobilizing fungus laccase on single-walled carbon nanotubes for improved current response in direct bioelectrocatalysis. *J. Am. Chem. Soc.* **2017**, *139*, 1565−1574.
(37) Roach, P.; Farrar, D.; Perry, C. C. Interpretation of protein adsorption: surface-induced conformational changes. *J. Am. Chem. Soc.* **2005**, *127*, 8168−8173.
(38) Rabe, M.; Verdes, D.; Seeger, S. Understanding protein adsorption phenomena at solid surfaces. *Adv. Colloid Interface Sci.* **2011**, *162*, 87−106.
(39) Rodriguez-Padron, D.; Puente-Santiago, A. R.; Caballero, A.; Balu, A. M.; Romero, A. A.; Luque, R. Highly efficient direct oxygen electro-reduction by partially unfolded laccases immobilized on waste-derived magnetically separable nanoparticles. *Nanoscale* **2018**, *10*, 3961−3968.
(40) Gutierrez-Sanchez, C.; Ciaccafava, A.; Blanchard, P. Y.; Monsalve, K.; Giudici-Orticoni, M. T.; Lecomte, S.; Lojou, E. Efficiency of Enzymatic O2 Reduction by *Myrothecium verrucaria* Bilirubin Oxidase Probed by Surface Plasmon Resonance, PMIRRAS, and Electrochemistry. *ACS Catal.* **2016**, *6*, 5482−5492.
(41) Lu, Y.; Gu, S.; Guo, J.; Rui, K.; Chen, C.; Zhang, S.; Jin, J.; Yang, J.; Wen, Z. Sulfonic Groups Originated Dual-Functional Interlayer for High Performance Lithium−Sulfur Battery. *ACS Appl. Mater. Interfaces* **2017**, *9*, 14878−14888.
(42) Muñoz-Batista, M. J.; Fontelles-Carceller, O.; Kubacka, A.; Fernandez-Garcia, M. Effect of exfoliation and surface deposition of MnOx species in g-C3N4: toluene photo-degradation under UV and visible light. *Appl. Catal., B* **2017**, *203*, 663−672.
(43) Franco, A.; Cebrián-García, S.; Rodriguez-Padron, D.; Puente-Santiago, A. R.; Muñoz-Batista, M. J.; Caballero, A.; Balu, A. M.; Romero, A. A.; Luque, R. Encapsulated Laccases as Effective Electrocatalysts for Oxygen Reduction Reactions. *ACS Sustainable Chem. Eng.* **2018**, *6*, 11058−11062.
(44) Xue, L. L.; Wang, Y. H.; Xie, Y.; Yao, P.; Wang, W. H.; Qian, W.; Huang, Z. X.; Wu, J.; Xia, Z.-X. Effect of Mutation at Valine 61 on the Three-Dimensional Structure, Stability, and Redox Potential of Cytochrome b5. *Biochemistry* **1999**, *38*, 11961−11972.
(45) Zhou, J.; Zheng, J.; Jiang, S. Y. Molecular simulation studies of the orientation and conformation of cytochrome c adsorbed on self-assembled monolayers. *J. Phys. Chem. B* **2004**, *108*, 17418−17424.
(46) Li, D. W.; Luo, L.; Pang, Z. Y.; Ding, L.; Wang, Q. Q.; Ke, H. Z.; Huang, F. L.; Wei, Q. F. Novel phenolic biosensor based on a magnetic polydopamine-laccase-nickel nanoparticle loaded carbon nanofiber composite. *ACS Appl. Mater. Interfaces* **2014**, *6*, 5144−5151.
(47) Rahman, M. A.; Noh, H.-B.; Shim, Y.-B. Direct Electrochemistry of Laccase Immobilized on Au Nanoparticles Encapsulated-Dendrimer Bonded Conducting Polymer: Application for a Catechin Sensor. *Anal. Chem.* **2008**, *80*, 8020−8027.
(48) Laviron, E. General expression of the linear potential sweep voltammogram in the case of diffusionless electrochemical systems. *J. Electroanal. Chem. Interfacial Electrochem.* **1979**, *101*, 19−28.
(49) Zhou, J.; Chen, S. F.; Jiang, S. Y. Orientation of adsorbed antibodies on charged surfaces by computer simulation based on a united-residue model. *Langmuir* **2003**, *19*, 3472−3478.
(50) Liu, J.; Xie, Y.; Peng, C. W.; Yu, G. B.; Zhou, J. Molecular Understanding of Laccase Adsorption on Charged Self-Assembled Monolayers. *J. Phys. Chem. B* **2017**, *121*, 10610−10617.
(51) Piontek, K.; Antorini, M.; Choinowski, T. Crystal structure of a laccase from the fungus Trametes versicolor at 1.90-Å resolution containing a full complement of coppers. *J. Biol. Chem.* **2002**, *277*, 37663−37669.
(52) Kamin, R. A.; Wilson, G. S. Rotating ring-disk enzyme electrode for biocatalysis kinetic studies and characterization of the immobilized enzyme layer. *Anal. Chem.* **1980**, *52*, 1198−1205.
(53) Liu, Y.; Qu, X. H.; Guo, H. W.; Chen, H. J.; Liu, B. F.; Dong, S. J. Facile preparation of amperometric laccase biosensor with multifunction based on the matrix of carbon nanotubes−chitosan composite. *Biosens. Bioelectron.* **2006**, *21*, 2195−2201.
(54) Qu, J.; Lou, T.; Kang, S.; Du, X. Simultaneous determination of catechol and hydroquinone using a self-assembled laccase biosensor based on nanofilm. *Sens. Lett.* **2013**, *11*, 1567−1572.
(55) Palanisamy, S.; Ramaraj, S. K.; Chen, S.-M.; Yang, T. C. K.; Yi-Fan, P.; Chen, T.-W.; Velusamy, V.; Selvam, S. A novel Laccase Biosensor based on Laccase immobilized Graphene-Cellulose Micro-fiber Composite modified Screen-Printed Carbon Electrode for Sensitive Determination of Catechol. *Sci. Rep.* **2017**, *7*, 41214.
(56) Mei, L. P.; Feng, J. J.; Wu, L.; Zhou, J. Y.; Chen, J. R.; Wang, A. J. Novel phenol biosensor based on laccase immobilized on reduced graphene oxide supported palladium−copper alloyed nanocages. *Biosens. Bioelectron.* **2015**, *74*, 347−352.

DOI: 10.1021/acssuschemeng.8b05107
ACS Sustainable Chem. Eng. 2019, 7, 1474−1484

8.4. *Anexo 4.* Controllable design of polypyrrole-iron oxide nanocoral architectures for supercapacitors with ultrahigh cycling stability

ACS APPLIED ENERGY MATERIALS Cite This: *ACS Appl. Energy Mater.* 2019, 2, 2161−2168 Article www.acsaem.org

Controllable Design of Polypyrrole-Iron Oxide Nanocoral Architectures for Supercapacitors with Ultrahigh Cycling Stability

Chunping Xu,[†,‡] Alain R. Puente-Santiago,[†,§] Daily Rodríguez-Padrón,[*,§] Alvaro Caballero,[⊥] Alina M. Balu,[§] Antonio A. Romero,[§] Mario J. Muñoz-Batista,[§] and Rafael Luque[*,§,∥]

[‡]School of Food and Biological Engineering, Zhengzhou University of Light Industry Zhengzhou, Henan 450002, PR China

[§]Departamento de Química Orgánica, Instituto de Química Fina y Nanoquímica, and [⊥]Departamento de Química Inorgánica e Ingeniería Química, Instituto de Química Fina y Nanoquímica, Universidad de Córdoba, Campus de Rabanales, Edificio Marie Curie (C-3), Ctra Nnal IV-A, Km 396, Cordoba E14014, España

[∥]Peoples Friendship University of Russia (RUDN University), 6 Miklukho-Maklaya Strasse, Moscow 117198, Russia

Supporting Information

ABSTRACT: Polypyrrole-modified iron oxide nanomaterials have been synthesized employing a one-step hydrothermal protocol. The influence of the reaction temperature has been investigated by performing the synthesis at four different temperatures (Ppy@Fe_2O_3-120 °C, Ppy@Fe_2O_3-140 °C, Ppy@Fe_2O_3-160 °C, and Ppy@Fe_2O_3-180 °C). Synthesized materials exhibited an unprecedentedly peculiar morphology (star/coral reef-like architectures), induced by the presence of pyrrole in the reaction media. Full characterization of the samples revealed the critical influence of temperature on the crystallinity, textural properties and specially on (C+N)/Fe surface ratios in the materials. As-synthesized nanohybrids were integrated into electrodes to construct supercapacitor devices. A effective tuning of the electrochemical features was achieved by controlling the (C+N)/Fe ratio on the surface, strongly dependent on reaction temperature. The best electrochemical performance was reached by Ppy@Fe_2O_3-180 °C nanohybrid, which exhibited a remarkable capacitance value of 560 F g^{-1} at a current density of 5 A g^{-1} and an outstanding cycling stability of ca. 97.3% after 20 000 cycles of charge−discharge at 40A g^{-1} was reached.

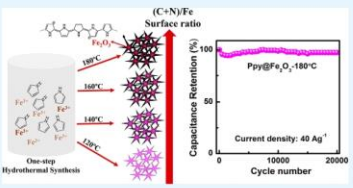

KEYWORDS: *iron oxide, pyrrole, nanocoral architectures, supercapacitor, electrochemical performance*

1. INTRODUCTION

The synthesis of hybrid (nano)capacitors has opened up new horizons toward a deeper study of electrochemical double-layer (EDL) processes at the nanoscale level as well as the opportunity to fabricate more efficient nanostorage systems.[1−5] Particularly, the development of redox active nanomaterials bearing pseudocapacitance including metal-oxide-based nanostructures, has been investigated in recent times. The aforementioned systems undergo fast and reversible surface redox reactions (faradaic reactions), favoring the enhancement of both energy and power densities.[6−9] In this sense, nanosized metal oxides structures are highly desirable toward the fabrication of effective supercapacitor electrodes taking advantages of their unique surface properties, which in fact enhance ion diffusion across materials and consequently redox reaction rates.[10] A myriad of strategies have been attempted to design supercapacitors with enhanced electrochemical properties fabricated from iron,[11] manganese,[12] cobalt,[13] or vanadium oxide nanoarchitectures.[14] The synthesis of binder-free nanomaterials,[15,16] the modification of metal oxides surfaces with carbonaceous materials or conducting polymers using different approaches such as core−shell,[17,18] core−branch,[19,20] and sandwich structure;[21] and most recently the anchorage of biomolecules onto metal oxides surfaces[22,23] are among most recently relevant reported examples. Despite these remarkable achievements in the preparation of advanced nanomaterials with improved supercapacitive performances, only a few research studies have addressed to date the possibility to control the electrochemical properties of the synthesized nanoarchitectures by tailoring their structural and/or surface properties. Bearing in mind such concept, Low and coworkers[24] have developed a facile synthetic method to tune the morphology of iron oxide nanostructures from 0D nanoparticles, 1D nanorods to 3D self-assembled nanorods, which directly impinges the supercapacitive activity of the obtained nanocapacitors. The development of tunable nanostorage systems therefore constitutes a promising alternative to solve current drawbacks of conventional metal oxides supercapacitor

Received: December 17, 2018
Accepted: February 12, 2019
Published: February 12, 2019

DOI: 10.1021/acsaem.8b02167
ACS Appl. Energy Mater. 2019, 2, 2161−2168

(33) Singh, A.; Salmi, Z.; Jha, P.; Joshi, N.; Kumar, A.; Decorse, P.; Lecoq, H.; Lau-Truong, S.; Aswal, D. K.; Gupta, S. K.; Chehimi, M. M. One Step Synthesis of Highly Ordered Free Standing Flexible Polypyrrole-Silver Nanocomposite Films at Air-Water Interface by Photopolymerization. *RSC Adv.* **2013**, *3*, 13329−13336.
(34) Jiang, Y. Z.; Nie, G. D.; Chi, M. Q.; Yang, Z. Z.; Zhang, Z.; Wang, C.; Lu, X. F. Synergistic Effect of Ternary Electrospun TiO_2/Fe_2O_3/PPy Composite Nanofibers on Peroxidase-like Mimics with Enhanced Catalytic Performance. *RSC Adv.* **2016**, *6*, 31107−31113.
(35) Yamashita, T.; Hayes, P. Analysis of XPS Spectra of Fe2+ and Fe3+ Ions in Oxide Materials. *Appl. Surf. Sci.* **2008**, *254*, 2441−2449.
(36) Zhu, J. F.; Chen, F.; Zhang, J. L.; Chen, H. J.; Anpo, M. Fe(3+)-TiO(2) Photocatalysts Prepared by Combining Sol-Gel Method with Hydrothermal Treatment and their Characterization. *J. Photochem. Photobiol., A* **2006**, *180*, 196−204.
(37) Grosvenor, A. P.; Kobe, B. A.; Biesinger, M. C.; McIntyre, N. S. Investigation of Multiplet Splitting of Fe 2p XPS Spectra and Bonding in Iron Compounds. *Surf. Interface Anal.* **2004**, *36*, 1564−1574.
(38) Boukerma, K.; Micusik, M.; Mravcakova, M.; Omastova, M.; Vaulay, M. J.; Beaunier, P.; Chehimi, M. M. Surfactant-Assisted Control of the Surface Energy and Interfacial Molecular Interactions of Polypyrrole. *Colloids Surf., A* **2007**, *293*, 28−38.
(39) Lin, Y.; Wang, X. Y.; Qian, G.; Watkins, J. J. Additive-Driven Self-Assembly of Well-Ordered Mesoporous Carbon/Iron Oxide Nanoparticle Composites for Supercapacitors. *Chem. Mater.* **2014**, *26*, 2128−2137.
(40) Xie, K. Y.; Li, J.; Lai, Y. Q.; Lu, W.; Zhang, Z. A.; Liu, Y. X.; Zhou, L. M.; Huang, H. T. Highly Ordered Iron Oxide Nanotube Arrays as Electrodes for Electrochemical Energy Storage. *Electrochem. Commun.* **2011**, *13*, 657−660.
(41) Grote, F.; Lei, Y. A. Complete Three-dimensionally Nanostructured Asymmetric Supercapacitor with High Operating Voltage Window based on PPy and MnO_2. *Nano Energy* **2014**, *10*, 63−70.
(42) Ling, T.; Da, P.; Zheng, X.; Ge, B.; Hu, Z.; Wu, M.; Du, X.-W.; Hu, W.-B.; Jaroniec, M.; Qiao, S.-Z. Atomic-level Structure Engineering of Metal Oxides for High-rate Oxygen Intercalation Pseudocapacitance. *Sci. Adv.* **2018**, *4*, No. eaau6261.
(43) Zhai, T.; Sun, S.; Liu, X.; Liang, C.; Wang, G.; Xia, H. Achieving Insertion-Like Capacity at Ultrahigh Rate via Tunable Surface Pseudocapacitance. *Adv. Mater.* **2018**, *30*, 1706640.
(44) Lu, X. H.; Zeng, Y. X.; Yu, M. H.; Zhai, T.; Liang, C. L.; Xie, S. L.; Balogun, M. S.; Tong, Y. X. Oxygen-Deficient Hematite Nanorods as High-Performance and Novel Negative Electrodes for Flexible Asymmetric Supercapacitors. *Adv. Mater.* **2014**, *26*, 3148−3155.
(45) Sassin, M. B.; Mansour, A. N.; Pettigrew, K. A.; Rolison, D. R.; Long, J. W. Electroless Deposition of Conformal Nanoscale Iron Oxide on Carbon Nanoarchitectures for Electrochemical Charge Storage. *ACS Nano* **2010**, *4*, 4505−4514.
(46) Li, Y.; Xu, J.; Feng, T.; Yao, Q. F.; Xie, J. P.; Xia, H. Fe_2O_3 Nanoneedles on Ultrafine Nickel Nanotube Arrays as Efficient Anode for High-Performance Asymmetric Supercapacitors. *Adv. Funct. Mater.* **2017**, *27*, 1606728.
(47) Liu, J. Q.; Zheng, M. B.; Shi, X. Q.; Zeng, H. B.; Xia, H. Amorphous FeOOH Quantum Dots Assembled Mesoporous Film Anchored on Graphene Nanosheets with Superior Electrochemical Performance for Supercapacitors. *Adv. Funct. Mater.* **2016**, *26*, 919.

DOI: 10.1021/acsaem.8b02167
ACS Appl. Energy Mater. 2019, 2, 2161−2168

8.5. *Anexo 5.* New bio-nanocomposites based on iron oxides and polysaccharides applied to oxidation and alkylation reactions

BEILSTEIN JOURNAL OF ORGANIC CHEMISTRY

New bio-nanocomposites based on iron oxides and polysaccharides applied to oxidation and alkylation reactions

Daily Rodríguez-Padrón, Alina M. Balu, Antonio A. Romero and Rafael Luque*

Full Research Paper

Open Access

Address:
Departamento de Química Orgánica, Grupo FQM-383, Universidad de Cordoba, Campus de Rabanales, Edificio Marie Curie (C-3), Ctra Nnal IV-A, Km 396, E14014, Cordoba, Spain

Email:
Rafael Luque* - q62alsor@uco.es

* Corresponding author

Keywords:
alkylation; benzyl alcohol; benzyl chloride; iron oxide; mechanochemistry; microwave-assisted oxidation; polysaccharide; toluene

Beilstein J. Org. Chem. **2017,** *13,* 1982–1993.
doi:10.3762/bjoc.13.194

Received: 23 May 2017
Accepted: 30 August 2017
Published: 21 September 2017

This article is part of the Thematic Series "Mechanochemistry".

Guest Editor: J. G. Hernández

Abstract

Polysaccharides from natural sources and iron precursors were applied to develop new bio-nanocomposites by mechanochemical milling processes. The proposed methodology was demonstrated to be advantageous in comparison with other protocols for the synthesis of iron oxide based nanostructures. Additionally, mechanochemistry has enormous potential from an environmental point-of-view since it is able to reduce solvent issues in chemical syntheses. The catalytic activity of the obtained nanocatalysts was investigated in both the oxidation of benzyl alcohol to benzaldehyde and in the alkylation of toluene with benzyl chloride. The microwave-assisted oxidation of benzyl alcohol reached 45% conversion after 10 min. The conversion of the alkylation of toluene in both microwave-assisted and conventional heating methods was higher than 99% after 3 min and 30 min, respectively. The transformation of benzyl alcohol and toluene into valuable product in both the oxidation and alkylation reaction reveals a potential method for the valorization of lignocellulosic biomass.

Introduction

Heterogeneous catalysis has played a crucial role in the development of the chemical industry. It has allowed the design of more efficient processes, both in an economical and environmental way, thanks to the higher activity and selectivity of heterogeneous catalysts [1-3]. These systems, in particular, are preferred over the use of catalysts in a homogeneous phase due to the difficulty in separation and recovery of the latter. Heterogeneous catalytic systems, as a priority of research activity in the field of green chemistry, open up new possibilities for further development of environmentally friendly, catalyzed processes [4]. In this sense, metal oxide nanoparticles have been extensively studied in recent decades because of their high ac-

15. Juárez, R.; Parker, S. F.; Concepción, P.; Corma, A.; García, H. *Chem. Sci.* **2010,** *1*, 731–738. doi:10.1039/c0sc00336k
16. Navalon, S.; Martin, R.; Alvaro, M.; Garcia, H. *Angew. Chem., Int. Ed.* **2010,** *49*, 8403–8407. doi:10.1002/anie.201003216
17. Mendes, D.; Garcia, H.; Silva, V. B.; Mendes, A.; Madeira, L. M. *Ind. Eng. Chem. Res.* **2009,** *48*, 430–439. doi:10.1021/ie8010676
18. Gonzalez-Arellano, C.; Luque, R.; Macquarrie, D. J. *Chem. Commun.* **2009,** 1410–1412. doi:10.1039/b818767c
19. Budarin, V. L.; Clark, J. H.; Luque, R.; Macquarrie, D. J.; White, R. J. *Green Chem.* **2008,** *10*, 382–387. doi:10.1039/B715508E
20. Gonzalez-Arellano, C.; Yoshida, K.; Luque, R.; Gai, P. L. *Green Chem.* **2010,** *12*, 1281–1287. doi:10.1039/c003410j
21. Yepez, A.; Lam, F. L. Y.; Romero, A. A.; Kappe, C. O.; Luque, R. *ChemCatChem* **2015,** *7*, 276–282. doi:10.1002/cctc.201402802
22. Ozin, G. A.; Arsenault, A.; Cademartiri, L. *Nanochemistry: A chemical approach to nanomaterials*; Royal Society of Chemistry: Cambridge, UK, 2009.
23. Tsuzuki, T.; McCormick, P. G. *J. Mater. Sci.* **2004,** *39*, 5143–5146. doi:10.1023/B:JMSC.0000039199.56155.f9
24. Mei, K.-C.; Guo, Y.; Bai, J.; Costa, P. M.; Kafa, H.; Protti, A.; Hider, R. C.; Al-Jamal, K. T. *ACS Appl. Mater. Interfaces* **2015,** *7*, 14176–14181. doi:10.1021/acsami.5b03577
25. Ding, J.; Tsuzuki, T.; McCormick, P. G. *J. Mater. Sci.* **1999,** *34*, 5293–5298. doi:10.1023/A:1004736602847
26. Koch, C. C. *Nanostruct. Mater.* **1993,** *2*, 109–129. doi:10.1016/0965-9773(93)90016-5
27. Ding, J.; Shi, Y.; Chen, L. F.; Deng, C. R.; Fuh, S. H.; Li, Y. *J. Magn. Magn. Mater.* **2002,** *247*, 249–256. doi:10.1016/S0304-8853(02)00173-7
28. Xu, C.; Ojeda, M.; Arancon, R. A. D.; Romero, A. A.; Domingo, J. L.; Gómez, M.; Blanco, J.; Luque, R. *ACS Sustainable Chem. Eng.* **2015,** *3*, 2716–2725. doi:10.1021/acssuschemeng.5b00568
29. Herea, D. D.; Chiriac, H.; Lupu, N.; Grigoras, M.; Stoian, G.; Stoica, B. A.; Petreus, T. *Appl. Surf. Sci.* **2015,** *352*, 117–125. doi:10.1016/j.apsusc.2015.03.137
30. Rodriguez-Padrón, D.; Puente-Santiago, A. R.; Balu, A. M.; Romero, A. A.; Luque, R. *Chem. Commun.* **2017,** *53*, 7635–7637. doi:10.1039/C7CC03975A
31. Rodríguez-Padrón, D.; Puente-Santiago, A. R.; Caballero, A.; Benítez, A.; Balu, A. M.; Romero, A. A.; Luque, R. *J. Mater. Chem. A* **2017,** *5*, 16404–16411. doi:10.1039/C7TA04135G
32. Huebsch, N.; Mooney, D. J. *Nature* **2009,** *462*, 426–432. doi:10.1038/nature08601
33. Salgueiriño-Maceira, V.; Correa-Duarte, M. A. *Adv. Mater.* **2007,** *19*, 4131–4144. doi:10.1002/adma.200700418
34. Zheng, Y.; Monty, J.; Linhardt, R. J. *Carbohydr. Res.* **2015,** *405*, 23–32. doi:10.1016/j.carres.2014.07.016
35. Majewski, P.; Thierry, B. *Crit. Rev. Solid State Mater. Sci.* **2007,** *32*, 203–215. doi:10.1080/10408430701776680
36. Tallury, P.; Payton, K.; Santra, S. *Nanomedicine* **2008,** *3*, 579–592. doi:10.2217/17435889.3.4.579
37. Kim, J.; Piao, Y.; Hyeon, T. *Chem. Soc. Rev.* **2009,** *38*, 372–390. doi:10.1039/B709883A
38. Pineda, A.; Balu, A. M.; Campelo, J. M.; Romero, A. A.; Carmona, D.; Balas, F.; Santamaria, J.; Luque, R. *ChemSusChem* **2011,** *4*, 1561–1565. doi:10.1002/cssc.201100265
39. Matsumoto, T.; Ueno, M.; Wang, N.; Kobayashi, S. *Chem. – Asian J.* **2008,** *3*, 196–214. doi:10.1002/asia.200700359
40. Dey, S. K.; Mukherjee, A. *Coord. Chem. Rev.* **2016,** *310*, 80–115. doi:10.1016/j.ccr.2015.11.002
41. Rajabi, F.; Naresian, S.; Primo, A.; Luque, R. *Adv. Synth. Catal.* **2011,** *353*, 2060–2066. doi:10.1002/adsc.201100149
42. Yang, J.-C. E.; Yuan, B.; Cui, H.-J.; Wang, S.; Fu, M.-L. *Appl. Catal., B: Environ.* **2017,** *205*, 327–339. doi:10.1016/j.apcatb.2016.12.046
43. Huang, X.; Wang, X.; Wang, X.; Wang, X.; Tan, M.; Ding, W.; Lu, X. *J. Catal.* **2013,** *301*, 217–226. doi:10.1016/j.jcat.2013.02.011
44. Rak, M. J.; Lerro, M.; Moores, A. *Chem. Commun.* **2014,** *50*, 12482–12485. doi:10.1039/C4CC04749D
45. Shi, F.; Tse, M. K.; Pohl, M.-M.; Brückner, A.; Zhang, S.; Beller, M. *Angew. Chem., Int. Ed.* **2007,** *46*, 8866–8868. doi:10.1002/anie.200703418
46. Campelo, J. M.; Luna, D.; Luque, R.; Marinas, J. M.; Romero, A. A. *ChemSusChem* **2009,** *2*, 18–45. doi:10.1002/cssc.200800227
47. Wilson, K.; Adams, D. J.; Rothenberg, G.; Clark, J. H. *J. Mol. Catal. A* **2000,** *159*, 309–314. doi:10.1016/S1381-1169(00)00185-0
48. Bastock, T. W.; Clark, J. H. *Speciality chemicals*; Elsevier Applied Science: London, New York, 1991; p 383.
49. Pineda, A.; Balu, A. M.; Campelo, J. M.; Luque, R.; Romero, A. A.; Serrano-Ruiz, J. C. *Catal. Today* **2012,** *187*, 65–69. doi:10.1016/j.cattod.2012.02.028
50. Gracia, M. J.; Losada, E.; Luque, R.; Campelo, J. M.; Luna, D.; Marinas, J. M.; Romero, A. A. *Appl. Catal., A* **2008,** *349*, 148–155. doi:10.1016/j.apcata.2008.07.023
51. Ojeda, M.; Balu, A. M.; Barrón, V.; Pineda, A.; Coleto, Á. G.; Romero, A. A.; Luque, R. *J. Mater. Chem. A* **2014,** *2*, 387–393. doi:10.1039/C3TA13564K
52. Bourlinos, A. B.; Simopoulos, A.; Boukos, N.; Petridis, D. *J. Phys. Chem. B* **2001,** *105*, 7432–7437. doi:10.1021/jp010286+
53. Gregg, S. J.; Sing, K. S. W. *Adsorption, Surface Area and Porosity*; Academic Press Inc.: London, 1982.
54. Luque, R.; Campelo, J. M.; Luna, D.; Marinas, J. M.; Romero, A. A. *Microporous Mesoporous Mater.* **2005,** *84*, 11–20. doi:10.1016/j.micromeso.2005.05.013

8.6. *Anexo 6.* Continuous flow synthesis of amines from the cascade reactions of nitriles and carbonyl-containing compounds promoted by Pt-modified titania

Green Chemistry

PAPER

Cite this: DOI: 10.1039/c8gc03037e

Continuous flow synthesis of amines from the cascade reactions of nitriles and carbonyl-containing compounds promoted by Pt-modified titania catalysts†

Cevher Altuğ,‡[a,b] Mario J. Muñoz-Batista,‡[b] Daily Rodríguez-Padrón,*[b] Alina M. Balu,[b] Antonio A. Romero[b] and Rafael Luque*[b,c]

The effective design of an active and stable catalytic system was performed by a simple modification of a commercial titania with a low platinum loading. The prepared material was fully characterized by XRD, XPS, N_2 adsorption–desorption measurements, ICP-MS, TEM and SEM analyses. Such techniques corroborated the successful incorporation of Pt onto the titania surface, without affecting its original structure, morphology and chemical nature. The obtained TiO_2–Pt catalyst was effectively applied in several continuous flow reactions between nitriles and carbonyl containing compounds for amine preparation. Remarkably, conversion of levulinic acid, a biomass derived molecule, was achieved with outstanding conversion (87%) and selectivity (80%) to 1-ethyl-5-methylpyrrolidin-2-one. The catalytic system demonstrated a high stability through 120 min of reaction. Moreover, the effect of the nitrile was investigated by performing the reaction with benzonitrile and ethylcyanoacetate. The TiO_2–Pt catalyst was also tested in the conversion of benzaldehyde, displaying remarkable results. The influence of substitution in the aromatic ring was investigated using *p*-nitro-benzaldehyde and *p*-chloro-benzaldehyde.

Received 27th September 2018,
Accepted 29th November 2018

DOI: 10.1039/c8gc03037e

rsc.li/greenchem

Introduction

Biomass transformation into useful organic molecules is one of the most promising methods to the use of petroleum-derived products being one of the most abundant and renewable carbon sources worldwide.[1–3]

Biomass valorization towards chemicals, added value compounds and fuels represent an attractive and challenging option for the chemical industry.[4,5] Carbonyl containing molecules play an important role, from simple living organisms to complex metabolites, and can be found in most biomass derivatives.[6] The reduction of carbonyl compounds to amines is an indispensable tool available to synthetic organic chemists. Amines have a pivotal role in synthetic organic chemistry, widely present in compounds from the pharmaceutical, dye, plastic and agrochemical industries.[7,8] A variety of useful methods have been used for the conversion of carbonyls to amines in the presence of transition metal catalysts and ammonia as a nitrogen-containing molecule, under batch conditions for years.[9] Besides nitrogen gas or ammonia derivatives, nitriles,[10] amides,[11] nitro derivatives,[12] urea,[13] sulfonylhydrazines,[14] azides[15] methyl carbamates[16] and isocyanate[17] functional groups have been investigated as a nitrogen source towards amine synthesis.

From an environmental and industrial point of view, *in situ* reduction of nitriles and further reaction with carbonyl compounds is a valuable synthetic transformation for amine preparation. Most of the nitrile reductions and transformations to substituted amines need harsh reaction conditions and noble metal catalysts. In order to overcome difficulties of dealing with systems which usually need high temperatures, pressures, and constant external gas, the continuous flow synthetic methodology, employing heterogeneous catalytic materials, has become a noteworthy option to obtain organic molecules through a "greener" pathway, with rather controllable reaction parameters (temperature, mixing, volume, time, amount of reagents, solvents and gases).[18]

Flow chemistry offers attractive advantages including improved mass and heat transfer, enhanced micro-mixing (improved reaction rates) as well as potential to scale-up under

[a]Department of Chemistry, Bolu Abant İzzet Baysal University, 14030 Bolu, Turkey
[b]Departamento de Química Orgánica, Universidad de Córdoba, Campus de Rabanales, Edificio Marie Curie (C-3), Ctra Nnal IV-A, Km 396, E14014 Cordoba, Spain. E-mail: dailydggs@gmail.com, rafael-luque@uco.es
[c]Peoples Friendship University of Russia (RUDN University), 6 Miklukho-Maklaya Str., 117198 Moscow, Russia

†Electronic supplementary information (ESI) available. See DOI: 10.1039/c8gc03037e

‡These authors contributed equally to this work.

27 A. Kubacka, M. Fernández-García and G. Colon, *Chem. Rev.*, 2012, **112**, 1555–1614.

Q6 28 H. Z. and J. F. Banfield, *J. Phys. Chem. B*, 2000, **104**, 3481–3487.

29 O. Fontelles-Carceller, M. J. Muñoz-Batista, E. Rodríguez-Castellón, J. C. Conesa, M. Fernández-García and A. Kubacka, *J. Catal.*, 2017, **347**, 157–169.

30 C. D. Wanger, W. M. Riggs, L. E. Davis, J. F. Moulder and G. E. Muilenberg, *Handbook of x-ray photoelectron spectroscopy: a reference book of standard data for use in x-ray photoelectron spectroscopy*, Physical Electronics Division, Perkin-Elmer Corp., 1979.

31 A. S. Karakoti, J. E. S. King, A. Vincent and S. Seal, *Appl. Catal., A*, 2010, **388**, 262–271.

32 C. Xu, W. Ouyang, M. J. Munoz-Batista, M. Fernandez-Garcia and R. Luque, *ChemSusChem*, 2018, **11**, 2604–2611.

33 M. J. Muñoz-Batista, O. Fontelles-Carceller, M. Ferrer, M. Fernández-García and A. Kubacka, *Appl. Catal., B*, 2016, **183**, 86–95.

34 A. Naldoni, M. D'Arienzo, M. Altomare, M. Marelli, R. Scotti, F. Morazzoni, E. Selli and V. Dal Santo, *Appl. Catal., B*, 2013, **130–131**, 239–248.

35 C. W. Jung, J. D. Fellmann and P. E. Garrou, *Organometallics*, 1983, **2**, 1042–1044.

36 Y. Huang, V. Adeeva and W. M. Sachtler, *Appl. Catal., A*, 2000, **196**, 73–85.

37 C. Ortiz-Cervantes, I. Iyañez and J. J. García, *J. Phys. Org. Chem.*, 2012, **25**, 902–907.

8.7. *Anexo 7.* Continuous flow synthesis of high valuable N-heterocycles via catalytic conversion of levulinic acid

frontiers in Chemistry

ORIGINAL RESEARCH
published: 26 February 2019
doi: 10.3389/fchem.2019.00103

Continuous Flow Synthesis of High Valuable N-Heterocycles via Catalytic Conversion of Levulinic Acid

Daily Rodríguez-Padrón[1], Alain R. Puente-Santiago[1], Alina M. Balu[1], Mario J. Muñoz-Batista[1] and Rafael Luque[1,2]**

[1] Grupo FQM-383, Departamento de Química Orgánica, Universidad de Cordoba, Cordoba, Spain, [2] Scientific Center for Molecular Design and Synthesis of Innovative Compounds for the Medical Industry, People's Friendship University of Russia (RUDN University), Moscow, Russia

Graphitic carbon nitride (g-C_3N_4) was successfully functionalized with a low platinum loading to give rise to an effective and stable catalytic material. The synthesized g-C_3N_4/Pt was fully characterized by XRD, N_2 physisorption, XPS, SEM-Mapping, and TEM techniques. Remarkably, XPS analysis revealed that Pt was in a dominant metallic state. In addition, XPS together with XRD and N_2 physisorption measurements indicated that the g-C_3N_4 preserves its native structure after the platinum deposition process. g-C_3N_4/Pt was applied to the catalytic conversion of levulinic acid to N-heterocycles under continuous flow conditions. Reaction parameters (temperature, pressure, and concentration of levulinic acid) were studied using 3 levels for each parameter, and the best conditions were employed for the analysis of the catalyst's stability. The catalytic system displayed high selectivity to 1-ethyl-5-methylpyrrolidin-2-one and outstanding stability after 3 h of reaction.

Keywords: N-heterocycles, heterogeneous catalysis, graphitic carbon nitride, continuous flow, platinum, Levulinic acid

OPEN ACCESS

Edited by:
Fabio Aricò,
Università Ca' Foscari, Italy

Reviewed by:
Steve Suib,
University of Connecticut, United States
Svetlana Ivanova,
Universidad de Sevilla, Spain
Christophe Len,
Université de Technologie de Compiègne, France

****Correspondence:***
Mario J. Muñoz-Batista
qo2mubam@uco.es;
jmunoz385x@gmail.com
Rafael Luque
q62alsor@uco.es

Specialty section:
This article was submitted to Green and Sustainable Chemistry, a section of the journal Frontiers in Chemistry

Received: *09 November 2018*
Accepted: *06 February 2019*
Published: *26 February 2019*

Citation:
Rodríguez-Padrón D, Puente-Santiago AR, Balu AM, Muñoz-Batista MJ and Luque R (2019) Continuous Flow Synthesis of High Valuable N-Heterocycles via Catalytic Conversion of Levulinic Acid. Front. Chem. 7:103. doi: 10.3389/fchem.2019.00103

INTRODUCTION

Biomass has emerged as a competitive alternative for the generation of highly sustainable fuels, chemicals, and drugs (Tuck et al., 2012; Sankaranarayanapillai et al., 2015; Ruppert et al., 2016; Hu et al., 2017; Tang et al., 2017; Filiciotto et al., 2018; Kucherov et al., 2018; Xu W. et al., 2018). A useful strategy for converting biomass feedstocks into fuels and chemicals is based on the transformation of platform molecules, which exhibit high functionality, to form added-value compounds (Serrano-Ruiz et al., 2011; Verma et al., 2017). In this direction, levulinic acid (LA) is a well-known platform molecule that has been widely used toward the fabrication of several valuable compounds such as γ-valerolactone (GVL), which represent a promising fuel source, levulinate esters, which are viable additives for gasoline and diesel transportation fuels, and pyrrolidones, which are involved in industry as surfactants, intermediates for pharmaceuticals, dispersants in fuel additive compositions, solvents and agrochemicals (Huang et al., 2011; Bermudez et al., 2013; Colmenares and Luque, 2014; Touchy et al., 2014; Chatzidimitriou and Bond, 2015; Yan et al., 2015; Ruppert et al., 2016; Gao et al., 2017; Sun et al., 2017; Xu C. et al., 2018).

In the last years, the use of heterogeneous catalysts for the valorization of LA into useful compounds, especially pyrrolidones, has been widely applied (Du et al., 2011; Ogiwara et al., 2016). For instance, the reductive amination of LA with amines in liquid phase has been described using precious metals such as Au, Pd, Pt, Ru, In, and Ir, supported on carbon or metal oxides owing

Tang, X., Wei, J., Ding, N., Sun, Y., Zeng, X., Hu, L., et al. (2017). Chemoselective hydrogenation of biomass derived 5-hydroxymethylfurfural to diols: key intermediates for sustainable chemicals, materials and fuels. *Renew. Sustain. Energy Rev.* 77, 287–296. doi: 10.1016/J.RSER.2017.04.013

Touchy, A. S., Hakim Siddiki, S. M. A., Kon, K., and Shimizu, K. (2014). Heterogeneous Pt Catalysts for reductive amination of levulinic acid to pyrrolidones. *ACS Catal.* 4, 3045–3050. doi: 10.1021/cs500757k

Tuck, C. O., Pérez, E., Horváth, I. T., Sheldon, R. A., and Poliakoff, M. (2012). Valorization of biomass: deriving more value from waste. *Science* 337, 695–699. doi: 10.1126/science.1218930

Verma, S., Baig, R. B. N., Nadagouda, M. N., Len, C., and Varma, R. S. (2017). Sustainable pathway to furanics from biomass via heterogeneous organo-catalysis. *Green Chem.* 19, 164–168. doi: 10.1039/C6GC02551J

Wanger, C. D., Riggs, W. M., Davis, L. E., Moulder, J. F., and Muilenberg, E. G. (1979). *Handbook of X-Ray Photoelectron Spectroscopy: A Reference Book of Standard Data for Use in X-Ray Photoelectron Spectroscopy*. Eden Prairie, MN: Physical Electronics Division, Perkin-Elmer Corp.

Wu, C., Zhang, H., Yu, B., Chen, Y., Ke, Z., Guo, S., et al. (2017). Lactate-based ionic liquid catalyzed reductive amination/cyclization of keto acids under mild conditions: a metal-free route to synthesize lactams. *ACS Catal.* 7, 7772–7776. doi: 10.1021/acscatal.7b02231

Xu, C., Ouyang, W., Munoz-Batista, M. J., Fernandez-Garcia, M., and Luque, R. (2018). Highly active catalytic Ru/TiO_2 nanomaterials for continuous flow production of γ-valerolactone. *ChemSusChem* 11, 2604–2611. doi: 10.1002/cssc.201800667

Xu, W., Wang, X., Sandler, N., Willför, S., and Xu, C. (2018). Three-dimensional printing of wood-derived biopolymers: a review focused on biomedical applications. *ACS Sustain. Chem. Eng.* 6, 5663–5680. doi: 10.1021/acssuschemeng.7b03924

Xue, J., Ma, S., Zhou, Y., Zhang, Z., and He, M. (2015). Facile photochemical synthesis of Au/Pt/g-C3N4 with plasmon-enhanced photocatalytic activity for antibiotic degradation. *ACS Appl. Mater. Interfaces* 7, 9630–9637. doi: 10.1021/acsami.5b01212

Yan, K., Jarvis, C., Gu, J., and Yan, Y. (2015). Production and catalytic transformation of levulinic acid: a platform for speciality chemicals and fuels. *Renew. Sustain. Energy Rev.* 51, 986–997. doi: 10.1016/J.RSER.2015.07.021

Zeng, Z., Li, K., Wei, K., Dai, Y., Yan, L., Guo, H., et al. (2017). Fabrication of highly dispersed platinum-deposited porous g-C3N4 by a simple *in situ* photoreduction strategy and their excellent visible light photocatalytic activity toward aqueous 4-fluorophenol degradation. *Chinese J. Catal.* 38, 29–38. doi: 10.1016/S1872-2067(16)62589-5

Zhang, J., Xie, B., Wang, L., Yi, X., Wang, C., Wang, G., et al. (2017). Zirconium oxide supported palladium nanoparticles as a highly efficient catalyst in the hydrogenation-amination of levulinic acid to pyrrolidones. *ChemCatChem* 9, 2661–2667. doi: 10.1002/cctc.201600739

Conflict of Interest Statement: The authors declare that the research was conducted in the absence of any commercial or financial relationships that could be construed as a potential conflict of interest.

The reviewer CL declared a past co-authorship with one of the authors RL to the handling editor.

8.8. *Anexo 8. Patent* P201930227 Procedimiento para la preparación de nanopartículas magnéticas de óxido de hierro a partir de residuos de café expendido.

MINISTERIO DE INDUSTRIA, ENERGIA Y TURISMO

Oficina Española de Patentes y Marcas

Justificante de presentación electrónica de solicitud de patente

Este documento es un justificante de que se ha recibido una solicitud española de patente por vía electrónica utilizando la conexión segura de la O.E.P.M. De acuerdo con lo dispuesto en el art. 16.1 del Reglamento de ejecución de la Ley 24/2015 de Patentes, se han asignado a su solicitud un número de expediente y una fecha de recepción de forma automática. La fecha de presentación de la solicitud a la que se refiere el art. 24 de la Ley le será comunicada posteriormente.

Número de solicitud:	P201930227	
Fecha de recepción:	12 marzo 2019, 16:39 (CET)	
Oficina receptora:	OEPM Madrid	
Su referencia:	EUG-UNIV.CORDOB	
Solicitante:	Universidad de Córdoba	
Número de solicitantes:	1	
País:	ES	
Título:	PROCEDIMIENTO PARA LA PREPARACIÓN DE NANOPARTÍCULAS MAGNÉTICAS DE ÓXIDO DE HIERRO A PARTIR DE RESIDUOS DE CAFÉ EXPENDIDO.	
Documentos enviados:	Descripcion.pdf (7 p.) Reivindicaciones-1.pdf (1 p.) Resumen-1.pdf (1 p.) Dibujos-1.pdf (4 p.) OLF-ARCHIVE.zip	package-data.xml es-request.xml application-body.xml es-fee-sheet.xml feesheet.pdf request.pdf
Enviados por:	CN=ISERN JARA NURIA - 46113085V,givenName=NURIA,SN=ISERN JARA,serialNumber=46113085V,C=ES	
Fecha y hora de recepción:	12 marzo 2019, 16:39 (CET)	
Codificación del envío:	9C:57:44:78:BC:92:37:99:0D:8C:BB:D0:43:45:9A:DA:FD:EC:41:94	

AVISO IMPORTANTE

Las tasas pagaderas al solicitar y durante la tramitación de una patente o un modelo de utilidad son las que se recogen en el Apartado "Tasas y precios públicos" de la página web de la OEPM (http://www.oepm.es/es/propiedad_industrial/tasas/). Consecuentemente, si recibe una comunicación informándole de la necesidad de hacer un pago por la inscripción de su patente o su modelo de utilidad en un "registro central" o en un "registro de internet" posiblemente se trate de un fraude.

La anotación en este tipo de autodenominados "registros" no despliega ningún tipo de eficacia jurídica ni tiene carácter oficial.

En estos casos le aconsejamos que se ponga en contacto con la Oficina Española de Patentes y Marcas en el correo electrónico informacion@oepm.es.

ADVERTENCIA: POR DISPOSICIÓN LEGAL LOS DATOS CONTENIDOS EN ESTA SOLICITUD PODRÁN SER PUBLICADOS EN EL BOLETÍN OFICIAL DE LA PROPIEDAD INDUSTRIAL E INSCRITOS EN EL REGISTRO DE PATENTES DE LA OEPM, SIENDO AMBAS BASES DE DATOS DE CARÁCTER PÚBLICO Y ACCESIBLES VÍA REDES MUNDIALES DE INFORMÁTICA.

Para cualquier aclaración puede contactar con la O.E.P.M.

/Madrid, Oficina Receptora/